THE UNIVERSITY OF CHICAGO

PRECISE MEASUREMENTS OF THE PARAMETERS ϕ_{+-}, Δm, AND τ_S IN THE NEUTRAL KAON SYSTEM AND TESTS OF CPT SYMMETRY

A DISSERTATION SUBMITTED TO
THE FACULTY OF THE DIVISION OF THE PHYSICAL SCIENCES
IN CANDIDACY FOR THE DEGREE OF
DOCTOR OF PHILOSOPHY

DEPARTMENT OF PHYSICS

BY
ROY A. BRIERE

CHICAGO, ILLINOIS
JUNE, 1995

ACKNOWLEDGMENTS

First I would like to thank my advisor, Bruce Winstein. He rescued me from countless hours of complicated theoretical physics and introduced me instead to countless hours of complicated experimental physics. His insightful ability to see through to the physics in our data has been an inspiration.

I would also like to thank Bob Sachs who first introduced me to the wonders of the neutral kaon. He tried to teach me to be a practical theorist, one in touch with the experiments. I hope I haven't gone too far overboard on that last bit of advice!

My thesis committee of B. Winstein, E. Blucher, K. Levin and R.G. Sachs provided valuable comments on this manuscript.

It was a great pleasure to participate in data taking for E773 and E799 at Fermilab. The lab staff helped to make it a successful run for both experiments.

The core working group for E773 analysis included Elliott Cheu, Pete Haas, Bill Hogan, John Matthews, Bernhard Shwingenheuer, Sunil Somalwar, and Bruce Winstein. Pieces of their hard work are scattered throughout this thesis. I should also acknowledge the long hours of the Fermilab gang of Greg Bock, Rick Coleman, Janice Enagonio, Rick Ford, Bob Hsiung, Erik Ramberg, Bob Tschirhart, and Taku Yamanaka who were heavily involved in getting our detector up and running. I'd also like to thank our spokesman for E773, George Gollin, for suffering through the practical dealings with Fermilab and making this experiment happen. It was a relief to leave the worrying for the 'other experiment', E799, to Yah Wah and Taku and friends; many fine papers came of their efforts.

I should also mention the physicists who have collaborated on the long sequence of kaon experiments at FNAL that led up to E773. Long live regenerators! I am particularly grateful

to the E731 group, especially Magnus Karlsson, Vaia Papadimitriou, Ritchie Patterson, and Hitoshi Yamamoto, who I had the pleasure of working with before they moved on. I've also benefitted from interactions with the new KTeV collaborators, both at Chicago and elsewhere. The electronics and mechanical shops at Chicago were very helpful with our E773 hardware. Thanks go to Harold, Mike, John, Son, Frank, Juanita, Dick, and Elizabeth. And then there's the HEP group at Chicago...I don't think the intensity and degree of interest in physics here can be truly appreciated without experiencing it firsthand.

To Bernhard Schwingenheuer, my cohort in all matters E773, what can I say after all these years? Bernhard always kept me honest with my explanations of things; even if he agreed at first (usually because I talk fast), he came back later to point out the flaws. I don't think either of us will ever be quite the same after all those years sitting at the 'klong' and 'kshort' terminals. Good luck in Germany!

A special thanks is due to Lawrence Gibbons, who taught me both how to do analysis as well as how to make pasta. We spent many fine moments immersed in fine food, spirits and physics. I am especially indebted to him for teaching me about drift chambers and causing me to hate computers just a little bit less than I once did. In addition, I have shamelessly stolen a figure or two from his thesis. And of course, to the staffs of the Hotel Patterson and Hotel Cheu, I appreciated the space. Thanks also to Jim Romano for teaching me a useful trade during grad school and to Lucy Fortson for keeping me sane in the final months. I am still sane, right?

The stress of eight and a half years of graduate school takes its toll on relationships of any sort, but particularly on close ones. Special thanks go to Malinda and Pam for their friendship and support over the years.

Finally, I thank my parents and family for their constant encouragement and support since I was a child. I'm sure they've long since lost track of exactly what it is that I study, but they stand by me nonetheless. It's nice to be trusted, even as an eccentric academic.

Thank God it's over!

TABLE OF CONTENTS

LIST OF TABLES

LIST OF ILLUSTRATIONS

ABSTRACT

This thesis describes the measurement of several parameters of the neutral kaon system by the E773 experiment at the Fermi National Accelerator Laboratory (Fermilab).

A measurement of ϕ_{+-}, the phase of the CP-violating amplitude ratio η_{+-}, has been made. The result, $\phi_{+-} = 43.53^{\circ} \pm 0.97^{\circ}$, helps limit CPT-violating effects in the kaon system.

Precise determinations of the K_S lifetime, τ_S, and the $K_L - K_S$ mass difference, Δm, have also been made, yielding $\tau_S = (0.8941 \pm 0.0017) \times 10^{-10}\, s$ and $\Delta m = (0.5297 \pm 0.0037) \times 10^{10}\, \hbar s^{-1}$.

CHAPTER 1

INTRODUCTION

> "Anyone who has played with these invariances knows that it is an orgy of relative phases."— *Abraham Pais, Inward Bound*

Symmetry principles have a long history in physics. In particular, the symmetries of space-time have been an integral part of the physics of the last century. The mathematical transformation properties of space-time are embodied in the Poincare group. Continuous symmetries of the Poincare group are associated with conservation laws (of energy, momentum and angular momentum) via the well-known Noether's Theorem [1].

The discrete symmetries of space-time are also important, but they only achieve their full power in quantum field theories. This fact has been discussed in terms of the linear superpositions of states allowed in quantum theory (see Wigner [2], who credits a remark by C.N. Yang). It is the validity of certain of these symmetries that will concern us in this thesis.

1.1 The Discrete Symmetries P, C and T

We now describe in more detail each of the discrete symmetries. These include

- Parity, or space-inversion, denoted by P.
- Charge-conjugation, the interchange of particle and antiparticle, denoted by C.
- Time-reversal, the inversion of the time coordinate, denoted by T.

1.1.1 Early History of Discrete Symmetries

We note that a useful source of historical references may be found in Ref. [3].

The parity operation was first introduced into quantum mechanics by Wigner in 1928 [4, 5]. He used parity to explain the LaPorte rules [6, 7] for atomic transitions in terms of the symmetries of the wavefunctions and transition operators. In quantum field theory, where particles are described as field excitations which may be created and destroyed, there is an additional twist: the particles themselves have *intrinsic* (relative) parities.

Parity was generally assumed to be a valid symmetry for all interactions for many years. An early criticism of such assumptions was given by Purcell and Ramsey in 1950 [8], where experimental tests were encouraged. In particular, Ramsey began efforts to determine the parity-violating electric dipole moment (EDM) of the neutron.

The questionable nature of the assumption of parity invariance was again emphasized by Lee and Yang in 1956 [9]. They realized that the available data on weak interactions did not test the question of parity. Several experiments were suggested and subsequently mounted. Shortly thereafter, three independent groups announced that parity was indeed violated in weak interactions [10, 11, 12]. These experiments studied nuclear β-decay, π decay, and μ decay.

Symmetry under charge-conjugation was embodied in the Dirac equation [13] that led to the prediction of the positron. The well-known Furry Theorem [14] is a consequence of this symmetry. More explicit formulations were given by Majorana [15] and Kramers [16]. The same experiments that demonstrated parity violation also implied that charge-conjugation symmetry was violated by weak interactions as well.

It was soon realized that the shock of parity violation could be partially ameliorated. If one assumed that the combined operation of charge conjugation and parity, CP, was a good symmetry, many nice results were obtained [17, 18]. First, Ramsey's search for a P-violating neutron EDM had resulted in stringent limits, but no measurable effect. Landau pointed out [18] that an EDM would also violate time-reversal symmetry. It had recently been shown [19, 20, 21, 22, 23, 24, 25, 26], as discussed further below, that the combined operation of CPT was a good symmetry for a very general class of theories. Thus, the

EDM also violates CP, and CP symmetry would explain its absence. Furthermore, the peculiar behavior of neutral kaons had been beautifully explained with the use of C-even and C-odd mixtures of states [27]. It was now realized that, although C was violated, the same formalism could be derived in terms of CP-even and CP-odd states. But nature had more in store for us!

In 1956, Sachs and Treiman [28] investigated the general behavior of the $K^0 - \bar{K}^0$ system, basing their discussion on the Wigner-Weisskopf method [29, 30] of treating perturbations of degenerate states. In particular, they explicitly discuss the possibility of interference and non-exponential decay curves. In 1957, Lee, Oehme and Yang [31] further developed the general treatment in a more well-known paper. Although CPT symmetry was assumed, the authors considered the possibility of CP violation in the system in detail for the first time.

Most physicists still believed that CP was a more general replacement for the now defunct idea of parity invariance and was an exact symmetry of nature. It came as a surprise to most when, in 1964, CP violation was reported in the neutral kaon system by Christenson, Cronin, Fitch and Turlay [32]. We will discuss precisely what they observed later.

The time-reversal operation was introduced by Wigner in 1932 [33]. The T operator is distinguished from the preceeding two by its anti-unitary nature. In general, one can write $T = UK$, where U is a unitary operator and K is complex conjugation. We note that the other discrete symmetries may be represented by unitary operators.

As a result of its anti-unitarity, some care is necessary in looking for T-violation in observables. Final state interactions (FSI) may mimic T-violating effects [34, 35]. Also, since T is anti-unitary, there is no quantum number associated with the transformation. One can, however, show that T^2 has eigenvalues ± 1, with the particular value depending on the spin of the system [34, 35]. This is the basis for the well-known Kramers degeneracy [36].

It is worth pointing out that there is no *direct* evidence for T violation. If one is willing to assume CPT invariance, then T violation follows from the observed CP violations. It is possible to produce arguments showing that any CPT violation is at most about 10%

of the size of CP violation [34]; this therefore implies that most, if not all, of the known CP violation is accompanied by T violation. However, no T-violating observable has ever been directly measured to be non-zero. In Chapter 10, we summarize the current state of experiments; we mention that explicit T violation will likely be established in the next few years.

1.1.2 The CPT Theorem

The combined operation of all three discrete symmetries has a special place in local relativistic quantum field theories. A very general result, known as the CPT theorem, states that this symmetry is valid for all such theories. The proof of the CPT theorem is based on very general principles [19, 21, 22, 23, 24, 25, 26]:

- Hermitian observables
- Lorentz invariance
- Weak locality.

The requirement of Hermiticity guarantees that for any interaction term, the corresponding term with the conjugated field operators also exists; this is necessary due to the C in CPT. The requirement of Lorentz invariance is natural, given the space-time nature of P and T. Weak locality is related to the (anti-)commutation properties of the field operators and is essentially the same as the spin-statistics theorem. A summary of all of these interrelated issues may be found in Ref. [37]. We also mention that some care is necessary when considering CPT in a context including general relativity [38].

It is CPT symmetry that we are interested in testing. We briefly list, then, some consequences of CPT symmetry. First, the masses and lifetimes of particle and anti-particle must be equal and their magnetic moments equal and opposite. We caution the reader that *partial* decay widths need not be equal [34]. A summary of current tests is given in Ref. [39]. With a few notable exceptions, the results test the fractional differences of parameters to at best a few parts in 10^5.

We now list the most sensitive tests [39]; in all cases, the denominator is the average value of the parameter for particle and anti-particle. The proton and antiproton mass difference is

$$\frac{(m_p - m_{\bar{p}})}{< m >} = (2 \pm 4) \times 10^{-8} \tag{1.1}$$

while the electron and positron masses obey

$$\frac{(m_{e^+} - m_{e^-})}{< m >} < 4 \times 10^{-8} \text{ at } 90\% \text{ CL.} \tag{1.2}$$

The difference of the μ^+ and μ^- g-factors (essentially, their magnetic moments) is

$$\frac{(g_{\mu^+} - g_{\mu^-})}{< g >} = (-2.6 \pm 1.6) \times 10^{-8} \tag{1.3}$$

and the same quantities for the electron and positron are

$$\frac{(g_{e^+} - g_{e^-})}{< g >} = (-0.5 \pm 2.1) \times 10^{-12}. \tag{1.4}$$

These limits are the results of very clever experimental techniques. Finally, we have the most stringent limit, where the cleverness is supplied by nature herself in the neutral kaon system:

$$\frac{(m_{\bar{K}^0} - m_{K^0})}{< m >} < \times 10^{-18} \text{ at } 90\% \text{ CL.} \tag{1.5}$$

This stringency of this last result can only be properly understood in the context of the detailed behavior of the neutral-kaon system. This behavior is the subject of the rest of this chapter, and most of the parameters necessary to obtain this type of limit are measured in this thesis.

1.2 The Neutral Kaon System: General Features

We hope the reader has gained some perspective on the history of discrete symmetries in particle physics and now turn to a detailed discussion of the neutral kaon system. We have tried to structure things in an easily digested manner, with frequent reference to the early experimental work that was so crucial to the theoretical developments; we apologize for any unintentional omissions. The treatment is more historical than most, but we believe this may be instructive.

It must be remembered that during the early 1950s, many of the ideas that form the basis of our current understanding of particle physics, in particular the weak interaction, were just being uncovered. In particular, the concept of strangeness and quark flavor mixing and the realization that parity was violated are completely entangled with the history of the kaon system.

We first discuss some of the general features of the neutral kaon system which occur *independently* of any discrete symmetry violations. In fact, many of these features follow from the approximate validity of these and other symmetries. Not only do the properties form the stage on which the symmetry violations will play themselves out, but they are intriguing in their own right. There are many excellent references covering the detailed history of this period, among them Refs. [40, 41, 42, 43].

1.2.1 The Strangeness Quantum Number and the Two Neutral Kaons

In 1944, the observation of a single charged-kaon event was reported [44]. The observation consisted of an elastic kaon-electron scattering in a cloud chamber and was sufficient to obtain an accurate mass for the new particle.

In 1947, Rochester and Butler [45] at Bristol reported two unique events observed in their cloud chamber. The first was a 'forked track'; in retrospect, this was a likely a $K \to \pi^+\pi^-$ decay. This was the first example of what became known as neutral V decays, due to their striking topology. The second was a 'kinked track': likely a charged kaon decay of the form $K^+ \to \pi^+ X$ or $K^+ \to \mu^+ X$, where X denotes unobserved neutrals. The first example of a 'tau' decay was observed in emulsion in 1949 [46]; in modern language, the process seen was $K^+ \to \pi^+\pi^+\pi^-$.

By 1951, it became clear that there were two types of neutral V decays, due to $\Lambda \to p\pi^+$ and $K \to \pi^+\pi^-$decays. Important work in this regard was done by both the Manchester [47, 48] and Indiana [49] groups. The former group had the larger statistics, but R. Thompson, at Indiana, performed very precise measurements of his events. In 1953, accelerators began to contribute new results [50, 51].

All of these new particles, including hyperons and kaons, had the following curious prop-

erty: although they were produced fairly abundantly, they had anomalously long lifetimes. The lifetimes were in fact about 10 *orders of magnitude* larger than expected on the basis of the coupling strengths deduced from their production.[1] Many ideas were advanced to explain this 'strange' behavior, [52, 53, 54, 55, 56] and among them was the successful idea of associated production. In this picture, the new particles were copiously produced in pairs, but were slow to decay singly, due to the particular structure of the interaction terms.

A more concrete attempt to systematize this was given by Pais in 1952 [57]. His 'Even-Odd rule' stated that only an even number of the new particles could be involved in any strong interaction; this was consistent with the idea of associated production. Any interaction term with an odd number of the new particles involved a distinct, weaker type of interaction. It is interesting to note that all previously known very weak interactions (β-decay, π decay and μ decay) had involved a neutrino. In many of the new particle decays, all decay products had been observed; thus, there were sometimes no neutrinos. Observation of the predicted *pairs* of the new particles proved to be very difficult with the low rates from cosmic rays. Explicit observation of associated production was reported in 1954 [58] by a group working at the Brookhaven Cosmotron. The Even-Odd rule effectively introduced a multiplicative quantum number, even for old particles (p, n, e, μ, π, ν) and odd for new (K, Λ), that was conserved in strong interactions.

A hint of the insufficiency of the Even-Odd rule had already been observed by the Manchester group [59]. They observed a single example of a 'cascade' decay: a parent particle decayed slowly into secondaries including a slowly-decaying V particle. Thus, there was a cascade of these novel new decay processes. In Pais's scheme, the parent particle (a Ξ^- in modern language) would be an even particle and presumably be allowed to undergo a strong decay.

Some organization among the new particles could be found by attempting to arrange similar-mass states into isospin multiplets. The relation between isospin and charge was already known to be different for the π mesons and the nucleon; one can express the relation as: $Q = I_3 + B/2$, where Q and B are charge and baryon number, and I_3 is the third component of isospin. The new, strange particles lived up to their name, and seemed to

[1] We mention that it was this same sort of mismatch of observed and predicted interaction that had led to confusion when the μ was thought to be Yukawa's exchange particle, the π.

require a different relation still. A more complete picture soon emerged, in terms of a new additive quantum number [60, 61, 62, 63, 64], known as 'η-parity', or 'strangeness'. A new quantum number of strangeness, S, was introduced and the isospin-charge relation was successfully amended to read: $Q = I_3 + (B + S)/2$. Eventually, this was all to be neatly systematized in the quark model of hadrons. Observation of pairs of Ks produced together [65, 66, 67, 68], as opposed to $K\Lambda$, provided further confirmation for the associated production and strangeness ideas.

It is interesting to look at a snapshot of what was know during this period. One such summary is found in a particle properties table from 1956 [69]. The list of new particles included the $\Lambda, \Sigma^+, \Sigma^-, \Xi^-$ hyperons, the θ^0 $(K_S \to \pi^+\pi^-)$, θ^+ $(K^+ \to \pi^+\pi^0)$, and $\tau^\pm$ $(K^\pm \to 3\pi)$ mesons, and many other semileptonic $K^\pm$ meson decay modes.

As data accumulated, it became clear that some of the plethora of observed meson decays might simply be alternate decay modes of one state. This does not seem surprising to the modern particle physicist, but we should remember that other unstable particles, such as the μ and π, were only known to have one decay mode each. In particular, the θ^+ and τ^+ modes seemed to come from parent particles of like mass, within small experimental errors. In a brilliant analysis, Dalitz [70, 71] showed that the 2π decay mode of the θ^+ and the 3π decay mode of τ^+ required the parent particles to have opposite intrinsic parity. There were only two solutions to this 'tau-theta puzzle': either the states were distinct and the close masses an accident, or parity was violated. For a time, theorists toyed with the idea of parity-doublets of particles and other similar explanations. This puzzle remained a mystery until the work of Lee and Yang [9]. After they pointed out the lack of an experimental basis for the assumption of parity conservation in weak interactions, experiments soon observed parity violation [10, 11, 12]. The puzzle was solved: the parent particles were the same, but parity was violated in the decays. Of course, there was now the new puzzle of discrete symmetry violation, a puzzle which still interests us greatly today.

All of the above phenomenology is neatly contained with our current picture of particles and interactions. In terms of the quark model, neutral kaons are members of a flavor SU(3) pseudo-scalar meson octet that also includes the $K^\pm$, the $\pi^\pm$ and π^0, and the η. The quark contents are $K^0 = (d\bar{s})$; $\bar{K}^0 = (\bar{d}s)$. These states are stable and degenerate with respect

to strong interactions, with a mass of about 0.5 GeV/c^2. The Λ has quark content (uds); associated production is just due to strong production of $s\bar{s}$ pairs, which then appear as constituents of pairs of strange particles. The strangeness quantum number is simply # ($\bar{s}$ quarks) − # (s quarks). Quark flavors, such as strangeness, are conserved by strong interactions; only the weak interaction changes flavors, accounting for the long lifetimes of strange particles.

Kaons were also involved in much of the subsequent excitement in particle physics in the 1960s. Among the issues they touched are quark mixing and weak neutral currents. In order to make the weak interactions of quarks, as evident in the decays of strange particles, and leptons, as evidenced in muon decay, universal, it was necessary to introduce mixtures of quarks. A linear combination of the s and d quarks, parameterized by the Cabibbo angle [72], participates in the weak interaction. This marked the beginnings of the modern CKM Matrix [73]. In addition, the absence of flavor-changing neutral-current (FCNC) effects in kaon decays lead to the presumption that weak neutral currents did not exist. The currents were, however, predicted if the eventually successful Weinberg-Salaam model [74] of weak leptonic interactions was extended to the quark sector. Soon, the absence of FCNC was understood, in terms of the GIM mechanism [75], leading to the prediction of a fourth, 'charm' quark. Weak neutral currents and the charm quark were indeed observed. Kaons have had a rich history, but we must now return specifically to the neutral kaon system in order to continue our journey in search of CPT violation.

1.2.2 K^0-$\bar{K}^0$ Mixing

The existence of two distinct neutral kaons, isospin partners of the two charged kaons, is predicted in Refs. [60, 76]. This observation was of central importance in understanding the behavior of neutral kaons.

In 1955, Gell-Mann and Pais [27] pointed out some interesting consequences of having two distinct neutral states. In particular, using arguments based on C invariance (later amended to be CP invariance), they showed that the physical states would be mixtures of

the states produced. That is, K^0 and $\bar{K}^0$ were produced by the strong interactions, but the decay states of definite lifetime would be linear combinations of these states.

The physics involved is straightforward. We have a two-state system, degenerate under the strong interaction. The degeneracy is broken via the weak interaction, which does not conserve the quantum number of strangeness, S. The K^0 has $S = +1$ and the $\bar{K}^0$ has $S = -1$. First-order weak interactions allow transitions with $\Delta S = \pm 1$. This not only renders kaons unstable, but allows for the possibility of K^0-$\bar{K}^0$ mixing. This mixing is possible due to the existence of common final states into which both the K^0 and $\bar{K}^0$ may decay. The weak interaction acts as a perturbation, generating an off-diagonal matrix element, $\langle K^0 \mid H \mid \bar{K}^0 \rangle \neq 0$, from second-order processes such as $K^0 \to \pi^+\pi^- \to \bar{K}^0$.

In order to go further, we need to get more mathematical. We take the action of the CP operation to be

$$CP \; |K^0\rangle = |\bar{K}^0\rangle \tag{1.6}$$

$$CP \; |\bar{K}^0\rangle = |K^0\rangle. \tag{1.7}$$

There is a freedom of the choice of phase when defining the CP operation, but there is no gain in maintaining an arbitrary phase; we choose the convenient one shown above. Let us further define the symmetric and anti-symmetric linear combinations

$$|K_\pm\rangle \equiv (|K^0\rangle \pm |\bar{K}^0\rangle)/\sqrt{2} \tag{1.8}$$

so that

$$CP \; |K_\pm\rangle = \pm \; |K_\pm\rangle. \tag{1.9}$$

Recall that the $\pi\pi$ final state from kaon decay is required by angular momentum considerations to be in an S-wave, such that

$$CP \; |\pi\pi\rangle = + \; |\pi\pi\rangle. \tag{1.10}$$

Therefore, we see that

$$K_+ \;\; \to \;\; \pi\pi \qquad CP - \text{allowed} \tag{1.11}$$

$$K_- \;\; \to \;\; \pi\pi \qquad CP - \text{violating}. \tag{1.12}$$

The $\pi\pi$ final state dominates the K_+ decay rate. The suppression of $K_- \rightarrow \pi\pi$ leads to states with very different lifetimes. The state rapidly decaying to $\pi^+\pi^-$ was already well-known; Gell-Mann and Pais now predicted the existence of a second, long-lived neutral-kaon state.[2] Note that the fact that the (mostly) CP-odd state is longer lived is merely due to the small partial widths for the allowed three-body decays, largely explained by phase-space considerations and the enhancement of the $\Delta I = 1/2$ transitions which contribute to the $\pi\pi$ modes. We denote the short- and long-lived states as K_S and K_L, respectively. If CP was a good symmetry, we could identify K_S with K_+ and K_L with K_-. This is still a good approximation, since CP-violating effects are known to be small. The long-lived K_L state was first observed in 1956 [78, 79].

Several groups [80, 81, 82] observed the $\bar{K}^0$ component in the K_L via strong-interaction production of hyperons, where this strong production is presumed to conserve strangeness. Eisler, *et al.* [83], determined that about half of the neutral kaons produced escaped their chamber without decaying, as expected.

Strangeness oscillations were further investigated in 1958 [84] and used to give the first crude measure of the K_L-K_S mass difference, Δm. This experiment was performed with a cloud chamber at Brookhaven Cosmotron; K^0 were produced by a low-energy π^- beam and later seen to interact as $\bar{K}^0$ via hyperon production.

1.2.3 Regeneration of K_S from K_L

The possibility of regenerating the short-lived eigenstate from the long-lived one was first pointed out by Pais and Piccioni [85] in 1955. They noted that, since the $\bar{K}^0$ was more strongly absorbed in matter, passing a beam of K_L through material would alter the relative sizes of the K^0 to $\bar{K}^0$ components in the wavefunction. Just as passing a horizontally-polarized light beam through a diagonal polarizer results in the vertical component reappearing, the K_S state is present in the exiting beam (This analogy is in fact

[2] There is perhaps no better illustration of the confusion of the 'tau-theta' puzzle in these days than a paper published after Gell-Mann and Pais' work. The publication in question [77] discusses the hypothetical neutral partner, τ^0, of the τ^+ meson, concluding that it, too, must be a particle mixture having long- and short-lived components, noting the generality of the Gell-Mann and Pais arguments. In fact, Gell-Mann and Pais' long-lived θ^0 *is* the τ^0! The article is otherwise quite sound, but the insight to identify these particles would have to await the downfall of parity.

used in the original Pais-Piccioni paper). In particular, if f ($\bar{f}$) is the scattering amplitude for K^0 ($\bar{K}^0$), then one has, after a single scatter

$$\begin{aligned} |K_L\rangle &\sim |K^0\rangle - |\bar{K}^0\rangle \\ \text{scatters} &\rightarrow f\,|K^0\rangle - \bar{f}\,|K^0\rangle \\ &\sim (f+\bar{f})\,|K_L\rangle - (f-\bar{f})\,|K_S\rangle. \end{aligned} \tag{1.13}$$

A numerical look at the problem was undertaken by Case [86] in 1956. Much of the difficulty perceived at the time was caused by the low energy of the kaons available: it was difficult for them to exit the regenerator medium before decaying. A more detailed analysis of the process was performed by M.L. Good [87]. Good distinguished between 'transmission' regeneration and 'diffractive' regeneration. The former is due to coherent effects of different K^0 and $\bar{K}^0$ scattering in the forward direction. The latter is due to the difference in scattering at finite angles (diffraction). The distinction is far from an academic one! Good realized that the forward process would remain coherent over macroscopic distances. The coherence is quickly lost away from the forward direction; the forward region is typically contained within a micro-radian. This seminal paper also contains the first calculation of the relative number of coherent events and near-forward diffractive events underlying the coherent peak (often called the 'Good ratio'). Given the narrow intrinsic width of the peak, this ratio depends on the experimental resolution in determining the scattering angle. However, the ratio contains further interesting physics pertaining to the length of the regenerator as well. Regeneration was cleanly observed in 1960 [88]; other significant early work is described in Ref. [89].

The net effect of transmission regeneration is that an incident $|K_L\rangle$ state is transformed into

$$(|K_L\rangle \;+\; \rho\;|K_S\rangle) \tag{1.14}$$

where

$$\rho \;=\; i\pi N L\,[(f-\bar{f})/k]\;\; g(L). \tag{1.15}$$

N is the number density of nuclei, L is the regenerator length, $\hbar\, k$ is the kaon momentum, and $g(L)$ is a 'geometric' correction for the time evolution of the regenerated K_S relative to the K_L as they traverse the regenerator. The amplitudes f and $\bar{f}$ are understood to be

those in the forward direction. The $K \to \pi\pi$ decay rate downstream of a regenerator is given by

$$\begin{aligned} R_{\pi\pi} &\sim |\rho/\eta|^2 \; e^{-\Gamma_S t} \\ &+ \; e^{-\Gamma_L t} \\ &+ \; |\rho/\eta| \; e^{-(\Gamma_S+\Gamma_L)\, t/2} \; cos\,(\Delta m t + \phi_\rho - \phi_\eta) \end{aligned} \tag{1.16}$$

where η is the amplitude ratio

$$\eta = \frac{\langle\, \pi\pi \mid H \mid K_L \,\rangle}{\langle\, \pi\pi \mid H \mid K_S \,\rangle}. \tag{1.17}$$

At high energies, regeneration is dominated by the ρ and ω Regge poles (see Appendix D), and one expects

$$\frac{f - \bar{f}}{k} \sim p^{\alpha - 1}. \tag{1.18}$$

Analyticity of the scattering amplitude then gives (see Appendix C)

$$\phi_{f-\bar{f}} = -\frac{\pi}{2}(1 + \alpha). \tag{1.19}$$

The phase $\phi_\rho = \pi/2 + \phi_{f-\bar{f}} + \phi_g$, where ϕ_g is the easily calculated phase of the geometric correction term.

We refer the interested reader to Appendix F, as well as the original papers, for further discussions and references concerning regeneration.

1.3 The Neutral Kaon System: Symmetries and Mixing

We now turn to the well-known phenomenology of CP violation in the kaon system. We will discuss the more complicated case of CPT violation in parallel. Note that we treat the phenomenology with the standard two-state formalism of Lee, Oehme and Yang [31]. If CPT breaks down, this implies that one of the general principles in its proof is invalid. One should bear in mind that the same principle which breaks down may be implicit in other parts of our analysis. However, this is the standard treatment, and we use it to obtain phenomenological parameterization of possible CPT-violating effects. There are many treatments of the phenomenology worthy of study. We first mention the pioneering work of Sachs [90, 91] and some classic early reviews [92, 93]. There is also the oft-quoted

treatment of Barmin, *et al.* [94], and an excellent paper with special emphasis on K^0-$\bar{K}^0$ tagging [95]. A recent book on T symmetry [34] treats all the discrete symmetries in a complete fashion. The past few years have seen a resurgence of interest in CPT phenomenology, resulting in many papers [96, 97, 98, 99, 100, 101], often with emphasis on specific aspects of the theory.

The term *indirect* CP violation is used to describe effects due to CP-violating asymmetries in K^0-$\bar{K}^0$ mixing; these are $\Delta S = 2$ processes. In contrast, *direct* CP violation refers to CP violation in the decay process; these are $\Delta S = 1$. A model with direct CP violation will generally also include indirect effects via higher-order interactions. The converse is *not* true, however: it is possible to entertain theories that possess CP violation only in connection with a $\Delta S = 2$ interaction term. Such an idea was put forth by Wolfenstein [102] shortly after the discovery of CP violation. The idea was motivated by the weakness of the newly found effect, even in comparison to the usual weak interaction. The term 'superweak' was coined for a hypothetical new $\Delta S = 2$ interaction potentially responsible for CP violation. This class of theories can be disproved by an observation of direct CP violation. However, 30 years have been insufficient to disprove the superweak hypothesis [103]. We note, however, that the absence of a direct CP-violating effect cannot prove the superweak hypothesis.

We will use the terms indirect and direct in an analogous sense for CPT violation. For the case of indirect symmetry violations, the additional baggage of not assuming CPT is relatively light.

1.3.1 Indirect CP and CPT Violation

Consider the 'mass matrix' for the neutral kaon system:

$$\mathbf{M} = M - \frac{i}{2}\Gamma = \begin{pmatrix} M_{11} - \frac{i}{2}\Gamma_{11} & M_{12} - \frac{i}{2}\Gamma_{12} \\ M_{12}^* - \frac{i}{2}\Gamma_{12}^* & M_{22} - \frac{i}{2}\Gamma_{22} \end{pmatrix}. \tag{1.20}$$

The component matrices, M and Γ are each Hermitian, $M = M^\dagger$ and $\Gamma = \Gamma^\dagger$; we have taken advantage of this in writing the matrix. The matrix elements are given by

$$\mathbf{M_{12}} = M_{12} - \frac{i}{2}\Gamma_{12} = \langle\, K^0 \mid \mathbf{M} \mid \bar{K}^0 \,\rangle \tag{1.21}$$

and so on, where the subscript 1 (2) denotes K^0 ($\bar{K}^0$). It is easily shown that [104]

$$M_{ij} = m_0\delta_{ij} + \langle\, i \mid H \mid j \,\rangle + \sum_f P\left(\frac{\langle\, i \mid H \mid f \,\rangle\langle\, f \mid H \mid j \,\rangle}{m_0 - E_f}\right) \tag{1.22}$$

$$\Gamma_{ij} = 2\pi\sum_f \langle\, i \mid H \mid f \,\rangle\langle\, f \mid H \mid j \,\rangle\delta(m_0 - E_f). \tag{1.23}$$

Symmetries impose constraints on the mass matrix elements; see Ref. [101], for example. Either CPT or CP invariance would require that

$$M_{11} = M_{22} \tag{1.24}$$

$$\Gamma_{11} = \Gamma_{22} \tag{1.25}$$

while either CP or T invariance would require that

$$|M_{12} - \frac{i}{2}\Gamma_{12}| = |M_{12}^* - \frac{i}{2}\Gamma_{12}^*|. \tag{1.26}$$

Note that there are two possibilities for CP violation, depending whether it is accompanied by T or CPT violation. The CP constraint is only on the magnitude of the off-diagonal elements because of the phase freedom between the K^0 and $\bar{K}^0$ states which makes the phase of the off-diagonal elements phase-convention dependent.

The evolution of the wavefunction, in the kaon rest-frame, is given by[3]

$$-i\hbar\frac{d\psi}{dt} = \mathbf{M}\psi \tag{1.27}$$

and the eigenvalues and states are

$$\mathbf{M}\ |K_S\rangle = \lambda_S\ |K_S\rangle \qquad \mathbf{M}\ |K_L\rangle = \lambda_L\ |K_L\rangle \tag{1.28}$$

where

$$\lambda_{S,L} = m_{S,L} - \frac{i}{2}\Gamma_{S,L}. \tag{1.29}$$

We also define

$$\Delta m \equiv m_L - m_S \qquad \Delta\Gamma \equiv \Gamma_S - \Gamma_L. \tag{1.30}$$

Note the sign difference in the definitions of Δm and $\Delta\Gamma$; with these definitions, both quantities are positive. Experiments find $\Gamma_S/\Gamma_L \simeq 580$ and $2\Delta m \simeq \Gamma_S \ll m_{S,L}$.

[3]It is important to remember that this is not a 'real' Schroedinger equation. The results of the detailed perturbation theory calculation may be conveniently expressed in this form, but incorrect results are easily obtained upon misinterpretation of such equations. We thank R.G. Sachs for emphasizing this point to us.

We write the eigenstates as (c.f. Eqn. 1.8)

$$\begin{aligned} |K_S\rangle &\sim (1+\varepsilon_K+\delta_K)|K^0\rangle + (1-\varepsilon_K-\delta_K)|\bar{K}^0\rangle \\ &\sim |K_+\rangle + (\varepsilon_K+\delta_K)|K_-\rangle \qquad (1.31) \\ |K_L\rangle &\sim (1+\varepsilon_K-\delta_K)|K^0\rangle - (1-\varepsilon_K+\delta_K)|\bar{K}^0\rangle \\ &\sim |K_-\rangle + (\varepsilon_K-\delta_K)|K_+\rangle. \qquad (1.32) \end{aligned}$$

We have introduced the small symmetry-violation parameters ε_K and δ_K: ε_K violates CP and T, while δ_K violates CP and CPT. These parameters summarize all the CP-violating effects of mixing. Expressions relating these parameters to the elements of the mass matrix are given in Appendix A.

There are 8 degrees of freedom in the complex 2×2 matrix $\mathbf{M}$. Of these, 7 appear as physical parameters: m_S, m_L, Γ_S, Γ_L, $\mathrm{Re}\varepsilon_K$ and δ_K. One arbitrary phase choice affects the off-diagonal entries. This is why ε_K is only one degree of freedom: $\mathrm{Im}\varepsilon_K$ is dependent on the particular phase chosen. We will see later that this phase freedom affects the splitting of a physical parameter into portions arising from $\mathrm{Im}\varepsilon_K$ and a particular decay amplitude.

We define the customary CP-violating amplitude ratios

$$\eta_{+-} = \frac{\langle\, \pi^+\pi^- \mid H \mid K_L \,\rangle}{\langle\, \pi^+\pi^- \mid H \mid K_S \,\rangle} \qquad (1.33)$$

$$\eta_{00} = \frac{\langle\, \pi^0\pi^0 \mid H \mid K_L \,\rangle}{\langle\, \pi^0\pi^0 \mid H \mid K_S \,\rangle} \qquad (1.34)$$

and a natural (superweak) phase

$$\phi_{SW} = tan^{-1}(2\Delta m/\Delta\Gamma) \simeq 43^\circ. \qquad (1.35)$$

If there is only indirect CP violation, then we have[4]

$$\eta_{+-} = \eta_{00} = \varepsilon_K - \delta_K. \qquad (1.36)$$

We next introduce the lepton asymmetry in K_L decay,

$$\delta_\ell = \frac{N(K \to \pi^-\ell^+\nu) - N(K \to \pi^+\ell^-\bar{\nu})}{N(K \to \pi^-\ell^+\nu) + N(K \to \pi^+\ell^-\bar{\nu})}, \qquad (1.37)$$

[4]Strictly speaking, this is true only in the Wu-Yang phase convention; see below.

where $l = \mu$ or e and N denotes the number of times a given decay occurs. This quantity is an explicit measure of CP violation. If we assume the $\Delta S = \Delta Q$ rule[5] and restrict ourselves to the indirect symmetry violations in mixing,

$$\delta_\ell = 2Re(\varepsilon_K - \delta_K). \tag{1.38}$$

Thus, this asymmetry is sensitive to the CP-even K_+ admixture in the mostly CP-odd K_L state. The effect is independent of lepton flavor, since it is due to mixing of the states before they decay.

The lepton asymmetries are discussed in Ref. [31] in terms of C violation; the violation of CP is pointed out in Ref. [105]. The lepton asymmetries in both $K \to \pi^\pm e^\mp \nu_e$ and $K \to \pi^\pm \mu^\mp \nu_\mu$ were observed in 1967 [106, 107]. This implied that the K_S and K_L states were *not* orthogonal [108]. In particular, one can easily show that (see, for example, Refs. [34, 93])

$$\langle K_L | K_S \rangle = 2(Re\ \varepsilon_K + iIm\ \delta_K). \tag{1.39}$$

Assuming CPT (i.e., $\delta_K = 0$), this overlap is just proportional to δ_ℓ.

1.3.2 Known Occurrences of CP Violation

All known violations of CP-invariance occur in K_L decays. Further, all confirmed observations of CP violation are consistent with being measures of the quantity $\varepsilon_K - \delta_K$ and hence are all indirect CP violation. There is currently no *direct* evidence that allows a separation of these two parameters, although indirect evidence indicates that at least 90% of the effect is due to ε_K [34, 101]. This is just the same as the statement made earlier that there is no direct experimental measure for T violation.

Good measurements of the following quantities have been performed [39]:

- The magnitude and phase of η_{+-}, a measure of CP violation in $K \to \pi^+\pi^-$.
- The magnitude and phase of η_{00}, a measure of CP violation in $K \to \pi^0\pi^0$.

[5] This rule states that the changes in strangeness, S, and charge, Q, of the hadron in weak semileptonic decays are equal; it is valid to extremely high precision for ordinary weak interactions. Thus the processes $K \to \pi^- \ell^+ \nu$ and $\bar{K} \to \pi^+ \ell^- \bar{\nu}$ are allowed, while $K \to \pi^+ \ell^- \bar{\nu}$ and $\bar{K} \to \pi^- \ell^+ \nu$ are forbidden.

- The magnitude and phase of $\eta_{+-\gamma}$, a measure of CP violation in $K \to \pi^+\pi^-\gamma$. This amplitude ratio is defined analogously to η_{+-}, and is expected to be essentially equal to it since it is dominated by the trivial inner-bremsstrahlung process.

- The lepton asymmetry, δ_e, in $K_L \to \pi^\pm e^\mp \nu_e$.

- The lepton asymmetry, δ_μ, in $K_L \to \pi^\pm \mu^\mp \nu_\mu$.

There is a large ongoing effort [103, 109, 110]. to observe direct CP violation by measuring ε'/ε (See Section 1.4). The next round of experiments will have sensitivity to ε'/ε at the 10^{-4} level, sufficient to see an effect if theoretical expectations are correct. In addition, the CPLEAR experiment at CERN is expected to obtain a 3σ T-violation signal (a measurement of $Re\varepsilon$) with decays of tagged K^0 and $\bar{K}^0$. These two measurements will mark an important step forward in our study of CP violation. However, although a non-zero ε'/ε at expected levels would help confirm the standard explanations of CP violation via the CKM Matrix, we will be no closer to a *fundamental* understanding of CP violation.

1.3.3 Some Comments on the Neutron EDM

Another measurement that has attracted considerable attention, both experimental and theoretical, concerns the electric dipole moment (EDM). A non-zero EDM for an elementary particle is a sign of both P and T violation, as is easily seen from the symmetry properties of the interaction term, $D\vec{\sigma} \cdot \vec{E}$, between an electric field, $\vec{E}$, and the EDM, $D\vec{\sigma}$. Ramsey's early experiments, as well as current ones, showed no measurable EDM. When P violation was discovered seven years later, T invariance could still be invoked to explain the lack of an observed EDM [17, 18, 111]. Several authors [112, 113, 114, 115] highlighted the necessity for experimental evidence to support this new assumption of T invariance. By 1964, even CP invariance, and by implication, T invariance, had fallen victim to experiment [32]. In current theories, the smallness on the neutron EDM can be explained by the structure of weak interactions; in particular, one needs to go to high order [116, 117] to get an effect and even then it is found to be GIM suppressed [75]. The neutron EDM is interesting, then, for

two reasons. First, it is a potential window into new physics, since current theory expects it to be tiny. Second, and more important for us, it is an opportunity to explicitly observe T violation as distinct from CP violation (the EDM is equally P- and T-violating).

It is also worth mentioning that the empirical smallness of the neutron EDM plays a central role in the 'Strong-CP problem' [118]. A discussion of this problem is, however, beyond the scope of this thesis.

1.3.4 Other Explanations for the CP-Violating Phenomena

The question often arises whether CP violation can somehow be explained by the preponderance of matter over antimatter in the universe, or at least in our part of it. Early work on this question may be found in Refs. [119, 120]. They note that many models lead to an energy dependence of CP violation parameters, such as η_{+-}, which was not subsequently observed. Further discussions of some related ideas may be found in Ref. [104]. In general, such explanations do not seem to be viable.

Although the excess of matter in the universe cannot explain our observations concerning CP, thinking about things in the opposite direction can be useful. In a classic paper in 1967 [121], Sakharov showed that for the observed asymmetry of matter and antimatter to evolve, three conditions were necessary: a departure from thermal equilibrium, baryon number violation, and CP violation. Thus, although it remains mysterious, CP-violation may be responsible for the current existence of matter as well as the physicists who study it.

1.4 The Neutral Kaon System: Symmetries and Decays

We now turn to the study of symmetry violations in the decay process itself and discuss the $K \to \pi\pi$ decay phenomenology. The decay amplitudes to $\pi\pi$ states of definite isospin are parameterized as [94]

$$\langle I \,|T|\, K^0 \rangle = (A_I + B_I)\, e^{i\delta_I} \tag{1.40}$$

$$\langle I \,|T|\, \bar{K}^0 \rangle = (A_I^* - B_I^*)\, e^{i\delta_I} \tag{1.41}$$

Table 1. Summary of the symmetry properties of the $K \to \pi\pi$ decay amplitude parameters. An 'X' denotes that the symmetry is violated by a non-zero value of the amplitude in question.

Amplitude	CP	T	CPT
ReA_I			
ImA_I	X	X	
ReB_I	X		X
ImB_I		X	X

where the isospin $I = 0, 2$ and δ_I are final-state interaction (rescattering) phase-shifts. The symmetry properties of these amplitudes are given in Table 1.

One can adopt the phase convention [94, 122] (the 'generalized Wu-Yang phase')

$$ImA_0 = 0 \tag{1.42}$$

This eliminates CPT-conserving, direct CP violation in the $I = 0$ channel *by definition.* It also fixes the phase ambiguity for ε_K mentioned earlier; Im ε_K and ImA_0 are mixed by a change of phase convention. Note that in the absence of such a phase convention, the distinction between direct and indirect CP violation becomes blurred. I will *not* adopt this convention; the number of extra terms added to the equations in the general case is tolerably small.

We write, as is customary

$$\eta_{+-} = \varepsilon + \varepsilon' \tag{1.43}$$

$$\eta_{00} = \varepsilon - 2\varepsilon'. \tag{1.44}$$

The factor of two appears due to the Clebsch-Gordon coefficients relating the isospin states to the charge states. We further split ε and ε' into two pieces each

$$\varepsilon = \varepsilon_T + \varepsilon_{CPT} \tag{1.45}$$

$$\varepsilon' = \varepsilon'_T + \varepsilon'_{CPT}. \tag{1.46}$$

Recall that all of the quantities in the preceeding equations are CP-violating. We now further distinguish between contributions which are T and CP-violating (ε_T and ε'_T) and

those which are CPT and CP-violating (ε_{CPT} and ε'_{CPT}). The subscripts thus denote which symmetry, in addition to CP, is violated by a given term. Our goal in this thesis is to study the CPT-violating terms.

Generating expressions for ε_T, ε_{CPT}, ε'_T, and ε'_{CPT} in terms of the mixing parameters, ε_K and delk, and the decay amplitudes, A_I and B_I, is a simple matter of algebra. One combines the state definitions in Eqn. 1.31 with the definitions of the η parameters in Eqn. 1.33. The resulting expressions contain pieces expressible in terms of the mixing parameters and the decay amplitudes, defined in Eqn. 1.40. We expand to first order in small quantities, and then identify the result according to Eqns. 1.43 and 1.45. We spare the reader the intermediate steps and simply present the results as appropriate in the forthcoming sections. More detail is given in Ref. [94].

1.4.1 Analysis Assuming CPT Symmetry

We now display full expressions for the parameters of interest, under the assumption that CPT symmetry is valid. After some algebra, we find (to lowest order in small quantities):

$$\varepsilon = \varepsilon_T \simeq \left[\varepsilon_K + i\,\frac{ImA_0}{ReA_0}\right] \tag{1.47}$$

$$\varepsilon' = \varepsilon'_T \simeq \frac{i}{\sqrt{2}}\frac{ReA_2}{ReA_0}\left[\frac{ImA_2}{ReA_2} - \frac{ImA_0}{ReA_0}\right] e^{i\,(\delta_2-\delta_0)} \tag{1.48}$$

Note that ε is due partly to CP-violating mixing (ε_K); in the Wu-Yang phase convention, it is entirely due to mixing. On the other hand, ε' is a *difference* in CP violation in the amplitudes for the $I = 0$ and $I = 2$ channels; it is independent of phase conventions.

It can be shown that

$$|\phi_\varepsilon - \phi_{SW}| < 0.001^\circ \tag{1.49}$$

with reasonable *theoretical* assumptions, or

$$|\phi_\varepsilon - \phi_{SW}| < 1.6^\circ \tag{1.50}$$

with only *experimental* input. The derivations and a discussion of the theoretical assumptions are given in Appendix A.

The final state phase shifts are [123]

$$\delta_2 - \delta_0 \simeq (-42 \pm 4)^\circ \tag{1.51}$$

implying that

$$\phi_{\varepsilon'} - \phi_{SW} \simeq (5 \pm 4)^\circ. \tag{1.52}$$

Thus, ε' is largely *parallel* to ε. We also know that $Re(\varepsilon'/\varepsilon) < 2 \times 10^{-3}$. Thus, we obtain the experimental constraint

$$\phi_{+-} - \phi_\varepsilon < 0.01^\circ. \tag{1.53}$$

Combining all these facts, we find, in the absence of CPT violation,

$$\phi_{+-} \simeq \phi_{SW} \tag{1.54}$$

and

$$\Delta\phi \equiv \phi_{00} - \phi_{+-} \simeq 0^\circ. \tag{1.55}$$

We next discuss how these predictions are affected if the assumption of CPT is relaxed. In short, the above relations will be disturbed, and hence measurements of these phases will allow us to test CPT.

1.4.2 Analysis Allowing for CPT Violation

If CPT is violated, then there are new contributions to ε and ε' which violate CPT (recall the notation of Eqns. 1.45 and 1.46):

$$\varepsilon_{CPT} = \left[\frac{ReB_0}{ReA_0} - \delta_K\right] \tag{1.56}$$

$$\varepsilon'_{CPT} = \frac{1}{\sqrt{2}}\frac{ReA_2}{ReA_0}\left[\frac{ReB_2}{ReA_2} - \frac{ReB_0}{ReA_0}\right] e^{i\,(\delta_2-\delta_0)}. \tag{1.57}$$

By comparing with Eqn. 1.48, we see that $\varepsilon'_T \perp \varepsilon'_{CPT}$. One can also show that we most likely have $\varepsilon_T \perp \varepsilon_{CPT}$; this is discussed in Appendix A. Note that the decay amplitudes in the numerator are always ImA and ReB. This is simply due to the fact the the η parameters we are disecting violate CP, while ReA and ImB do not.

This implies that the effect of CPT violation is to change the phases of η_{+-} and η_{00}. CPT violation can show up as a nonzero value of either $\phi_{+-} - \phi_{SW}$ or $\Delta\phi$, or both. This is the central point of the entire phenomenology we have been developing.

1.4.3 The Lepton Asymmetries

We complete our discussion by calculating the full expression for the lepton asymmetry 1.37, with no assumptions of CPT invariance. Define

$$\langle\, \pi^-\ell^+\nu \mid T \mid K^0 \,\rangle \;=\; a \;+b \tag{1.58}$$

$$\langle\, \pi^+\ell^-\bar{\nu} \mid T \mid \bar{K}^0 \,\rangle \;=\; a^* - b^* \tag{1.59}$$

and

$$\langle\, \pi^+\ell^-\bar{\nu} \mid T \mid K^0 \,\rangle \;=\; x(a \;+b) \tag{1.60}$$

$$\langle\, \pi^-\ell^+\nu \mid T \mid \bar{K}^0 \,\rangle \;=\; \bar{x}(a^* - b^*). \tag{1.61}$$

We have ignored any (small) final-state interactions. We use x and $\bar{x}$ to parametrize possible $\Delta S = \Delta Q$ rule violations, which are expected to be negligible but are not so well-limited experimentally [39].

The lepton asymmetry for K_L is given by

$$\delta_\ell = \left(\frac{1-|x|^2}{|1-x|^2}\right) 2\,(Re\varepsilon_K - Re\delta_K) + 2\,(Reb/Rea) \;+\; 2\;Re(x-\bar{x}) \tag{1.62}$$

where we have retained the $\Delta S = -\Delta Q$ correction to the leading term. Invariance under CP gives

$$a = a^*, \quad x = \bar{x}^*, \quad \text{and} \quad b = -b^* \tag{1.63}$$

while invariance under CPT yields

$$\delta_K = b = 0 \quad \text{and} \quad x = \bar{x}. \tag{1.64}$$

Note that if we assume CPT, and knowing that ε'/ε is small, a comparison of δ_ℓ and $|\eta_{+-}|$ gives a measure of ϕ_{+-}. Unfortunately, the interest in ϕ_{+-} is for use in CPT tests and CPT violation adds new terms to the expressions for both δ_ℓ and η_{+-}. The comparison is still somewhat interesting, since the CPT-violating effects presumably do not cancel in general, and hence some information constraining CPT violation is gained [124].

We also display the form of the lepton asymmetry as a function of proper time, t, after a regenerator,

$$\delta_\ell(t) = 2 \left(\frac{1 - |x|^2}{|1 - x|^2} \right) |\rho| \; e^{-(\Gamma_S + \Gamma_L)/2} \; cos(\Delta m t + \phi_\rho) \quad + \quad \delta_\ell. \tag{1.65}$$

Note that $\delta_\ell(\infty) = \delta_\ell$, the K_L asymmetry. This interference pattern after a regenerator allows a direct measurement of ϕ_ρ [125].

1.5 Summary

We began this thesis by discussing the evolution of the concepts of discrete symmetries in particle physics. We then presented an overview of the phenomenology of the neutral kaon, including a historical introduction to its many intriguing properties. Several key equations parameterizing symmetry violation in the kaon system were presented. The basic conclusion is as follows: the values of certain CP-violating phases can be predicted assuming CPT symmetry. Not only is this assumption necessary, but we have shown that CPT violation necessarily invalidates these predictions by adding contributions 90° out of phase with the CPT-conserving ones. We are thus interested in precision measurements of these CP-violating phases. We now move on to a description of the experiment we have performed to measure these phases.

CHAPTER 2

THE EXPERIMENTAL TECHNIQUE

The current chapter discusses the general principles underlying our experimental technique. The physics information we wish to extract is contained in the shape of the $K \to \pi^+\pi^-$ decay rate as a function of proper time. We describe the necessary elements of a successful experimental determination of this rate, as well as some issues related to the extraction of physics results from the decay rate.

2.1 Related Experiments by our Collaboration

Our experiment is one of a series of kaon experiments carried out by an evolving collaboration based at Fermilab. Frequent reference will be made to a previous experiment, FNAL E731, which was performed with largely the same apparatus as ours. E731 took data from August 1987 to March 1988 with the primary goal of measuring $Re\ \varepsilon'/\varepsilon$ to high precision [109]. In addition, E731 performed measurements [126] of all three quantities addressed in the current thesis, as well as many others [127, 128, 129, 130, 131, 132, 133].

In addition, we mention that highly successful analyses of rare decay modes in the E731 data, which had very general triggers, led to the proposal of a dedicated rare-decay experiment, E799 [134]. The first phase of this experiment took data immediately after the the E773 run. As a result, we were not concerned with performing rare-decay physics measurements with the E773 data; this allowed a more focused approach. In general, the

two experiments, E773 and E799, had little effect on each other in spite of their sharing of the apparatus and their closeness in time.

2.2 The Measurement

As shown in the previous chapter, Equation 1.16, the $\pi^+\pi^-$ decay rate as a function of proper time downstream of a regenerator is sensitive to ϕ_{+-}, Δm, and τ_S. It is straightforward to fit for these quantities given an experimental determination of the rate. We will extract measurements of all three of these parameters in this thesis.

The determination of the decay rate from the data depends on two crucial steps:

- The identification of the signal and the separation of this signal from background.
- The application of a detector acceptance correction to recover the true decay rate from the observed rate.

Only the unscattered kaons and those undergoing transmission (coherent forward) regeneration constitute the signal in this experiment. Decays of kaons after diffractive and inelastic scattering are treated as background. As discussed below, we use two nearly parallel kaon beams with a regenerator in each beam. We will work in the kaon energy range $20 - 160$ GeV and use long decay volumes, some extending more than 35 m from the regenerators.

The acceptance for a kaon decay is a strong function of the kaon momentum, p, and the position of the decay vertex, z, along the beam direction. For a given p and z, the acceptance may be averaged over the small variations in kaon direction and transverse position. The only other quantities characterizing a given decay involve the orientation of the decay products, but these are easily averaged over in a the trivial case of a two-body decay. Given p and z, one can construct the proper time needed for the decay rate calculation, $t = z/\gamma\beta c$, where γ and β are the usual Lorentz factors and z has a suitably chosen origin, typically the downstream face of the regenerator. In practice, fitting is done with finite-sized bins; the bin acceptance then develops some small sensitivity to other parameters which affect the shape of the decay rate across the bin. This is discussed in more detail in Chapter 7.

2.3 Double Beams and the Two Regenerators

We now describe the original idea behind E773 and the evolution of plans to perform the analysis described in this thesis. The experiment as proposed [135] was a dedicated measurement of $\Delta\phi$. The idea was based on a modification of the E731 technique for measuring ε'/ε. E731 had two K_L beams, one of which was entirely in vacuum, and the other of which struck a regenerator. We often refer to these beams as the vacuum beam and the regenerator beam. The analysis was based on fitting the double ratio, R, of decays

$$R = \left(\frac{N_{vac}(\pi^0\pi^0)}{N_{reg}(\pi^0\pi^0)}\right) \Big/ \left(\frac{N_{vac}(\pi^+\pi^-)}{N_{reg}(\pi^+\pi^-)}\right) \tag{2.1}$$

where N_{vac} (N_{reg}) denotes the number of events in the vacuum (regenerator) beam. It is easily shown, in the approximation that N_{vac} (N_{reg}) corresponds to K_L (K_S) decays, that $R \simeq |\eta_{00}/\eta_{+-}|^2 \simeq 1 - 6Re\ \varepsilon'/\varepsilon$. Fits, of course, use the full expression for R, employing wavefunctions with the appropriate K_L and K_S components in both beams. R is very close to one, due to the small value of ε'/ε [109].

The original idea behind E773 was to use this same double ratio, but to place a regenerator in both beams, at different z positions. Then, the 'vacuum' and 'regenerator' beams in the expression above are replaced by two regenerator beams:

$$R = \left(\frac{N_{reg1}(\pi^0\pi^0)}{N_{reg2}(\pi^0\pi^0)}\right) \Big/ \left(\frac{N_{reg1}(\pi^+\pi^-)}{N_{reg2}(\pi^+\pi^-)}\right). \tag{2.2}$$

The z positions are chosen so that the interference curves are about 90° out of phase at the mean beam energy. The decay rates in each beam are very different at a given z, due to the differing distances from the two regenerators, but the double ratio is once again about equal to one because it compares charged and neutral decays. A non-zero value of $\Delta\phi$ will cause a shift of the double ratio away from one since it alters the charged and neutral rates even in the same beam (the effects of ε'/ε are very small). Simulations showed that $R \simeq 1 + (1\%/degree) \times \Delta\phi$, for a typical experimental setup.

A deeper appreciation of the physics potential of E773 evolved during the analysis of E731, which occurred after the original proposal. E731 found that the detector acceptance was understood well enough to permit fitting of the regenerator beam decay rate directly, without recourse to the double ratio. This motivated us to plan similar measurements in

E773. In particular, the possibility arises of measuring ϕ_{+-} itself, in addition to the phase difference, $\Delta\phi$. A vacuum beam is still very useful for determining the incident kaon flux, however, even in a single-beam fit.

The most significant modifications made to the E731 detector involved the two new regenerators. The E731 regenerator [136] was composed of four blocks of boron carbide (B_4C) with scintillator planes following each block. These planes allowed some vetoing of inelastic interactions. The final plane of scintillator was preceeded by a sheet of lead to convert photons; this aided suppression of inelastics and also gave a clear edge to the beginning of the decay volume for $K \to \pi^0\pi^0$ decays. A well-defined edge is crucial in a counting experiment such as the ε'/ε measurement of E731. The total material was approximately two kaon interaction lengths. This length maximizes the K_S-to-K_L ratio, while also minimizing the diffractive background (see Appendix F).

In E773, the regenerators were built from blocks of scintillator. This resulted in improved vetoing of inelastic interactions since the entire regenerator was active material which could be monitored. There was no lead converter at the end. A sharp edge is not crucial for a phase measurement, which can simply start fitting downstream of the regenerator face. The lead also has somewhat different regeneration characteristics than the scintillator; we wished to avoid this complication.

The regenerators were chosen to be less than two interaction lengths: this increases the diffractive background, relative to two interaction lengths, but results in a more pronounced interference between K_L and K_S decays. The rate is dominated by K_S decays, which are proportional to $|\rho|^2$, while the $K_L - K_S$ interference is proportional to $|\rho\eta|$. Thus, the fraction of the decays constituting interference is proportional to $|\eta/\rho|$ and a smaller ρ is beneficial.[1] Of course, many other parameters, such as the regeneration amplitude itself, must be fit for. Not all of these benefit from a larger interference term, but may instead prefer the higher K_S statistics that come with a larger ρ. Monte-Carlo studies assisted us in choosing the particular optimized configuration that was used.

[1] This argument ignores the K_L decays and thus breaks down when ρ becomes *too* small compared to η. For the shorter regenerator in E773, $|\rho/\eta| \sim 5$, and the argument is still valid.

2.4 Detector Requirements

In this section, we will discuss the general detector requirements needed in our studies of $\pi\pi$ decays. Details of all the detector components are given in the following chapter; we will just paint a general picture of our strategy here.

2.4.1 $K \to \pi^+\pi^-$ Decays

For $K \to \pi^+\pi^-$ decays ('charged mode'), the detector uses a tracking system to determine the trajectories and momenta of charged particles and particle identification to separate pions, muons, and electrons. The tracking is performed with a set of precision drift chambers and an analysis magnet. Particle identification is achieved with a lead-glass calorimeter and a muon filter and hodoscope.

The track momenta and directions are necessary to determine the kaon momentum and decay vertex of each event; these quantities are the essential parameters in the decay rate expression. They are also used for calculating kinematic quantities, principally invariant mass and transverse (to the beam) momentum. Both of these quantities are useful in reducing semileptonic backgrounds. The transverse momentum is also crucial in separating coherent and non-coherent $\pi^+\pi^-$ decays.

Particle identification is necessary to assist in separating the signal from other decay modes. The major backgrounds are $K \to \pi^\pm e^\mp \nu_e$, $K \to \pi^\pm \mu^\mp \nu_\mu$, $K \to \pi^+\pi^-\pi^0$, and $\Lambda \to p\pi$. The $K \to \pi^+\pi^-\pi^0$ background is easily handled with kinematics, since we always have $M_{\pi\pi} < M_K - M_{\pi^0}$. We remove the Λ background by cutting on the $p\pi$ mass. For semileptonic decays, the invariant mass and transverse momentum distributions of the charged particles are broad, extending through the signal region in mass and transverse momentum squared (p_T^2). Kinematic cuts on these same two quantities reduce the semileptonics substantially, but the initial rates are very large. These backgrounds require separation of pions from electrons and muons to augment the kinematics. Electrons are identified by their energy deposition in an electromagnetic calorimeter: due to electromagnetic showering, they deposit all of their energy, while the pions do not. Muons are easily identified by their ability to penetrate substantial amounts of steel.

2.4.2 $K \to \pi^0\pi^0$ Decays

We will briefly discuss the requirements imposed by the $K \to \pi^0\pi^0$ ('neutral mode') decays, since these affect the overall detector design. The neutral-mode reconstruction requires the identification of photons and the measurement of their energies and positions.

$K \to \pi^0\pi^0$ events are characterized by four photons in the final state. Background is due to $K \to 3\pi^0$ where photons are lost or overlap. A lead-glass calorimeter is used to reconstruct the energy and position of photons. It must have good resolution and be fine-grained enough to distinguish nearby pairs of photons. For neutral decays, *all* of the information used to reconstruct the event comes form this calorimeter.

The veto system in our detector is responsible primarily for detecting escaping photons from $K \to 3\pi^0$ decays. Most of the vetoes contain both scintillator for vetoing charged particles and lead-lucite sandwiches to convert and detect photons. For the most part, the scintillator signals are used at the trigger level and the lucite signals are used in off-line analysis.

2.5 Accounting for the Regeneration Phase

As discussed in in Appendix F, there is a simple relation between the nuclear scattering amplitudes, $(f - \bar{f})/k$, and the regeneration amplitude, ρ. We will often change between the two parameters; ρ is more directly related to the experimental aspects, and $(f - \bar{f})/k$ is more appropriate to the detailed discussions of systematics. All of the subtle issues involving regeneration are contained in the behavior of $(f - \bar{f})/k$; the other factors in ρ cause no difficulties.

The interference between K_L and K_S decays is sufficient to measure only $(\phi_\rho - \phi_{+-})$ and $(\phi_\rho - \phi_{00})$. If one is interested in $\Delta\phi$

equiv $\phi_{00} - \phi_{+-}$, then the value of ϕ_ρ tends to cancels in the difference. The cancelation is not complete, since ϕ_ρ must still be known in order to predict the decay rate when fitting. In E773 fits, a change of ϕ_ρ by δ would induce a change in $\Delta\phi$ of about $\delta/4$, whereas the full shift would appear in ϕ_{+-}.

There are fortunately connections between the phase and energy dependence of a scattering amplitude. If one assumes the scattering amplitudes are analytic, then dispersion integrals may be employed to constrain the behavior of the amplitude. The *magnitude* of ρ can be measured in our experiment. It is known from many experiments [126, 137, 138] that $((f - \bar{f})/k$ at high energies is well-represented by a power law as a function of kaon energy. It can easily be shown that if

$$(f - \bar{f})/k \propto E^{\alpha}/k \tag{2.3}$$

then the relation (the 'phase-power' relation)

$$\phi_f = arg(f - \bar{f}) = -(\pi/2)(1 + \alpha) \tag{2.4}$$

follows from analyticity of the scattering amplitudes (see Appendix C). This is the central fact around which our treatment of the regeneration phase is built. Note that only the energy dependence enters this relation, not the overall scale of regeneration. Without some kaon flux normalization, only $|\rho/\eta|$ can be measured (see Eqn. 1.16). However, $|\eta|$ is well-known [39] and does not disturb the momentum dependence in any case. The power law form given above is the natural behavior of regeneration from the exchange of a single Regge pole (see Appendix D).

If we knew for certain that regeneration *did* follow an exact power law, then we could fit for the power law exponent and determine the phase. Simultaneous fitting for this exponent and the physics parameters of interest would assure that all correlations were properly accounted for. However, we must consider possible deviations from this idealized power-law behavior. Since dispersion relations involve integrals over all energies, we must also worry about deviations outside the energy range of our experiment. A more detailed discussion of the regeneration phase can be found in Chapter 9 and Appendix H. We show there that the deviations from the idealized behavior given above can be studied and limited by other experimental data. Possible systematics involved in correcting for the regeneration phase are not a serious limitation to E773.

2.6 Summary

We have presented an overview of our experimental technique and an outline of how we will perform the necessary tasks. We need to cleanly identify the $K \to \pi^+\pi^-$ events and determine their energies and decay vertices. This must be done in an unbiased and reproducible manner, so that we may determine the acceptance and use it to reconstruct the true decay rate containing the physics of interest. In the following chapters, we move on to a detailed description of the detector, the data-taking run, and the analysis which accomplish these tasks.

CHAPTER 3

THE BEAMLINE AND DETECTOR

This section will describe the beamline and detector used in this experiment. The facilities were located at the Meson-Center Beam Line at the Fermi National Accelerator Laboratory (Fermilab) in Batavia, IL. The E773 run extended from mid-July through September 1991.

3.1 The Coordinate System

We first define the coordinate system used. The $+z$ direction is defined to be along the line connecting the kaon production target and the center of the calorimeter; this is the mean kaon beam direction. We take $+y$ to be vertical, and $+x$ is horizontal with the sign chosen to complete a right-handed, orthogonal coordinate system. The origin is taken to be the center of the kaon production target.

3.2 The Accelerator

The Fermilab Tevatron supplied 800 GeV protons during spills of 21 s duration approximately once every minute. Each spill typically delivered 1.7×10^{12} protons onto our target. Within each spill, there was a 53 MHz bucket structure due to the accelerator RF; the protons were contained in a roughly 2 ns window every 19 ns. Thus, a spill consisted of about 1.1×10^9 buckets of 1,500 protons each. Our beams contain on the order of one kaon in our energy range of $20 - 160$ GeV every 50 buckets. The accelerator supplied an RF

signal to our experiment so that our trigger could be synchronous with this substructure in the spills.

3.3 The Secondary Beamline

The collimation system produced two nearly parallel kaon beams, each square in cross-section. The target consisted of a 3.2 mm $\times$ 3.2 mm $\times$ 0.36 m beryllium rod in an annular ceramic holder. The beam position was monitored by two ion chambers, one in each transverse direction, just upstream of the target. The final steering dipole magnets were under the experimenter's control, allowing us to move the beam spot relative to the target while monitoring rates in the detector. This allowed an empirical determination of the optimal transverse targeting by observing the trigger rates, which were monitored on scalars for each spill. The primary proton beam was nominally contained in the horizontal (x-z) plane, with a targeting angle of 4.9 mrad relative to the z axis, towards $+x$. The targeting angle is a compromise between rate, which is highest in the forward direction, and the ratio of kaons to neutrons produced, which increases away from the forward direction. The number of kaons and neutrons in our beam are approximately equal. The extracted neutral beam pointed roughly towards geomagnetic north, which canceled the effect of one component of the earth's magnetic field on decay products traveling roughly parallel to z.

The kaon beam collimation and filtering elements are shown in Figure 1. The primary collimation element, the two-hole collimator, was a 5.8 m water-cooled copper dump with two tapered holes to define the secondary beam. The exit holes were squares 9.96 mm on each side and were located 14.8 m from the target. The beams are separated symmetrically about $y = 0$, but are centered in x; the beam centers are at ± 0.64 mrad with respect to z. The beams are aimed at the centers of the holes in the calorimeter, described below. A common absorber was placed in both beams to improve the kaon-to-neutron ratio and convert photons. It consisted of 0.508 m of Be followed by 0.076 m of Pb. A second movable (shadow) absorber, 0.457 m of Be, was placed in only one beam; it alternated between the beams such that it always shadowed the downstream regenerator (see below). Two rectangular slabs were located between the beams to prevent cross-over between them

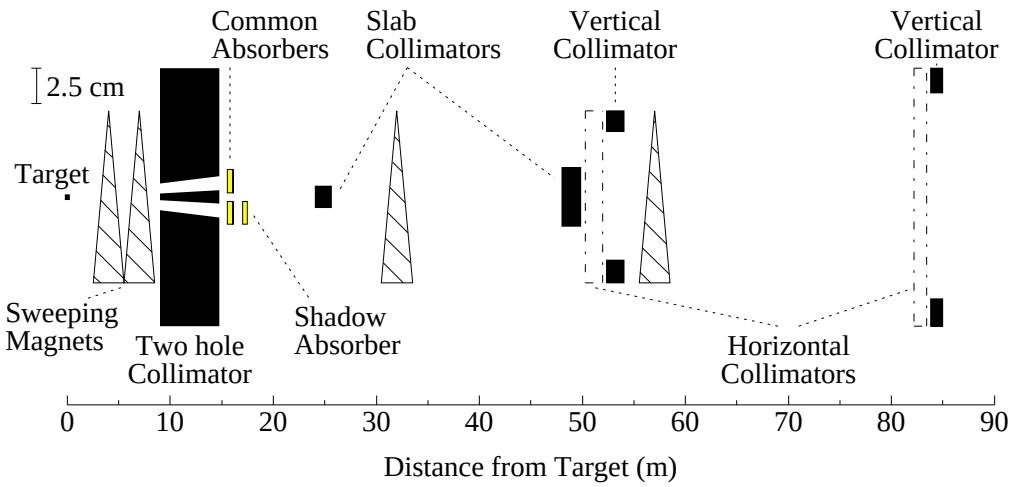

Figure 1. Elevation view of the E773 collimation system. Note the large difference in the y and z scales.

due to scattering in the absorbers. The first (second) was 1.52 m (1.83 m) long, centered at 24.8 m (48.9 m), and had a height of 15 mm (41 mm). The second slab defined the inner y edges of the beams. The outer y edges of the beams were defined by two sets of collimator jaws. The first (second) was located at 53.2 m (84.4 m) and had an opening 90 mm (144 mm) wide. The x edges of the beams were determined by an analogous set of jaws at 51.1 m (82.8 m) with an opening of 24 mm (35 mm). The first (second) sets of jaws were 1.7 (1.2) m long. The resulting beams were about 50 mm square at the regenerators and 75 mm square at the lead glass. Each beam subtended 0.17 μsterrad. Sweeping magnets were located at 30 m and 56 m to remove debris created by interactions in the absorbers and collimators. The neutral beam thus consisted primarily of kaons and neutrons. There was also a component of high-energy lambdas that survived, as well as photons and other decay products not removed by the conversion and sweeping.

We point out that the small angle the beams make with respect to the z axis has a negligible effect in terms of the distance traveled by the kaon. The true distance differs from the z projection by only about 2 parts in 10^7; henceforth, we neglect this distinction

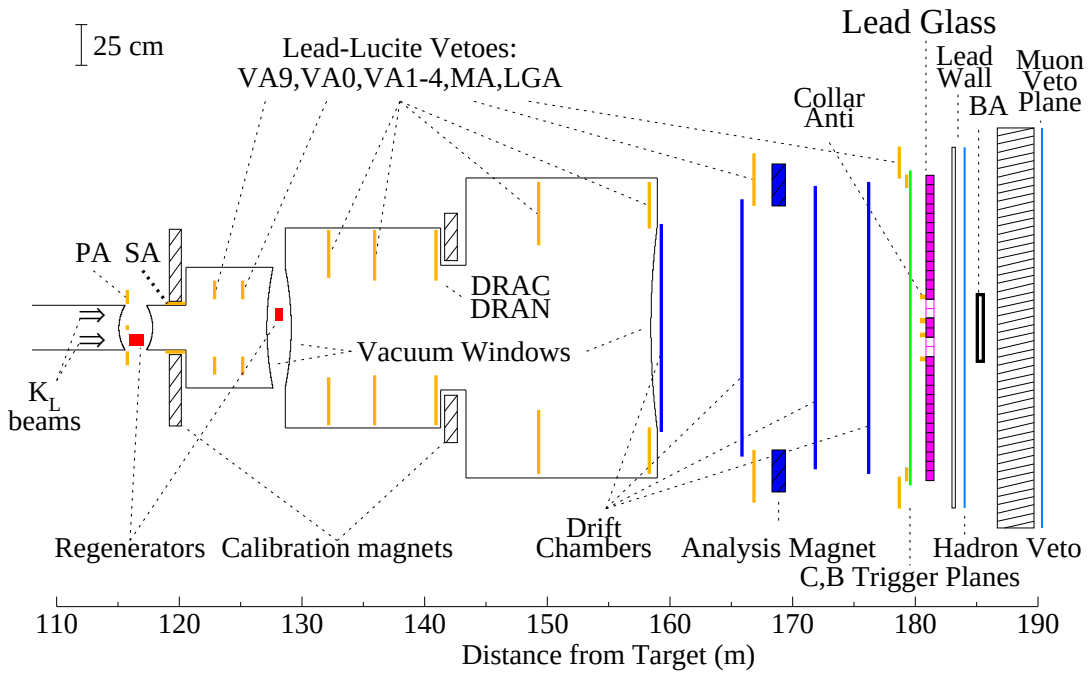

Figure 2. Elevation view of the E773 Detector. Note the large difference in the y and z scales.

and discuss only distance along z. We may *not*, however, neglect the beam angles when calculating transverse momenta; this will be discussed later.

3.4 The E773 Detector

We now turn to a description of the elements of the detector, shown in Figure 2. The z positions of the detector elements are listed in Table 2; transverse dimensions are given in Table 3.

3.4.1 The Regenerators

For E773, a new approach to regenerator design was used for the first time. The regenerators were 'fully active': they were constructed out of blocks of scintillator which could be

Table 2. The detector components and their distances from the target. The regenerator positions refer to the downstream faces. The VA positions are the centers of each unit. The drift chamber positions are the average position of the four sense planes. The magnet position is the center of the pole face. The lead glass position is 1/3 of the way into the array, about at the position of maximum development of the electromagnetic showers. The BA and CA positions are the upstream faces. The other elements are thin.

Detector Element	m from target	Detector Element	m from target
Vacuum Window	115.575	Vacuum Window	158.946
Pinching Anti	115.735	Drift Chamber 1	159.287
Upstream Regenerator	117.139	Drift Chamber 2	165.861
Vacuum Window	117.330	Magnet Anti (MA)	166.836
Vacuum Anti 9 (VA9)	122.873	Analysis Magnet	168.864
Vacuum Anti 0 (VA0)	125.175	Drift Chamber 3	171.856
Vacuum Window	127.641	Drift Chamber 4	176.197
Downstream Regenerator	128.420	Lead Glass Anti (LGA)	178.710
Vacuum Window	128.623	Iron Ring	179.266
Vacuum Anti 1 (VA1)	132.172	C Hodoscope	179.536
Vacuum Anti 2 (VA2)	135.933	B Hodoscope	179.635
V hodoscope	140.913	Collar Anti (CA)	180.700
T hodoscope	140.936	Lead Glass Array	181.089
DRAC veto counter	140.948	$\mu 1$ Hadron Veto	183.996
DRAN veto counter	140.988	Back Anti (BA)	185.047
Vacuum Anti 3 (VA3)	149.291	$\mu 2$ Muon Veto	189.914
Vacuum Anti 4 (VA4)	158.273		

viewed by phototubes. The Upstream (Downstream) Regenerator was 1.2 m (0.4 m) long; note that one meter of scintillator is one kaon interaction length.

The downstream and upstream regenerators were both constructed out of the same size scintillator blocks. Each block of Bicron Pilot-U scintillator was 3.3 cm (z) $\times$ 7.6 cm (x) $\times$ 3.7 cm (y). Pairs of blocks were stacked on top of each other, in y, such that an

Table 3. Transverse dimensions of important detector elements. 'ir' ('or') is inner (outer) radius. 'ix' ('ox') is inner (outer) x half-width, with analogous notation for the y view. The 'square pipe' is the decay pipe immediately downstream of the UR. The chamber sizes are taken to be the distance between the extreme wires in a given plane pair.

Detector Element	Dimensions
Pinching Anti	ix: 0.010, iy: 0.025, ox: 0.23, oy: 0.23
Vacuum Window after UR	ir: 0.152
Square Pipe	ix: 0.078 iy: 0.136
Vacuum Anti 9 (VA9)	ix: 0.095, iy: 0.178, ox: 0.205, oy: 0.286
Vacuum Anti 0 (VA0)	ix: 0.095, iy: 0.172, ox: 0.205, oy: 0.289
Vacuum Windows near DR	ir: 0.368
Vacuum Anti 1 (VA1)	ir: 0.303, or: 0.595
Vacuum Anti 2 (VA2)	ir: 0.303, ir: 0.595
HDRA	ix: 0.249, iy: 0.309, or: 0.605
Vacuum Anti 3 (VA3)	ir: 0.502, or: 0.885
Vacuum Anti 4 (VA4)	ir: 0.606, or: 0.889
Vacuum Window	ir: 0.609
Drift Chamber 1	ix: 0.638, iy: 0.638
Drift Chamber 2	ix: 0.810, iy: 0.708
Magnet Anti (MA)	ix: 0.908, iy: 0.743
Drift Chamber 3	ix: 0.860, iy: 0.810
Drift Chamber 4	ix: 0.886, iy: 0.886
Lead Glass Anti (LGA)	ir: 0.908, or: 1.403, oy: 1.105
Iron Ring	ir: 0.853, or: 0.935
C Hodoscope	ox: 0.96, oy: 0.90
B Hodoscope	ox: 0.91, oy: 0.96
Collar Anti (CA)	ix: 0.052, iy: 0.052, ox: 0.088, oy: 0.088
Lead Glass Array	or: $\sim$ 0.93
Mu2 Muon Bank	ox: 1.27, oy: 1.22

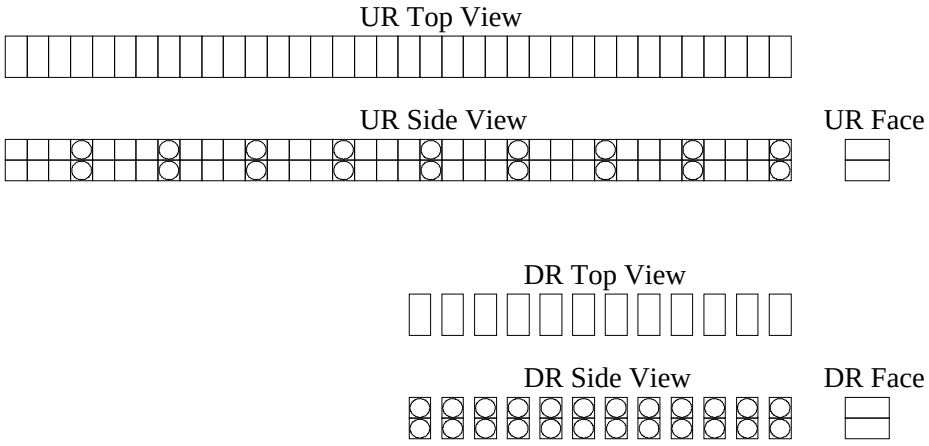

Figure 3. The arrangement of scintillator blocks in the Upstream and Downstream Regenerators. Top, side, and face (beam's-eye) views of each device are shown. Circles are drawn to represent the phototubes. For the DR, tubes were placed on both ends of each block; for the UR, tubes were placed on one end of the indicated blocks. The beams enter from the left.

approximately square cross-section was presented to the beam. Elevation and plan views of the layout of the blocks in each regenerator are shown in Figure 3.

The downstream regenerator consisted of 12 subunits of two blocks stacked one atop the other. Each block was wrapped in Teflon^{TM} tape; the high reflectivity aided light collection. Each pair of blocks was then further wrapped to be light-tight. There were gaps of about 1.7 cm between each subunit; these allowed more space to fit the phototubes and bases. The overall length was thus about 59 cm, with 40 cm of scintillator. The DR was instrumented with a Hamamatsu 3082 phototube on each end of every scintillator block, for a total of 48 channels. The tubes were glued directly to the blocks. A perspective view of the DR is shown in Figure 4.

Each signal was fed to a specially-designed amplifier near the regenerator. These amplifiers shaped the pulses, partly to compensate for long signal cables. In addition, they grounded large signals in order to maintain high sensitivity while allowing fast recovery in

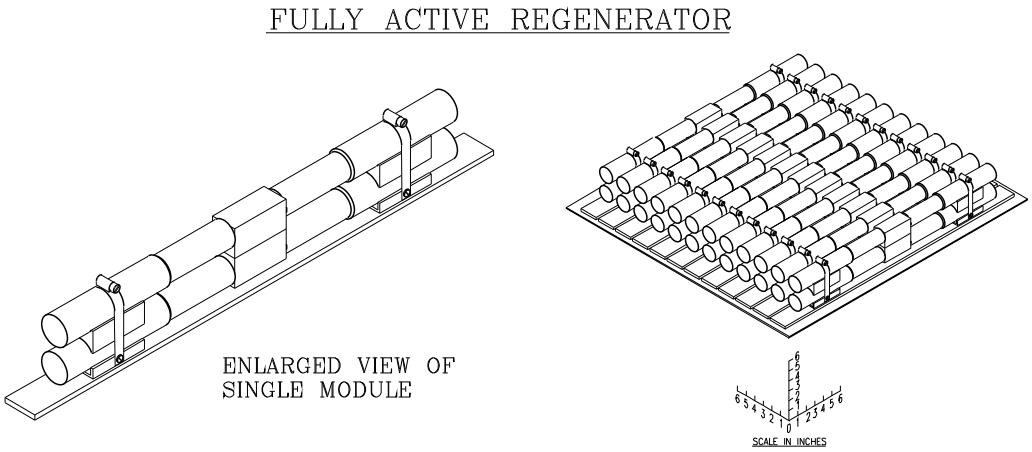

Figure 4. A perspective view of the Downstream Regenerator. The beam crosses from the upper left to the lower right. The phototubes and bases at each end of each block are shown.

a high-rate environment. The DR was shadowed by a beryllium absorber in the collimation system which reduced the beam flux. The fully-instrumented DR clearly demonstrated of the power of active regenerators; further discussion is given in Chapter 6.

The UR was constructed out of 36 pairs of blocks with no gaps between them, giving a bulk length of about 120 cm. Only every fourth pair was wrapped and instrumented; each block in these pairs was viewed by a single phototube. Short lucite light guides were used to couple these tubes to the blocks.

Further details of all of the materials in the regenerators are given in Appendix G.

Both regenerators, and the movable shadow absorber, were placed on moving platforms which allowed them to be toggled between the two kaon beams (or be taken out entirely, if desired) every accelerator beam spill. The positions of the regenerators and the shadow absorber were monitored and read out as part of each event recorded.

3.4.2 The Decay Tank and Vacuum Windows

The decay region consisted of two sections of evacuated pipe and started after the UR. The pipe was rectangular in cross-section after the UR until 120.65 m, and was cylindrical thereafter. The vacuum region was interrupted near each regenerator (see Figure 2); this made construction of the regenerators and their movers easier. At each break in the vacuum, as well as at the end of the decay volume at 159 m, were thin vacuum windows, all of identical construction. They were a sandwich of a 584 μm weave of Kevlar-29, for strength, and 127 μm of mylar, for a gas-tight seal. We give the bulk thickness of the Kevlar weave, but note that the weave has a packing fraction of 56% relative to solid material. The two windows near the UR have a negligible effect on the experiment. The two windows near the DR, and the air between them, affect the UR beam somewhat: they contribute to the mass and decay vertex resolution with multiple scattering and add some regeneration in the UR beam decay volume. Our treatment of these effects of the materials will be discussed later.

3.4.3 The Spectrometer

The magnetic spectrometer consisted of four drift chambers and an analyzing magnet, shown in Figure 2. Each chamber contained four planes of sense wires, two each for the x and y coordinate views. The two sense planes in a given view were staggered to resolve the two-fold ambiguity. We will frequently refer to the two sense planes in a given view of a chamber as a 'plane pair', and refer to the upstream and downstream members of a pair. The sense wires were 25 μm gold-plated tungsten, while the field wires were 100 μm copper-beryllium. The field wires formed a hexagonal cell around each sense wire. The wire geometry is shown in figure 5. The entire system included 1972 sense wires.

The wires were strung on an aluminum frame. The active area was enclosed between two thin mylar and Saran windows. A complete description of the mechanical construction is given in Ref. [139]. The chambers were filled with a 50-50 mixture of argon and ethane. Approximately 1% by volume of isopropyl alcohol was added as a quench gas. The flow rate was such that the gas volume was changed about twice per day. The field wires were operated at -2650 V relative to the sense wires. The drift speed was 45-50 μm/ns. The

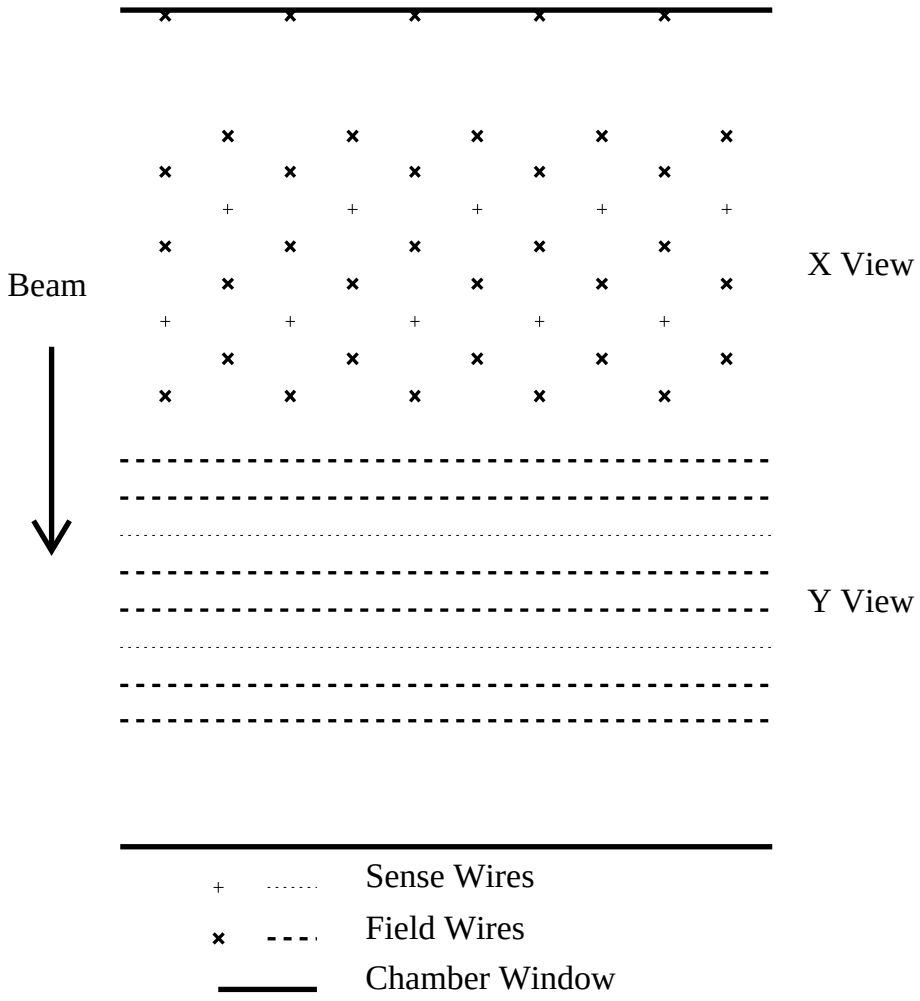

Figure 5. The drift chamber cell geometry. A section of the chamber is viewed from above, along the vertical x-sensing wires.

single-hit resolution was approximately 90 μm. The sense wires were grounded through a resistor; the signal was the voltage drop across this resistor due to the ionization current.

The signals were amplified and discriminated by electronics located on cards on the chamber frames. A LeCroy hybrid chip put out 50 ns ECL logic pulses when the signal crossed a threshold. This threshold level was determined by a reference voltage supplied

individually to each chamber; hence, the levels could be varied to account for variations in noise and environment of the chambers. In practice Chambers 3 and 4 were quieter than the first two; the analysis magnet swept out some low-momentum debris produced by beam interactions.

The analysis magnet had a nominal p_T (transverse momentum) kick of 200 MeV/c, corresponding to a field integral of about 0.67 T-m; the central field was about 0.38 T. This kick was matched to the maximum p_T^2 of the $K \to \pi^+\pi^-$ decay; that is, in-bending tracks were roughly parallel to z after the magnet. The field was carefully mapped for a previous experiment (E731), and varied by $\pm 10\%$ across the aperture; plots of the field may be found in Ref. [136].

The momentum resolution was $(\sigma_p/p)^2 = (0.0050)^2 + (0.00013\ p)^2$, with p given in GeV/c. The first term comes from multiple scattering and the second from chamber resolution. The contributions to each of these terms is discussed further in Appendix I. The track-finding algorithm is described in detail in Chapter 5.

3.4.4 The Trigger Planes

Several segmented planes of scintillator, often referred to hereafter as 'banks' or 'hodoscopes', were available for triggering on charged particles. Each of theses planes was perpendicular to the beam.

For the early portion of the data run (Set 1), two counters known as T and V located at 141 m were used in the charged-mode trigger.[1] The V (T) counter consisted of six horizontal (vertical) strips. The scintillator was 1 mm thick.

The T and V counters were removed midway through the run when the Level 2 trigger was upgraded. This allowed the charged-mode decay volume to extend much further downstream. It also lowered the amount of material in the beam, reducing multiple scattering and beam interactions.

Two hodoscopes were located just upstream of the calorimeter, as shown in Figure 2.

[1] The names stand for Trigger and Veto; these refer to the use of the counters in E731A for triggering on events with converted photons. See [139] for more history.

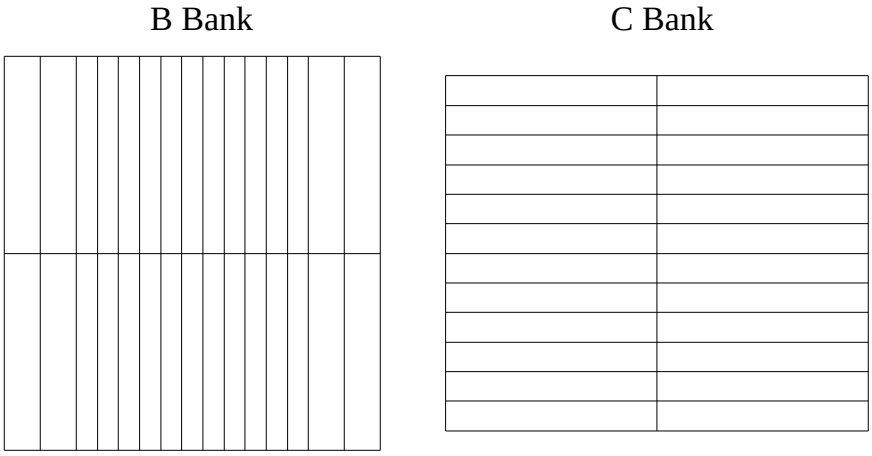

Figure 6. The arrangement of scintillator paddles in the B and C Bank hodoscopes. The view shown is looking downstream.

The B bank (C bank) consisted of vertically (horizontally) oriented scintillator paddles.[2] The geometry of the banks is displayed in Figures 6. The scintillator was about 1 cm thick. Most of the B bank paddles were 10 cm wide; eight outer counters were 18 cm wide. The C bank paddles were each 15 cm wide. The segmentation allowed us to count the number of charged particles as well as impose requirements on their transverse location for triggering.

3.4.5 The Electromagnetic Calorimeter

The electromagnetic calorimeter consisted of 804 blocks of Schott F2 Lead Glass. Each block was 5.82 cm $\times$ 5.82 cm square and 18.7 radiation lengths deep. The blocks were stacked in a roughly circular array of radius 0.93 m with two holes left open for the kaon beam to pass through; the array is pictured in Figure 7.

Electrons and photons striking the lead glass initiated electromagnetic showers and the Cerenkov light from the shower particles was collected at the rear of the block by Amperex

[2]Yes, there once was an A bank [139].

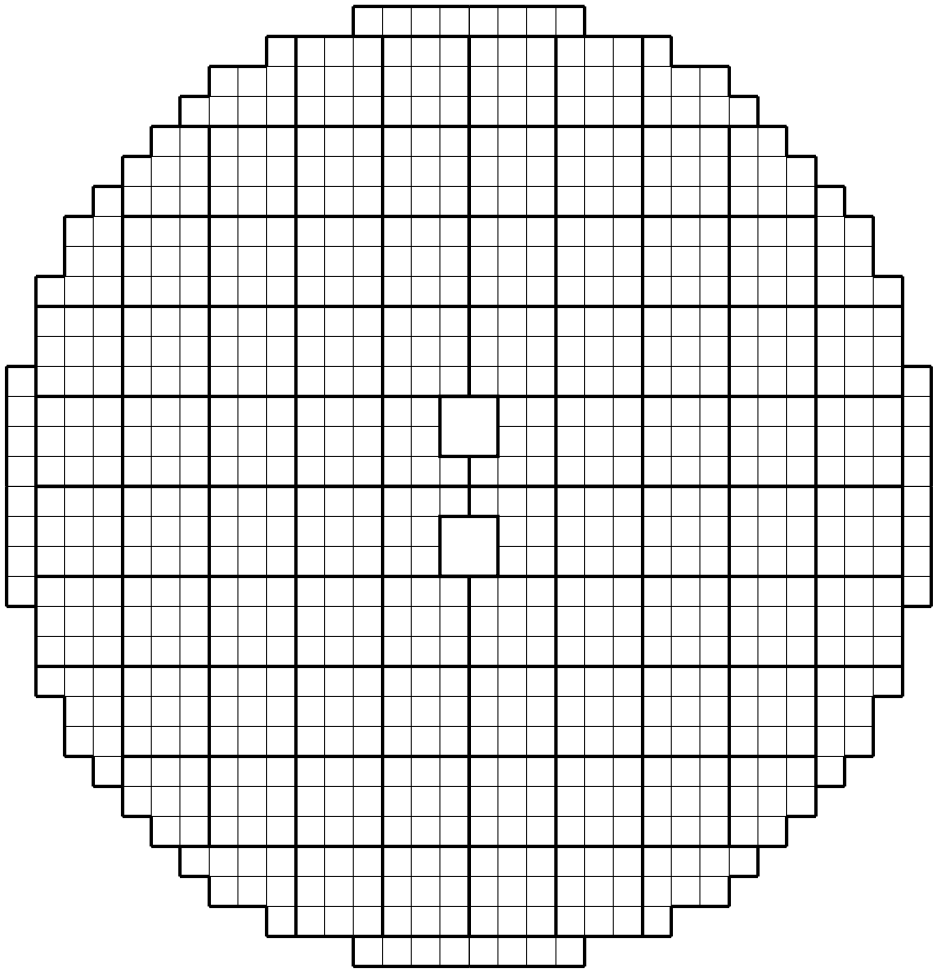

Figure 7. The arrangement of lead glass blocks in the calorimeter. The heavy lines show the groupings of blocks into 'adders' (see text).

2202 phototubes pressure-mounted to the blocks. These tubes had bialkali cathodes, and a filter was placed between the block and tube. More details on the construction on the calorimeter may be found in Refs. [136, 140]. A small constant amount of light was distributed to the front face of each block through an optical fiber; this stabilized the phototube response by maintaining a small anode current. The operating voltages were

periodically adjusted to track changes in response; this was necessary because of the use of the calorimeter in some triggers.

The signals from each phototube were split. The bulk of the signal went through a long delay cable, about 84m of RG58, to a LeCroy 1885N ADC. The ADCs used a 150 ns gate; the long gate length was necessary to obtain good resolution. The other portion of the signal was used in forming 'adder' signals. Each adder signal was the linear sum of a group of about nine blocks. The actual groupings of blocks into adders are shown in Figure 7. The gate used for the adder ADCs was 30 ns; the shorter gate still contained most of the energy of in-time showers and allowed these signals to be used for identification of out-of-time clusters in the calorimeter.

The energy reconstruction and calibration are described later. The resolution of the calorimeter varied from about $3-6\%$, depending on the energy and location of the incident particle. It also provided information on the position of the incident electron or photon to an accuracy of about 2 to 3 mm in each transverse direction.

The array was housed in a temperature-controlled enclosure with a thin (paper) front window. The glass blocks were radiation damaged noticeably over time; the damage degraded the transparency of the blocks. Periodically throughout the run, the lead glass array was exposed to a high-intensity xenon lamp. The ultraviolet light helped to 'cure' some of the radiation damage; most of the damage could be recovered in a cure with duration of about 12 hours.

3.4.6 The Veto System

Many planes of 'Photon Vetoes' were located throughout the spectrometer. These were most useful to detect escaping photons from $3\pi^0$ decays; such decays could contribute significantly to our neutral trigger, designed to select four-cluster events from $K \to \pi^0\pi^0$ and six-cluster events from $K \to 3\pi^0$, and contribute to the background to the $K \to \pi^0\pi^0$ signal. In addition, they were useful in suppressing triggers where charged particles escaped the fiducial volume. These might be due to any of several causes, including loss of actual

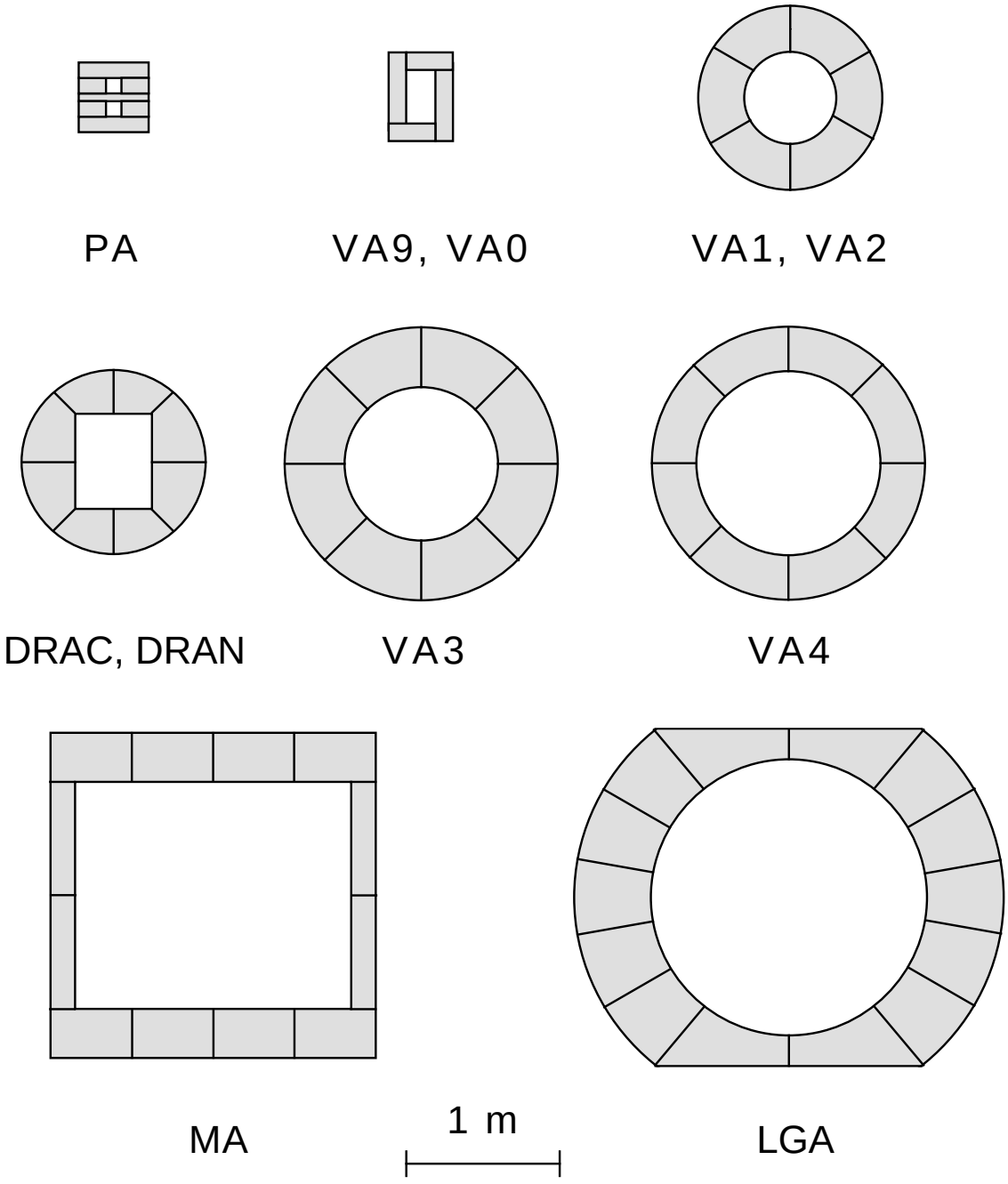

Figure 8. The size and segmentation of the veto counters. Each is shown as viewed by the beam. The segmentation is displayed, but overlaps between counters are not shown.

decay products, inelastic interactions in the regenerators, or hadronic interactions of the beam in material such as the vacuum windows.

The PA (Pinching Anti-counter) was composed of 7 pieces of scintillator. Located just upstream of the UR, it formed a rectangular mask, with two holes to allow passage of the kaon beams. The PA was useful for vetoing events with decay products coming from upstream of the fiducial decay volume.

The SA (Sweeper Anti-counter) was a set of long scintillator paddles that lined the inner face of the BM109 magnet located just downstream of the UR. The magnet was not turned on, but the steel yoke formed a useful shield, blocking some of the products of beam interactions in the UR. The SA counters were very noisy and were not used in the trigger or the analysis.

The set of vetoes VA9, VA0, VA1, VA2, VA3, VA4 (Vacuum Anti-counter 9, etc.) all shared similar construction.[3] Each consisted of a plane of scintillator (6 mm thick) followed by a pair of lead-lucite sandwiches. Each sandwich was formed from five layers each of lead (3 mm per layer) and lucite (6 mm per layer). The scintillator and lead-lucite packages were each enclosed in aluminum boxes such that the inner edge was not active. VA9 and VA0 consisted of four rectangular segments arranged to form a rectangle with a hole in the center. These two vetoes had an additional aluminum skin enclosing the entire device. VA1 and VA2 (VA3 and VA4) were segmented into six (eight) pieces in azimuth. Each transverse segment in each of the three longitudinal sections (scintillator and two lead-lucite sandwiches) was viewed by a phototube; thus three pieces of lucite were viewed by the same phototube. The scintillator signals were discriminated and latched. The lucite signals were digitized. Comparison of the energies in the two lead-lucite sections allows some discrimination of hadronic versus electromagnetic showers.

The HDRA (Hodoscope Decay Region Anti-counter), at $z = 141$ m, was composed of two pieces. DRAC (Decay Region Anti Charged) was a scintillator plane segmented into eight azimuthal sections. DRAN (Decay Region Anti Neutral) was a lead-scintillator sandwich of the same segmentation. Each was circular on the outer edge and each formed a rectangular

[3] VA1-4 were in the original E731 detector; VA9 (or VA-1) and VA0 were added further upstream for E773 and E799.

inner aperture designed to match the structure of the T and V counters. Each of the planes was viewed by eight phototubes located at the junction of the azimuthal segments.

The MA (Magnet Anti-counter) and LGA (Lead Glass Anti-counter) were both constructed of scintillator and two lead-lucite sandwiches similar to the VAs. The MA veto was located just upstream of the analysis magnet and defined an inner aperture inside the magnet steel. The LGA consisted of twelve modules forming an annulus with an inner radius roughly equal to the size of the calorimeter.

The LGA allowed some photons from far downstream decays to pass within its aperture but still miss the lead glass array. In an attempt to fix this, and make the detector more hermetic, an annular iron ring, 8.26 cm wide, was hung at 179.3 m to fill the gap. Photons hitting the ring would shower and leave energy in many of the B and C hodoscope paddles, and possibly form clusters at the edge of the calorimeter. In the neutral-mode analysis [141], cuts are made on the multiplicities in the B and C hodoscopes. Both the extra cluster and the hodoscope activity therefore help identify potential background to the $K \to \pi^0\pi^0$ signal with photons that hit the iron ring. There is a small unfortunate side-effect due to the ring causing sufficient energy loss from electrons at the extreme periphery of the calorimeter to compromise the particle ID in the charged analysis; this is discussed further in Chapter 6.

Photons vetoes surrounded all of the critical outer apertures of the detector. A beam's-eye view of those discussed so far is shown in Figure 8. The remaining photon vetoes covered areas in the beam region.

The CA (Collar Anti-counter) consisted of two identical units, each one surrounding one of the beam holes in the calorimeter. Each unit contained 4.45 cm of copper and 2.8 cm of lead followed by scintillator. They covered the inner half of the lead-glass blocks adjacent to the beam holes. Both energy and position resolution of showers from particles landing in this area would be compromised by lateral leakage of shower energy into the hole region. The CA allowed us to veto such events in the neutral trigger. In charged mode, this veto was not necessary; one could simple cut on tracks that projected into this area where the particle identification was compromised by leakage into the holes and energy loss in the CA itself.

The BA (Back Anti-counter), located behind the lead wall but in front of the muon

steel (see below), was 48 layers of lead-lucite sandwich (16 cm total lead), 28 radiation lengths deep. It was preceeded by a scintillator plane of the same transverse size which aided in triggering on tracks used to calibrate the device. The depth allowed discrimination between photons going down the beam holes in the lead glass and beam hadrons; photon showers could not penetrate the full depth, while hadronic showers generally penetrated deep into the device. Its primary use was vetoing lost photons in the neutral-mode trigger and analysis. It was not used in the charged mode. Figures depicting the CA and BA may be found in Ref. [140].

3.4.7 The Hadronic and Muon Systems

Behind the calorimeter was a lead wall 21 radiation lengths thick. The combined radiation lengths of the lead glass and this wall were sufficient to completely absorb any electromagnetic showers. After the wall was a hodoscope bank, Mu1, with two holes to allow the beams to pass. This counter was used in veto in the neutral trigger. Pions interacting in the Lead Glass and/or lead wall would fire this counter bank, allowing it to function as a hadron veto. An illustration of the counter bank may be found in Ref. [140]. These counters were not used in the charged trigger or analysis.

Downstream of Mu1 and the BA, 3.2 m of steel served as a muon filter. Muons above 7 GeV/c were passed with very high probability. A scintillator hodoscope, Mu2, was placed behind the steel to detect these muons. This hodoscope consisted of 34 overlapping paddles of scintillator for complete coverage; an illustration of the paddle arrangement may be found in Ref. [142]. These counters were used in the trigger to veto events with muons. This removed $K \to \pi^{\pm}\mu^{\mp}\nu_{\mu}$ decays which would have otherwise comprised a large fraction of the charged trigger. In addition events with $\pi \to \mu$ decays in flight and events with extra tracks from accidental muons from the proton beam dump were also vetoed at the trigger level.

Some transition radiation detector (TRD) modules which were under development for E799 were hung between the fourth drift chamber and the LGA. These were not used in E773; only the small addition of material is relevant. There were no radiators accompanying

them or xenon gas in the chambers during our running, such that the amount of additional material was minimal compared, say, to that in the B and C banks.

3.5 Summary

This chapter has presented an overview of the beamline and detector components used in E773. We now turn to more detailed discussions of the data collection, calibration, and analysis that we have performed.

CHAPTER 4

DATA COLLECTION

In the previous chapter, we described the basic structure of the detector elements. We now turn to a discussion of how these devices were used to form a trigger, and how the data was read out from the detector.

4.1 The Trigger

The trigger for E773 employed a two-level system. The first-level trigger was formed by prompt signals from the detector; it was thus fast and available for each 19 ns bucket in the proton spill structure. When a first level trigger was received, further triggers were inhibited. The next step depended on the type of trigger. For some first level triggers, such as accidentals or ADC pedestal data (see below), data readout was started immediately. The physics triggers, however, had a second level trigger requirement to further reduce the rate. Neutral-mode triggers required a specific number of clusters of energy deposition in the calorimeter. For charged-mode triggers, the requirement involved the number and distribution of hits in the four drift chambers. A failed second-level requirement resulted in an abort of digitization and a fast clearing of the data acquisition (DAQ) system so that we could resume acceptance of any first-level trigger. The ADCs were allowed to settle for 500 ns before resuming. A successful-second level requirement initiated readout of the event; upon completion of readout, the first-level triggers were re-enabled.

4.1.1 The Fast First-Level Trigger

The first level trigger consisted of prompt signals from the trigger hodoscopes (B,C,T, and V) and veto counters, and a fast energy sum from the calorimeter.

For charged mode, the active part of the trigger consisted of requirements on the T and V scintillator planes and the B and C hodoscopes. The T and V counters were only in place for the first portion (Data Set 1) of the run. An analog sum of the six counters in each plane was formed and discriminated at 1.5 minimum-ionizing equivalents. Since the counters were thin (1 mm), only a signal in either T *or* V was required in the trigger, to maintain high efficiency.

Each of the B and C Banks was required to have two or more counters firing in order to trigger. In addition, there was an left-right requirement in the B Bank, and an up-down requirement for the C Bank. The counters forming the left section of the B Bank, etc. are shown in Figure 9. There was some overlap of counters included in the up-down and east-west regions to maintain high efficiency for $K \to \pi^+\pi^-$ decays. The two-or-more requirement preventing firing of the trigger by a single accidental track passing through a counter in the up-down or left-right overlap regions. The topology requirements were useful at reducing the trigger rate from $K \to \pi^\pm \ell^\mp \nu$ and $K \to \pi^+\pi^-\pi^0$ events where the charged particles need not have balancing transverse momentum, and can thus both appear on the same side of the detector centerline.

The coincidence between T/V hits and B/C hits was very powerful in selecting a two-track sample. Accidental coincidences were rare, and the counters formed a telescope guaranteeing that particles had traversed the active region of the spectrometer. When T and V were removed, much of this power was lost; the remaining B and C banks had no lever-arm in z. Thus, noise in B and C or accidental muon tracks on the periphery of the detector could satisfy the hodoscope portion of the first-level trigger. The burden was then shifted to the second-level trigger described below.

Events were vetoed if there was a signal in any of the following photon vetoes: PA, VA9, VA0, VA1, VA2, DRAC, VA3, VA4 or LGA. Each of these used the fast signal from the scintillator portion of the device, except for the LGA, which used the output of the lucite in

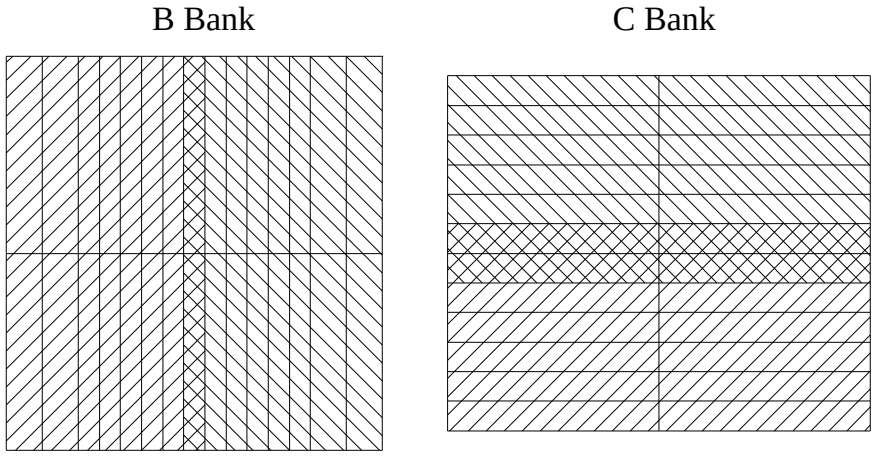

Figure 9. The scintillator paddles in the B and C Bank hodoscopes, showing the groups used in the trigger. The two styles of hatching denote the left and right (up and down) regions of the B Bank (C Bank).

the lead-lucite sandwiches. Having some of the lead-lucite photon detectors in the trigger helped to reduce the rate from $K \to \pi^+\pi^-\pi^0$ decays where photons were lost outside the fiducial volume.

The two counters in the last plane of the DR were available as trigger vetoes. The counters in the 28th and 36th (last) planes of the UR were used in the trigger. Events were vetoed if any counter included in the trigger saw more than about 0.5 minimum-ionizing equivalents.

Any signal in the Mu2 counter, located behind the steel muon filter, was also sufficient to veto an event.

For neutral mode, the non-veto portion of the trigger consisted of a requirement on the total energy deposit in the calorimeter of greater than 25 GeV. The vetoes were similar to those used in the charged trigger: PA, VA9, VA0, VA1, VA2, DRAC, VA3, VA4, LGA, CA and BA. The CA veto prevented us from taking events with photons in the inner half of the glass blocks surrounding the beam holes; the reconstruction here would be compromised. The BA only vetoed an event if there was significant energy in the front section, but very

little in the rear; this distinguished photon showers from interactions of beam hadrons. The Mu2 bank and the regenerators were used exactly the same as for the charged trigger. Some of the less important photon veto sources were added during the run, in order to be consistent with the charged-mode vetoes. For more details, see Ref. [141].

4.1.2 The Charged-Mode Second-Level Trigger

The charged mode employed two distinct methods of second-level triggering. First, we describe the signals that were available for use in making the decision.

The sixteen planes of sense wires in the drift-chamber system contained a total of 1972 channels. Each of these was individually sent to a TDC for off-line analysis, where the digitized drift time was converted to a distance determining the point of passage of the particle relative to the sense wire. Just before the TDC modules, the ribbon cables carrying the pulses were tapped with high-impedance pickoffs by 'Repeater Boards' attached to an in-line connector in each cable. These boards copied the signals for use in triggering. Each Repeater Board received 16 signals from the upstream member of a plane-pair and the corresponding 16 signals from the downstream partner plane.

Two 'OR' signals were formed from these wires by a logical OR of the signals. Each OR included eight wires from each of the plane pairs and physically corresponded to a contiguous 10 cm strip of the drift chamber. This is illustrated in Figure 10. The strips were sometimes smaller at the chamber edges, where not all electronics channels were matched to actual sense wires. Thus, each view of each chamber produced from 14 to 18 such ORs, depending on the size of the particular chamber. A total of 128 signals were produced. In addition, copies of all 1972 channels were sent to a hit-counting processor (hence the name 'Repeater Boards') which was being readied for use in the rare-kaon decay experiment, E799 [143]. Only the OR signals were used in E773. A summary of the number of wires and OR signals formed for each plane pair is given in Table 4. We are now prepared to explain the two triggering strategies using these ORs employed in E773

The first second-level trigger we used, known as Chamber East-West logic (CHEW), required that each of the four drift chambers had at least one hit on each side of the centerline

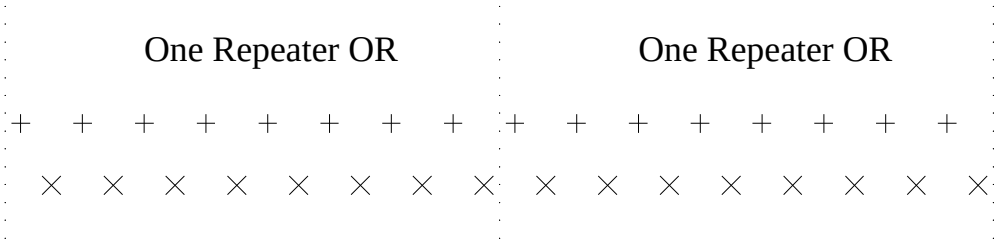

Figure 10. An illustration of the mapping of drift chamber wires into TDC cables and Repeater Board ORs for use in triggering. A small section of a chamber plane pair is shown. The dotted lines delimit the group of wires included in each OR.

in the x-view. This method was used for Data Set 1 when the T and V hodoscopes were still present. CHEW was easily implemented by further combining the OR signals from each chamber to obtain eight signals, one including all wires from each half on the four x plane-pairs. All eight of these signals were required to be on to satisfy the trigger. The gate for accepting valid hits was about 300 ns, somewhat longer than that used in off-line analysis. This gate width compensated for small variations in the cable delays. The x view was used since the beams are both centered in this view. A simple calculation demonstrates that, for an event with no initial transverse momentum, the decay products must *still* be one on each side of center even after the analysis magnet imparts its kick, which is also in the x direction. The CHEW requirement cuts many of the $K \to \pi^{\pm}\ell^{\mp}\nu$ and $K \to \pi^{+}\pi^{-}\pi^{0}$ decays while keeping most of the $K \to \pi^{+}\pi^{-}$: the three-body decays may have both charged particles on one side of center. The CHEW logic was not always imposed during Data Set 1 due to work in progress on the newer Level 2 system. However, for ease of analysis, it is always imposed in software for this data.

The other second-level trigger method involved crude pattern recognition on the group

Table 4. Number of sense wires and trigger signals for the drift chamber plane pairs.

Plane Pair	wires per plane	OR signals per plane pair
Chamber 1 x	101	14
Chamber 2 x	128	16
Chamber 3 x	136	16
Chamber 4 x	140	18
Chamber 1 y	101	14
Chamber 2 y	112	14
Chamber 3 y	128	16
Chamber 4 y	140	18

of ORs that fired. This method was referred to as 'ZUMA' logic. The ORs were fed into custom-designed FASTBUS boards, colorfully denoted ZUMA after a California beach. Each ZUMA board received ORs from one view, x or y, of all four drift chambers. ZUMA was based on two cascaded stages of brute-force memory lookup tables and was hence very fast. Roughly speaking, the first stage of lookup tables counted the number of potential track segments on each side of the analysis magnet, and the second stage applied requirements on the number and distribution of segments. The logic was such that if a given set of hits passed the trigger, the same set plus any distribution of additional hits also passed. This avoided sensitivity to accidentals. The x and y view ZUMA boards worked independently; both were required to pass an event in order to satisfy the trigger. The answer was ready approximately 100 ns after the end of the gate defining the valid time region for chamber hits. ZUMA was used for Data Set 2, after the T and V hodoscopes were removed from the decay volume.

We now describe the programming of the look-up tables in detail. The number of possible patterns presented to the look-ups was very large. We therefore designed a simple algorithm to make the decision, and used this algorithm to determine how to load the tables. The organization of the OR signals and the memory look-ups is illustrated in Figure 11.

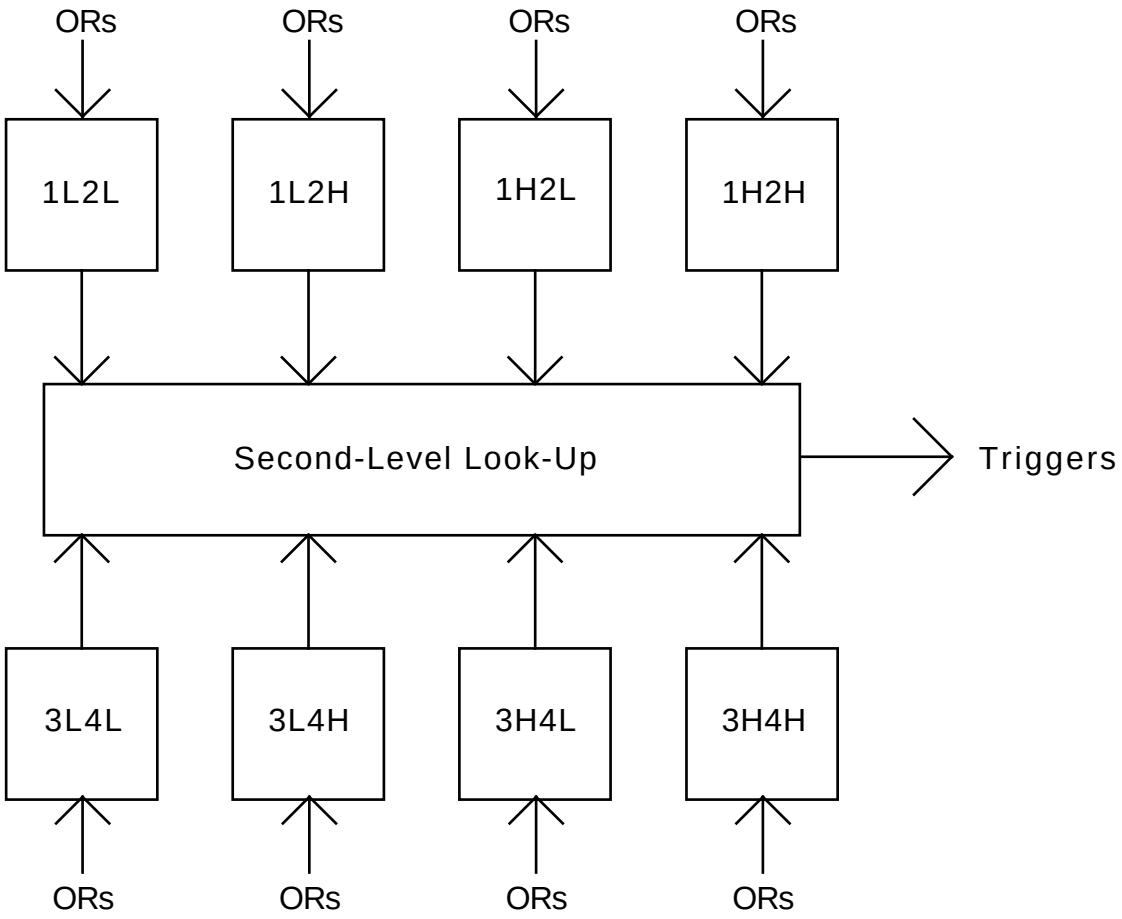

Figure 11. A basic schematic of the inputs and memory look-ups on the ZUMA Level-2 Trigger board. The eight small boxes are the first-level memory look-ups. They are labeled according to the OR signals that form the address. 'NL' ('NH') denotes the wires from the $-x$ ($+x$) half of chamber N. The output of the first level memories addressed the second level memory, which produced the trigger bits.

For ease of discussion, we will discuss the x board; the y board worked in an analogous fashion.

Each board received about 64 signals (66 for x and 62 for y, to be precise). About half were upstream of the magnet, half downstream; each of these sets was treated independently by the boards for the first-level look-ups. The signals upstream of the magnet were formed into four (non-exclusive) groupings:

- ORs from the $-x$ half of chamber 1 and the $-x$ half of chamber 2.

- ORs from the $-x$ half of chamber 1 and the $+x$ half of chamber 2.
- ORs from the $+x$ half of chamber 1 and the $-x$ half of chamber 2.
- ORs from the $+x$ half of chamber 1 and the $+x$ half of chamber 2.

Similar groupings were made with the ORs on chambers 3 and 4. Referring to Table 4, we see that each grouping had from 14 to 18 bits of data from the OR signals. Each of these eight sets of ORs formed the address to its own memory chip (or set of chips) containing two bits of data per address. The data is interpreted as follows: the two bits encode the number of valid segments found in the pattern of ORs that addressed the memory. Since we were looking for two-track events, the only responses encoded in the two output bits were: 0, 1, and 2 or more.

Each first-level memory was loaded with these responses according to the following algorithm. All pairs of ORs, one from each chamber providing OR bits, were looped over. Each pair was compared to a list of valid OR pairs, and the number of valid pairs was totaled. The pairings of ORs corresponding to valid segments are shown in Figure 12. There are two points to note. First, we really wish to determine the number of valid segments in Chambers 1 and 2, say. The problem was further subdivided into the four half-chamber combinations because the number of address bits would otherwise be impossibly large for a memory look-up. Reducing the number of bits by making the ORs correspond to wider strips of the chamber would have lost much of the rejection power. Second, we need a criteria for determining which OR pairings form valid segments to form the 'OR Maps' seen in Figure 12. These were determined by examining which combinations occurred frequently for Monte-Carlo samples of $K \to \pi^+\pi^-$ decays. We mention that much of the charged trigger rate is due to the $K \to \pi^\pm e^\mp \nu_e$ decays; these can be partially discriminated against by the list of valid segments, especially with the list for the x view downstream of the analysis magnet. A three-body decay will have steeper track segment angles than a two-body decay, and this is reflected in which pairs of chamber ORs are fired by the tracks.

Each board contained 4 16-bit lookup tables (upstream) and 4 18-bit lookup tables (downstream), each putting out two bits. The total data for the first-level lookups on each board was thus $2 \times (4 \times (2^{16} + 2^{18})) = 2.6$ megabits.

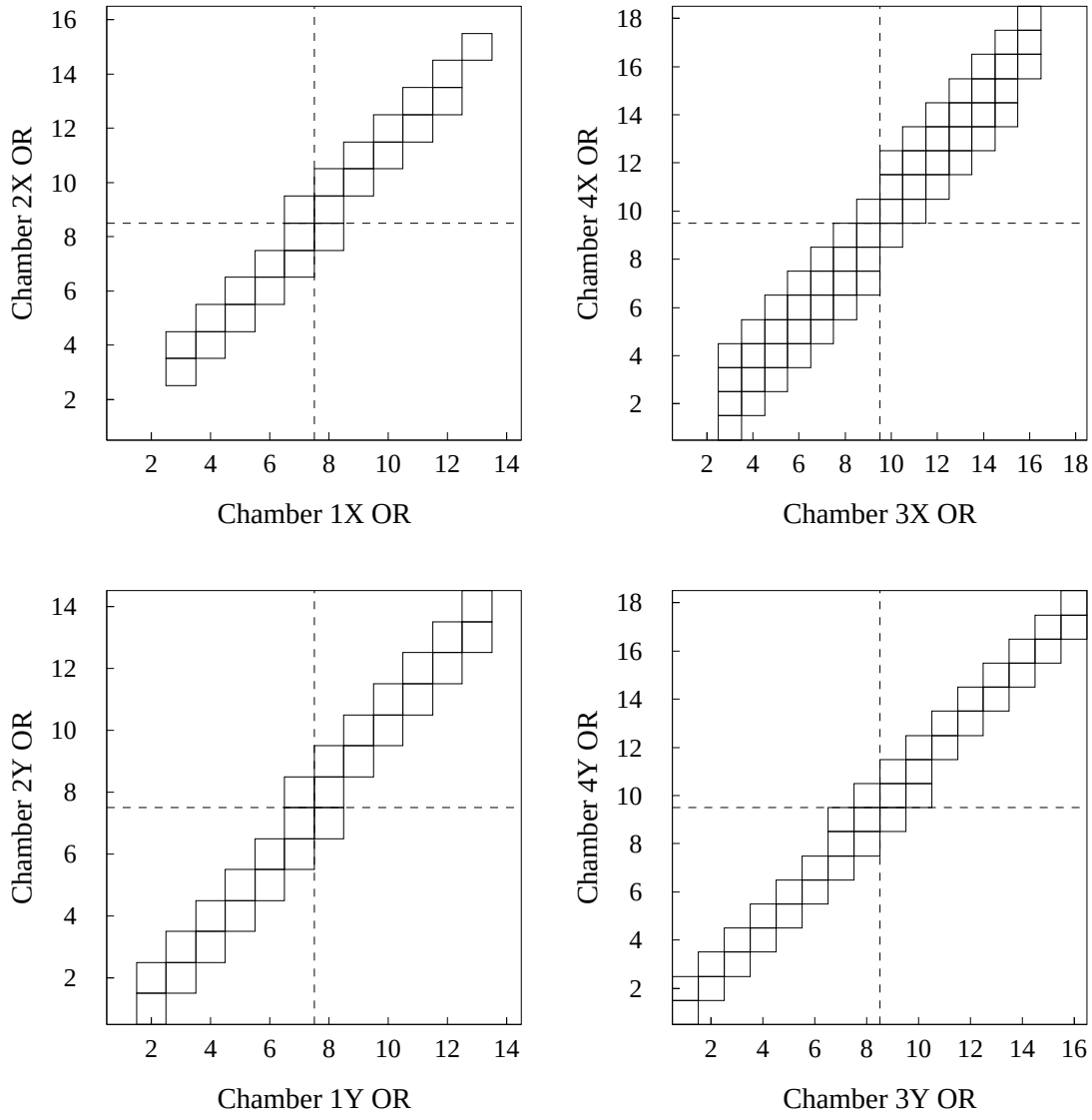

Figure 12. The combinations of chamber ORs forming valid track segments in the Level 2 Trigger. In each plot, the axes are the number of a particular OR of wires that fired; each OR corresponds to a 10 cm strip of the chamber. Boxes are shown for each combination of ORs corresponding to a valid segment. The dotted lines delimit the four first-level look-up tables corresponding to each plot. Each first-level look-up table used the information from one of these quadrants. Recall that there were two boards, each with eight first-level look-ups, giving rise to the four plots shown.

Table 5. Track segment requirements for the charged-mode Level 2 Trigger. Each column corresponds to the output from one first level look-up; the naming convention is the same as in Figure 11. Each line corresponds to a distinct minimum requirement. If the number of segments found equaled or exceeded the numbers listed in any given row, the trigger was satisfied.

Segment Type	1L2L	1L2H	1H2L	1H2H	3L4L	3L4H	3H4L	3H4H
X View Board								
	1	0	0	1	1	0	0	1
	1	0	0	1	0	1	1	0
Y View Board								
	1	0	0	1	1	0	0	1
	1	1	0	0	1	0	0	1
	0	0	1	1	1	0	0	1
	2	0	0	0	1	1	0	0
	2	0	0	0	1	0	0	1
	0	0	0	2	0	0	1	1
	0	0	0	2	1	0	0	1
	2	0	0	0	2	0	0	0
	0	0	0	2	0	0	0	2

ZUMA second-level look-up tables were addressed by the 16-bit output from the first-level memories and imposed requirements on the number of segments found. The requirements are summarized in Table 5; these requirements are the minimum accepted; more segments are always allowed. The trigger required that both the x and y view boards accept the event.

In addition, three looser triggers were taken to allow studies of the effects of the main trigger. The looser the requirement, the higher the pre-scale that was applied. The first extra trigger was similar to the main trigger, but somewhat looser. The second was designed to require only one or more tracks. The third had no requirements at all. All shared the same first-level lookup tables; this was necessary due to the hardware.

The number of chamber hits per event is shown in Figure 13 for various trigger configurations to demonstrate the effects of T and V, CHEW and ZUMA.

4.1.3 The Neutral-Mode Second-Level Trigger

The second-level trigger decision for neutral mode was based on the Hardware Cluster Finder (HCF), which has been described in detail elsewhere [144]. This device provided a count of the number of distinct clusters of energy in the calorimeter. Each of the 804 blocks was discriminated at approximately 1 GeV and these 804 bits sent to the HCF. This processor counted the number of islands of bits that were on. The information was available about 30 μs after a first-level trigger. We generally accepted events with either 4 or 6 clusters, corresponding to $K \to \pi^0\pi^0$ and $K \to 3\pi^0$ decays. Early in the run, 5 and 7 cluster events were also taken to help study the effect of these requirements.

For triggers where both the neutral and charged first-level triggers fired, the event was treated as a charged trigger. Studies showed that there were a negligible number of good $K \to \pi^0\pi^0$ decays in these overlapping triggers.

4.1.4 Other Triggers

Several special-purpose triggers were taken simultaneously with the two main physics triggers just described.

An accidental trigger was used to sample the average activity in the detector that accompanies a real K decay event. The trigger consisted of the coincident firing of three small scintillators that were arranged about 38 m downstream and 3.4 m to the west of the secondary beamline and collimation system (about 85 mrad from the proton direction). The scintillators were collinear with each other and the target, and thus sampled the instantaneous rate of the proton beam spill. This is a better method of collecting accidental events than a random-bucket trigger because of rate variations among the buckets in each spill. Real physics triggers, as well as this accidental trigger, both fire more frequently when the number of protons in a bucket is larger. These accidental events are useful for overlaying

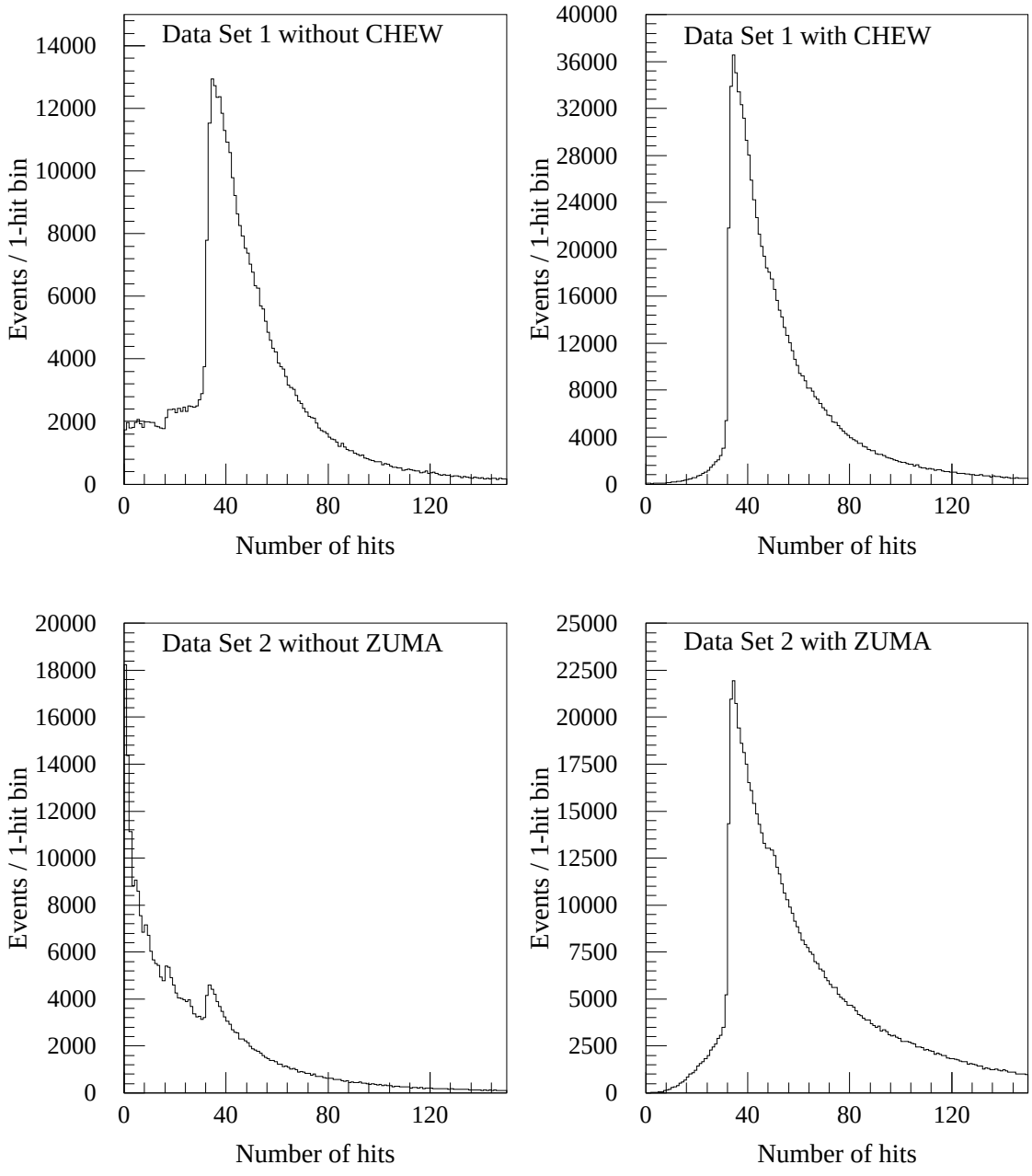

Figure 13. The number of drift chamber hits per event for various triggers. All plots include the vetoes and the B and C bank requirements; in addition, the Data Set 1 plots include the T *or* V requirement.

with Monte-Carlo events to simulate the data more accurately. About 1% of the events written were from this trigger.

A pedestal trigger was taken both during and between the beam spills to monitor the ADC pedestals for all ADCs in the experiment. Typically, about 10 pedestal events were taken each spill cycle. These pedestals were averaged and downloaded into the ADC controllers in each FASTBUS crate for subtraction during the next beam spill. It was noted in E731 that there was an effect on the lead-glass ADC pedestals which correlated with the use of the HCF on a particular event (the HCF was not needed for the charged trigger). This is due to the flash ADCs in the HCF causing noise that is communicated via the cabling. As a result of this knowledge, the HCF was 'flashed' on every trigger in E773, regardless of whether its result was necessary for a trigger decision.

There was a flasher system installed to monitor the lead-glass gains for each channel. A xenon lamp was flashed, and the light distributed by fibers to the front of each block in the array. About $10 - 15$ of these events were taken each spill.

4.2 The Data Acquisition System

4.2.1 Read-Out

The data available from each detector element are summarized in Table 6.

The experiment used LeCroy 1885N (dual-range) FastBus ADCs. A PDP 11/43 communicated with the ADC modules in order to change the digitization from low to high range for taking pedestals and to download updated pedestal values between spills. The ADC data was read out with a 5-count threshold used to sparsify the data. The drift chamber TDC system used CAMAC modules: LeCroy 4291B TDC modules with LeCroy 4298 crate controllers. All scalers and latches were CAMAC devices also. These CAMAC crates were read out with Smart Crate Controllers (SCC) into a FastBus module. The data streams were: lead-glass ADCs, non-lead-glass ADCs, CAMAC, TRD ADCs, and charged Level 2 trigger monitoring (via FastBus). Each data stream was buffered in a LeCroy 1892 FastBus Event Buffer. The total readout and digitization times for the CAMAC and FASTBUS subsystems were similar; events took about 800 μs to be read out. This allowed the data

Table 6. The data available from the detector components. The regenerator latches are only for those counters in veto. The BA latch is for the scintillator plane upstream of it. MABS is the movable shadow absorber upstream of the DR.

Component	ADC	TDC	Latch
Drift Chamber Wires		X	
Lead Glass Blocks	X		
Lead Glass Adders	X		
T and V Counters	X		X
B Bank Counters	X		X
C Bank Counters			X
Mu1 Bank Counters	X		
Mu2 Bank Counters			X
Regenerators	X		X
PA, SA			X
VA,MA,LGA Scint.			X
VA,MA,LGA Lead/Lucite			X
DRAC	X		X
DRAN	X		
CA	X		X
BA	X		X
MABS, UR, DR positions			X
Trigger Sources		X	X

from a 21 s spill to be read out over the entire minute-long spill cycle. A General Purpose Manager module (by Dr. Struick) built each event from the subunits in each event buffer. The data was sent to a VME crate containing Omnibyte ACP modules; these modules again buffered the data before it was written to one of four Exabyte 8mm cassettes operating in parallel. A typical event was 1.75 KB and the throughput was 12,500 events/spill. The buffers required almost the entire one minute spill cycle to be emptied onto tape. One full data run took approximately 6 hours to fill the four tapes with about 8 Gigabytes of data. Runs were often stopped prematurely for various reasons; on average the tapes were half full. E773 wrote about 500 million events onto about 1000 8mm tapes. We wrote out just over 3 times as many charged triggers as neutral triggers.

4.2.2 Live Time

A few comments about live time are in order. One easy way to monitor live time was provided by scalars counting the number of first and second level triggers. All first level triggers were counted, regardless of whether the experiment was live or dead. The input to the second level processors was only enabled if the DAQ was live. Thus the ratio of first-level triggers to second-level alerts gave the effective live-time. We point out that this quantity is *not* the same as one would naively calculate based on the number of events read out times the mean read-out time. The difference is due to intensity fluctuations in the primary proton beam. Due to such fluctuations, the triggers are somewhat correlated in time, such that the detector tends to be dead more often when the instantaneous trigger rate is fluctuating above average. This causes an increase in real dead-time as compared to the naive calculation. In practice, we were about $40 - 50\%$ live.

4.3 Special Runs

4.3.1 Single Muons for Drift Chamber Alignment

In order to align the drift chambers, special runs were taken. For these runs the trigger was simply at least one hit in the B Bank and at least one hit in the Mu2 bank ($B \cdot Mu$);

or at least one hit in the C Bank and at least one hit in the Mu2 bank ($C \cdot Mu$). Each run used only one of the ($B \cdot Mu$) or ($C \cdot Mu$) triggers; these were alternated so that these runs could also be used to monitor the performance of the hodoscope not required in the current trigger.

4.3.2 Other Monitoring Runs with Muons

Many runs with triggers of the form $B \cdot Mu \cdot Detector$ runs; where 'Detector' denotes that another detector element was required to fire in coincidence. This was done for each regenerator, and the photon vetoes to allow monitoring of their performance.

4.3.3 Electron Calibration Data for the Calorimeter

At four times during the run, special electron calibration runs were taken to calibrate the lead glass calorimeter. For these runs, a special target was used, and a photon converter placed after near the target to create e^+e^- pairs. The trigger used was very similar to the charged-mode trigger. These electron calibration runs are described in more detail in Ref. [140]. The large, concentrated samples could be rapidly analyzed and the results used to adjust the phototube voltages to maintain gain balance between the channels. This was important both for the total energy sum used in the first-level neutral trigger as well as the proper operation of the HCF.

4.3.4 Special Studies

Many special runs were also taken to allow studies of the effects of various trigger elements. Various runs were taken with each of the following modifications: no photon vetoes, no regenerator vetoes, no CHEW requirement, no ZUMA requirement, and no ADC readout threshold. In addition, a run was taken with no regenerators in the beam.

4.4 Summary

We have now completed our discussion of the trigger and data acquisition systems used by E773. We will continue with an explanation of our analysis techniques, including the calibration procedures as well as the physics analysis.

CHAPTER 5

EVENT RECONSTRUCTION AND DETECTOR CALIBRATION

We next describe how the raw data read out from the detector components is processed in order to obtain more useful information. The most relevant part for our purposes is the reconstruction of tracks from the drift-chamber hits.

Calibration of the detector is also an important task. The charged-mode analysis is sensitive to the performance of the charged spectrometer system; we describe these calibration procedures in detail. The calibration of the rest of the apparatus is also summarized.

5.1 Track Reconstruction

We first describe how the charged-particle tracks in the spectrometer are reconstructed. Broadly speaking, tracking consists of identifying which hits to use, performing pattern-recognition to locate tracks, and fitting the resultant tracks to determine the direction of the particle.

5.1.1 Basic Terminology Relating to the Chambers

A brief introduction to some of the oft-used terms used when discussing the chambers. We refer to the chambers by number from 1 to 4; the larger numbers being further down-

stream. The two planes of sense wires in a given view (x or y) of the same chamber are termed a 'plane pair'. For each plane, the other member of its plane pair is known as its 'partner plane'. We define a 'hit pair' to be two adjacent hits, one from each member of a plane pair. Thus, for a given hit wire, there are exactly two wires (except at the chamber edge) with which it may form a hit pair.

There is also one measured quantity which is so common and useful that it deserves special exposition. The sum of the two drift-distances for the hits in a hit pair should equal the cell size, after including a few simple corrections; the most important of these is due to the track angle. A very useful quantity is the appropriately corrected sum-of-drift-distances (SOD) minus the nominal cell size. It is useful to always subtract the cell size by default; we do so, and loosely refer to the summed distance minus the cell size as the SOD. This SOD peaks at zero for real, in-time hit pairs; it is useful for detecting out-of-time hits and also for monitoring the chamber resolution. The width of the SOD distribution is $\sqrt{2}$ times the chamber position resolution, ignoring any correlated contributions to the resolution. A plot of the SOD from one plane pair for a large sample of tracks is shown in Figure 14. Note the prominent left shoulder due to the production of δ-rays. These only affect the distribution if the δ-ray ionization arrives at the sense wire *before* that from the parent particle, hence the asymmetry.

5.1.2 Valid Hits

In order to identify the sub-sample of hits to use, the hits read out from the drift chamber TDCs were subjected to a timing cut restricting them to a window 240 ns wide. The window was located such that prompt hits from tracks immediately adjacent to a wire were located about 10 ns from one end, leaving an effective range of about 230 ns. A plot of a typical raw hit-time distribution is shown in Figure 15. We have inverted the raw time from the TDC, which was run in common stop-mode. The inversion makes increasing times correspond to increasing drift distances, which is more intuitive. All hits falling within this window were considered valid and were added to a list. For each hit in the list, the transverse position of the hit wire and the drift distance were calculated. The wire position is corrected for the

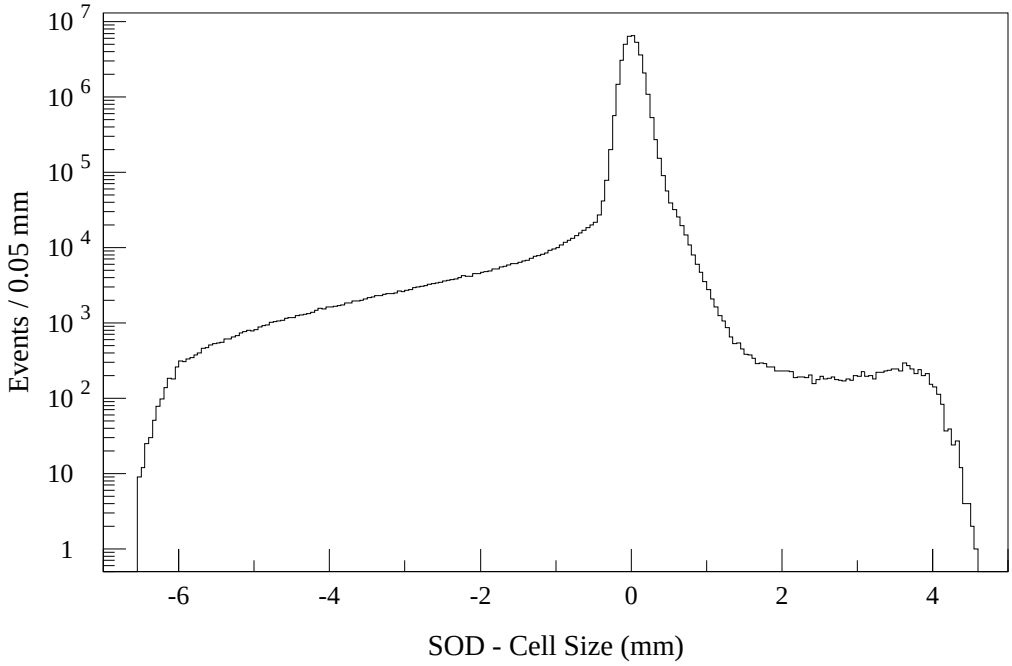

Figure 14. The sum-of-drift-distances minus the cell size (SOD) for one wire plane pair. Corrections for track angle and other smaller effects have been applied. The cutoff at 4 mm is due to a cut in the tracking algorithm. The prominent left shoulder is due to δ-rays. This plot contains tracks from all $K \rightarrow \pi^{\pm} e^{\mp} \nu_e$ decays from Data Set 2. The single-hit resolution of each plane in this pair is about 82 μm; this is the best resolution achieved in the system.

transverse position of the chamber; the drift distance is determined from a time-to-distance look-up table described later in this chapter.

Any event with more than 150 valid hits is discarded as too noisy to be trackable. The distribution of the total number of hits was shown in Figure 13 for a variety of trigger configurations. The fraction of events with two reconstructible tracks was observed to decrease smoothly by almost an order of magnitude as the total number of hits increased from about 30 to 150; this is illustrated in Figure 16.

The tracking algorithm used in E773 is largely the same as that used in E731 [136]. The main changes involved different aperture cuts, a loose timing cut on hit pairs, and a modified matching algorithm used to pair candidate x segments into full tracks.

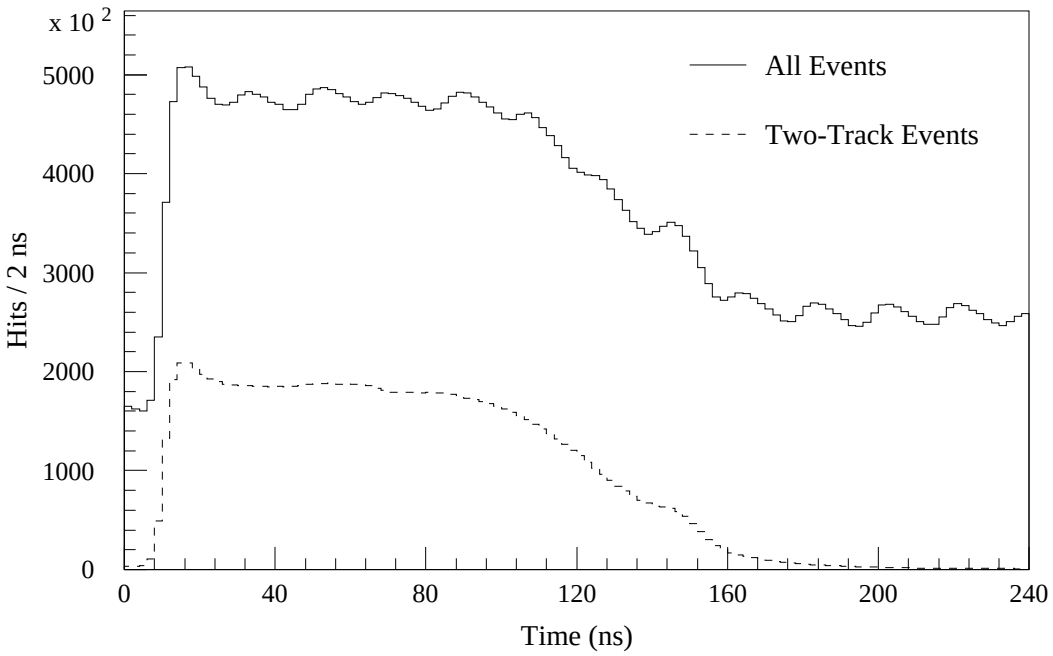

Figure 15. The time of drift chamber hits from raw events. The solid line shows all hits; the dashed line shows hits on tracks for two-track events. The events are from Data Set 2. Note the sharp edge due to prompt hits from tracks passing near the sense wires. The 19 ns bucket structure of the proton spill is also visible.

5.1.3 Overview of the Pattern Recognition

We first give a quick overview of the algorithm to orient the reader. In the x view, candidate track segments are found separately upstream and downstream of the magnet. This is done by looping over pairs of hits in two chambers and subjecting these candidate segments to various cuts to identify valid segments. These segments are then formed into full x tracks by matching their projections at the mid-plane of the analysis magnet. Since y tracks are largely straight, they are found in one step by a similar process of looping over hit pairs in two chambers and identifying appropriate hits in the remaining chambers. As with the x view, we impose various criteria to select valid tracks. Matching of the x and y views involves the use of reconstructed clusters in the calorimeter, and will be discussed shortly. The algorithm was designed to be most efficient for two-track events. A flag is

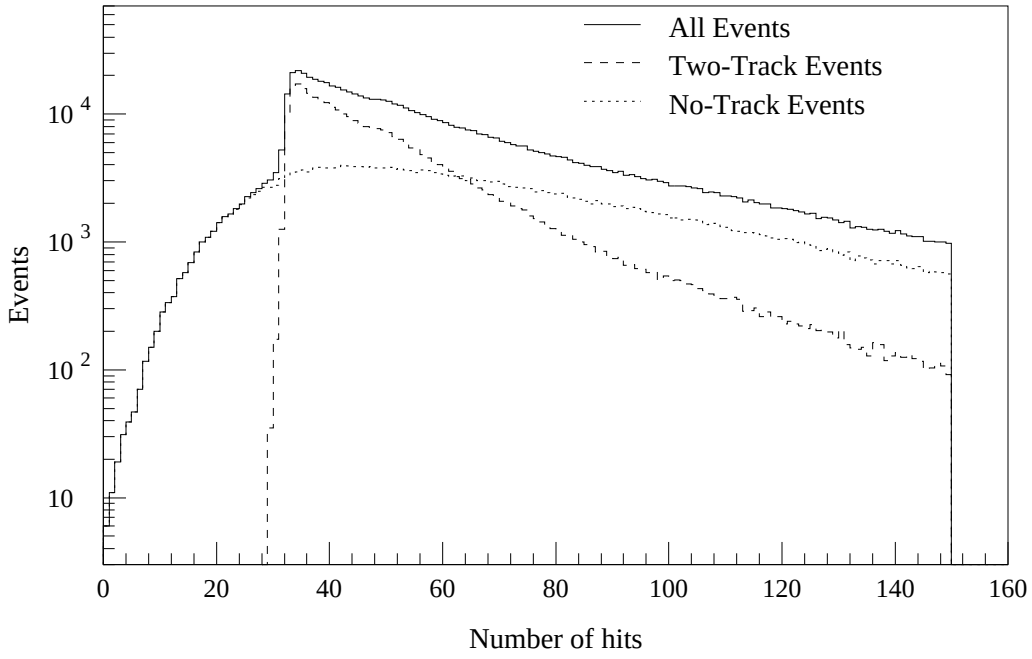

Figure 16. The number of hits from raw events. The solid line includes all charged-mode triggers. The dashed line corresponds to events with 2 in-time tracks, and the dotted line to events with no in-time tracks. The events are from Data Set 2.

provided to slightly modify the algorithm when explicitly searching for single-track events; this is used to track single-muon data taken for various calibrations.

5.1.4 X Track Segments

The x segment finding algorithm operates on a pair of chamber planes; one plane each from chambers 1 and 2 (chambers 3 and 4) for finding segments upstream (downstream) of the analysis magnet. We will refer to these as 'seed planes'. The upstream and downstream segment finding is done separately, but we discuss them in parallel since the algorithms are virtually identical.

All pairs of valid hits, one from each of the seed planes used, are looped over. The two neighboring wires in each of the partner planes are searched for hits to find hit pairs. If a given hit has an associated hit on both sides in the partner plane, then it is paired with

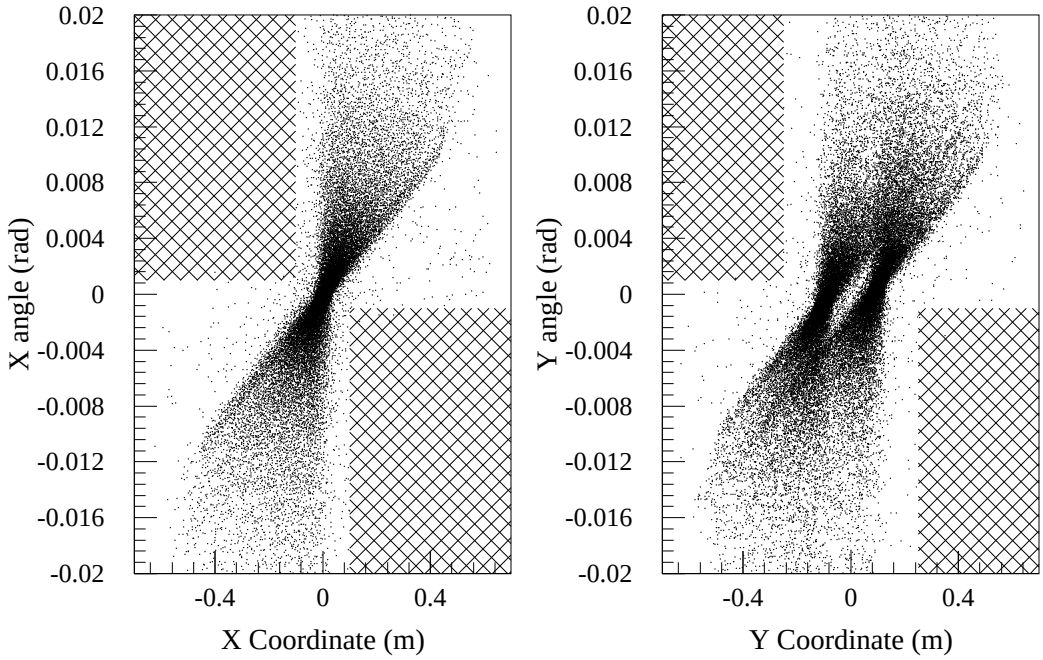

Figure 17. The allowed range of angles and intercepts at the last vacuum window for upstream x track segments and y tracks. The hatched regions are removed by the cuts. The events are from Data Set 2, but without ZUMA in the trigger in order to give a sense of the natural distribution.

the hit giving the best sum-of-distance. A full segment has four hits: a hit pair in each chamber. To be a valid segment, there must be at least three total hits; i.e., at most one of the expected four hits may be missing. If there is a missing hit, then two segment candidates are generated: one for each sign of the ambiguous drift direction for the unpaired hit.

These conditions satisfied, the candidate segment is subjected to aperture cuts. These cuts greatly reduce the number segments.

The upstream segments are found first. Candidate upstream x segments must pass loose aperture cuts at the HDRA, the final vacuum window, and at the MA. We extrapolate the segment to determine its x coordinate at the z of these detector elements and cut on the resulting value. The allowed regions are all symmetric about $x = 0$ and have half widths of 0.30 m (HDRA), 0.66 m (Vacuum Window) and 0.96 m (MA). The actual aperture half-widths at these locations are 0.249 m, 0.609 m, 0.908 m, respectively. The extra 0.05 m

compensated for the fact that only the hit wire position, with no drift distance information, was used when making these cuts.

The transverse projection of the upstream segments and the segment angle are restricted to certain regions in the two-dimensional 'angle-intercept' space that they span. The region, shown in Figure 17, removes some segments clearly inconsistent with coming from decays of kaons in the beams.

Candidate downstream x segments must have an extrapolated position at the lead glass smaller than 1 m in magnitude (the actual size of the array is ± 0.93 m). At this stage, any downstream track must point to within 3 cm of some upstream track at the magnet.

The number of combinations is often very large, especially when there are many extra hits. These can arise from electronic noise in the chambers and particle spray from beam interactions (often from beam in neighboring RF buckets) in the regenerators and other material. The upstream chambers tend to have more extra hits since the analysis magnet sweeps away some of the soft tracks from interactions before the downstream chambers. The combinatorics problem was also exacerbated by the removal of the requirement (in Data Set 2) that upstream candidate segments point through the HDRA aperture surrounding the T and V counters; this is clearly not mandatory for decays after the HDRA.

The TDCs are inhibited from taking late hits after a trigger is received, but nothing prevents the presence of late hits. Late hits correspond to long drift times; in fact a second peak in the SOD distribution is observed at twice the cell size. This is from out-of-time hit pairs where both hits are so early that they are both assigned the maximum drift distance. To remove this peak, a cut is made requiring the quantity (SOD minus cell size) to be less than 4 mm The distribution cut on by the tracking algorithm is shown in Figure 18. Note that this cut is on the *opposite* side of the SOD peak from the δ-ray tail.

Since one missing hit is allowed on a segment, the entire procedure is then repeated with a different pair of seed planes to avoid missing any segments. Three of the four possible seed-plane combinations must be used to insure that all segments are found. Any duplicated segments are removed from the accumulating list. Note that there is as yet no restriction on the different segments sharing hits.

Now that the hits on each segment are found, a line is least-squares fit to the space

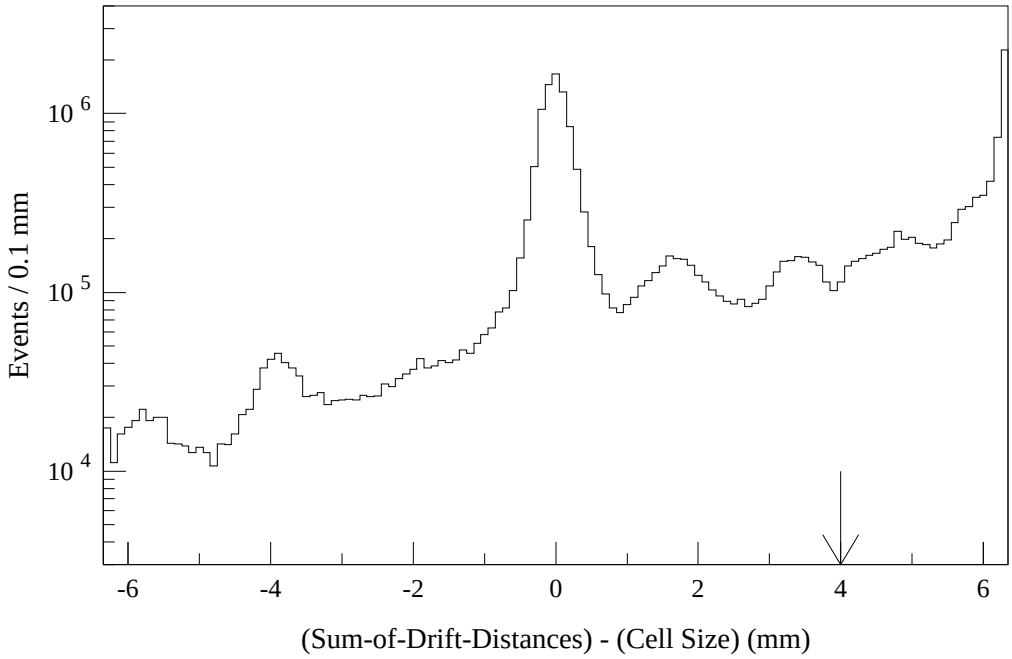

Figure 18. The SOD distribution during track-finding and the cut made. The large peak at the far right is due to hit pairs from early tracks. The events are from Data Set 2.

points. The fits yield the slope and intercept describing the segments. These fits are redone later when refinements to the space-points are made; see the discussion of corrections to the tracks in Section 5.4.

5.1.5 X Tracks

We must now match the upstream and downstream segments into full tracks. All pairs of upstream and downstream segments are considered; for each pair, the difference in their projected position at the center-plane of the analysis magnet, '*offmag*', is calculated. Any pairing with an *offmag* less than 1 cm is retained. We thus produce a list of track candidates.

Now, the list of candidates is searched to see if any pairing shares hits with any other pairing. If not, we are done, and have produced a list of disjoint x tracks. If there are track candidates with shared hits, we discard tracks until there are no shared hits. We

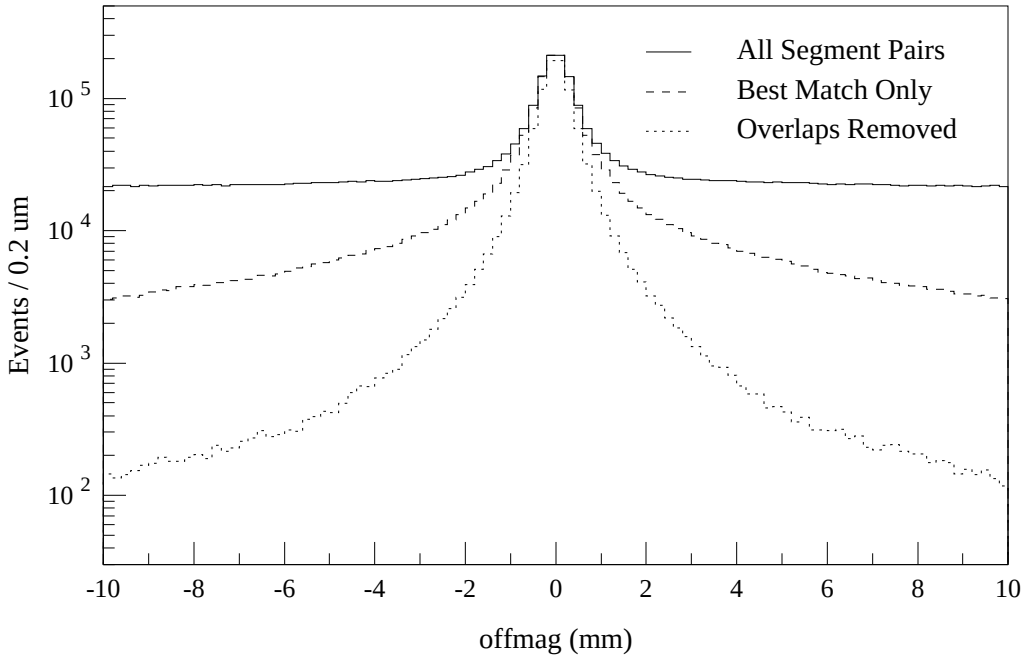

Figure 19. The miss-distance of track segments at the magnet during the track-finding. The solid line shows the values for all combinations of upstream and downstream segments. The dashed line shows the values of the best match to each upstream segment. The dotted line shown the values for the final tracks, after overlaps have been removed. The events are from Data Set 2.

remove first the track candidate which overlaps with the most other candidates. If this choice of which track candidate to remove is not unique, we choose among the subset of possibilities the track candidate with the largest value of *offmag*. We now examine the remaining candidates for shared hits to determine once again if we are done. This process is iterated until all tracks consist of disjoint sets of hits.

A short example will illustrate why the value of offmag alone is not used as the criteria for choosing the track candidate to remove at each step. Suppose there are three candidates, A, B, and C, with A having the best *offmag* and C having the worst. Suppose also that C shares hits with B and B shares hits with A. Our algorithm removes track B first, and terminates finding two non-overlapping tracks. If we removed the track with shared hits having the worst *offmag*, we would remove track C first, and be left with A and B still sharing hits. Track B would then be discarded on the next iteration, leaving only A.

Neither algorithm always maximizes the number of tracks found, but this is not the goal, in any case: we wish to find all of the in-time tracks, without losing any due to additional out-of-time tracks. Our chosen method is a good compromise between the number of tracks and the quality of the tracks, expressed in the values of *offmag*. Figure 19 shows the values of *offmag* at various stages of tracking.

Recall that for segments with single hits, both directions of drift are used to form candidates. This ambiguity is resolved during matching by keeping the one with the better *offmag* in the final, full track.

If more than two tracks (or one track, if the one-track flag is on) were found, an explicit attempt was made to cut out-of-time tracks. Any tracks with more than one SOD greater than 1 mm different from the cell size is cut.

We mention that the *offmag* comparisons were done without considering the momentum-dependent resolution on this quantity. Including the resolution would be a straightforward improvement.

5.1.6 Y Tracks

Tracks in the y view are found in all four chambers, since the tracks are nearly straight. As with x segments, the process is run with two seed planes; all pairs of hits in these two planes are looped over. All planes are then searched for hits within 1.5 cm of an extrapolated line passing through the original two hits. In addition, if the a wire on the edge of this search road is hit, the next wire just outside of the road is also checked, so that hit pairs are not separated. When seeding the track with hits from Chambers 1 and 4, for example, the 1.5 cm road allows for some bending of the track when searching for hits in Chambers 2 and 3. The measured rms width of the bend in y is about 0.12 mrad; this is due to scattering and chamber resolution as well as small magnetic fields from the analysis magnet.

The best hit or hit pair is chosen from each plane pair. The criteria used are SODs and distance from the seeded track. In the following list, we give the criteria used for various cases, denoted (m, n), with m hits in one plane and n hits in the other plane near the road being searched.

- (1,1): Take both hits, unless they are not from the same drift cell; otherwise, take the hit nearest to the seeded track.
- (0,0) or (1,0) or (0,1): Take the hit, if one exists.
- (> 1,0) or (0,> 1): Take the hit closest to the seeded track.
- (1,n) or (n,1): If pairs exists, take the best one based on the SOD; if there is a tie, take the hits closest to the seeded track. If no pairs exist, take the single hit closest to the seeded track.
- (2,2): If there are two pairs, take the better pair, based on SODs.
- (> 1,> 1): [Includes (2,2) when not contained above.] Take the best pair if SOD is small; otherwise, take the single hit closest to seeded track.

A y track must have at least 5 hits and pass loose aperture cuts at the HDRA, the final vacuum window, and at the lead glass. The cuts are all symmetric about $y = 0$ and have half widths of 0.36 m (HDRA), 0.66 m (Vacuum Window) and 1.0 m (Lead Glass). The actual aperture at these locations are about 0.309 m, 0.609 m and 0.93 m, respectively. As with the upstream x segments, the cut at the HDRA is only made for Data Set 1.

The angle-intercept cut, checking that tracks are consistent with originating in the beam, is somewhat looser that in the x view because of the beam separation in y. This cut is also illustrated in Figure 17. A SOD cut identical to that described for the x view is made.

Once again, to find all tracks in spite of possible missing hits, three combinations of planes in Chambers 1 and 4 are used as the seed planes for the algorithm. Furthermore, if the number of y tracks is then one less than the number of x tracks already found, seed planes from chambers 2 and 3 are used in an attempt to find another track. This makes greater allowance for missing hits; we are not measuring the momentum with y tracks, and can be less selective than in x. It should also be remembered that when tracks are close in the y view, and thus hardest to find, they are well-separated in x where the momentum is measured.

No hits may be shared between different tracks. If two track candidates have common hits, attempts are made to resolve them. This involves separating the hits uniquely between

the tracks; no hits are used on more than one track. In the case that three wires comprising two adjacent drift cells all fire, two tracks may use these hits. The middle hit is paired off according to the better SOD: thus, one track will be assigned two of the hits, and the other track will get the remaining hit.

If more than the desired number of tracks (always two, except for muon runs) are found, out-of-time tracks are cut with SOD information exactly as done for x tracks.

The entire y track is fit to a line, yielding the slope and intercept describing the track. The upstream and downstream y segments are fit separately later, after the corrections described in Section 5.4 are made to the tracks.

5.2 Cluster Reconstruction in the Calorimeter

The raw data from the calorimeter consists of the number of ADC counts for each lead-glass block. A gain is applied to each, converting the counts to energy. We first find localized clusters of energy and then correct the cluster energy for several effects. The total correction can be as large as 10%; much of this is due to non-linearity in response as a function of energy.

The cluster-finding algorithm for the calorimeter was identical to that of E731 [140]. The object was to find isolated clusters of energy deposit in the calorimeter. A cluster consists of a 3 by 3 group of blocks where the central block was required to have at least 200 MeV of energy and contain more energy than any of its eight neighbors. The energy sum from all nine blocks in the cluster had to be at least 500 MeV. The values are a compromise: low energy requirements give high efficiency for finding low-energy clusters, while higher requirements prevent the identification of multiple clusters inside one physical cluster. Hadronic showers are particularly prone to having large fluctuations in the pattern of energy deposition and can appear as multiple clusters. We also note that distribution of accidental clusters is peaked at low energy. A particle leaving only minimum-ionizing energy deposition, such as a muon or a non-interacting charged pion, reconstructs as an approximately 700 MeV cluster. The thresholds are low enough that most of these clusters

are found; this is desirable so that they may be used to match tracks from the two views of the spectrometer.

We mention in passing that a distinct clustering algorithm is used for neutral mode due to the HCF trigger requirement on the number of clusters. Only blocks which set bits in the HCF are used to find clusters. Further details may be found in Ref. [141]

After clusters are found, any overlapping clusters are split. An algorithm splits the ADC counts in shared blocks between the clusters according to a parameterization describing the average energy-deposition pattern as a function of energy and cluster location in the block.

We now briefly describe the reconstruction of cluster energies. More details may be found in Ref. [141]. In gross terms, a gain constant for each of the nine blocks in a cluster converts the ADC counts recorded to energy, and we sum the nine energies. In practice there are many corrections, which we now describe. The calibration procedure used to extract the gain constants is described in Section 5.11.

Many of the corrections have there roots in two effects and their interplay: light absorption in the blocks and the longitudinal shapes, and particularly the fluctuations, of the showers.

The blocks are not perfectly transparent, and the light absorption varies with block and time due to radiation damage. Most blocks had absorptions from 2-7% per radiation length. The largest absorptions were for the blocks near the beam holes, which were most heavily irradiated. This absorption couples into the fluctuations in the longitudinal shower development, and is a large component of the final energy resolution.

Effects relating to shower shapes were investigated with a Monte-Carlo simulation based on the popular EGS code package [145]. Many electromagnetic (EM) showers were generated for various energies and incident positions of electrons on the block face. Blocks were subdivided into small cells, and the amount of Cerenkov light produced by the shower in each cell was calculated. This was a versatile way of handling the data: the light could then be corrected for any given absorption between production and the phototube. Photon showers were modeled with the same data: a photon first converts into two electrons and is thus equivalent to two lower-energy showers in a shorter (due to the conversion depth) block. The conversion depth and energy split between the electrons were given by the stan-

dard Bethe-Heitler expression. The simulation yielded a table giving the average amount of light as a function of energy, absorption, and conversion depth (0 for electrons).

We are now prepared to discuss the corrections, which are grouped into three classes:

- Corrections involving the EM shower process and light production.
- Corrections due to system response to the light produced.
- Corrections to the nine-block sum of observed light.

First, we discuss subtleties connected with the EM shower development. The absorption makes us sensitive to any effects which change the average longitudinal shower profile.

Electrons can radiate in the material after the magnet, such that the bremsstrahlung photon lands in the cluster. This shifts the reconstructed energy due to non-linearities and the differing responses to photons and electrons. There is about 7% of a radiation length of material, resulting in a 0.28% average correction.

Photons may convert in material before the calorimeter. This is an important effect, since the EM shower is started before the photon encounters the glass block. Photon clusters were corrected if there was a hit in the B bank counter corresponding to the photon trajectory and if the trigger TDC for one-or-more B counter firing was in time. This latter requirement avoids hits from splash-back off the calorimeter from an earlier beam bucket. The correction is 3.5% at $\alpha = 4\%$, and changes by 0.62% per 1% change in α.

We calculated the average photon-electron response difference as a function of energy and absorption by averaging over the conversion depth and energy split. The decreased absorption, due to the shower starting nearer the phototube, is partially offset by increased leakage of the shower out the rear of the block. The amount of light collected varies between 0.95 and 0.99 for a photon compared to an electron of the same energy.

Next, we discuss the response of the detector to the Cerenkov light produced in the blocks. During the first portion of the run, the temperature in the lead glass enclosure varied somewhat due to insufficient air conditioning. The gains varied by about 0.7%/°C; the temperatures varied by about 3°C. Temperature readings were available in the data, but corrections were ultimately obtained in 20 minute intervals by examining the changes in response to electrons, whose momenta were known from the spectrometer. This treatment

was simpler than directly using the temperature readout, in part due to a time-lag between the recorded temperature changes and the response changes.

The pedestals vary with trigger rate during the spill; the rate affects the amount of time the capacitors holding the signal have to clear. These effects were studied with accidental events, which were read out without pedestal subtraction. Shifts were parameterized as a function of the time since the last Level 2 trigger and a scalar counting the ambient rate in the DR for the previous 100 μs. We note that the LeCroy 1885N ADC modules contained FET switches to multiplex stored charge to the ADC and drain the charge to ground for clearing. Bench tests showed that these switches varied appreciably in their on resistance; one wants the on-resistance of switches low so that settling and clearing times are fast. These switches contributed to the pedestal shifts seen in E731. Many switches were tested before E773 and we selected the ones with the best performance for use in our ADC modules.

Finally, we comment on corrections to the naive nine-block energy sum. Some energy leaks outside the 3×3 array of blocks. The amount is determined by the EGS MC, and is typically 2.6%, with little energy dependence.

Only blocks having more than ADC counts above the pedestal were read out; this effect was most important for low-energy clusters. A special run with no readout threshold was used to determine an energy-dependent correction. The correction was 2.8% for a 1.5 GeV cluster and decreased rapidly with increasing energy. The decrease is due both to the larger cluster energy relative to the threshold as well as a reduced tendency for blocks to be below threshold.

For clusters near the beam holes or the array edge, all nine blocks might not be physically present. An average correction of 0.6% (1.1%) for a missing corner (edge) block was used, independent of the cluster energy or location.

5.3 Matching X and Y Tracks

The clusters found in the calorimeter were used to find the proper matching of the x and y tracks. For two-track events, there are only two possible combinations. If there

are no clusters, matching fails. This can happen due to tracks pointing down the beam holes or outside of the calorimeter, or pions leaving only minimal energy and failing the minimum cluster-energy cut. An $x - y$ track and a cluster match if the projected track is within 7 cm of the cluster center; only the closest cluster to a given track is considered. If no track-cluster matches are found with either $x - y$ pairing, then matching fails. If one pairing matches more tracks than the other, then that match is used. If both match equal, non-zero numbers of tracks, then the match which minimizes the sum of the squares of the track-cluster separations is used. Successful matching is required by all of our charged-mode analyses; this insures reliability of the particle identification cuts based on comparing calorimeter and spectrometer information.

Any cluster with $E > 1.5$ GeV and not matched to a track is counted as an 'extra cluster'. The energy threshold reduces the chance of extra clusters being created by soft bremsstrahlung, accidental photons, or tails of hadronic showers. Although the number of extra clusters is not explicitly cut on in our analysis, we will find it useful later when examining backgrounds.

5.4 Corrections to Reconstructed Tracks

Once an event was completely reconstructed, a number of corrections were made to refine the locations of the tracks. Most of these require the x and y tracks to be matched properly, hence their application at the end of the reconstruction.

The first correction involves a small common adjustment, usually < 1 ns, to the measured TDC hit times. This is largely from event-to-event variations in the relative time of the accelerator RF signal, which determines the offset of our TDC times, and the time of kaon production. More discussion of this effect, in particular how the timing offset is determined, is postponed until calibration is discussed below. Many relevant concepts are explained there, making the presentation easier; see Section 5.7.2.

The hits in the y view are corrected for the gravitational sag of the wires. The wires were strung at a known tension, and a straightforward calculation gives the sag as $\delta y \simeq$

75 μm/m$^2 \times (x^2 - x_{max}^2)$, where x is the track coordinate and x_{max} is the half-width of the chamber.

The next two corrections require matched tracks: corrections to the x coordinate depend on the y position and vice versa. The hit positions are corrected for the rotations of the sense wire planes about the z-axis, as determined from the chamber calibration procedures. A correction is also made for the propagation delay of the signal along the sense wire. The propagation speed is taken as c; this correction is small.

The tracks are now re-fit; again with a least-squares fit for the best line through the corrected space points. This time, each track has all four segments, upstream and downstream, x and y, fit separately. The χ^2 of each fit is retained for later use during the analysis. The fit gives the slope and intercept for each segment; these are used for kinematic calculations and also to project the tracks to various z locations.

5.5 Track Momentum Determination

The track momentum is determined by

$$p = \frac{k(x,y)}{\theta_{bend}} \tag{5.1}$$

where

$$\theta_{bend} = \frac{\theta_x^{dn}}{\sqrt{1+(\theta_x^{dn})^2+(\theta_y^{dn})^2}} - \frac{\theta_x^{up}}{\sqrt{1+(\theta_x^{up})^2+(\theta_y^{up})^2}} \tag{5.2}$$

and $k(x,y)$ is the position-dependent p_T kick of the magnet The variable $\theta_x^{up} = p_x/p_z$ is the direction tangent of the upstream x track segment, with analogous definitions for the other track angles. The nominal value of k is 200 MeV/c; more precise values as a function of the transverse location are available from a field map. Note that the x position used at the magnet bend plane when looking up the field is *not* the track extrapolation: we correct for the fact that the average x during passage is biased due to the track angle. The correction is proportional to $(\theta_x^{dn} - \theta_x^{up})$ and depends on the longitudinal profile of the field, being smaller for a more localized field . This correction is quite small in practice; 6 mm for a 7 GeV/c track. This is the only correction made: the magnet is modeled as giving a single, localized kick.

5.6 Vertexing and Kinematic Calculations

The basic vertex finding was performed by calculating the distance of closest approach of the extrapolated upstream track segments. The vertex coordinates were taken as the centroid of this closest approach. The vertexing failed only if the tracks were nearly parallel. No attempt was made to fold in measurement errors. The only quality variable was the distance of closest approach.

A more complicated vertex fitter was then used to refine the vertex position. This included the errors on angles and intercepts due to multiple scattering in vacuum windows, air and the spectrometer, as well as errors due to chamber resolution. The material tracks have passed through was determined using the preliminary vertex from the distance of closest approach.

Events were next classified according to which regenerator they are associated with. For the $K \to \pi^+\pi^-$ analysis, the reconstructed kaon trajectory was extrapolated back to the z plane of the downstream faces of the UR and DR. A region 5.0 cm in x by 5.5 cm in y was defined, centered on the nominal beam locations at the regenerator faces. A UR (DR) event must pass through *only* the UR (DR) region. Some events fell within neither of the boxes. These were mostly due to events with kaons originating in the UR beam where the kaon scattered in the material near the DR before decaying, and also $K \to \pi^\pm e^\mp \nu_e$ decays where the kaon direction was incorrectly determined due to the missing neutrino. Other events fell into both boxes. These were due to kaons that scatter in the regenerators, primarily the UR, such that the kaon trajectory appeared to go through both regions defined above. For the $K \to \pi^\pm e^\mp \nu_e$ analysis, the beam was simply assigned according to the sign of the y coordinate of the decay vertex relative to the regenerator positions in the current beam spill.

The $\pi\pi$ invariant mass is calculated, as well as the $p\pi$ mass. In the latter case, the p is taken to be the higher-momentum track, regardless of the sign of the charge (see Appendix I). The calculation uses the known rest-masses of the assumed decay products and the measured particle momenta and directions.

The kaon p_T^2 is calculated assuming straight flight from the target to the regenerator

with a possible scatter in the regenerator. Note that it is important to calculate the p_T^2 relative to the kaon direction, *not* the z axis. An unscattered 70 GeV kaon in the center of one of our beams has a p_T^2 relative to the z axis of 2000 MeV$^2/c^2$, very much larger than our resolution and our analysis cut. The p_T^2 is calculated assuming scattering at the downstream face of the appropriate regenerator. The calculation is insensitive to the location of scattering inside the regenerator and furthermore data and Monte-Carlo events are treated identically.

We have now completed our discussion of event reconstruction, and move on to detector calibration.

5.7 Drift Chambers Time-to-Distance Calibration

We now describe the calibration of the drift chamber system. For each of the steps, we discuss the principles involved as well as the selection of appropriate data for the task. There are two major tasks: the determination of the time-to-distance relations and the chamber locations.

5.7.1 Timing Offsets: Delays

We use one time-to-distance relation per sense-wire plane. We first remove any timing offsets between wires, so that the data from an entire plane may be properly combined for calibration. These relative offsets are due to the variations in the lengths of the cables connecting the amplifier and discriminator card and the TDCs. There are also effects due to time of flight of the particles between chambers, and the timing of the stop signal for each crate (one per chamber) of TDCs; these do not affect an the relative times of any wires sharing a time-to-distance relation and were roughly canceled by adjusting the length of the cable delivering the common stop.

E731 used 100 ft twisted-pair cable, with 16 differential channels and 2 grounds each, to connect the amp cards and the TDC modules; E773 replaced these with 200 ft twisted-pair cables. The additional delay was useful in order to have time to fully inhibit the TDCs from

re-firing due to late hits. It was also needed to be able to gate the hits for use by the drift chamber Level 2 triggers in E773 and E799 [143]. For E731, good results were achieved by using a single timing offset for all 16 channels sharing one ribbon cable. For E773, it was found that the new, longer cables necessitated individual offsets for each channel in order to maintain good resolution. The timing offsets are easily obtained by plotting the raw TDC times and locating the sharp edge due to prompt hits from tracks passing right by a wire (see Figure 15). An overall timing offset for each cable was first determined. An automated program then compared the timing for each wire with the plane average and calculated an individual constant shift to make them match. The matching criteria was a simple χ^2 comparison of the shape of a 50 ns region including the sharp timing edge. This was iterated, and quickly converged. Each constant was determined to the nearest nanosecond. A plot of the variation of the individual wire times with respect to the appropriate cable average is shown in Figure 20. The rms width of the time delays in a given cable was 2.7 ns; this is sufficient to dominate the resolution if left uncorrected. The difference in times between neighboring channels in a cable were quite random, showing only a small correlation.

5.7.2 Timing Offsets: Event Time

.

An additional timing concern is the time of passage of the tracks relative to the stop signal that is sent to the TDCs. In E773, this stop was generated by the first-level trigger, which was synchronous with an accelerator RF signal. The largest source of time jitter here is from the longitudinal position of the kaon-producing proton in its RF bucket. We denote the Gaussian width of this jitter by σ_t.

One way to determine the jitter is to use TDC information from a scintillator bank. The times of the one-hit and two-hit triggers from the B and C banks were digitized to 0.1 ns accuracy. To use these times, one must be sure that the TDC was fired by the reconstructed particles, and correct for the time the light takes to reach the phototube as a function of position. A more straightforward method using the hits themselves was adopted instead.

The chamber single-hit resolution, σ, is about 90 μm on average. Each pair of chamber

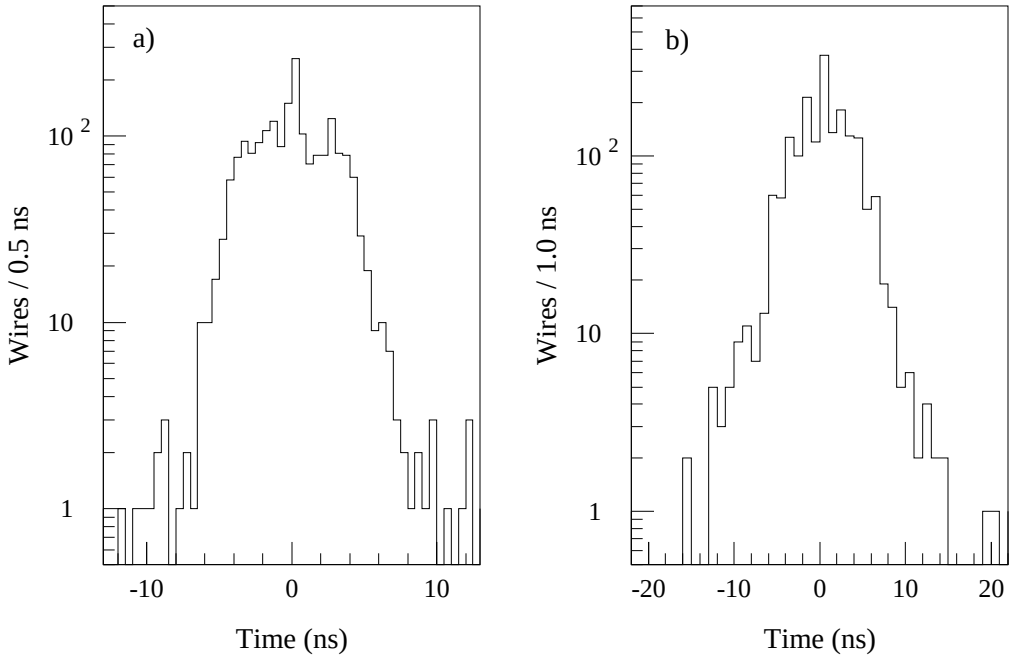

Figure 20. The distribution of drift chamber wire timing offsets. In Plot a), we give the timing offset of each wire relative to the mean of all wires in its cable. The spike at 0 is due to about 5% of the wires having insufficient statistics in the sample used to perform an offset measurement. The rms width is 2.7 ns. In Plot b), we show the difference in times of pairs of neighboring wires in the same cable. The rms width is 3.4 ns, indicating little correlation between neighbors.

hits measures the cell size, via the sum of drift-distances (SOD), with a resolution of $\sqrt{2}\sigma \sim$ 125 μm. Given the drift speed of $v_D \simeq 50$ μm/ns, the SOD of the hit pair provides a measure of the relative stop time to about 1.3 ns. If we average many SODs, the resulting 'mean SOD' distribution decreases in width, but any shift in the mean due to a common timing offset is coherent and undiluted. There are sixteen independent pairs in a perfect two-track event, so that the total time resolution is four times better than that from a single SOD. If the rms jitter, σ_t, in the production vs. stop time is of this order or larger, then we can easily measure it with the SODs. We actually determine, using the time-to-distance relations, the time offset required to give a perfect SOD for each pair, and then average these times to determine an apparent time shift in the stop signal. This properly accounts for variations of drift speed with time, plane, and position (in a drift cell). To

avoid a systematic bias due to δ-rays, we only include SODs within 0.5 mm of the cell size and require that there be at least 10 such SODs to contribute to the average. The distribution of mean-SOD times for many events will have a width of $(\sqrt{2}\sigma)/(8v_D) \sim 0.3$ ns, due to intrinsic chamber resolution, convolved with a width[1] of $\sigma_0 = 2v_D\sigma_t$, due to the rms jitter of σ_t in the stop time t_0. A plot of the mean-SOD times for typical two-track events is shown on Figure 21. The distribution is Gaussian, with an rms width of 0.67 ns. Correcting for the chamber resolution, we find that $\sigma_t \sim 0.60$ ns. This is consistent with expectations based on the longitudinal structure of the primary proton beam bunches. The mean-SOD time is used to adjust the drift times of all of the hits in a given event. This time shift and the propagation delay shift are applied simultaneously; the time-to-distance relation is interpolated to give values for the resulting non-integral values of drift times. Apart from small systematic effects, our correction thus removes a Gaussian smearing of 0.60 ns, measured with a resolution of 0.30 ns. We mention that the flight-time difference between production and decay for 20 and 160 GeV kaons is about 0.15 ns.

To determine the chamber resolution, we study the SOD distributions for each plane pair. There is a subtlety, however, introduced by the t_0 correction algorithm described above. The SOD distribution being studied will have contributed one of the sixteen SOD measurements used to determine the t_0 shift for a given event. This self-correlation tends to artificially narrow the SOD distribution. One could determine the t_0 for each plane-pair individually, by using all *other* SODs, but this is unattractive since it results in sixteen different t_0 shifts being used for one physical effect. We therefore choose to live with the correlation, and calculate the effect of this on the observed SOD. For a given event, let each SOD have an independent Gaussian rms width of $\sqrt{2}\sigma$ and a common time shift drawn from a distribution with width σ_t. This common time shift is uncorrelated for each different event. We then apply the algorithm described above, and find that the calculated SOD for a given plane will have width $\sqrt{15/16}\ \sqrt{2}\sigma$. The additional factor of $\sqrt{15/16}$ gives about a 3 μm underestimate of σ if ignored. Had we used all SODs *except* the one under consideration, we would have found a width of $\sqrt{16/15}\ \sqrt{2}\sigma$. The resulting resolutions are in the range from $85 - 105$ μm, depending on the particular plane (see Table 7). The variations are not

[1] We write σ_t as the width of the actual *time* shifts. Then σ_0 is then the width of the SOD (a *distance*) induced, where we have used a mean drift speed of v_D for simplicity.

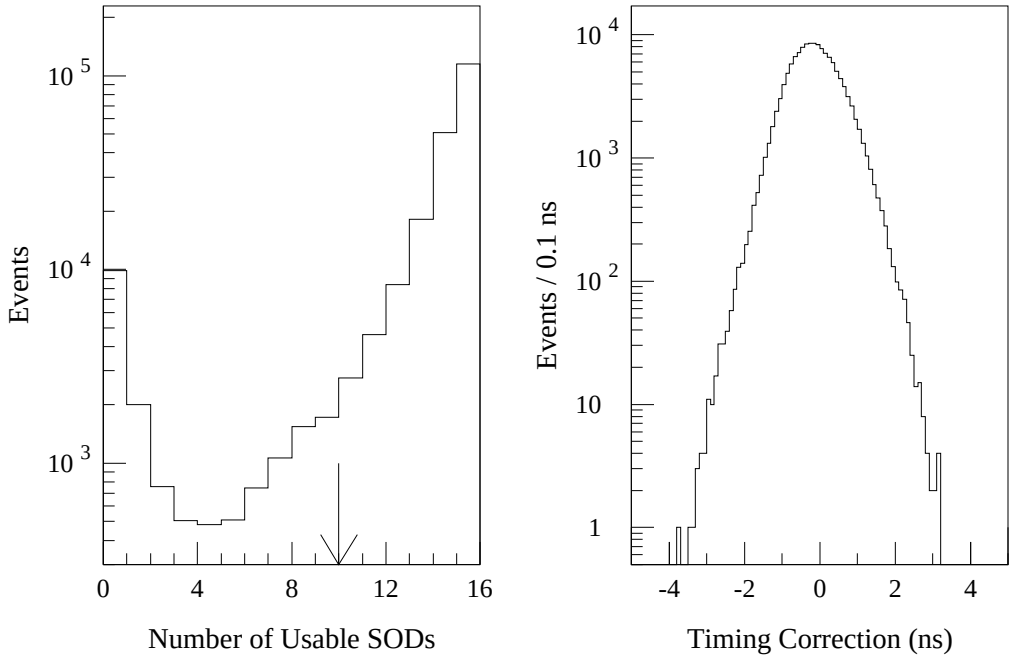

Figure 21. The number of SODs used in extracting the chamber timing shift and the calculated shift, from 2-track events with no other cuts. Note the peak at low number of SODs used; this is from out-of-time tracks where all SODs are bad. At least 10 good SODs were required to calculate a shift.

well-understood; the identity of the planes with superior resolution is stable with time. If one examines the mean of the SOD for each cell in each plane pair, one sees that part of the increase in SOD width for the bad plane pairs is due to an increased scatter in the SODs for each cell.

5.7.3 Time-to-Distance Relation

With the timing offsets in hand, the relation between observed drift time and actual distance between the track and the hit wire can be determined. The original description of our calibration technique is given in Ref. [146].

Our procedure relies on the fact that on average, for an entire plane pair, the illumination across each drift cell is uniform. Note that even if the illumination varies linearly with position in the chamber, it will be higher on one side of a given wire, and lower on the other

side in a symmetric fashion, hence canceling locally. There is also symmetry in illumination with respect to the chamber centers. Given this uniform illumination, one can convert the distribution of observed times into a lookup table from time to distance. There are two subtleties in this procedure. First, one must isolate a clean but unbiased sample of tracks. Second, the effect of missing hits due to inefficiencies must be accounted for.

We calibrated with raw data from standard runs; events with two tracks in each view were used to extract the time-to-distance relation. The most crucial requirement is that the tracks used be in time with the event, since the measured TDC times are relative to the event trigger and hence a specific RF bucket. One would like to avoid using any information from the drift chambers themselves. The B and C hodoscopes provided useful information. Each bank had latch and TDC information for the trigger sources set to detect the passage of one or more particles and two or more particles. Each of the four latches was required to have been set in the event, and each of the four TDC times was required to correspond to the in-time bucket. Note that the single particle TDC was useful for detecting the presence of an additional out of time track, which may have come early, even when the two-particle trigger source was in time. The track reconstruction algorithm itself had only very loose timing requirements on the tracks; these were not troublesome.

Times for all hits on tracks were accumulated in a separate array for each of the 16 chamber planes. The times are corrected for the propagation delay along the wire. Missing hits pose a problem because inefficiencies are often correlated with the track position in the drift cell, leading to a bias. To correct for this, an additional array of the times of single hits was made for each plane as the events were processed. When a pair was found with one of the hits having the same time as one of these singles, the other hit of the pair was entered into the appropriate array to replace the missing partner of that single hit. Thus, the data itself was used to find, on average, the times of the missing hits.

Once the table was complete, the time-to-distance relation is given by

$$d(t) = d_{cell} \times \frac{\sum_{t_0}^{t} N(t)}{\sum_{t_0}^{t_m} N(t)} \tag{5.3}$$

where d_{cell} is the maximum drift distance (cell size) of 6.35 mm, and we are summing over the number of events $N(t)$ in each 1 ns bin. We have assumed that the distribution of times is ordered so that larger times are larger distances. In the coordinates of Figure

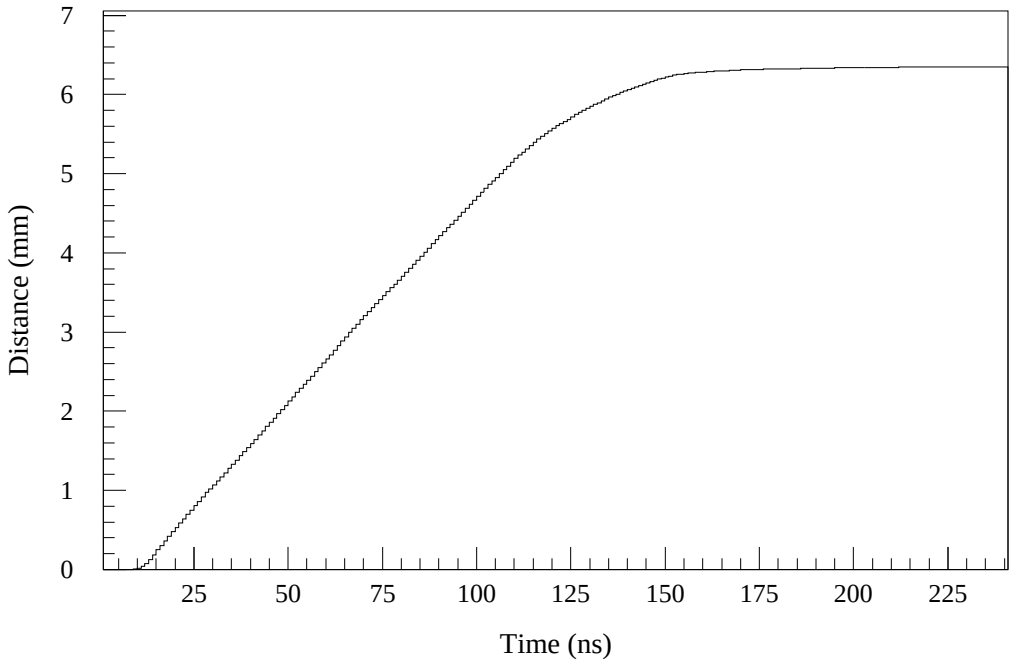

Figure 22. A sample time-to-distance relation for the drift chambers. We use one such relation per plane, and update them about once per day. The relation is quite linear between 10 and 110 ns, with a slope of about 50 μm/ns.

15, $t_0 = 0$ ns and $t_m = 240$ ns. A typical time-distance relation is shown in Figure 22. The typical maximal variation between relations for different planes, or the same plane in different calibrations, is on the order of 100 μm at a fixed TDC time.

5.7.4 Chamber Resolution

We now give a short discussion of contributions to chamber resolution. The TDCs have 1 ns resolution, as do the individual time-delay constants for each wire. These two effects combine to give a contribution of $\sqrt{2}v_D/\sqrt{12} \simeq 20\mu$m to the plane resolution.

The placement of the wires in the chamber frames also contributes to the resolution. Holes were drilled with better than 25 μm precision; there is an additional contribution of about 20 μm from the plastic inserts ('pac men' [139]) used to precisely locate the wires in these holes.

Table 7. Typical resolutions for each plane pair of the drift chambers.

Plane	Resolution μm	Plane	Resolution μm
Ch. 1 X	101	Ch. 1 Y	108
Ch. 2 X	90	Ch. 2 Y	94
Ch. 3 X	84	Ch. 3 Y	85
Ch. 4 X	95	Ch. 4 Y	98

The diffusion of the electrons towards the wire also gives a contribution varying with the square-root of the distance to the wire. The contribution is approximately $\sqrt{d/d_{cell}} \times 50\mu$m [147]. The mean distance between ionizations in the gas, about 300 μm, also contributes a smearing effect to the drift distance. This contribution decreases with distance from the wire, and somewhat cancels the spatial dependence of the diffusion term.

Another error is introduced by statistical and systematic errors in the time-to-distance relation. A sample of 100,000 events (typical for our calibration) corresponds to a statistical error of about 10 μm at the center a drift cell, where it is maximum. We have tried to avoid any sizeable systematic effects. The time-to-distance relations slowly become outdated due to changes in temperature, pressure, and gas mixture. The pressure variation is given by $\delta v_D \simeq 0.06\,(\delta P/P)\,\mu$m/ns, while the pressure variation is $\delta v_D \simeq -0.03\,\delta T\,(^\circ\mathrm{C})\,\mu$m/ns [147].

Typical chamber resolutions are given in Table 7. The combination of all of the above effects is sufficient to explain the bulk of the observed chamber resolution in the best planes.

5.8 Alignment of the Drift Chambers

We begin with a short list of the various steps in the alignment procedure. The chambers are first aligned relative to each other. In particular, we determine relative transverse offsets and relative rotations for each plane; x and y planes are not assumed to be orthogonal. This first step involves assuming positions for Chambers 1 and 4. We then determine the

relative rotation between these two chambers. Finally, we determine the absolute transverse positions referenced to the target and calorimeter. The chambers are carefully surveyed in place to be perpendicular to z; we are not sensitive to the residual errors in this placement, except for one small effect mentioned below.

5.8.1 Relative Alignment of the Drift Chambers

We first determine the positions of the chambers. Special muon data runs with the analysis magnet off are taken periodically to allow this calibration. There was about one usable run per day available. Various cuts selected a clean track sample. We required exactly one track in each view. The track had to match a cluster within 4 cm, and that cluster had to have at least 65% of its energy inside the short lead-glass adder gate. As with the time-to-distance calibration, the B and C banks are very useful. We demand exactly one hit in each bank, and the reconstructed track must point to the hit counters. The one-hit triggers must fire and be in-time for each bank. The two-hit trigger must not fire. Analogous requirements are made on the Mu2 counter bank, except that there is no two-hit trigger source. Fiducial cuts are made to keep the tracks away from the bank edges to further assure that the reconstructed track was indeed the one firing the counter.

We now must select which hits will be used to locate a given plane. In order for a track to be used for a plane, it must have no missing hits in that view, x or y as appropriate. The sum-of-distances of all hits pairs in the event are calculated; no more than two may be off by more then 700μm. This is about a 5.5 sigma cut on each SOD; hit pairs from one beam bucket away have SODs of about 2 mm.

The hits in chambers 1 and 4 are used to predict the locations of the hits in chambers 2 and 3: a line is fit to the hits in the outer chambers and extrapolated to the planes in the inner chambers. Then, these residuals between the predicted and observed values are examined as a function of the track position in the chamber. We fit a line to the x residual as a function of y for the four x planes in chambers 2 and 3. The slope of this line gives the rotation angle of each x sense plane, and the offset at $y = 0$ gives the offset for the planes.

We also do the analogues fits for the y residuals as a function of x. Typically, we wrote out about 115,000 triggers and had 25,000-30,000 usable tracks for each offset after all cuts.

Because of the tails in the scatter plot of residuals versus track coordinate, we do not fit this two-dimensional plot directly. Rather, we slice the data into many bins of position across the face of the chamber and fit a Gaussian to the residuals in each bin. The Gaussian is quite insensitive to the small tails from background. We then fit a line to the Gaussian centroids as a function of position. The procedure is illustrated in Figure 23.

In addition, one may study the x residuals as a function of x, and similarly for y. In this case, the slope of the fit line is a measure of chamber size (expansion) relative to the nominal size. A typical 'expansion' is less than 100 μm across an entire chamber of about 200 cells; this is small and the nominal sizes are used without modification. The intercept of the fit line is another measure of the offset of the given plane. These offsets agree well with the other measurement described above.

The transverse offsets of the planes in a given plane pair were not the same in general (after accounting for the intentional wire stagger). This may be due partly to the construction, but there is also an induced separation if the chambers are not exactly perpendicular to z. Surveys placed the chambers with all four corners within 0.5 mm of the same z. The sense planes in a plane pair are separated by 11 mm; this lever arm can lead to a few μm apparent shift between the planes in a pair with the allowed skew relative to z. The offset of each member of a plane pair is measured separately, and the splitting of each plane pair is stable over time. An average splitting is determined for the entire run; the splittings were typically 10 μm. The offsets for a given plane pair in each calibration were adjusted to have the appropriate mean split, holding the measured average fixed.

In the procedure described above, the splittings are only determined for chambers 2 and 3. To determine the splitting for chambers 1 and 4, we have re-done the calibrations assuming positions for chambers 2 and 3, and extrapolating the tracks to chambers 1 and 4. This allows us to measure the offset splittings for the rest of the plane pairs. The rotations for each plane in a pair were consistent with being equal, and were averaged for each calibration; i.e., any measured difference was ignored.

The rotations of the x and y sense wire planes in a given chamber are not the same

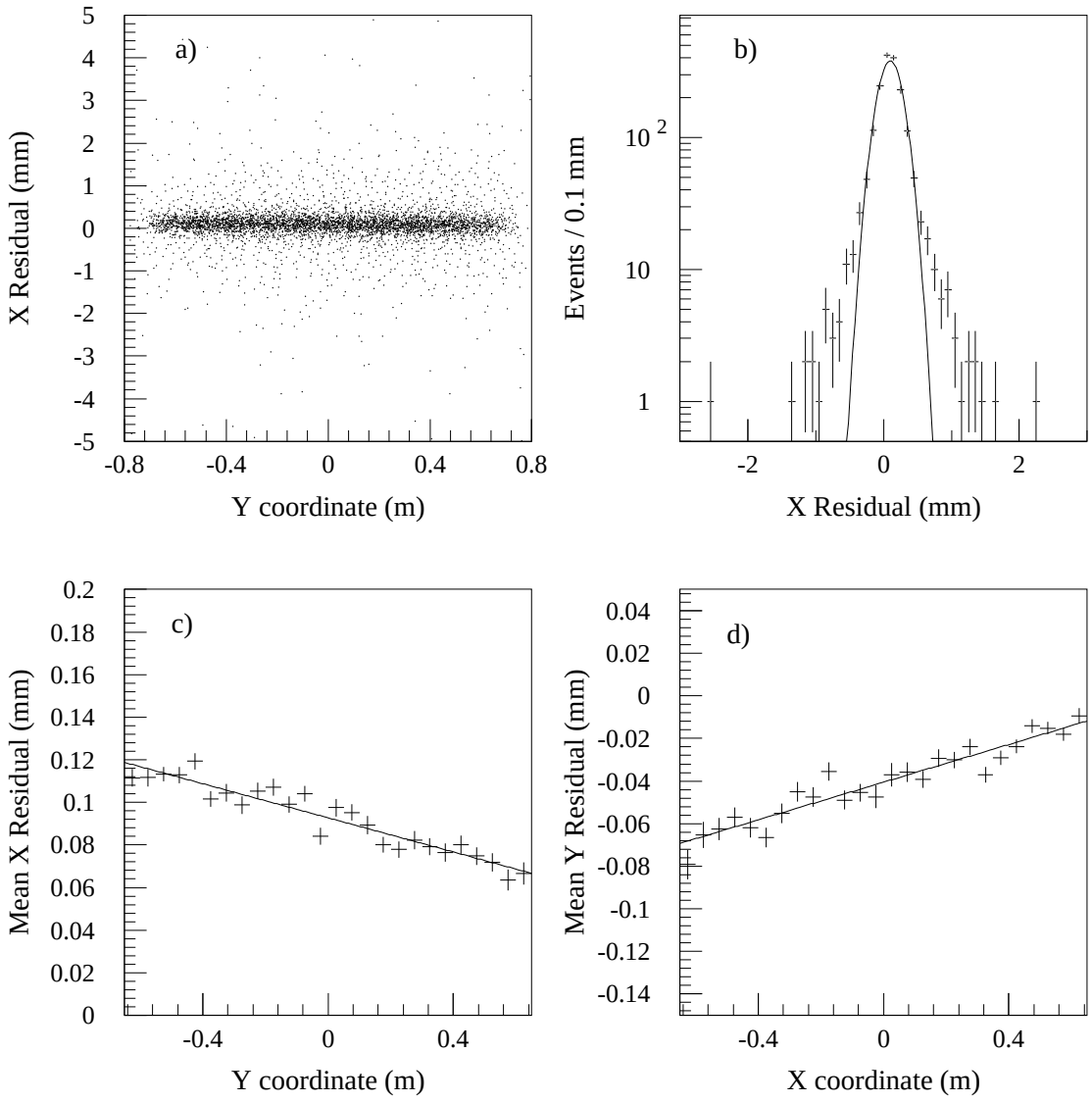

Figure 23. Illustration of the use of muons to locate the chambers. Plot a) show the residuals (observed−predicted position of tracks) in the x view vs. the y coordinate. Plot b) shows a projection onto the vertical axis for a narrow band of the abscissa. We have fit a Gaussian to find the mean residual in this band. Plot c) shows all such mean residuals plotted versus y. We have fit the points to a line; the intercept gives the offset of the x plane, and the slope gives its rotation. Plot d) shows the analogous mean y residuals plotted versus x.

due to small non-orthogonalities arising from construction. The non-orthogonality of the x and y planes had been determined from bench measurements before E731. These measurements were somewhat dated, and the chambers had been handled in the interim, so small changes were possible. In practice, one can easily measure only two combinations of the four independent (one for each chamber) non-orthogonality angles with straight tracks. A common non-orthogonality angle, or an angle proportional to the separation in z, are not easily detected. We used the E731 non-orthogonalities for chambers 1 and 4, and we measured them for chambers 2 and 3. The measured values are similar (within 20 μrad) to the values from E731, which helps justify our assumptions for chambers 1 and 4. However, we can not in principle rule out a large common change of all four angles; this is however very unlikely.

Several cross-checks are available to gain confidence in the procedure. The fitting procedure could be iterated to check that no further adjustments were necessary after the initial determination; the process did indeed converge with one fit. A large data sample was split into two samples to check for consistency between the results obtained with each; the variations observed were slightly larger than expected from the statistical errors, but still quite acceptable. Offsets were reproducible to about 2 μm, and rotations to about 5 μrad. Also, fitting chambers 1 and 4 relative to 2 and 3 gives consistent results with fitting chambers 2 and 3 relative to 1 and 4.

5.8.2 Corkscrew Rotations

There is one remaining item concerning internal alignment. If the rotations about the z axis assumed for chambers 1 and 4 in the preceeding step are incorrect, then the positions of chambers 2 and 3 may be found in a 'corkscrewed frame'. Imagine that we assumed chambers 1 and 4 were set with their sense planes exactly parallel to our coordinate axes, not realizing that chamber 4 was rotated by α μrad around z. For simplicity, assume that the chambers are evenly spaced along z, and that chambers 2 and 3 are set exactly orthogonal to the axes. Our single-track calibration procedure described above will then mistakenly find chambers 2 and 3 rotated by $-\alpha/3$ μm and $-2\alpha/3$ μm about z due to

the incorrect assumption about chamber 4. Thus, a spurious corkscrew rotation about the z-axis, proportional to the distance along z is introduced. There is no easy way to detect this small effect with single tracks. We thus turn to our two-track sample to measure the corkscrew rotations.

We need only measure the relative rotation between the first two chambers to ascertain the rotation per unit distance. This allows us to use our regular data with the magnet on. We take advantage of the fact that two-track decays are planar. We then construct two vectors, $\vec{r}_1$ and $\vec{r}_2$. The vector $\vec{r}_1$ ($\vec{r}_2$) connects the points of intersection of the two tracks with chamber 1 (chamber 2). If the tracks are planar, and the coordinate system is not corkscrewed, then $\vec{r}_1 \times \vec{r}_2 = 0$. But if there is a residual corkscrew rotation, then[2]

$$\vec{r}_1 \times \vec{r}_2 = |\vec{r}_1||\vec{r}_2| \; sin\phi \tag{5.4}$$

where ϕ is the corkscrew rotation between chambers 1 and 2. To do the calibration, we plot $\vec{r}_1 \times \vec{r}_2$ versus $|\vec{r}_1||\vec{r}_2|$. In principle, we could simply plot $(\vec{r}_1 \times \vec{r}_2)/(|\vec{r}_1||\vec{r}_2|)$. However, this is dominated by events with small $|\vec{r}_1||\vec{r}_2|$, and since the width of the $(\vec{r}_1 \times \vec{r}_2)$ distribution varies with $|\vec{r}_1||\vec{r}_2|$, it is safer to treat the data as follows. We fit the mean of the $\vec{r}_1 \times \vec{r}_2$ distribution in bins of $|\vec{r}_1||\vec{r}_2|$. The resulting centroids are then fit to a line as a function of $|\vec{r}_1||\vec{r}_2|$; the slope gives ϕ.

We typically used 500,000 $K \to \pi^{\pm} e^{\mp} \nu_e$ decays. This gave a statistical accuracy on the corkscrew angle between chambers 1 and 2 of less than 5 μrad. The technique is illustrated in Figure 24.

The sample of $K \to \pi^{\pm} e^{\mp} \nu_e$ decays isolated in our first-pass data crunch (see Chapter 6) is subjected to further cuts to obtain a clean sample. The trigger bits and TDC timing for the one- and two-counter B and C bank triggers are checked to guarantee in-time events. We require successful track-cluster matching and vertexing. Tracks are required to have a good χ^2 and SODs, and must have momentum greater than 10 GeV/c. The upstream track segments may have no more than one missing hit each. No cut is made on the vertex χ^2 since this quantity is directly affected by the spurious corkscrew rotations we wish to remove.

[2]Note that this method of measuring the corkscrew rotation is mathematically equivalent to the method given in Refs. [136] and [143]. However, the expression used here has the advantage of being much more clearly related to ϕ; see Appendix I.

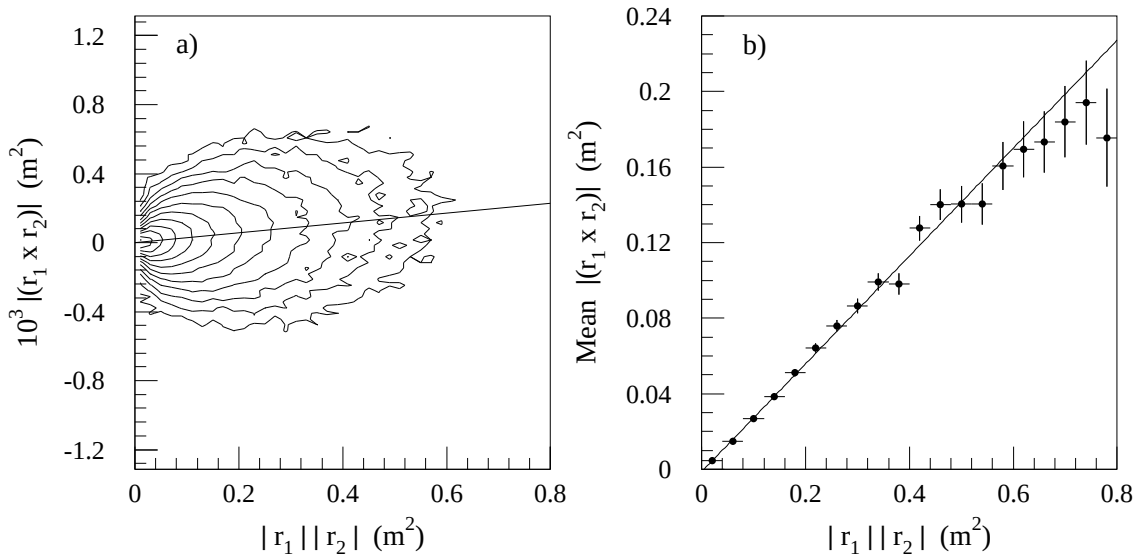

Figure 24. The variation of $(\vec{r_1} \times \vec{r_2})$ with $|\vec{r_1}||\vec{r_2})|$, used to measure corkscrew rotations of the drift chambers, for one calibration. Plot a) shows a logarithmic-scale contour plot of these two quantities. Most events are at small $|\vec{r_1}||\vec{r_2})|$, but a trend is clearly visible. Plot b) shows shows the means and errors derived from fitting Gaussians to projections of plot a) sliced into narrow bands of the abscissa. The fit line gives the corkscrew rotation between chambers 1 and 2. The rotation shown here is 286 ± 4 μrad.

5.8.3 Alignment to the Target and Calorimeter

It is important to tie the drift chamber coordinate system to stable fixed points. Many critical apertures are measured with the excellent pointing ability of the tracking system, and hence the coordinates must be stable over the entire run. We choose the production target and the calorimeter as our references.

The coordinate system can be tied to the target by reconstructing decays and pointed the kaon back to the target. Since kaons may scatter in the regenerators, we need to fully reconstruct decays and select those that do not scatter. The $K \to \pi^+\pi^-$ mode is well-suited for this purpose; we note that in similar experiments with a vacuum beam, $\Lambda \to p\pi$ decays were used [136]. The same $K \to \pi^+\pi^-$ events used for our final analysis were used to find the target; a typical result is shown in Figure 25. The procedure was iterated since the position

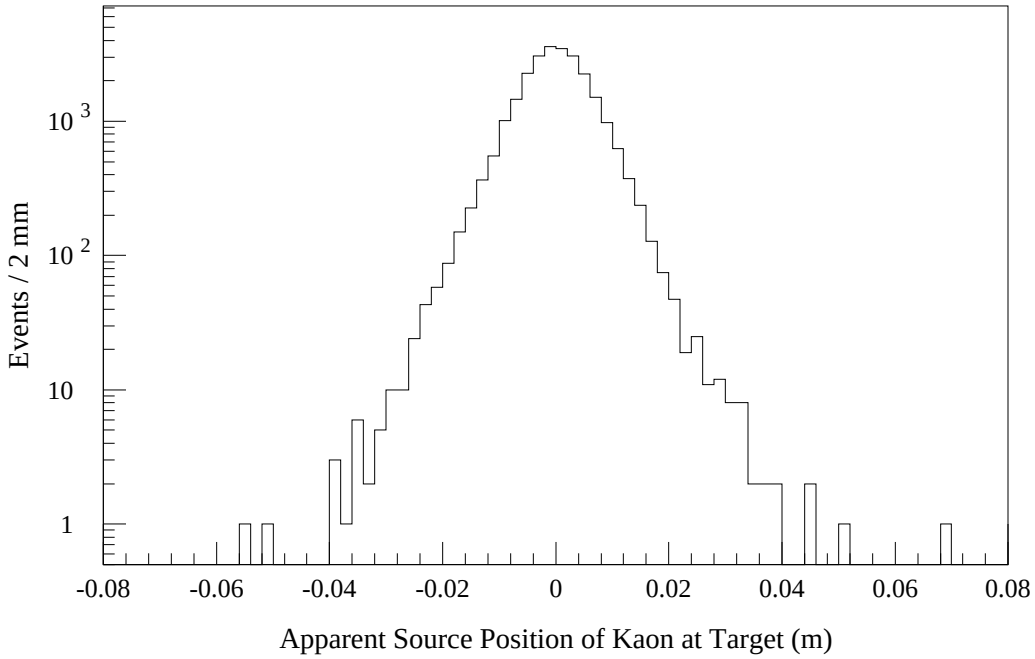

Figure 25. The reconstructed x coordinate of a sample of kaons at the target plane. The rms width of the distribution is 7 mm.

of the target has a small effect on the calculated p_T^2 which is used to identify unscattered kaons.

The coordinate system is then fixed to the calorimeter in the x and y directions. This is accomplished with a clean sample of electrons from $K \to \pi^{\pm} e^{\mp} \nu_e$ decays. One examines the residuals between the projected tracks and the reconstructed cluster centers. The same sample of events used for determining the corkscrew rotations was used as a starting point. Only the electrons are used, and further cuts are applied. $\Lambda \to p\pi$ decays were removed with a mass cut. The minimum track momenta accepted was 5 GeV/c. The electron cluster in the calorimeter was required to be more than 20 cm (35 cm) form other clusters (showering pions) and pass fusion cuts designed to remove overlapping clusters. The track momentum and calorimeter energy must agree to within 10%. Aperture cuts were made near the CA and iron ring. The electron track was required to have all hits present and have downstream track segment $\chi^2 < 30$ for both views. The track angle was limited to within 15 mrad of normal incidence on the calorimeter, such that the energy deposition pattern used

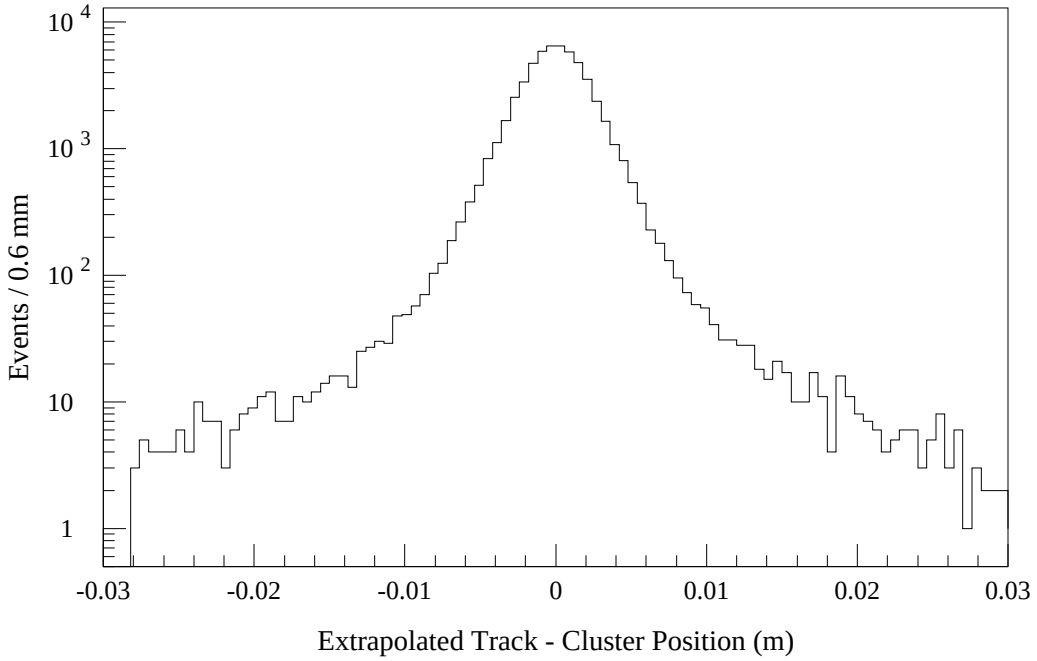

Figure 26. The difference between extrapolated track position and cluster position in the calorimeter for a sample of electrons. The x component of the difference is plotted. The central peak has a Gaussian width of 2.2 mm; the rms width of the entire plot is 3.1 mm.

to measure the positions was not biased by steep tracks. A plot of the difference between the extrapolated track and the cluster center for a typical calibration is shown in Figure 26.

In principle, one would finally consider a rotation of the chamber coordinate system with respect to the rest of the detector. In particular, the calorimeter should be a quite stable reference. We have ignored this small effect; the chamber calibrations assumed that the fourth drift chamber was well-positioned by the surveyors and relatively stable with respect to rotations about the z axis. One can plot the residuals for the projected track positions compared to the cluster positions across the face of the calorimeter for a clean electron sample (i.e., plot the x residuals vs. y, as is done with the muon calibration of relative chamber rotations). In Ref. [136], it is demonstrated that the *relative* rotations between calibrations are easily tracked, whereas absolute measurements are sensitive to systematic effects in the precise lead-glass block positions and cluster position-finding algorithm. In

Table 8. Typical efficiencies for each plane of the drift chambers. The raw numbers include *all* wires in the plane; the corrected numbers have a handful of the most inefficient wires removed.

Plane	Efficiency Raw	Efficiency Corrected	Plane	Efficiency Raw	Efficiency Corrected
Ch. 1 XU	98.5	98.6	Ch. 1 YU	99.0	99.0
Ch. 1 XD	97.7	98.3	Ch. 1 YD	99.3	99.3
Ch. 2 XU	98.6	99.1	Ch. 2 YU	99.5	99.5
Ch. 2 XD	98.6	98.9	Ch. 2 YD	99.3	99.3
Ch. 3 XU	98.8	98.8	Ch. 3 YU	99.3	99.3
Ch. 3 XD	99.0	99.0	Ch. 3 YD	99.4	99.4
Ch. 4 XU	99.4	99.4	Ch. 4 YU	99.5	99.5
Ch. 4 XD	99.3	99.3	Ch. 4 YD	99.4	99.4

other words, the residual vs. coordinate plot for finding the rotation, analogous to Figure 23, Plot c), has a lot of non-trivial structure, but the *difference* of two such plots is well-behaved.

5.8.4 Chamber Wire Efficiencies

The efficiencies were measured for each wire in the system by analyzing a large event sample and keeping track of the distribution of missing hits. The average efficiency for each plane was first calculated. Then, any wire that deviated significantly from the plane average was added to a list with its actual efficiency. The plane average was then recalculated for the remaining good wires.

Only a handful of the 1972 wires had efficiencies below 90%. Typical average efficiencies for the planes are listed in Table 8. The efficiencies are quite high; much of the inefficiency is due to a few problem wires. We note that formerly, in E731, the inner two planes (XD and YU) in each chamber had lower efficiencies. This effect was due to the absence of a ground plane between the x and y portions of the chamber. The resulting low-field region

allows ionization from in-time tracks to straggle in to the sense wires late. This can re-start a TDC channel which had previously detected ionization from near the point of closest passage of the track. This effect was *not* present in E773 since we had longer signal cables and hence had sufficient time to inhibit the TDCs against the late pulses.[3] Note that the TDCs are dead for about 250 ns after receiving a start; this self-inhibiting also prevented inefficiencies from late ionization associated with the in-time tracks. The highest singles rates are at the center of chamber 1, about 50 KHz as determined from accidental events. The rates drop by a factor of 2 at the chamber edges, and also are lower in the downstream chambers. The TDC dead-time resulting from this ambient rate is a sizeable fraction of the observed inefficiency.

The upstream chambers tend to have lower efficiencies, even after the worst wires are removed from the efficiency calculation. This is partially due to the low-energy spray of particles from the beam interactions in the regenerators and vacuum windows; these particles are swept out by the magnets. In addition, the most upstream chamber was built first, and is observed to have more quirky behavior than the others.

The efficiency determination was done separately for 12 time periods spanning the run; the data used spanned the entirety of each period. The information obtained is used by our Monte-Carlo simulation.

5.9 The Field of the Analysis Magnet

The field of the analysis magnet was carefully mapped for the E731 run. We have used the same field measurements. The location of the bend plane was taken from a survey of the location of the pole pieces.

Another issue is the scale of the magnetic field. The E731 map we used was measured at the same nominal current the we employed. The only effect we monitored was small scale shifts due to the precise current in the coils. As discussed previously, many data runs of muons with the magnet off were taken throughout our run. This resulted in the current in the magnet being ramped down to zero and back up to full power approximately twice

[3] This improvement was largely due to the persistence of L.K. Gibbons.

per day. The field was monitored by observing the mean reconstructed kaon mass for each normal data run. In general, the deviations were very small. There were two exceptions where the magnet power supplies required maintenance; these resulted in small shifts (the largest was about 0.5%) in the current. The entire run is therefore dependent on only three independent scale factors determined by demanding that kaon mass agree with the accepted value.

As an independent check, we may reconstruct the Λ mass from $\Lambda \to p\pi$ decays. The Λs cover a wide range of energies, and we analyze the Λ and $\bar{\Lambda}$ separately. The Λs provide another fully-reconstructible decay mode, but one with less symmetry that the $K \to \pi^+\pi^-$. The proton carries most of the momentum and the softer pion largely determines the acceptance. Since the magnetic field always had the same sign, these pions sample different regions of the magnetic field depending on their sign. Figure 27 shows the deviations from the nominal Λ mass; the means are within 0.2 MeV/c^2 of the nominal value; this small deviation is the same for Λ and $\bar{\Lambda}$. The analysis used to isolate this sample is discussed in Chapter 6.

5.10 Trigger Counter Location

At the end of E773, a long muon run was taken with two triggers. Both triggers required a hit in the Mu2 hodoscope. The first trigger also required at least one hit in the B hodoscope but *no* hit in the C hodoscope; the second trigger reversed the roles of the B and C counters. Many of the triggers came from events that hit portions of the B hodoscope that extended beyond the periphery of the C hodoscope, and vica-versa. However, a significant number of triggers came from events where a muon passed through a crack between two of the counters in a counter bank. After applying track quality cuts to isolate a clean sample, the location of such tracks can be used to find the positions of each counter. The distributions from each trigger are shown in Figure 28. The outlines of the counters are clearly visible. Each gap was fit for a slope and intercept to describe its location. These positions could then be used by both by the software trigger verification in the analysis (see Chapter 6) and the Monte-Carlo simulation (see Chapter 7).

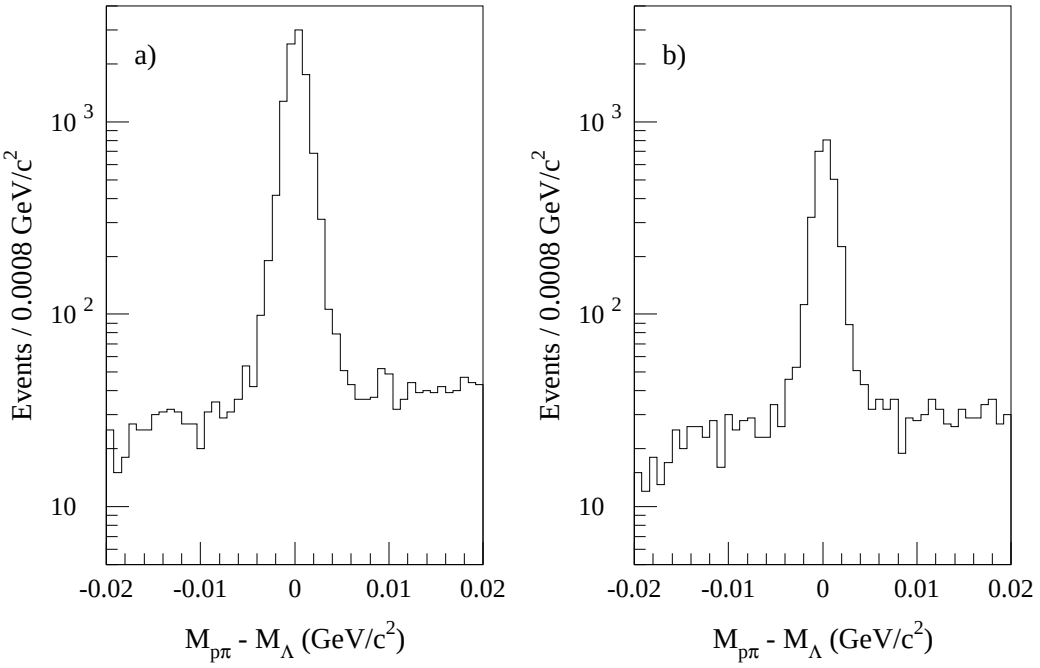

Figure 27. The $p\pi$ invariant mass for $\Lambda \to p\pi^-$ and $\bar{\Lambda} \to \bar{p}\pi^+$ events.

5.11 Calorimeter Calibration

Only a summary of the calibration of our calorimeter is presented here. For more detail, see Ref. [141]. Further general information is also found in Ref. [136, 140].

The main use of this device in our charged-mode analysis is for particle identification. In particular, it helps to separate electrons from other charged tracks (primarily pions, protons and muons). This analysis is not nearly as sensitive to details of the calibration as neutral-mode analysis.

The final calibration was performed with a sample of electrons from $K \to \pi^\pm e^\mp \nu_e$ decays. Most of the corrections described in the cluster reconstruction discussion were determined from the EGS simulation, and are included in the reconstruction used during calibration. The data is also used to determine the temperature corrections and pedestal corrections described earlier.

There are two main types of quantities to be determined. The first quantity is the gain

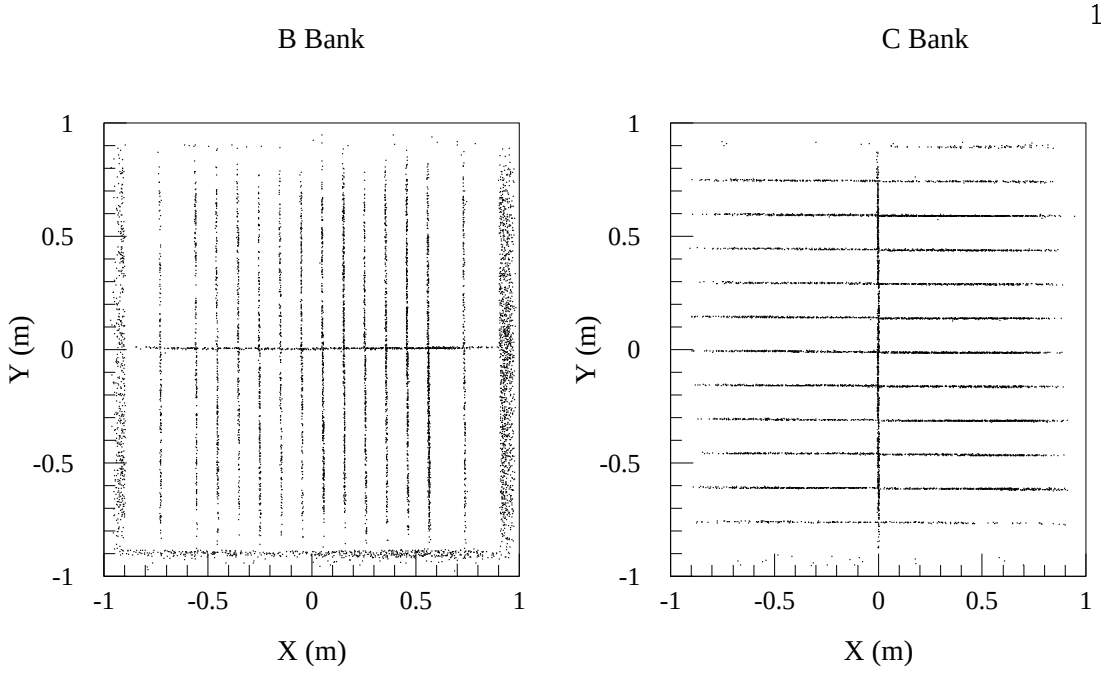

Figure 28. The B and C Bank counters imaged with muon tracks. The points are the projected location of muons *not* firing any counter in a given bank. Note how clean the plots are away from the cracks and edges.

of each channel, including the block, phototube and electronics. This can be extracted by comparing the calorimeter energy, E, to the spectrometer momentum, p, for the electron sample. The second quantity is the ratio between the amounts of charge giving one count in the high and low range of each ADC channel. This 'high range slope' is nominally equal to 8, but the actual values vary significantly: the full range is of order 10%. It can be determined by studying the ratio of calorimeter energy to track momentum, E/p, as a function of E.

5.12 Regenerator Calibration

Special runs were taken to obtain data with muons passing through the regenerators, as discussed in Chapter 4. These were used to calibrate each channel of the UR and DR in terms of minimum-ionizing equivalents. The DR was calibrated once; it was then monitored throughout the run, and its response was found to be quite stable. For the UR, this calibration was done 10 times throughout the run. The UR used no amplifiers, and the

phototubes were instead run at high gain and anode current; this can easily lead to a loss of gain over time.

5.13 Photon Veto Calibration

As with the regenerators, special runs were taken to obtain data with muons passing through the vetoes. With these muons, the lead-lucite modules could be calibrated in terms of minimum-ionizing equivalents.

During the data crunch, a special event class was saved in order to aid calibration of the photon vetoes. We selected events with two pion tracks, based on E/p (see Chapter 6), with an invariant mass consistent with a $K \to \pi^+\pi^-\pi^0$ decay, but only a single photon (unmatched cluster) in the calorimeter. These events were mostly due to $K \to \pi^+\pi^-\pi^0$ decays where one photon escaped the detector. It is possible to reconstruct the energy and direction of the missing photon with information from the observed particles, assuming the kaon did not scatter. When the missing photon was pointed at a veto module, these events could be used to help calibrate the response of these modules to photons of known energy.

These counters were not explicitly used in the $K \to \pi^+\pi^-$ analysis. The lead-lucite portion of the LGA was in the trigger, however. In practice, any cuts on the energy deposit in these modules for neutral mode analysis were set individually for each to account for the variations in accidental energy. Therefore, only uniformity (spatial and temporal) within each counter was important.

5.14 Summary

We have finished our discussions of data collection, reconstruction, and calibration. We next discuss the extraction and analysis of the signal.

CHAPTER 6

DATA ANALYSIS

This chapter describes the analysis of the $K \to \pi^+\pi^-$ and $K \to \pi^\pm e^\mp \nu_e$ samples. The $K \to \pi^+\pi^-$ decays are later analyzed to extract the physics of interest; the $K \to \pi^\pm e^\mp \nu_e$ are used as a check of our understanding of the detector. Since the $K \to \pi^\pm e^\mp \nu_e$ decays are essentially independent of regeneration, they form a clean check of our modeling of the detector acceptance for two-track decays. We also briefly discuss the selection of a $\Lambda \to p\pi$ sample.

6.1 The First-Pass Data Crunch

Shortly after the data was collected, a first-pass data analysis ('crunch') was made. The detector calibrations were sufficiently well-maintained during the run to use in this crunch. Loose cuts, insensitive to the final refinements in calibrations, were made on the events to separate them into various (possibly overlapping) classifications. The most important cuts for charged-mode were the $\pi^+\pi^-$ invariant mass and the ratio of calorimeter energy to track momentum, E/p, used to obtain electron-pion separation.

The $\pi^+\pi^-$ invariant mass for a raw data tape is shown in Figure 29. We also illustrate the effect of an E/p cut, which removes events with electrons, and a decay vertex cut, which removes beam interactions.

The output of the crunch was saved in a denser format than the raw data, although no useful information was thrown out. Many of the data structures were compressed after

their integrity was checked. There were also data blocks for studying the prototype TRDs and the hit-counting trigger for E799; these were deleted. The event size for charged-mode data was reduced from an average of about 1650 bytes to 900 bytes.

The output 8mm tapes consisted of pure samples of each crunch class, except that the smallest classes were combined. This made subsequent analysis very simple. Approximately 730 tapes, just over half-full on average, were crunched. The output was written to 167 8mm tapes. Most of the events removed are charged-mode triggers where two tracks cannot be found, or neutral-mode triggers where four clusters were seen which did not form a $K \to \pi^0\pi^0$ decay. The final set of $K \to \pi^\pm e^\mp \nu_e$ candidates consisted of 57 tapes, and the $\pi^+\pi^-$ sample comprised only 12 tapes! A substantial $\Lambda \to p\pi$ component is also contained in the $\pi^+\pi^-$ sample.

6.1.1 $\pi^+\pi^-$ Cuts

The $K \to \pi^+\pi^-$ sample was selected with a few loose cuts designed to separate this sample from junk (i.e., untrackable events) and other, more copious two-track decays. The first requirements involved basic track reconstruction. Two full tracks with opposite charge were required. Vertexing and $x - y$ matching of the views had to be successful, with the loose criteria described in Chapter 5. The minimum track momentum had to be at least 5 GeV/c.

The rest of the requirements removed the bulk of non-$\pi\pi$ two-track decays. The $\pi^+\pi^-$ invariant mass was required to be between 450 and 550 MeV/c^2, eliminating $K \to \pi^+\pi^-\pi^0$ decays. The ratio of the energy deposit in the calorimeter to the track momentum, E/p, was required to be less than 0.85, for both tracks, to remove $K \to \pi^\pm e^\mp \nu_e$ decays. In addition, there was a loose cut on possible $\Lambda \to p\pi$ decays. This cut was only made when the kaon energy was larger[1] than 170 GeV/c and thus did not affect our final sample, which is all at lower energy.

Some effects of the small differences between the calibrations used in the crunch and the final ones are illustrated in Figure 30. Note that the track-finding algorithm may in

[1] This is a leftover from E731, where there were many high-energy Λ's in the vacuum beam.

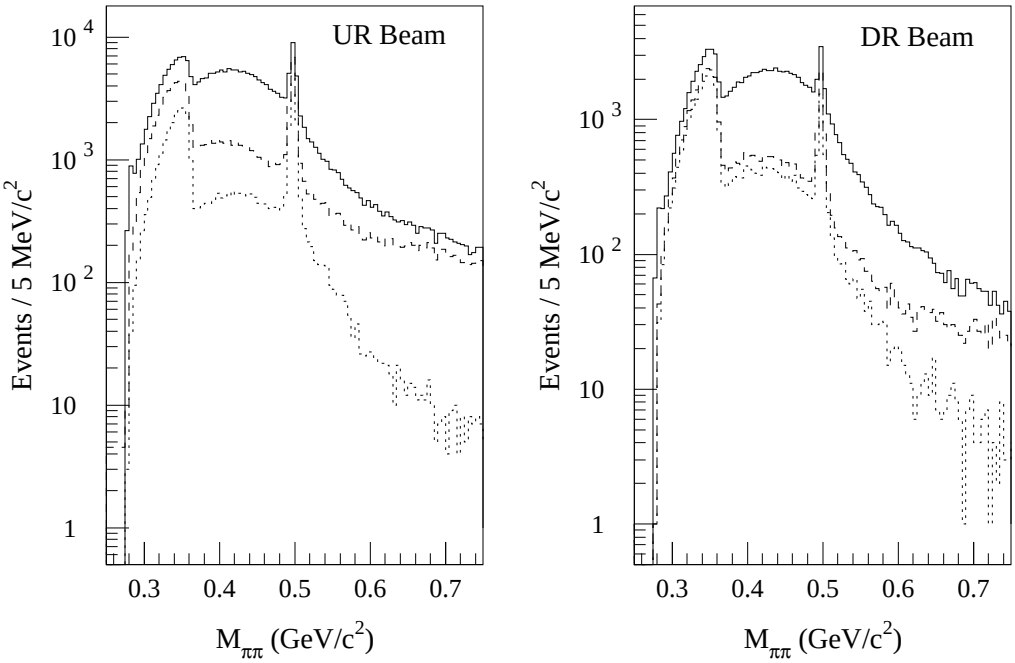

Figure 29. The $\pi^+\pi^-$ invariant mass from a Data Set 2 raw data tape. The solid line shows the mass for all events; the dashed line after an E/p cut, and the dotted line after a decay vertex cut in z to remove regions with beam interactions in material. One can easily identify the $K \to \pi^+\pi^-$, $K \to \pi^+\pi^-\pi^0$, and $K \to \pi^\pm e^\mp \nu_e$ components in the spectrum. Note that fiducial cuts, particularly at the calorimeter, further reduce the $K \to \pi^\pm e^\mp \nu_e$ background.

rare cases find different tracks with updated calibrations; this can cause large changes in the plotted quantities.

6.1.2 $K \to \pi^\pm e^\mp \nu_e$ Cuts

For the $K \to \pi^\pm e^\mp \nu_e$ sample, the cuts were very loose. We required two oppositely charged tracks, with successful vertexing and x-y track matching. At least one of the tracks was required to have $E/p > 0.85$.

6.2 Analysis Cuts for $K \to \pi^+\pi^-$ Sample

We now turn to the full set of analysis cuts used in our analysis. Very dense summary files containing a select set of quantities characterizing each event were written out after

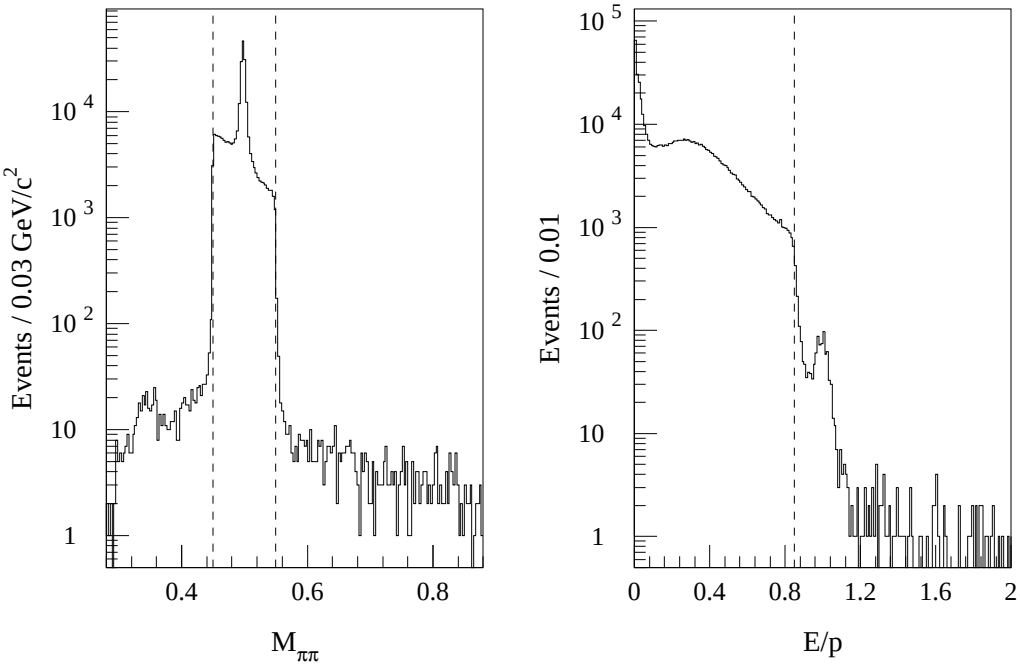

Figure 30. The $\pi^+\pi^-$ invariant mass and E/p distributions after the first-pass crunch but with final calibrations. The dashed lines show the cuts applied in the crunch.

a preliminary analysis. The small sample size allowed this process to be quickly redone if different information was desired and the resultant dense files allowed rapid investigation of further cuts.

We first describe the tracking and fiducial aperture cuts applied to obtain a cleanly reconstructed two-track sample; these cuts are summarized in Table 9. We then describe the rest of the cuts, including particle identification and kinematics, used to separate the signal from background; these cuts are summarized in Table 10.

6.2.1 Tracking Cuts

We required that exactly two tracks were found in each view, and that they had opposite charge. The x and y views must be successfully matched by using clusters in the calorimeter. The simple vertex-fitter, based on the distance of closest approach, must succeed. The relevant algorithms were described in Chapter 5.

Table 9. The tracking and fiducial cuts for the $K \to \pi^+\pi^-$ analysis. The transverse size of a lead glass block is $d_{blk} = 5.82$ cm. X, Y, and R refer to projected transverse and radial locations of the tracks.

Track Reconstruction Cuts	
Tracks	two tracks in both x and y views
Charge	opposite charge
Vertex	successfully found
x-y matching	successful match using calorimeter clusters
Tracking Cuts	
Segment χ^2	$\chi^2 < 30$ (for all track segments)
Vertex χ^2	$\chi^2 < 30$
Segment Match at Magnet	mis-match $< 5\sigma$
Fiducial Cuts	
Beam ID	reconstructed kaon points into 5.0×5.5 cm region at downstream face of exactly one regenerator
VA0	-0.70 m $< X < 0.80$ m; -0.146 m $< Y < 0.150$ m
DR (Upstream UR events)	$Y > 0.0$ m ($Y < 0.0$ m) for UR High (Low) Beam Events
Vacuum Window	$R < 0.59$ m
Helium Box (Set 1)	$X > -0.62$ m
Collar Anti	$X, Y > 1.6 \times d_{blk}$ from hole centers
Lead Glass Outer	$R < 0.88$ m
Yswap	$\lvert X_2 - X_1\rvert > 0.02$ m or $max(\lvert X_1\rvert, \lvert X_2\rvert) > d_{blk}$
Mu2 Bank	$\lvert X\rvert < 1.2$ m; $\lvert Y\rvert < 1.1$ m

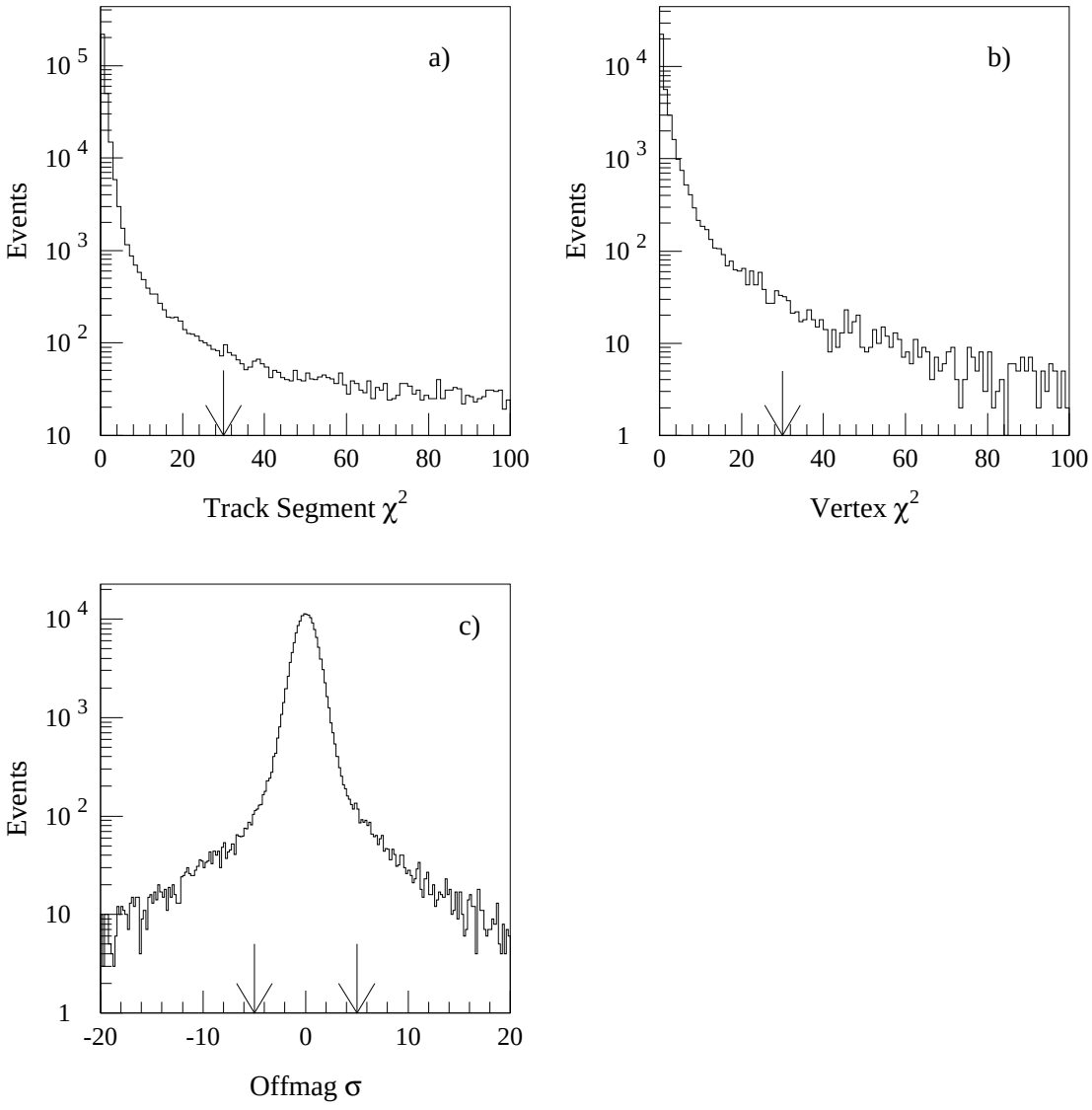

Figure 31. Distributions of tracking quality variables showing cuts made. Plot a) shows the track segment χ^2. Plot b) shows the vertex χ^2. Plot c) shows the mismatch of the tracks at the magnet plane, in standard deviations. The data sample is the final $K \to \pi^+\pi^-$, with all cuts other than tracking applied.

The χ^2 of the best fit line to each of the track segments was required to be less than 30.[2] This will remove most tracking errors, but it is also effectively a loose cut on the sum-of-drift-distances (SODs). The connection between segment χ^2 and SODs is explored further in Appendix I. Here, we simply note that for a full segment, our cut corresponds to about a ± 1.1 mm cut on the SODs. A typical segment χ^2 distribution is shown in Figure 31.

A χ^2 describing the vertex quality, including the effects of chamber resolution and multiple scattering between the vertex and the chambers, was formed. The distribution of this quantity and the cut applied are shown in Figure 31.

The upstream and downstream track segments for each track were extrapolated to the bend-plane of the analysis magnet; the difference in these positions is a measure of track quality. The observed resolution is (in mm)

$$(\sigma_x)^2 = (4.10/p)^2 + (0.15)^2 \tag{6.1}$$

$$(\sigma_y)^2 = (3.70/p)^2 + (0.15)^2 \tag{6.2}$$

where p is in GeV/c. The resolution naively calculated from the chamber resolution and multiple scattering agrees with the y resolution given here. T he calculation is very similar to that for the momentum resolution given in Appendix I. The degraded resolution in the x view is presumably due to assuming that the analysis magnet causes all of the bend at one z, and possibly also effects of the earth's magnetic field. The distributions and cuts are shown in Figure 31.

6.2.2 Fiducial Cuts

Many cuts were necessary to assure that the decay products were in a region of the detector where they could be well-measured. This is important since we need a precise understanding of the acceptance. The most important apertures were the DR enclosure, the HDRA (the veto counter at 141 m) and the calorimeter.

[2] This χ^2 is actually normalized with a nominal chamber resolution of 100 μm; since the actual resolution is somewhat better, the cut is actually looser than indicated.

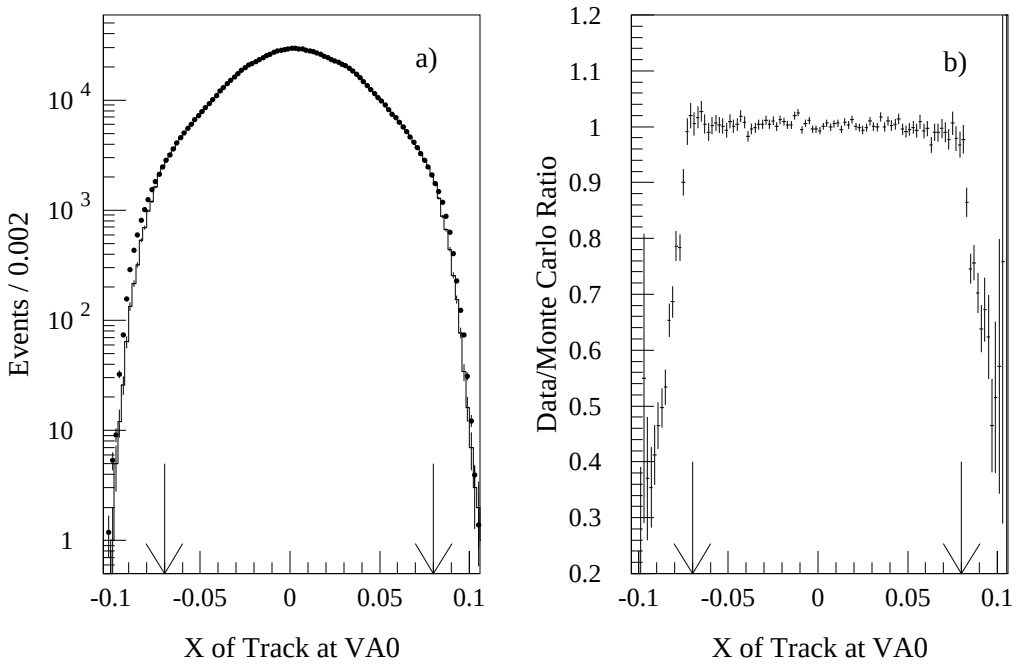

Figure 32. The track illumination in x at the plane of VA0. Plot a) Shows a comparison of data (histogram) and Monte Carlo (dots). Plot b) shows the ratio of data to Monte Carlo, clearly illustrating the localized discrepancy.

Unfortunately, the VA0 counter was a limiting aperture for decays occurring just after the UR. An aluminum skin at the inner edge of the device covered the active counter material. The edges of the active components could be located with the data easily, but inactive apertures are more difficult. A comparison of data and Monte-Carlo[3] track illuminations at VA0 is shown in Figure 32; the disagreement at the edges is caused by the aluminum. The cuts employed are also shown.

The support structure for the downstream regenerator (DR) formed an obstacle for tracks coming from upstream decays. Such events were required to have both of the tracks remain on the same side of the vertical centerline as the decay vertex until they passed the z of the plane containing the downstream face of the DR.

The inner edges of the HDRA are formed by the DRAC and DRAN counters. DRAC (scintillator) was in veto in the trigger. The large circular metal flange surrounding the

[3]The Monte-Carlo simulation of the experiment is discussed in detail in Chapter 7. Comparison of the data and Monte-Carlo events is a useful technique for locating unexpected effects in the data.

final vacuum window at 159 m also limited acceptance. Events containing tracks with a radius larger than 0.59 m were rejected.

The helium bag between the first two drift chambers was supported on four sides by an aluminum box. The box was very near to limiting the acceptance of tracks, and would in fact do so if misaligned. For Data Set 1, comparisons of data and Monte Carlo show evidence that such misalignment occurred. The sides of the box are nominally parallel to z, but become an aperture partway between the chambers as tracks spread. Comparing data and Monte Carlo, we found that the effect was sharpest when projected to a z midway between the chambers. A cut was made when either track had a projected X-coordinate less than -0.62 m at a z midway between the first two chambers.

The remainder of the aperture cuts concern the location of tracks at the calorimeter and muon system. These are necessary to maintain good particle identification capability.

Events where one track was within the central two columns of glass blocks and the two tracks were within 2 cm in x were cut. These events are susceptible to having the x-y track matching inverted; this compromises the E/p cut used to identify electrons by associating the incorrect cluster with the momentum-determining x track segment.

The Collar Anti (CA) covered inner halves of all lead-glass blocks adjacent to the beam holes in the calorimeter. Electrons would begin showering in this device and the calorimeter would see only part of the energy. Events in which either track projected into a square of half-width of 9.31 cm (equal to 1.6 lead-glass block widths) were discarded.

At the outer edge of the calorimeter, significant energy could be lost by portions of the shower exiting the side of an edge block. The LGA was designed to detect most particles which would miss the calorimeter. However, there was still a gap, which was filled by the iron ring. The ring was somewhat smaller than the calorimeter in radius and slightly off-center during E773. By looking at the track illumination at the calorimeter for events with a bad $\pi^+\pi^-$ mass, one can view directly the enhancement of $K \to \pi^\pm e^\mp \nu_e$ decays in which the $e^\pm$ have a low E/p and hence contaminate the $\pi^+\pi^-$ sample (see Figure 33). This plot was used to locate a cut on the projected track radius at the calorimeter. Events with either track radius greater than 0.88 m were discarded.

The hodoscope behind the steel muon filter was large enough to detect most tracks

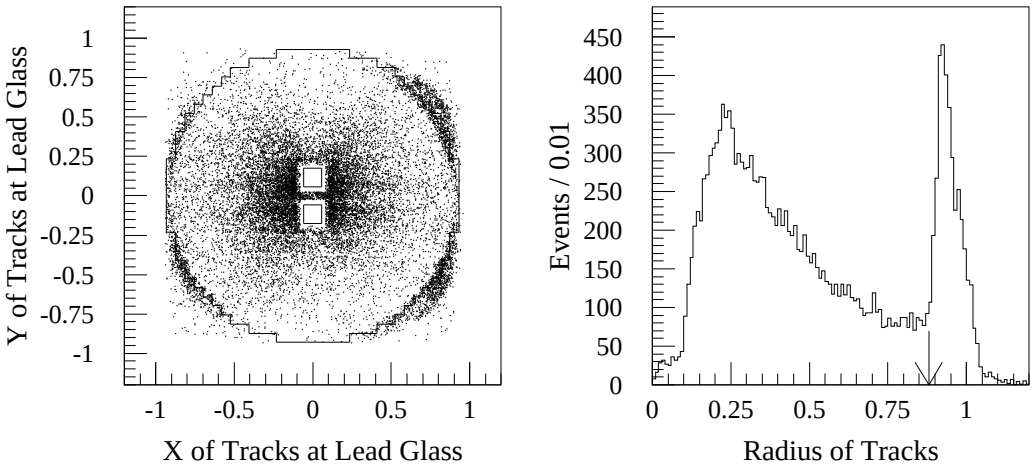

Figure 33. The position of tracks at the calorimeter from kinematic regions rich in $K \to \pi^{\pm} e^{\mp} \nu_e$ background; in particular events with p_T^2 on the interval $(250, 40\,000)$ MeV$^2/c^2$ and $M_{\pi\pi}$ on one of the intervals (0.45, 0.47) MeV/c^2 or (0.52, 0.55) MeV/c^2. Plot a) is shows the track projections at the plane of the calorimeter. Lines show the outline of the calorimeter. Plot b) shows the radius of the tracks; the cut at 0.88 m is also displayed.

accepted by the rest of the spectrometer. However, a small fraction of the events had tracks extrapolating outside the instrumented region. The counter bank was 2.54 m (x) by 2.44 m (y) in size. Tracks were required to project within a region of ± 1.2 m (x) by ± 1.1 m (y). The smaller fiducial size allows for tracks scattering in the steel and pion decays in flight; both effects degrade pointing accuracy.

6.2.3 Particle Identification

Particle identification was crucial for reducing the semileptonic backgrounds; i.e., the processes $K \to \pi^{\pm} e^{\mp} \nu_e$ and $K \to \pi^{\pm} \mu^{\mp} \nu_{\mu}$. The only other copious two-track decay modes, $K \to \pi^+ \pi^- \pi^0$and $\Lambda \to p\pi$, were easily removed with mass cuts. The semileptonic modes can easily reconstruct inside our mass cut when the lepton is assigned the pion mass.

We calculate the ratio of calorimeter energy to track momentum, E/p, for each track. This quantity is near unity for electrons, but is generally small for pions. A distribution of E/p for $K \to \pi^{\pm} e^{\mp} \nu_e$ events is shown in Figure 34. There is a an electron peak at $E/p = 1$

Table 10. The remaining analysis cuts for the $K \to \pi^+\pi^-$ analysis.

Particle ID Cuts	
E/p	$E/p < 0.8$
π momentum	$p_\pi > 7\text{GeV}/c$
Trigger Verification Cuts	
B and C Banks	Counters hit by two tracks must satisfy trigger
CHEW or ZUMA	Hits of two tracks must satisfy trigger
Regenerator Cuts	
UR and DR energy deposit	max. signal < 0.2 (0.8) min-I for DR (UR)
Kinematic Cuts	
$p\pi$ mass	$\lvert M_{p\pi} - 1116\ \text{MeV}/c^2\rvert < 6\ \text{MeV}/c^2$
$\pi\pi$ mass	$\lvert M_{\pi\pi} - 498\ \text{MeV}/c^2\rvert < 14\ \text{MeV}/c^2$
Kaon p_T^2	$p_T^2 < 250\ \text{MeV}^2/c^2$
Kaon energy	$20\ \text{GeV} < E_K < 160\ \text{GeV}$
Decay vertex	$118.5\ \text{m} < z < 127\ \text{m}$ or $129 < z < 154\ \text{m}$ for UR
	$130\ \text{m} < z < 154\ \text{m}$ for DR

and a characteristic pion shape. The pion shape includes three main features. First, there is a peak at $E/p = 0$ due to unmatched tracks. Second, there is another peak at very low E/p is due to pions which do not shower; the minimum ionizing deposition reconstructs as about 0.7 GeV in our calorimeter (this is roughly the real energy deposit; the reconstruction is designed to correct the calorimeter response for the characteristics of electro-magnetic showers). Finally, the rest of the pions form a broad hump; these have initiated hadronic showers in the calorimeter. Note that since we tune our calibration for electromagnetic showers, the E/p for pions extends past one. In particular, hadronic showers may occur deeper in the blocks, and hence be less affected by light absorption. The shape of the pion response for the hadronic showers is only very weakly dependent on energy. The min-I energy deposit is essentially constant and thus the E/p from this peak shifts as p changes, but it is far away from any cut.

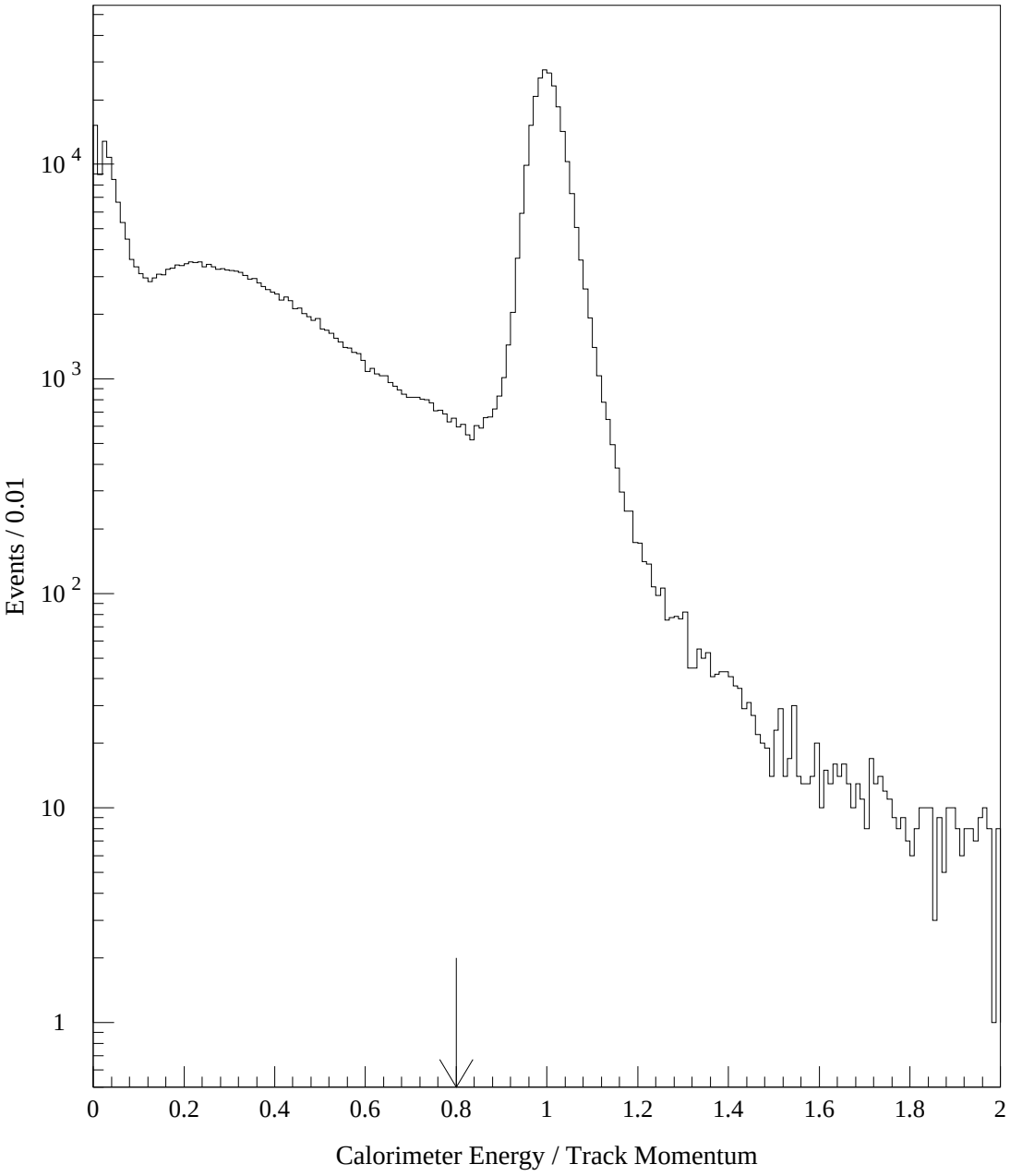

Figure 34. The E/p distribution from a sample of $K \to \pi^{\pm} e^{\mp} \nu_e$ decays.

To ensure that the muon veto system is fully efficient, the track momenta are both required to be at least 7 GeV/c; at low energies, muons range out in the filter. The momentum cut also reduces the chance of pion decays in flight. We also check all of the

Mu2 counter latches, demanding that none fire. The trigger veto takes care of this in principle, but we wish to avoid even small inefficiencies since the $K \to \pi^{\pm}\mu^{\mp}\nu_{\mu}$ rate is large.

6.2.4 Trigger Verification

We must be able to understand our acceptance precisely in this experiment. Some of the otherwise good $K \to \pi^+\pi^-$ events are in our data sample only because of accidental activity in our detector. That is, the $\pi^+\pi^-$ tracks themselves would not have satisfied the trigger, and the accidentals cause us to gain data. We must of course also consider the possibility of bias due to accidentals causing *losses* of data, and do so in Chapter 9. We point out here, however, that these losses are far less of a problem: most losses are due to veto counters firing from activity uncorrelated with any real kaon decay, and do not bias the shape of the decay rate as a function of p and z. Accidental gains, on the other hand, are drawn from a biased sample: only those decays otherwise failing the trigger may be re-gained due to accidental activity.

To avoid having to precisely model these effects, we verified that the trigger would be satisfied by the pion tracks from the reconstructed $K \to \pi^+\pi^-$ decay, without any associated accidental activity. The fiducial cuts described above are sufficient to guarantee that the two pions would fire no vetoes. All that remains is the the B and C trigger counters and the Level 2 requirement in the drift chambers.

For Data Set 1, simply requiring that the reconstructed decay vertex was upstream of the T and V counters was sufficient for that portion of the trigger. Since the trigger required only T *or* V to see two tracks, the efficiency was excellent and uniform. For the B and C bank components of the trigger, the geometry of the banks was determined as described in Chapter 5, and the two pion tracks were projected to determine which counters would fire from their passage.

The Level 2 chamber trigger, either CHEW or ZUMA as appropriate, was simulated using only the hits on the two pion tracks. These hits were required to satisfy the trigger.

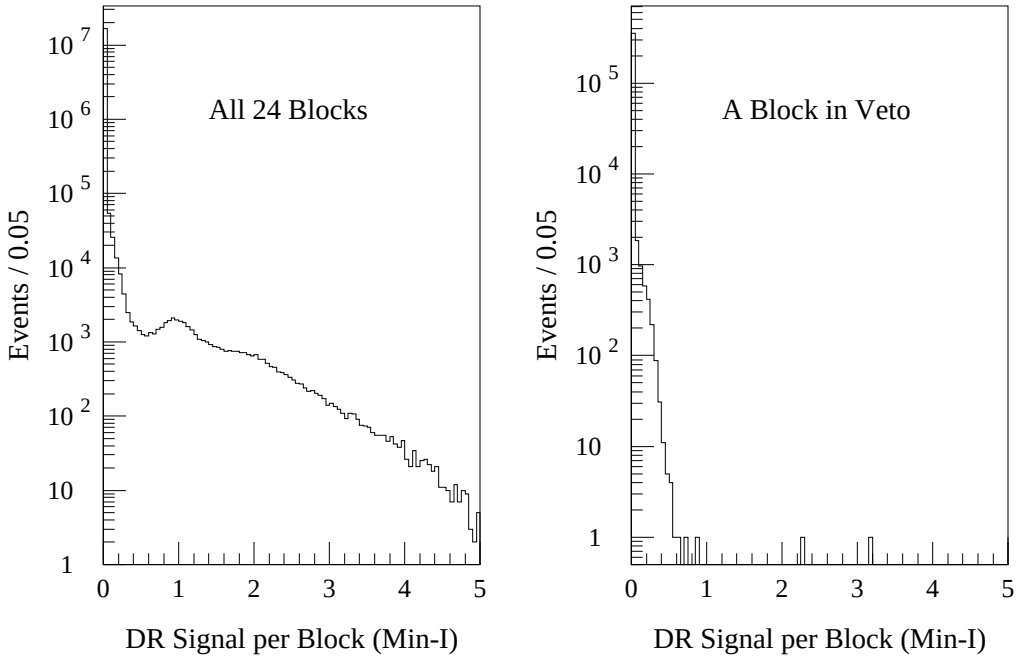

Figure 35. The signal in the DR scintillator blocks for raw events. The first plot shows the signals in all 24 blocks for each event; the other plot shows the signal from a single block used in the on-line veto. All signals are calibrated in terms of minimum-ionizing equivalents; the on-line trigger veto is active for this data.

6.2.5 Regenerator Vetoes

Each instrumented counter in the regenerators (2 phototubes on each of the 24 DR blocks and 1 phototube each on 18 of the 72 UR blocks) was used. The signals were converted into minimum-ionizing (Min-I) equivalents and the maximum signal in any single counter of each regenerator determined. Events were required to have this maximum less than 0.2 (0.8) Min-I for the DR (UR). The distribution of signal size in the DR blocks is shown in Figure 35. Note that the device is very quiet in spite of the high ambient rate: the DR (UR) trigger veto fires at about 0.5 MHZ (1.8 MHz) at our average beam intensity. The effect of the analysis cut is shown in Figure 36; we remind the reader that an on-line veto cut applied at the trigger level is *already included* in all plots. The loss of coherent

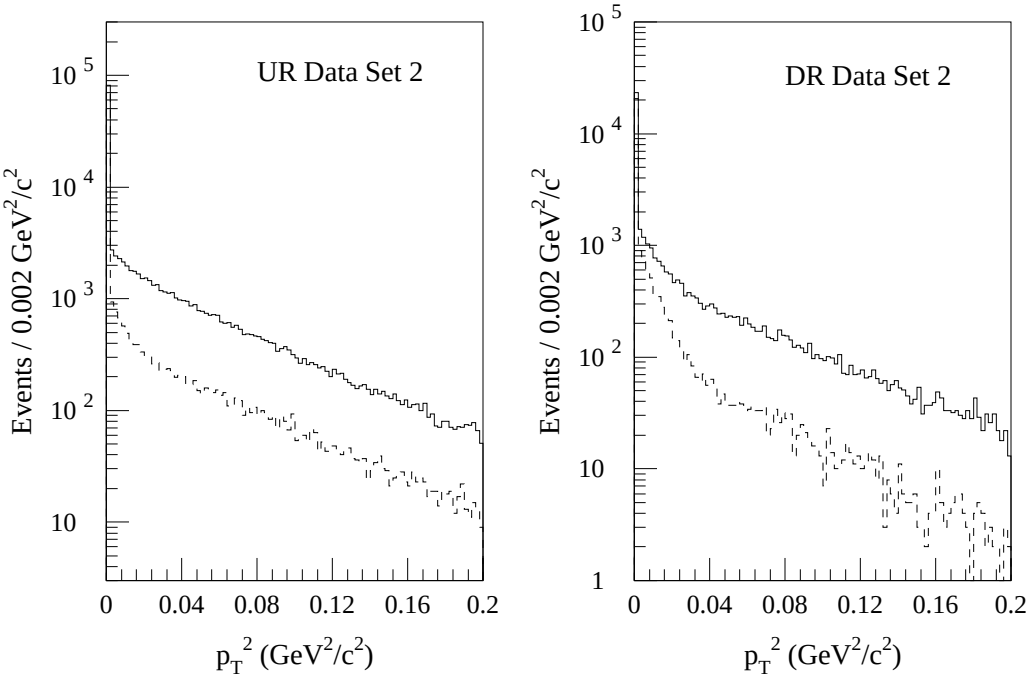

Figure 36. The effect of off-line cuts on regenerator activity. The solid line is before any cut on regenerators; the dashed line is after the cut described in the text. All other analysis cuts have been applied.

signal events due to accidentals is about 5% for each beam. The active regenerators were responsible for an enormous suppression of inelastic interactions.

6.2.6 Kinematic Cuts

We cut on the $p\pi$ invariant mass to remove Λ decays. It is easy to show that for a real Λ decay in our experiment, the proton track has the higher momentum. Cutting on the momentum ratio of the two tracks is often a useful trick, but it is redundant in our case. A discussion of $\Lambda \to p\pi$ kinematics is given in Appendix I, and further details of Λs in our experiment are given below. We display the $p\pi$ mass in Figure 37. Note that there is little background in the coherent signal, but that the Λ decays do contaminate the $K \to \pi^+\pi^-$ sample at larger p_T^2.

The kaon momentum, p, and decay vertex, z, are the key variables used to fit the decay

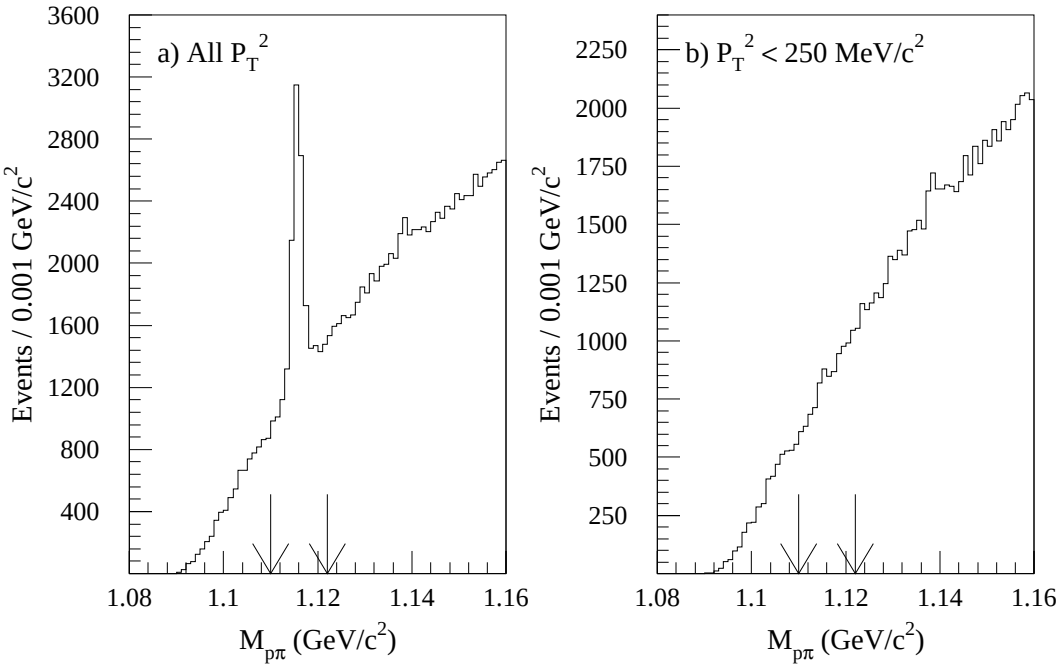

Figure 37. The $p\pi$ mass in the $K \to \pi^+\pi^-$ sample. Plot a) shows the $p\pi$ mass with all $K \to \pi^+\pi^-$ cuts except the cut on p_T^2. Plot b) shows the $p\pi$ mass with all $K \to \pi^+\pi^-$ cuts except the cut on $M_{\pi\pi}$. The p_T^2 cut has a large effect since the Λs originate in the regenerator, not the target. The plots include both beams from Data Set 2.

distribution. The other two central variables in the analysis are the $\pi^+\pi^-$ mass and the kaon p_T^2. These variables may be used to separate the coherent $K \to \pi^+\pi^-$ signal from the backgrounds. In Figure 38, we display a plot of the the $\pi^+\pi^-$ mass versus p_T^2 for the DR in Data Set 2. The coherent peak and diffractive background are clearly visible, as is the $K \to \pi^\pm e^\mp \nu_e$ background in the mass sidebands.

The $\pi\pi$ mass resolution is about 3 MeV/c^2; it varies with beam (UR or DR) and data set due to changes in the accepted momentum spectrum and scattering. Mass plots are shown in Figure 39; note the low-side tail due to $K \to \pi^+\pi^-\gamma$ decays. We require the $\pi^+\pi^-$ mass to lie between 484 MeV/c^2 and 512 MeV/c^2.

Our signal consists of a combination of transmitted K_L and coherently-regenerated K_S. The intrinsic width in p_T^2 of the coherent regeneration is negligible. All of the observed

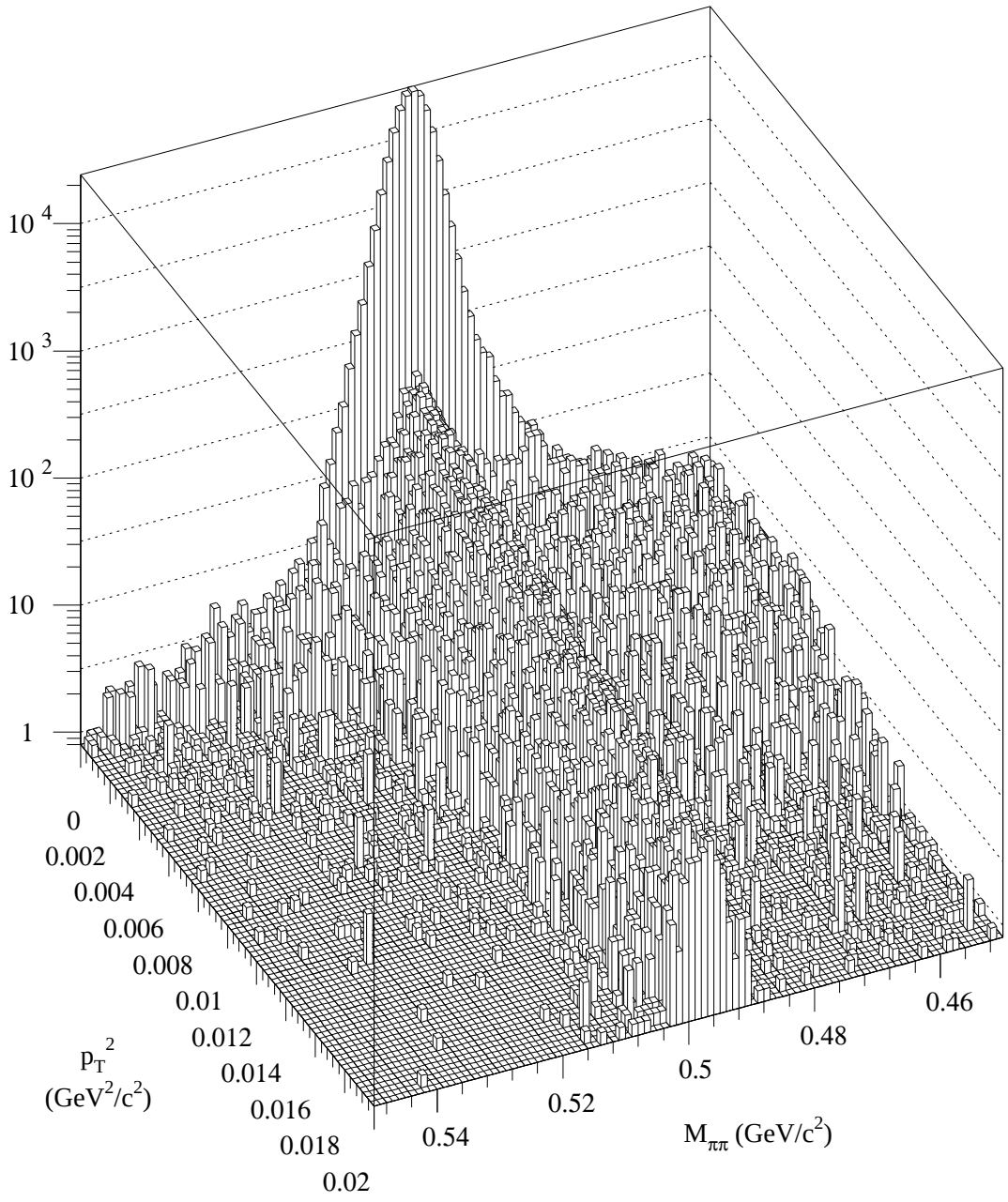

Figure 38. The $\pi^+\pi^-$ mass vs. kaon p_T^2 in the $K \to \pi^+\pi^-$ sample; events from the DR beam of Data Set 2 are plotted. The first bin in p_T^2 corresponds to the analysis cut ($0 - 250$ MeV$^2/c^2$) used to select coherent events. Note the large coherent peak and long diffractive tail. A broad distribution of residual $K \to \pi^\pm e^\mp \nu_e$ decays is also visible.

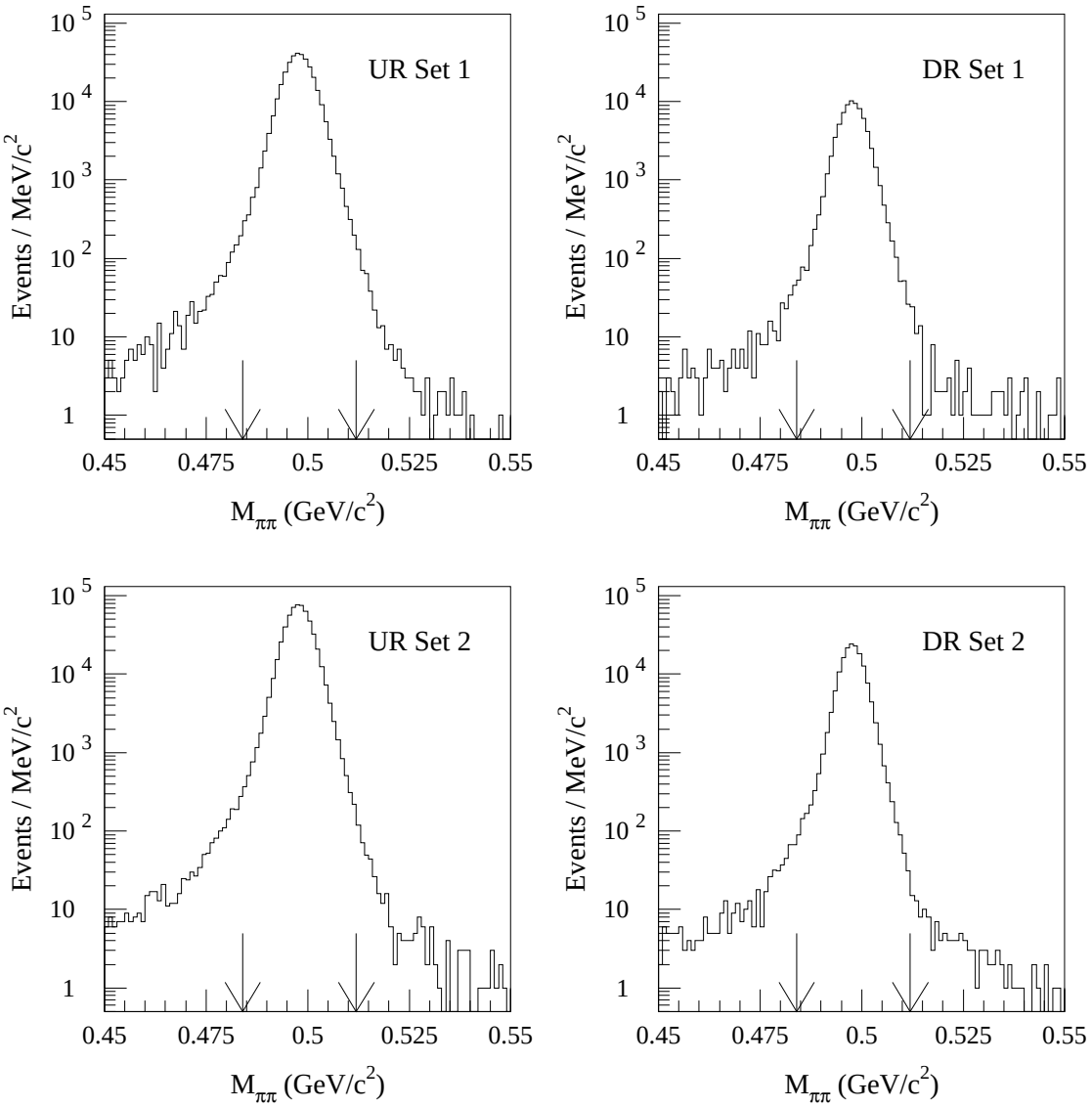

Figure 39. Two-body invariant mass for the final data samples. Each plot is labeled by beam and data set; arrows indicate the analysis cut.

width in p_T^2 of the coherent peak is due to detector resolution and inner-bremsstrahlung $K \to \pi^+\pi^-\gamma$ decays.

The distribution of p_T^2 is shown in Figure 40. We take $p_T^2 < 250$ MeV$^2/c^2$ as our signal region. In the region around 60,000 MeV$^2/c^2$, one can see the characteristic Jacobian peak of $K \to \pi^+\pi^-$ decays from Primakoff production [148, 149] of the $K^*(892)$; the K^* are

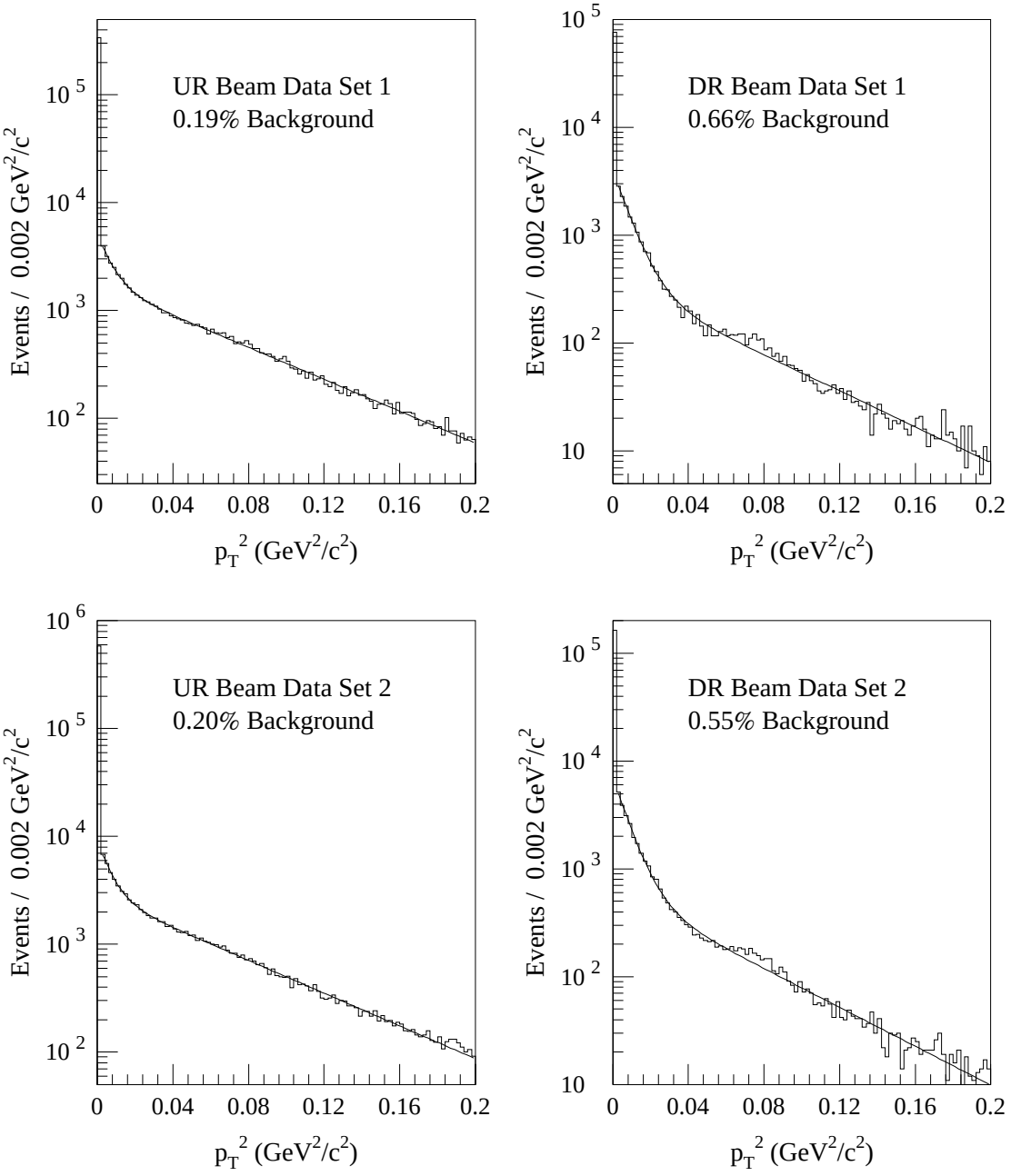

Figure 40. Transverse momentum squared (p_T^2) of final data samples. Each plot is labeled by beam and data set. The analysis cut retains 1/8 of the first bin. The structure seen is discussed in detail in Appendix F. The curves are fits to a sum of two exponential and are used only to illustrate the background level. The actual background subtraction technique is described in the text.

sharply forward-peaked, and the subsequent decay $K^* \to K\pi^0$ gives a distinctive shape to the K p_T^2.

The reconstructed decay vertex must lie between 118.5 m and 127 m, or 129 m and 154 m, for the UR. The analogous cut for the DR is 130 m - 154 m. The kaon energy, E_K, must satisfy 20 GeV $< E_K <$ 160 GeV.

6.3 Analysis Cuts for $K \to \pi^\pm e^\mp \nu_e$ Sample

For $K \to \pi^\pm e^\mp \nu_e$ the size of the sample necessitated an intermediate crunch to further reduce the sample before a final analysis. This involved more cuts to reduce the number of events as well as a selective elimination of non-essential information to reduce the event size. This process reduced the volume of data by 1/3. We describe this second crunch and the final analysis together, since the distinction is unimportant to us now.

The cuts on the $K \to \pi^\pm e^\mp \nu_e$ sample were kept as similar as possible to those on the $K \to \pi^+\pi^-$ sample, since we wished to use them as an acceptance check. The tracking, fiducial and trigger verification cuts were all identical except for the separation into UR and DR beam events; this was based on the sign of the y decay vertex and hence different than the $K \to \pi^+\pi^-$ mode as discussed in Chapter 5. The DR activity cut was tighter, for historical reasons, we required less than 0.1 minimum-ionizing equivalents (instead of 0.2). The particle identification cuts were necessarily different. We required $|E/p - 1| < 0.15$ for the electron, and $E/p < 0.8$ for the pion. We require that the extrapolated position of the two tracks at the calorimeter be more than 0.35 m apart. This prevents the pion showers from affecting the electron showers. There are, of course, many differences in the kinematic cuts for the $K \to \pi^\pm e^\mp \nu_e$ data, compared to the $K \to \pi^+\pi^-$ data; we now discuss these in detail.

6.3.1 $K \to \pi^\pm e^\mp \nu_e$ Kinematic Cuts

The track momentum cuts were: $p_e > 7$ GeV/c and $p_\pi > 10$ GeV/c. The invariant mass of the charged tracks is required to lie in the physical range, in particular we ask that $M_{\pi e} <$

M_K. The invariant mass, assuming both particles were electrons, had to satisfy $M_{ee} > 60$ MeV/c^2. Any $K \to \pi^+\pi^-$ background was removed with a cut of $|M_{\pi\pi} - M_K| > 10$ MeV/c^2. If the total observed momenta was above 100 GeV/c, a ± 15 MeV/c^2 cut on $M_{p\pi} - M_\Lambda$ was made.[4] Events from $K \to \pi^+\pi^-\pi^0$ decay were eliminated by a two-dimensional cut on $M_{\pi\pi}$ and k_{+-0}, a kinematic quantity proportional to the square of the π^0 longitudinal momentum in the center of mass. Events with $k_{+-0} > -0.04$ and $M_{\pi\pi} < 0.373$ GeV/c^2 were rejected. Details of the kinematics are presented in Appendix I. Also, see Ref. [136] for a nice plot illustrating this cut.

If the kaon does not scatter, then the p_T of the ν is known by balancing with the p_T observed for the charged tracks. One may solve for the kaon energy with only a two-fold ambiguity. The kinematics determines only the *square* of the longitudinal neutrino momentum in the kaon center-of-mass, $(p_L^*)^2$: its sign is ambiguous. Because of this, two solutions are obtained for the kaon energy, E_{lo} and E_{hi}. We require $E_{lo} > 20$ GeV and $E_{hi} < 160$ GeV and -1500 MeV$^2/c^2 < (p_L^*)^2 < (229)^2$ MeV$^2/c^2$. The negative value of the low cut allows for resolution effects; the high-side cut is the kinematic limit, but has no effect in practice.

6.4 $\Lambda \to p\pi$ Cuts

We now describe cuts used to isolate a Λ sample; this data provides a useful; check on the spectrometer calibration. In addition, it gives some insight into the structure of the background to $K \to \pi^+\pi^-$. A significant sample of $\Lambda \to p\pi$ decays is retained by the $K \to \pi^+\pi^-$ crunch cuts. Only the $\pi^+\pi^-$ mass cut leads to a noticeable loss of events. It is instructive to point out the differences between vacuum and regenerator beams. A vacuum beam contains Λs from production in the target (and also the absorbers, to some extent). A noticeable number survive only at high energies. These 'target Λs' also have no intrinsic p_T^2. This motivates a cut being applied only at high energies [136]. With a regenerator, the target Λs are suppressed, both by the additional absorption and also by removing the most upstream portion of the decay volume. However, new Λs are created by hadronic

[4] The energy cut is left over from vacuum beam analysis in E731. In principle, one should cut for all energies, but there is no sign of a Λ peak in the $K \to \pi^\pm e^\mp \nu_e$ data.

interactions in the regenerators. These Λs span all energies, but have a spread of p_T^2 from production. If one applies the rest of the $K \to \pi^+\pi^-$ analysis, there is no hint of Λs left. However, if one relaxes the the p_T^2 cut then a Λ mass peak is evident, as demonstrated in Figure 37. We therefore conclude that making an explicit lambda mass cut is important to obtain a proper p_T^2 shape from the data. In addition, one should remember this in an experiment with a vacuum and regenerator beam; if the mass plot is checked only after a p_T^2 cut, false conclusions concerning the occurrence of Λ background might be drawn. A cut applied only at high energies may leave contamination in the regenerator p_T^2 distribution.

We make all of the fiducial, tracking, trigger verification, particle identification, and regenerator cuts exactly the same as for the $K \to \pi^+\pi^-$ analysis. We make the same decay vertex and energy cuts, but *invert* the $\pi^+\pi^-$ mass and p_T^2 cuts to remove $K \to \pi^+\pi^-$ background. The resulting Λ sample was displayed in Figure 27.

6.5 Background Subtraction

The modes of concern are non-coherent $K \to \pi^+\pi^-$ and $K \to \pi^\pm e^\mp \nu_e$. We also give a discussion of how the radiative decay $K \to \pi^+\pi^-\gamma$ is handled.

6.5.1 Structure of Data in Mass and p_T^2

The key quantity for studying backgrounds is p_T^2. The coherent forward peak which forms our signal is very sharp; essentially the entire width is due to detector effects, and the signal is well-contained within the cut region extending from 0 to 250 MeV/c^2. The total background can be estimated by fitting the p_T^2 distributions near the peak, and extrapolating under it. The results of such fits are shown in Figure 40. The background is quite small, 0.2% (0.6%) for the UR (DR) beam. In spite of their small size, the backgrounds need to be treated carefully due to the fact that their z dependence is very different from the signal. In particular, the $K \to \pi^\pm e^\mp \nu_e$ decay rate is flat in z, and the relative amount of background is higher downstream. The non-coherent $K \to \pi^+\pi^-$ are dominated by single diffraction, which has z distribution with both K_S and K_L components, but with a distinctly different

structure that the coherent signal. This is due to a different amount of K_S regeneration and an opposite sign of the interference for diffraction versus transmission (see Appendix F).

6.5.2 Treatment of $K \to \pi^+\pi^-\gamma$

A few comments on $K \to \pi^+\pi^-\gamma$ decays are in order. No attempt is made to separate $K \to \pi^+\pi^-\gamma$ events from the $K \to \pi^+\pi^-$ sample; events with sufficiently soft photons will pass our analysis cuts, including the mass and p_T^2 requirements. The radiative decay has two main components: inner bremsstrahlung (IB) from both K_S and K_L and direct emission (DE) from K_L[132].

The total DE rate is 1.6% of the $K_L \to \pi^+\pi^-$ rate. The DE has a hard photon spectrum which varies as $(E_\gamma^*)^3$ for small E_γ^* and is then cut off by phase space. A typical photon center-of-mass energy, E_γ^*, is of order 100 MeV. As a result, only a negligible portion ($< 0.1\%$) of the direct emission has a low enough E_γ^* to pass our $\pi^+\pi^-$ mass and p_T^2 cuts, and we thus ignore them.

The size of the IB contribution with any E_γ^* cutoff is easily determined using the measured branching ratio at a given cutoff to set the scale and the known matrix element to determine the shape as a function of E_γ^*. With a 15 MeV E_γ^* cut, the IB is $\sim 0.9\%$ of the $K \to \pi^+\pi^-$ rate (the fraction is the same for K_L and K_S), and the spectrum varies as $1/E_\gamma^*$ in the limit of soft photons. To pass our cuts, E_γ^* must typically be less than 15 MeV. Therefore, there is a component of $K \to \pi^+\pi^-\gamma$ in our data. The IB process is a trivial modification of $K \to \pi^+\pi^-$ decay, and one expects the CP characteristics of the decay to be identical with those of the $\pi^+\pi^-$ final state. This has been the study of some recent investigations [133, 150, 151]. Our analysis does not distinguish the low-E_γ^* $\pi^+\pi^-\gamma$ events from the $\pi^+\pi^-$and we actually measure the combination. We do not treat the $\pi^+\pi^-\gamma$ as a background, but generate IB concurrently with $\pi^+\pi^-$ events in our Monte Carlo.

6.5.3 Non-coherent $K \to \pi^+\pi^-$ Background

We now discuss the non-coherent $\pi^+\pi^-$ background, which comes from two distinct sources. The diffractive component consists of kaons that are scattered elasticly (perhaps more than once) in the regenerators. In addition, there is an inelastic component, where the kaon has scattered inelasticly in the regenerator. Diffraction has a p_T^2 distribution characteristic of the size of the entire nucleus, whereas inelastics have a distribution characterized by the size of a single nucleon. Both are roughly distributed according to $exp\,(-bp_T^2)$, with $b \sim 60$ for single diffraction off carbon and $b \sim 5$ for diffraction off hydrogen and all inelastics. Multiple-diffraction with n scatters results in a slope equal to b/n. More details concerning diffraction are presented in Chapter 7 and Appendix F. The size of the non-coherent background relative to the signal is illustrated in Figure 41.

6.5.4 $K \to \pi^\pm e^\mp \nu_e$ Background

The $K \to \pi^\pm e^\mp \nu_e$ background has an intrinsic p_T^2 distribution due to the undetected neutrino in addition to the effects from kaon scattering. The maximum neutrino p_T^2 is $\sim 40{,}000$ MeV$^2/c^2$. To subtract the $K \to \pi^\pm e^\mp \nu_e$ background, we pass a Monte-Carlo sample of $K \to \pi^\pm e^\mp \nu_e$ decays thorough the full $\pi^+\pi^-$ analysis, but with the E/p cut inverted (i.e., requiring the maximum $E/p > 0.8$). The analyzed $K \to \pi^\pm e^\mp \nu_e$ sample is then normalized to the mass sidebands in a region of p_T^2 away from the coherent peak, where the $K \to \pi^\pm e^\mp \nu_e$ fraction is high. The procedure and results are illustrated in Figure 42. The disagreement on the falling edge of Plots c) and d) is due to the lack of δ-rays in the Monte-Carlo. The disagreement on the right side of Plot f) is due to K decays resulting from the Primakoff production of the K^*. The improvement obtained in data-Monte Carlo comparisons by adding in a small component of $K \to \pi^\pm e^\mp \nu_e$ decays is quite good. The size of the $K \to \pi^\pm e^\mp \nu_e$ background relative to the signal is illustrated in Figure 41.

Table 11. Size of the final charged-mode event samples.

Sample	UR Set 1	DR Set 1	UR Set 2	DR Set 2
$K \to \pi^+\pi^-$	333,272	70,707	573,241	152,870
$K \to \pi^\pm e^\mp \nu_e$	2,770,185	1,359,957	7,328,783	4,681,086

6.6 Summary

We have now completed our description of the $K \to \pi^+\pi^-$ signal analysis. Table 11 shows the size of the event samples available for charged-mode analysis and studies. The $K \to \pi^+\pi^-$ numbers are background-subtracted. In the next chapter, we discuss the Monte Carlo used to obtain the acceptance necessary to extract the physics.

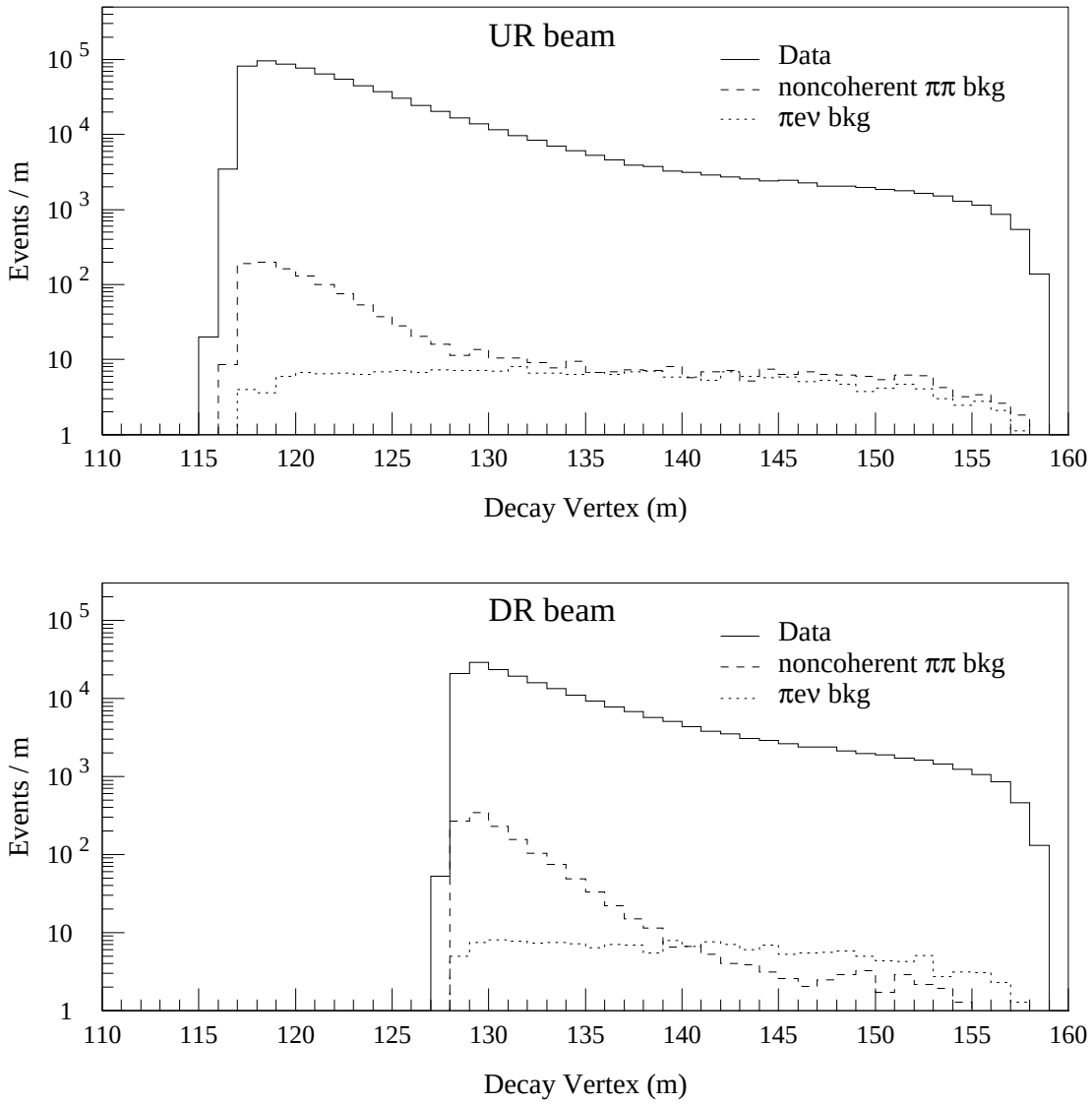

Figure 41. The observed $K \to \pi^+\pi^-$ signal and the calculated backgrounds (bkg). Note the shape differences between all three distributions.

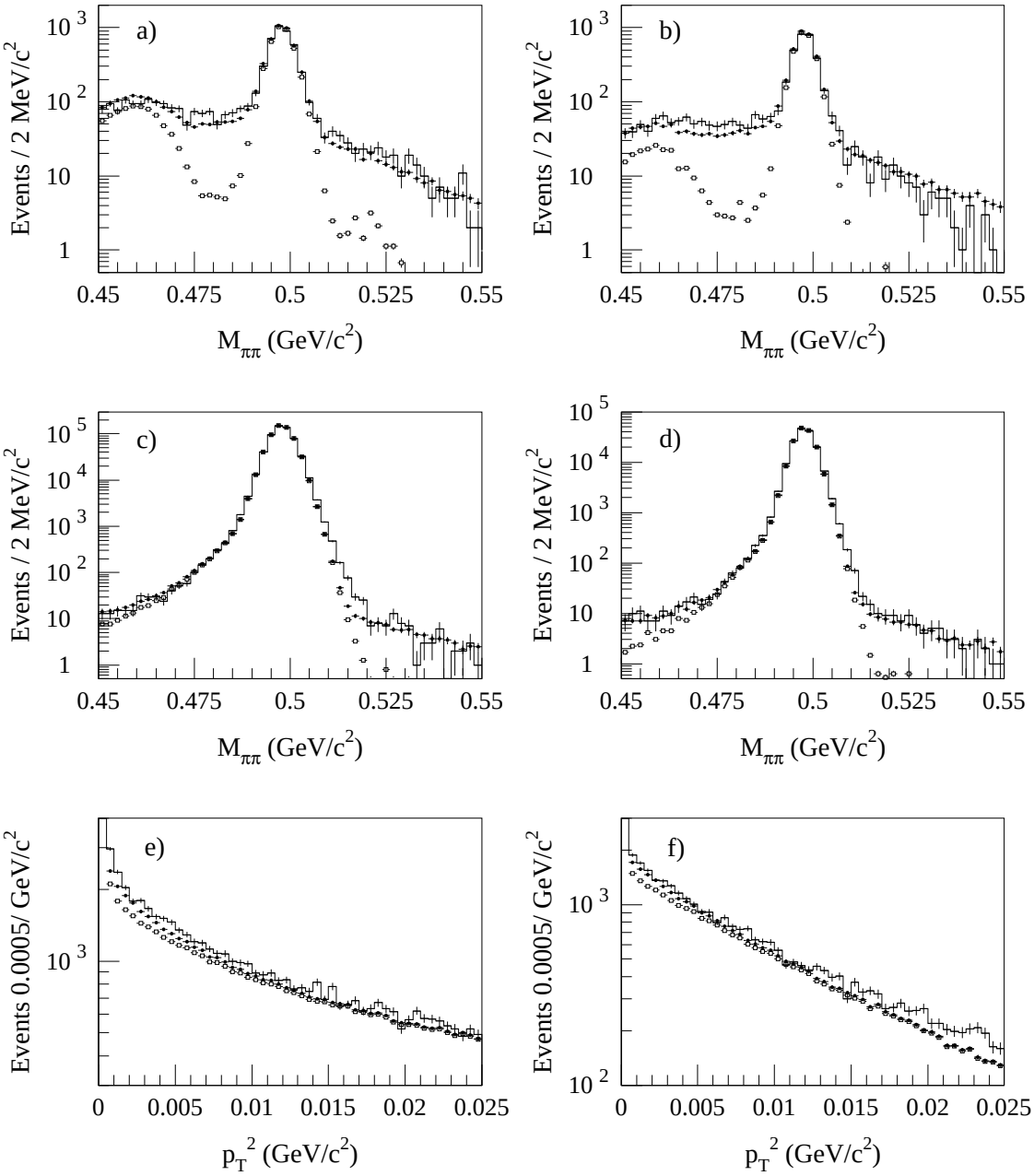

Figure 42. Plots illustrating the treatment of the $K \to \pi^{\pm} e^{\mp} \nu_e$ background. Plots a) and b) show the $M_{\pi\pi}$ distribution for events with p_T^2 between 1000 MeV$^2/c^2$and 2000 MeV$^2/c^2$. Plots c) and d) show the $M_{\pi\pi}$ distribution for events in the coherent peak. Plots e) and f) show the p_T^2 for events with a good kaon mass. In all plots, the histogram is data, the open circles are $\pi^+\pi^-$ Monte Carlo, and the closed circles are $\pi^+\pi^-$ Monte Carlo plus $K \to \pi^{\pm} e^{\mp} \nu_e$ Monte Carlo. All data is from Data Set 2 and all standard analysis cuts not mentioned explicitly have been applied.

CHAPTER 7

THE MONTE CARLO

This chapter describes the Monte Carlo (MC) simulation of our experiment. The MC serves two purposes. First, by comparing the data with MC generated based on our understanding of the detector, we gain confidence in our calibration and analysis. Second, the MC is necessary so that we may acceptance correct the data to obtain the true decay rate, from which we will ultimately extract the physics.

7.1 Philosophy

The Monte-Carlo calculation of the acceptance is central to our experimental technique. We define the acceptance as the ratio of the following two quantities:

- The number of coherent kaon decays reconstructed in a given p-z bin.
- The number of coherent kaon decays generated in the same p-z bin.

This is not the only possible choice for a definition of acceptance, but it is the most reasonable. The important point is to be consistent in the definition and usage of this quantity. With this choice, we must treat non-coherent kaons as background in the data, and subtract them before applying the acceptance correction to get the true rate.

We generate events with the same distribution in data run number (i.e., time) as the actual data. The Monte Carlo then makes use of the same calibration files determined from the data. For example, the chamber positions and orientations are read in from the

Table 12. Values of parameters describing the kaon production spectrum.

Particle	A	B	D	M^2 $(\mathrm{GeV}/c^2)^2$
K^+	2.924	14.15	19.89	1.164
K^-	6.107	12.33	17.78	1.098

calibration file corresponding to the run being simulated.

Except for a few small exceptions, the Monte-Carlo events are treated exactly as the data during reconstruction and analysis. Some examples of the small differences are given below.

7.2 Kaon Beam Simulation

We now describe how we simulate the properties of the kaon beams that strike the regenerators. We need the flux of kaons as a function of energy, transverse position, and direction. We also take care to retain the correct superposition of K_S and K_L as the kaon evolves after production.

7.2.1 Production Spectrum

The first step is to parametrize the kaon production spectrum obtained in proton-Beryllium collisions. Our starting point is the Malensek parameterization [152] of the Atherton, *et al.* data [153] for K^+ and K^- production on Beryllium by 400 GeV/c protons:

$$\frac{d^2N}{dp\,d\Omega} = \frac{E_B}{400\ \mathrm{GeV}/c}\,B\,x\,\frac{(1-x)^A(1+5e^{-Dx})}{(1+p_t^2/M^2)^4}. \tag{7.1}$$

Here, x is the ratio of the kaon momentum, p, to the incident proton momentum, E_B. A, B, C and M^2 are constants fit to the data; a different set is used for K^+ and K^-. The values obtained by Malensek are given in Table 12.

We relate K^0 and $\bar{K}^0$ production to K^+ and K^- according to

$$N_{K^0} = (N_{K^+} + N_{K^-})/2 \tag{7.2}$$

$$N_{\bar{K}^0} = N_{K^-} \tag{7.3}$$

These relations are motivated by quark-counting arguments, and are discussed further in Appendix B. The Malensek parameterization is based on general behaviors of hadronic production observed in many other experiments, such that the extrapolation to our experimental conditions is well-motivated. However, the original data was sparse, and we can expect only general agreement and will thus need to correct the formula somewhat. We adopt the correction obtained by E731 [140] via a study of $K_L \to \pi^+\pi^-$ decays. The correction function is

$$1 + a_1 p + a_2 p^2 + a_3 p^3 + a_4 p^4 \tag{7.4}$$

where

$$a_1 = 6.03315 \times 10^{-3} \tag{7.5}$$

$$a_2 = -4.28304 \times 10^{-6} \tag{7.6}$$

$$a_3 = -1.01624 \times 10^{-7} \tag{7.7}$$

$$a_4 = 1.80224 \times 10^{-10}. \tag{7.8}$$

This is used a a multiplicative correction to the Malensek parameterization. Only the dependence of the flux on kaon energy is changed; the correction is assumed to be the same for K^0 and $\bar{K}^0$. In principle, the K^0 and $\bar{K}^0$ may be affected differently, and the angular dependence of production may differ from the Malensek form. Fortunately, we have almost no sensitivity to such changes. The beams striking the regenerators are almost purely K_L beams and the K_L flux is proportional to the *sum* of K^0 and $\bar{K}^0$ production. These issues are discussed further in Appendix B. We also float small corrections to the spectrum in our fitting procedure, as discussed in Chapter 8.

7.2.2 Kaon Propagation

We next discuss how kaons are propagated along the beamline. We first discuss the treatment of kaons which are not scattered away from the exact forward direction; we do include effects of coherent forward regeneration in this discussion, however.

The decay of the states as they propagate, as well as any absorption and transmission regeneration in material, are easily treated with a transfer-matrix method. In the K_L-K_S

basis, we have

$$\begin{pmatrix} a'_S \\ a'_L \end{pmatrix} = \begin{pmatrix} T_{SS} & T_{SL} \\ T_{LS} & T_{LL} \end{pmatrix} \begin{pmatrix} a_S \\ a_L \end{pmatrix}. \tag{7.9}$$

where the initial state characterized by the amplitudes a_S and a_L is transformed into the final state characterized by the amplitudes a'_S and a'_L. The transfer matrix, T, is diagonal for vacuum propagation; in the presence of material, the off-diagonal elements are non-zero, and describe regeneration. Such a matrix may be used to describe the evolution through any fixed arrangement of material; the matrix will be energy-dependent. The construction of transfer matrices is discussed in more detail in Appendix F.

7.2.3 Propagation Through the Collimation System

Most of the flight path of the kaons from the target to the regenerator is in vacuum, with a short distance of air at the outset. There are three major exceptions to this which must be accounted for. These are the production target, the beam absorbers, and the edges of the collimators.

After the kaon is produced, it must exit the remainder of the target. Since the beam spot is smaller than the target, as is the target length times the production angle, the bulk of the kaons traverse the target fully (as opposed to exiting the side). Absorption of the primary proton is included when choosing the z of production. The absorption and transmission regeneration of the exiting kaon are treated with the transfer matrix described earlier. No finite-angle scattering is included; since there is no lever arm, the only effect of such scattering is a blurring of the production spectrum. Since we adjust the production spectrum to match the data, we can effectively treat this smearing as part of the production itself.

The absorption and transmission regeneration in the common and movable absorbers are treated with the transfer matrix technique. In addition, the absorbers also cause a large amount of elastic scattering. This scattering is very forward-peaked, and many of the scattered particles remain in the beam. The forward elastic scattering cross-section behaves as $d\sigma/dq^2 \sim exp(-bq^2)$, where q^2 is the momentum transfer ($q^2 \simeq p_T^2$ for small angles) and b is the forward slope, which is largely independent of momentum. Since the

Table 13. Values of parameters describing beam scattering in absorbers.

Material	Probability of Single Elastic Scattering	Slope $[(\mathrm{GeV}/c)^{-2}]$
Common Abs. Pb	0.178	-420
Common Abs. Be	0.086	-65
Movable Abs. Be	0.078	-65

mean p_T^2 of scattering is roughly constant with energy, the mean *angle* of scattering *varies* with kaon energy. This causes the fraction of the events staying within the beam to be energy-dependent, and hence affects the kaon spectrum seen at the regenerators. The parameters used are given in Table 13; the numbers are taken from charged-kaon scattering data in Ref. [154]. The probability of a single diffractive scatter relative to such a scatter or transmission is simply $\alpha X/(1+\alpha X)$, where X is the total number of interaction lengths, and $\alpha = \sigma_{el}/\sigma_{tot}$, the ratio of elastic to total cross-sections. We simulate only single elastic scatters of $K_L \to K_L$ and $K_S \to K_S$; double elastic scatters are less frequent by an order of magnitude. We also ignore inelastic interactions.

The final complication arises from the edges of the collimator jaws. There are three regimes of interaction possible. Particles not hitting the jaws are simply evolved in vacuum. Particles which encounter the full length of the collimators, about 7 interaction lengths, are treated as completely absorbed. The remaining case involves particles at grazing incidence on the collimator faces; this occurs mostly due to imperfect alignment of the collimators. The amount of material to be traversed is calculated and converted into the number of kaon interaction lengths, X; the particles have one of three fates: a fraction e^{-X} of the particles are transmitted with no interaction, a fraction $\alpha X e^{-X}$ of them are elastic scattered once, and the remainder of the particles are treated as lost. We use a forward slope of $b = -145\ (\mathrm{GeV}/c)^{-2}$ and an elastic-to-total ratio of $\alpha = 26.8\%$ for the steel [154].

7.2.4 Kaon Beam Collimation

At the end of E773, a detailed survey of the collimators was performed. These positions provide an excellent starting point for the Monte Carlo simulation of our kaon beam. As explained in Chapter 5, the target can be located in the detector coordinate system quite easily. Unfortunately, the construction of the target pile and dump makes precise surveying of the target relative to the collimation elements very difficult. As a result, small adjustments must be made by comparing data and Monte Carlo beam profiles.

Using fully-reconstructible events, such as $K \to \pi^+\pi^-$, one can determine the beam profiles by projecting unscattered events. One can also do quite well with $K \to \pi^\pm e^\mp \nu_e$ decays by looking at the distribution in angle of a line connecting the target to the decay vertex. However, with no vacuum beam available in E773, there are always large tails in the profiles from events where the kaon scatters in the regenerators.

For some elements, there was a noticeable tilt in the collimator edges; thus there was a region where kaons saw only part of the full collimator length. This was due to reliance upon external fiducial marks to adjust the collimator jaws, which were enclosed in a vacuum pipe. The end-of-run survey measured the actual jaws and the observed tilts are used without tuning in our simulation. Such scattering occurs further upstream than the regenerator scattering and is distinguishable by the wider spread in the beam profile tails. A comparison of the data and Monte-Carlo target-to-decay-vertex angles for $K \to \pi^\pm e^\mp \nu_e$ decays is shown in Figure 43; the scattering tails are reproduced quite nicely.

The collimator geometry was tuned independently in three data periods to allow for small time variations in the positions. Originally, the geometry was done separately for Data Set 1 and Data Set 2. Later, Data Set 2 was split into two pieces due to an apparent settling of the floor near the calorimeter. Since the coordinates are tied to the target and calorimeter, such a settling causes an apparent motion of the collimation elements. The motion is small and is coincident with the movement of a heavy new detector into the beamline area in preparation for E799. A comparison of the data and Monte-Carlo beam shapes from $K \to \pi^+\pi^-$ events is shown in Figure 44.

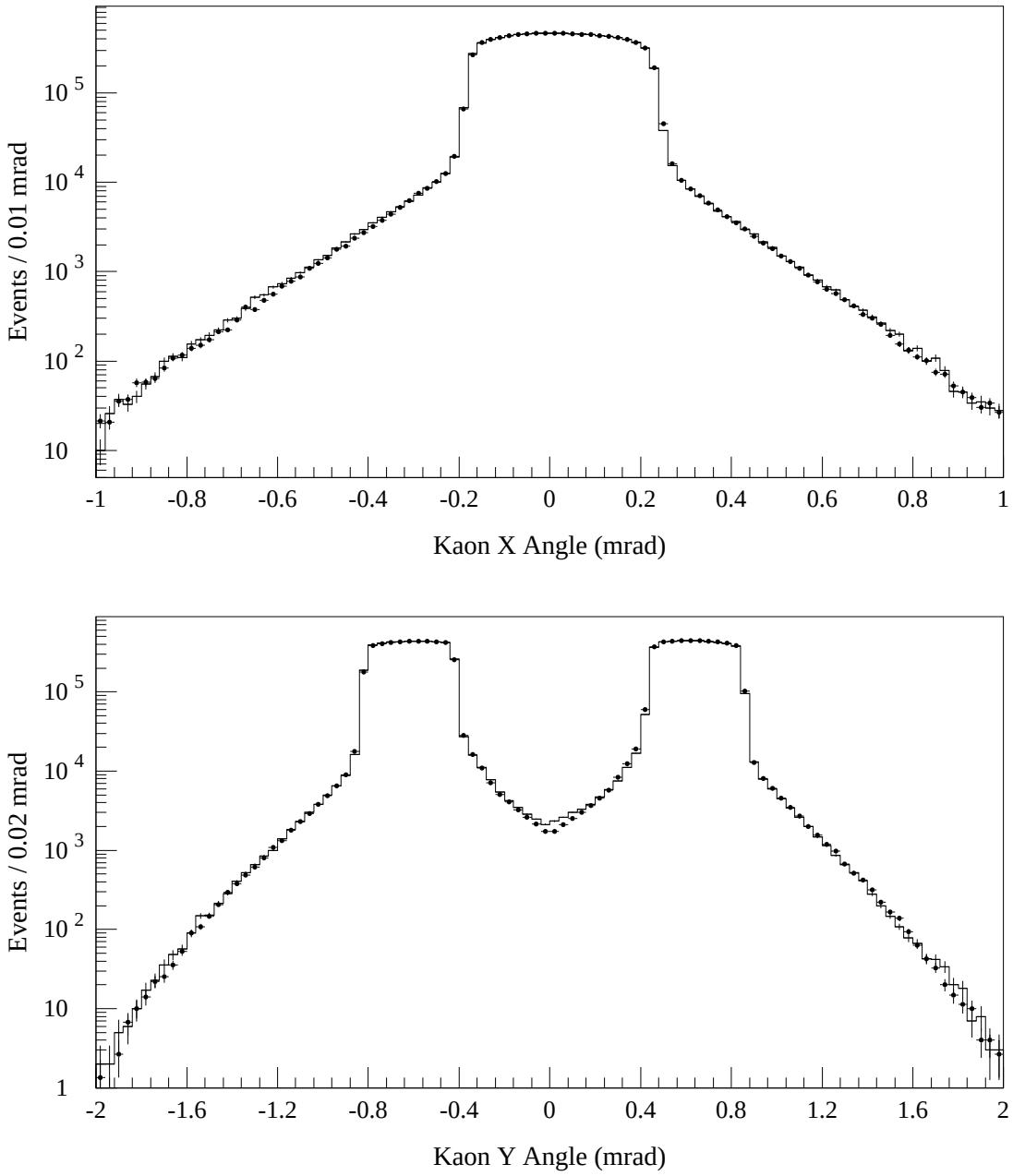

Figure 43. The x and y angles of the apparent kaon direction in $K \to \pi^{\pm} e^{\mp} \nu_e$ decays for the UR beam in Data Set 2. The histograms are data and the dots are Monte-Carlo.

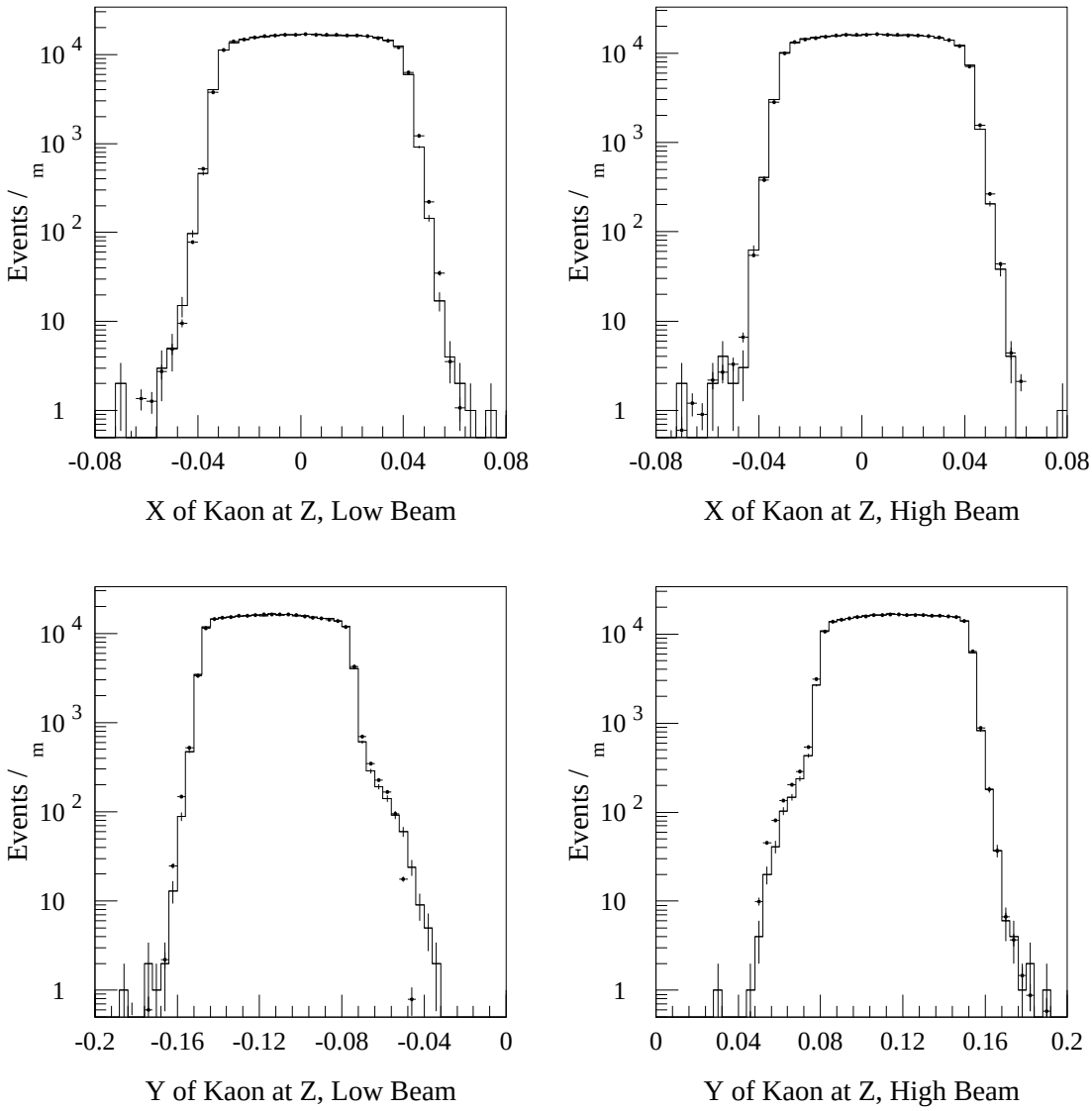

Figure 44. The x and y projections of the kaon at the z of the calorimeter, from $K \to \pi^+\pi^-$ events in Data Set 2. The histograms are data and the dots are Monte-Carlo.

7.3 Kaon Propagation through the Regenerators

We next discuss the simulation of kaon interactions in the regenerators. The upstream regenerator is treated as a solid block of scintillator with an effective length that includes the contribution from the materials used to wrap the blocks. The downstream regenerator is treated as 12 identical units with 11 uniform gaps. The units have an effective length which includes the wrapping. Details of the materials in the regenerators and their properties are given in Appendix G. We note here that the wrappings are a 3% correction to the amount of material for the DR and much smaller for the partially-instrumented UR.

The treatment of backgrounds from the non-coherent kaons is crucial to the neutral-mode analysis. There, the background is much higher since the p_T^2 cannot be directly measured and cut on. The detailed Monte-Carlo treatment of non-coherent events was motivated by the need to understand this background. The details of the neutral-mode background analysis are presented in Ref. [141]. We have also used the Monte Carlo to correct for background in our $K \to \pi^+\pi^-$ analysis, and thus describe the simulation here also.

The p_T^2 dependence of scattering is approximated by an exponential, $exp\,(-bp_T^2)$ for each particular scattering process. The slopes employed are given in Table 14. The hydrogen diffractive slopes are taken from the literature; the others are fit to the data.

For diffraction, we distinguish regenerative from non-regenerative scattering. We treat single scattering from carbon and hydrogen, and double scattering where as least one scatter is from carbon. Triple scattering is a small correction and is ignored. We use the same diffractive slope parameters for the UR and DR. The ratio of carbon to hydrogen scattering is taken from the known forward scattering amplitudes. The normalization of the diffractive to coherent events for the UR and DR are separately determined from the data. The normalizations determined from the data are consistent with the expectations calculated from first principles, given the approximations used. The ratio of single to double scattering is approximately that given by the theory, but is adjusted slightly to match the data; the need for this tuning is not surprising, since we have neglected higher-order scatterings.

The key difference with respect to coherent forward regeneration is that regeneration

Table 14. Values of the forward slope parameters describing regenerator scattering. A represents any nucleus.

Scattering	Slope $(\mathrm{GeV}/c)^{-2}$
Diffraction	
$K_L C \to K_L C$	-58
$K_L C \to K_S C$	-90
$K_L H \to K_L H$	-6
$K_L H \to K_S H$	-8
Inelastic	
$K_L A \to K_S X$ (UR)	-4.9
$K_L A \to K_S X$ (DR)	-6.0

may occur during the finite-angle scattering itself as well as due to the forward propagation before and after scattering. A proper accounting of this shows that the effective regeneration at finite angle, for single scattering and for our relatively short regenerators, is larger than and opposite in phase to the regeneration in the exact forward direction. This leads to dramatic differences in the z distribution of such events as compared to the coherent events in the signal. Thus, despite the small size of the background, it still must be properly accounted for in a precise measurement. Further details of the interesting physics involved in diffraction are provided in Appendix F.

The inelastic slopes are naively expected to be of the order of the kaon-nucleon slopes, since an inelastic process is basically an interaction with a single nucleon in a nucleus. However, the slopes are also affected by the particular vetoes employed by the regenerators, and they also absorb some the effects of other approximations. For these reasons, the empirically-determined values are different for the UR and DR. We observe no evidence of K_L in the inelastic region; the data are consistent with a pure K_S exponential decay. Although inelastic K_L must exist in principle, the amount is quite small and hence we have ignored such a term. The normalizations of the inelastics for the UR and DR are determined from the data.

7.4 Decays and Kinematics

The $K \to \pi^+\pi^-$ decay is trivial; the decay axis is randomly chosen in the kaon center-of-mass.

The inner-bremsstrahlung portion of the $K \to \pi^+\pi^-\gamma$ decay is simulated concurrently with $K \to \pi^+\pi^-$ decays. We generate events where photons have a center-of-mass energy of 1 MeV and greater. The branching ratio has been well-measured [132]. Integrating the decay rate, we find that the rate of inner-bremsstrahlung with a photon of energy greater than 1 MeV is 3% of the $\pi^+\pi^-$ decay rate. The matrix element is

$$\frac{p_+ \cdot \epsilon}{p_+ \cdot k} - \frac{p_- \cdot \epsilon}{p_- \cdot k} - \tag{7.10}$$

where $p_\pm$ and k are the $\pi^\pm$ and γ four-momenta, and ϵ is the photon polarization.

The decay $K \to \pi^\pm e^\mp \nu_e$ kinematics are described by the usual structure function for the hadronic current [39],

$$f_+(q^2) = f_+(0) \left[1 + \lambda_+ \left(q^2/m_\pi^2 \right) \right] \tag{7.11}$$

where q is the momentum transfer to to the leptons. We use $\lambda_+ = 0.030$ [39].

Finally, the decay $\pi \to \mu\nu$ is simulated as each π is traced through the detector.

7.5 Tracing of Decay Products

Multiple scattering of charged particles in material is included in simulation. A list of the thicknesses of the relevant detector components is shown in Table 15. We note that the vacuum window radiation length used is actually too large; the packing fraction of 56% for the Kevlar weave was inadvertently ignored. The correct value is 1.6×10^{-3}. The packing fraction was correctly used when treating the regeneration due to the windows, however. The drift chamber wires are approximated as square in cross section, with the size fixed to give the correct total material. A mean probability of hitting a wire is used, independent of particle trajectory.

The rms multiple scattering angle used is

$$\theta_{rms} = (14.1/p)\sqrt{X_r} \ [\ 1 + (log_{10} X_r)/9 \ ] \tag{7.12}$$

Table 15. Thickness of sources of scattering in radiation lengths. Air near the vacuum windows (not listed) is also included.

Detector Element	Location (m from Target)	Thickness X_r (Radiation Lengths)
Vacuum Window	117.330	2.50×10^{-3}
Vacuum Window	127.641	2.50×10^{-3}
Vacuum Window	128.623	2.50×10^{-3}
V hodoscope	140.913	3.32×10^{-3}
T hodoscope	140.936	3.30×10^{-3}
Vacuum Window	158.946	2.50×10^{-3}
Drift Chamber 1	159.287	4.31×10^{-3}
Drift Chamber 2	165.861	4.49×10^{-3}
Drift Chamber 3	171.856	4.20×10^{-3}
Drift Chamber 4	176.197	2.34×10^{-3}
Chamber Field Wires[a]	—	5.70×10^{-3}
Chamber Sense Wires[b]	—	6.43×10^{-3}
C Hodoscope	179.502	4.0×10^{-2}
B Hodoscope	179.520	4.0×10^{-2}

[a]This is the average material seen by the 9.9% of tracks, per chamber, which hit a field wire.
[b]This is the average material seen by the 0.7% of tracks, per chamber, which hit a sense wire.

where θ_{rms} is in mrad and p is in GeV/c. X_r is the thickness of the material in radiation lengths. A non-Gaussian tail due to hard scattering is also added; the final distribution is shown in Figure 45.

Bremsstrahlung from electrons and photon conversions were also included. These effects utilized the same data listed in Table 15. A realistic bremsstrahlung energy spectrum was used; the photons generated were taken to be collinear with the electrons. Conversions were allowed for all photons with energy greater than 0.1 GeV. The electron and positron energies were chosen according to the Bethe-Heitler spectrum; no opening angle was used between the tracks.

A particle is considered lost if it leaves the active detector volume; this generally con-

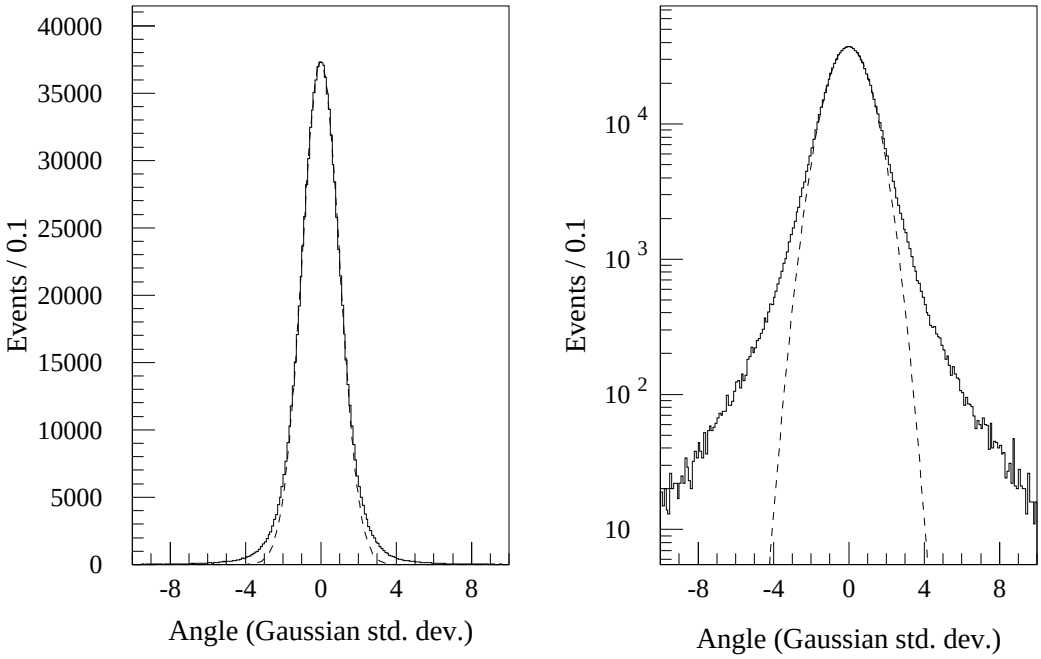

Figure 45. The distribution of the multiple scattering angle used in the Monte-Carlo simulation. The angle is normalized to the RMS scattering angle in the Gaussian approximation. The dashed line shows a normal Gaussian for comparison. Both figures show the same curves; the scales are changed for clarity.

sists of striking outside the aperture of one of the photon vetoes or the drift chambers. They were lost from upstream decays if they hit the DR scintillator and when they extrapolated outside of the large vacuum window. If either of the charged decay products from $K \to \pi^+\pi^-$, $K \to \pi^+\pi^-\gamma$, or $K \to \pi^\pm e^\mp \nu_e$ decay is lost in tracing, the generation of that event is terminated. The photon from inner-bremsstrahlung in $K \to \pi^+\pi^-\gamma$ as well as any externally radiated photons, and e^+e^- pairs from their conversion, were allowed to be lost without terminating generation. The chance of an accidental track replacing a lost track and successfully forming a good vertex and passing all other cuts, is negligible.

7.6 Digitization of Signals

We briefly describe some aspects of the conversion of the physical parameters of the events into detector signals recorded by the experiment.

7.6.1 Drift Chambers

For the z of each drift chamber plane a particle passed, the transverse position was noted. These positions were then smeared to account for chamber resolution, and the nearest wire was determined. The wire efficiencies are taken into account. The drift distance was converted to a drift time using the time-to-distance relation corresponding to the current plane and data run.

No attempt was made to simulate δ-rays in the MC. This leads to some inconsequential differences in the Monte-Carlo prediction of the mass and p_T^2 resolutions and those in the data. Wire sag and propagation times in the sense wires are not included in the simulation nor corrected for when analyzing MC.

7.6.2 Calorimeter

Hadronic showers from charged pions are not simulated. Instead, a fixed energy deposit of 0.7 GeV, corresponding to a minimum-ionizing particle is used. Thus, a cluster is potentially always available for matching to the track.

For electromagnetic particles, the energy is smeared according to a parameterization of the resolution function which includes a central Gaussian, and low- and high-side tails. The pattern of energy deposition in a 5×5 array of blocks centered on the struck block was determined with a library of EGS showers. The library includes showers of various energies and incident positions on the block face. The energies in each block are then converted to ADC counts, using the measured gains from the appropriate calibration, and a readout-threshold is applied.

No direct attempt is made to simulate pedestal shifts in the ADCs. For charged mode, the data is not sensitive to these small effects. For neutral mode, where such effects may

matter, one always overlays an accidental event with each MC-generated event. These accidentals contain pedestal shifts and thus add the proper effect back into the simulated events. The accidentals were not pedestal subtracted before readout, and therefore all blocks were read out. The same pedestals used for all other events in the given spill were subtracted in later data processing.

No attempt is made to simulate the temperature dependence observed in the data; for Monte-Carlo events, no correction is applied during reconstruction.

7.6.3 Miscellaneous

For each particle traversing the B and C banks, the hit counter, determined using the positions measured from special muon runs, is fired.

For the Mu2 bank, it was not necessary to simulate the particular counter hit. All such hits were from $\pi \rightarrow \mu$ decays in flight; it was sufficient to simulate the trigger veto only. The trigger latch was set if the muon projected to within the boundaries of the counter bank. A very rough treatment of μ scattering in the muon filter steel was implemented.

The latches of the photon veto scintillator detectors were set when particles traversed them. Energy was deposited in the lead-lucite portion of the vetoes. The energy deposits in the photon vetoes were not crucial, since the majority of the lead-lucite counters were not used in the trigger, and none was used in the off-line analysis of the charged triggers.

7.7 Comparisons with Data

We now display some comparisons of data and Monte Carlo events to demonstrate the accuracy of the Monte-Carlo simulation.

7.7.1 Track Illuminations and Separations

We begin by displaying the track illuminations at various z locations. Figure 46 shows the locations of tracks at the HDRA and the magnet bend plane for Data Set 1; Figure 47

is the analogous plot for Data Set 2. In Figure 48, we present the distribution of events versus track separation in both views at the first drift chamber.

7.7.2 Energy and Decay Vertex of $K \to \pi^+\pi^-$ decays

In Figure 49 (Figure 50), we show a comparison of the data and Monte-Carlo kaon energy distributions from the $K \to \pi^+\pi^-$ decay mode for Data Set 1 (Data Set 2). In Figure 51 (Figure 52), we show a comparison of the data and Monte-Carlo decay vertex distributions from the $K \to \pi^+\pi^-$ decay mode for Data Set 1 (Data Set 2).

7.7.3 Decay Vertex of $K \to \pi^\pm e^\mp \nu_e$ decays

Figures 53 and 54 show the agreement between data and Monte-Carlo decay vertex distributions for the $K \to \pi^\pm e^\mp \nu_e$ mode. Each plot gives the slope a a line fit to the data-to-MC ratio. We will see in Chapter 9 that we are sensitive to slopes at the 3×10^{-4}/m level; the $K \to \pi^\pm e^\mp \nu_e$ comparisons shown all agree somewhat better than this.

7.8 Accidental Activity

After generation and digitization of a kaon decay, the data could be combined ('overlayed') with that from an accidental event if desired. About 1% of the triggers written to tape were accidentals. This provides a large sample for use in overlays. For neutral-mode generation, accidentals were routinely overlayed. For charged-mode, the effect of accidentals was small, and overlays were done only for special studies.

Accidentals were chosen from the same run being simulated. The trigger bits in the accidental event were examined before the overlay was done. If any signals which were in veto for the trigger being used fired, the accidental was discarded and a new one was read in. This was done to speed up the generation process.

For the drift chambers, the two lists of valid hits were merged. Since the double-pulse resolution of the TDCs was 250 ns, which is longer than the time window for valid hits, the earlier hit was taken in cases were both the generated event and the accidental fired a

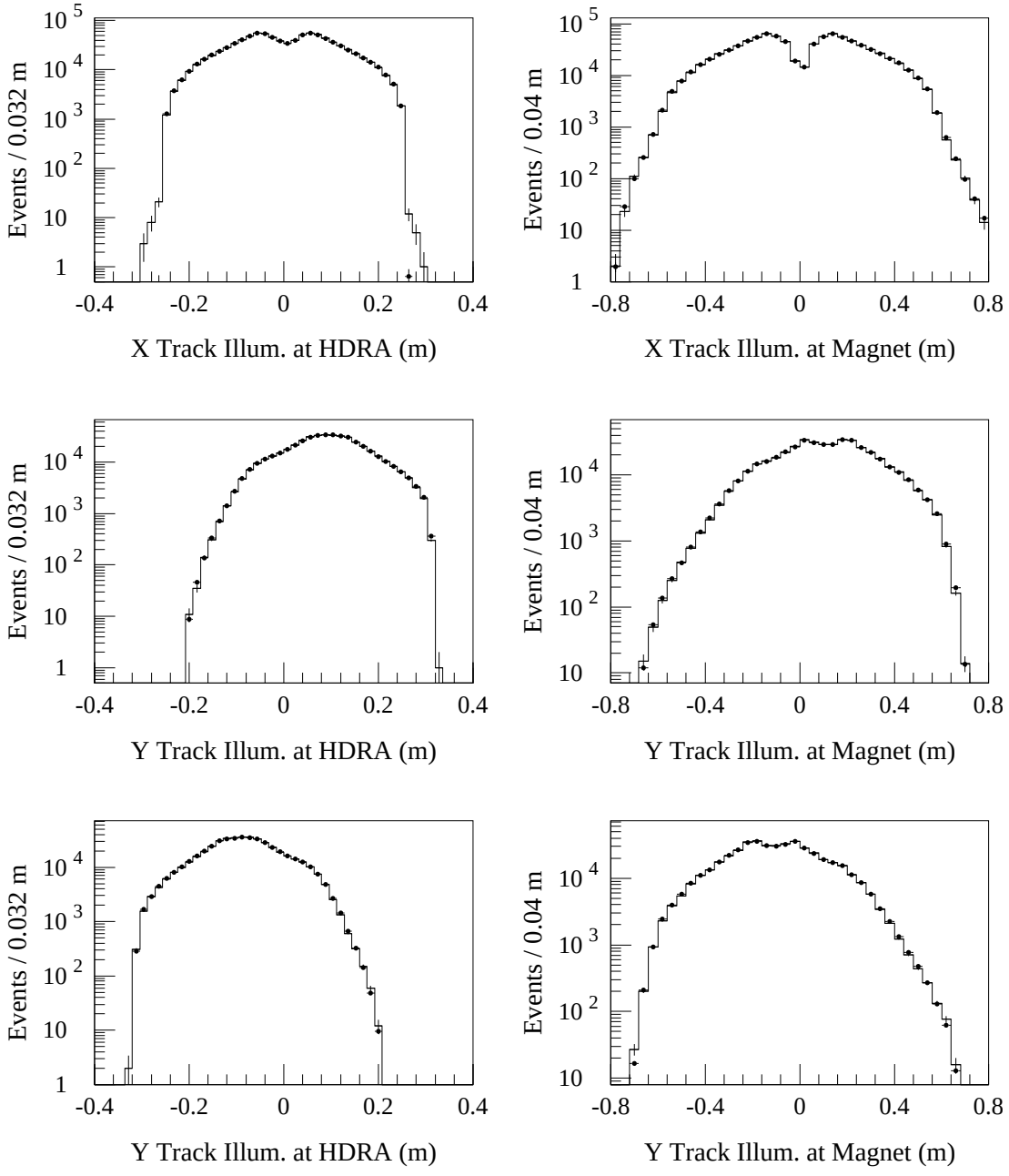

Figure 46. Track illuminations for $K \to \pi^+\pi^-$ from Data Set 1. The y plots are separated into high and low beams. The histograms are data and the dots are Monte Carlo.

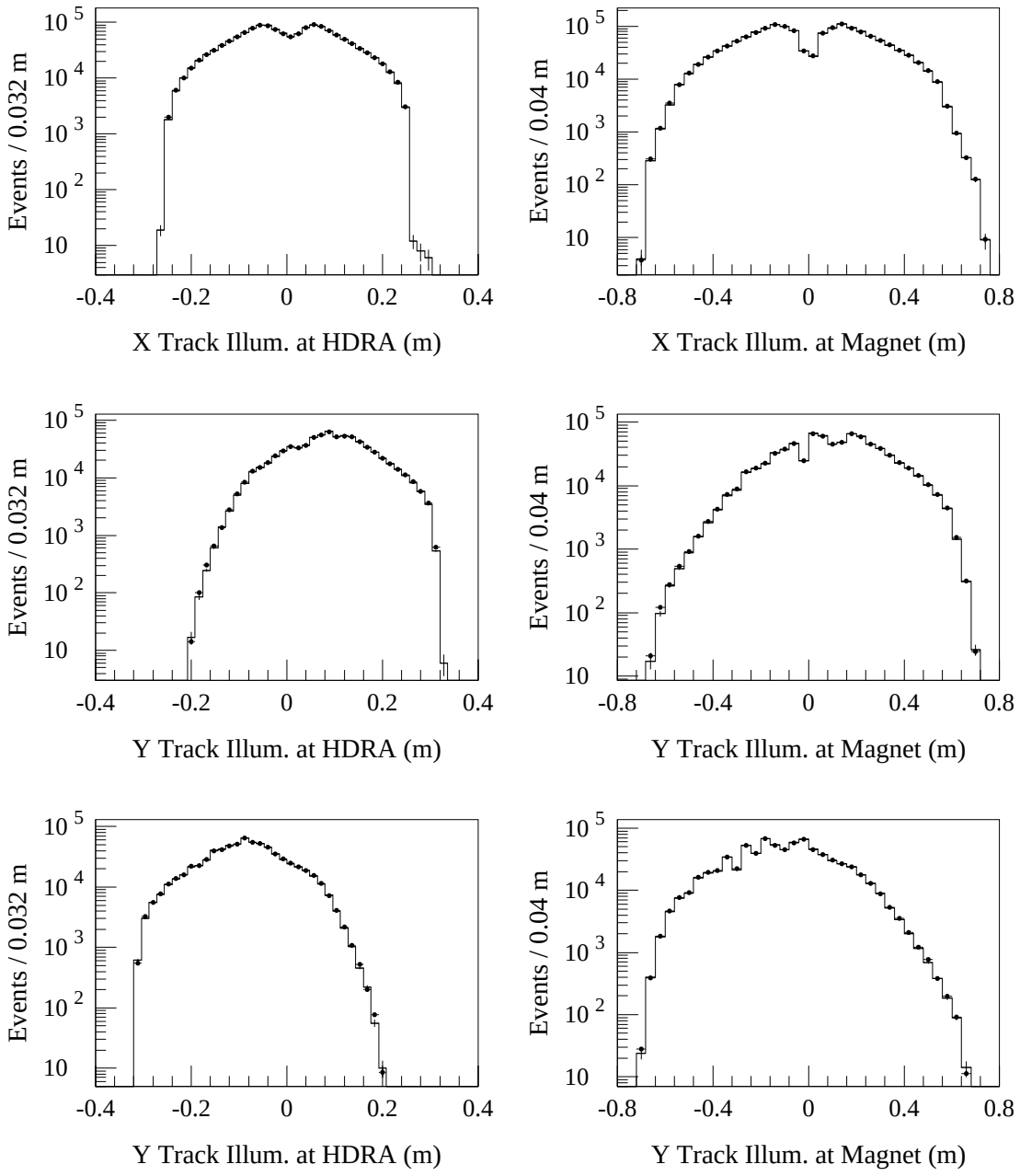

Figure 47. Track illuminations for $K \to \pi^+\pi^-$ from Data Set 2. The y plots are separated into high and low beams. The histograms are data and the dots are Monte Carlo.

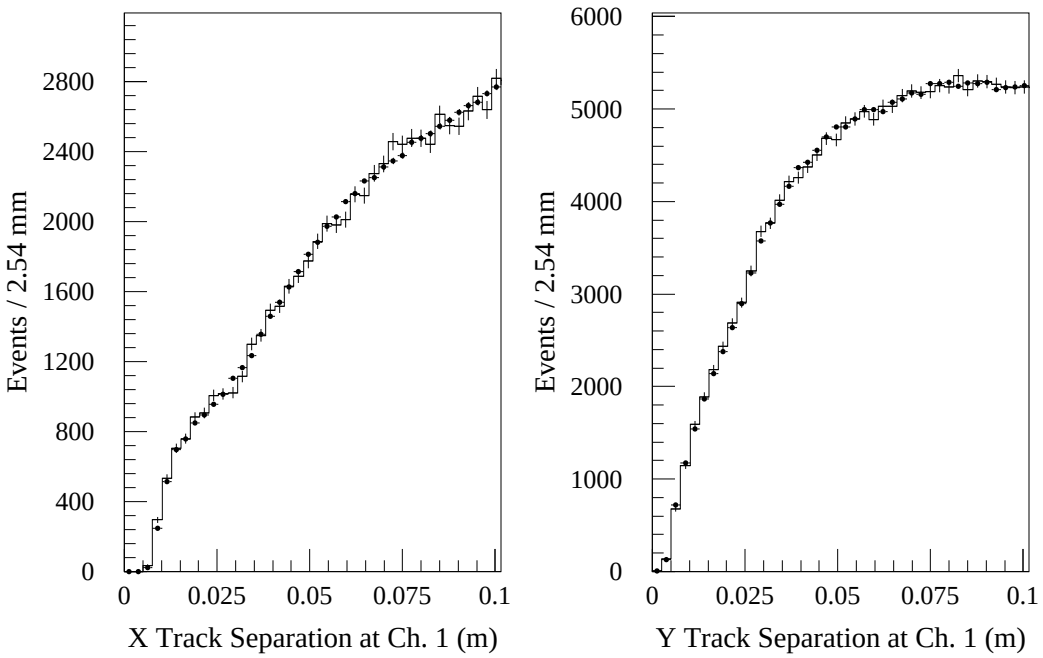

Figure 48. The track separations in the x and y views at the first drift chamber. Events from Data Set 2 are shown; the histograms are data and the dots are Monte Carlo.

given wire. This was done before the second level trigger was checked. Accidentals in the chambers are a possible source of bias. Losses due to inefficiencies caused by out-of-time hits are very small, and are already included (neglecting correlations) in the wire efficiencies used in digitization. More problematic is a possible sensitivity of the tracking algorithm to the presence of extra hits. Since we are extracting only the *shape* of the decay rate, only p and z dependent biases need worry us.

The counter latches were combined via a logical OR; This was done before the first level trigger was checked. Since trigger elements in veto were already checked, only the B and C hodoscope latches were important. We verify the trigger using only the two reconstructed tracks during the analysis, so no significant effects are expected.

For the lead glass and other ADCs, the number of counts above pedestal in the accidental event were added to the generated event. This was done prior to the application of the relevant readout thresholds. The only portion relevant to the charged analysis is the pattern of energy deposit in the calorimeter, since the clusters are used to match the x and y tracks.

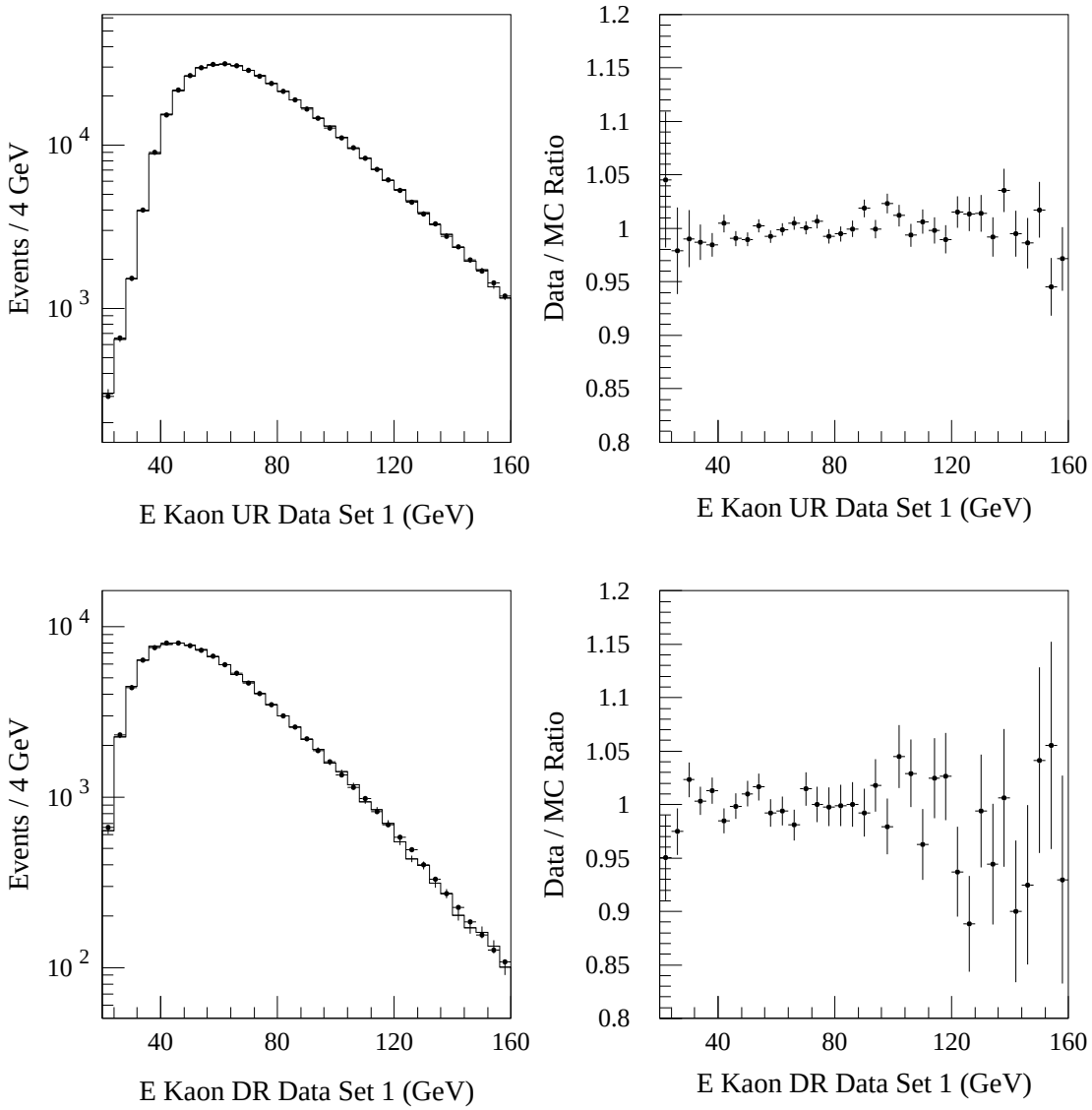

Figure 49. A comparison of the data and Monte-Carlo kaon energy distributions for $K \to \pi^+\pi^-$ decays from Data Set 1. The histograms are data and the dots are Monte Carlo.

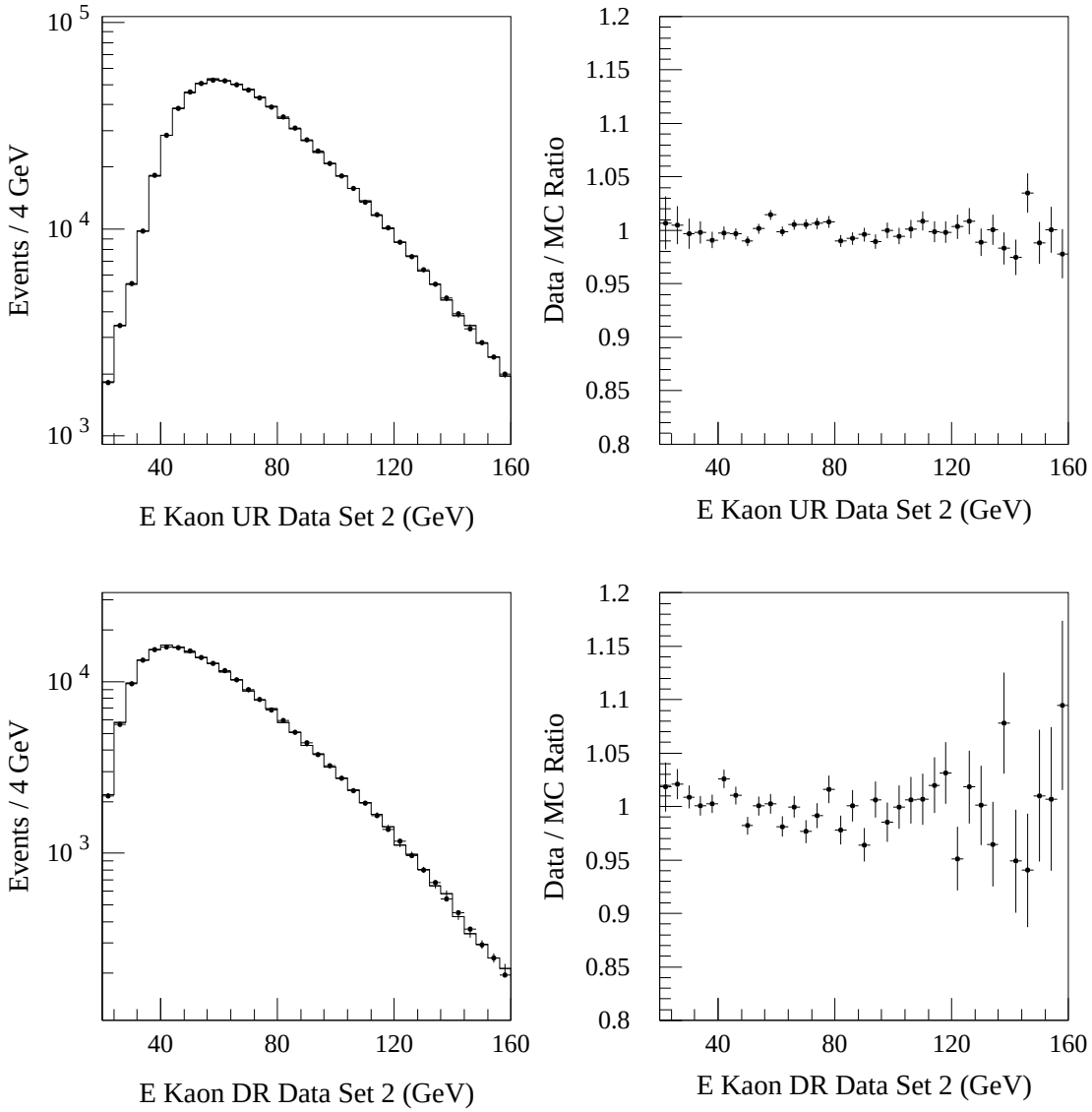

Figure 50. A comparison of the data and Monte-Carlo kaon energy distributions for $K \to \pi^+\pi^-$ decays from Data Set 2. The histograms are data and the dots are Monte Carlo.

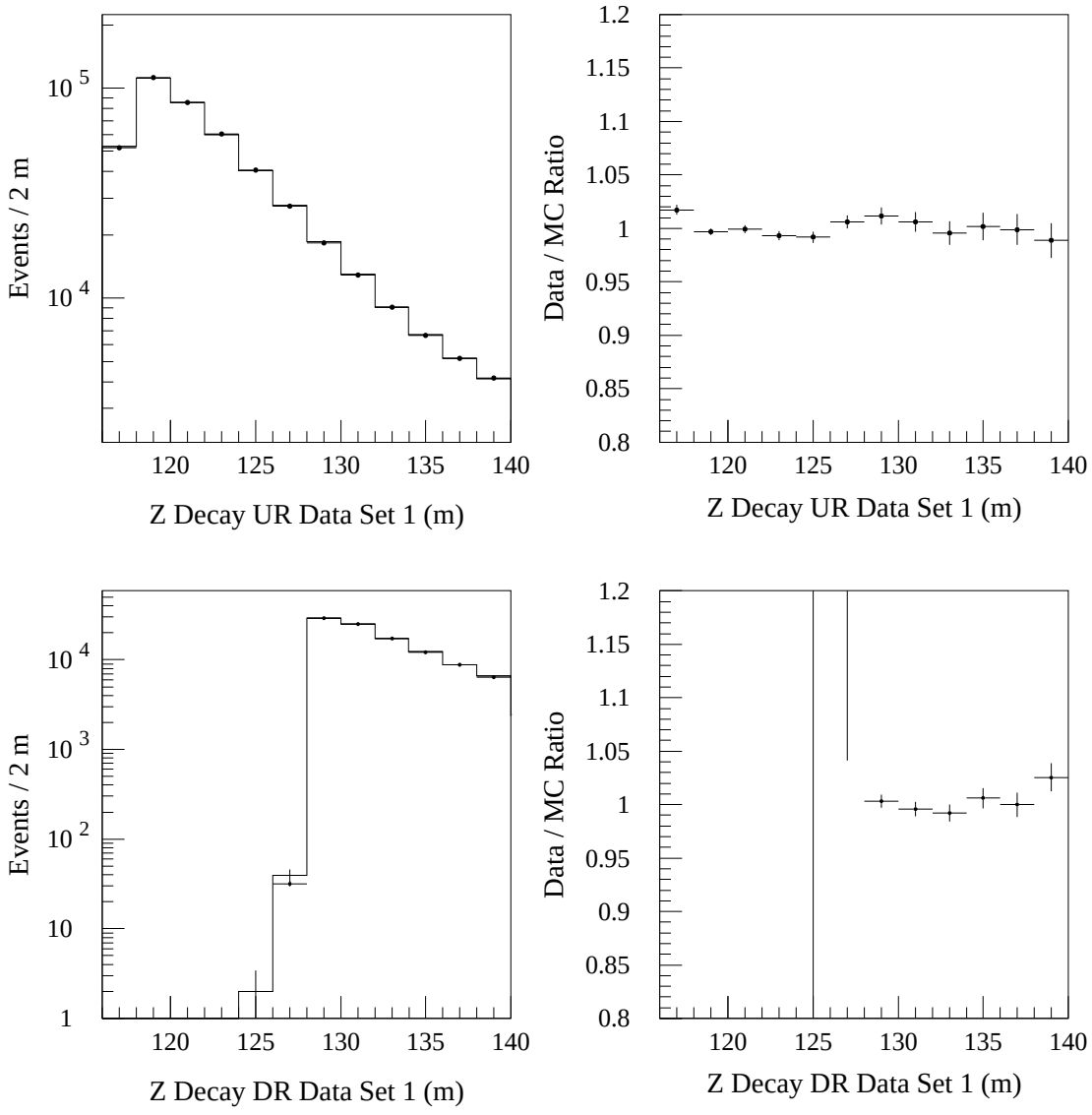

Figure 51. A comparison of the data and Monte-Carlo decay vertex distributions for $K \to \pi^+\pi^-$ decays from Data Set 1. The histograms are data and the dots are Monte Carlo.

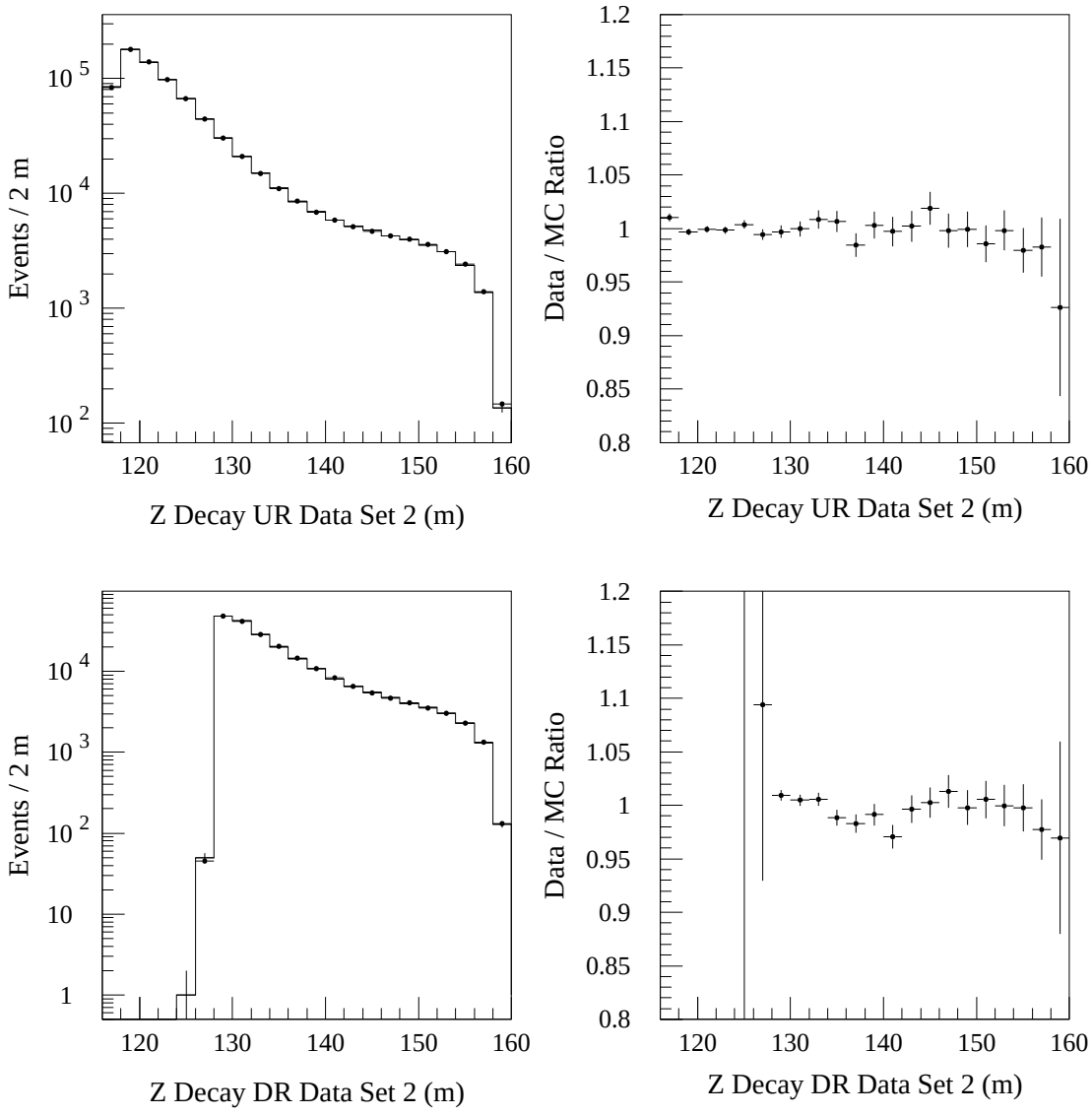

Figure 52. A comparison of the data and Monte-Carlo decay vertex distributions for $K \to \pi^+\pi^-$ decays from Data Set 2. The histograms are data and the dots are Monte Carlo.

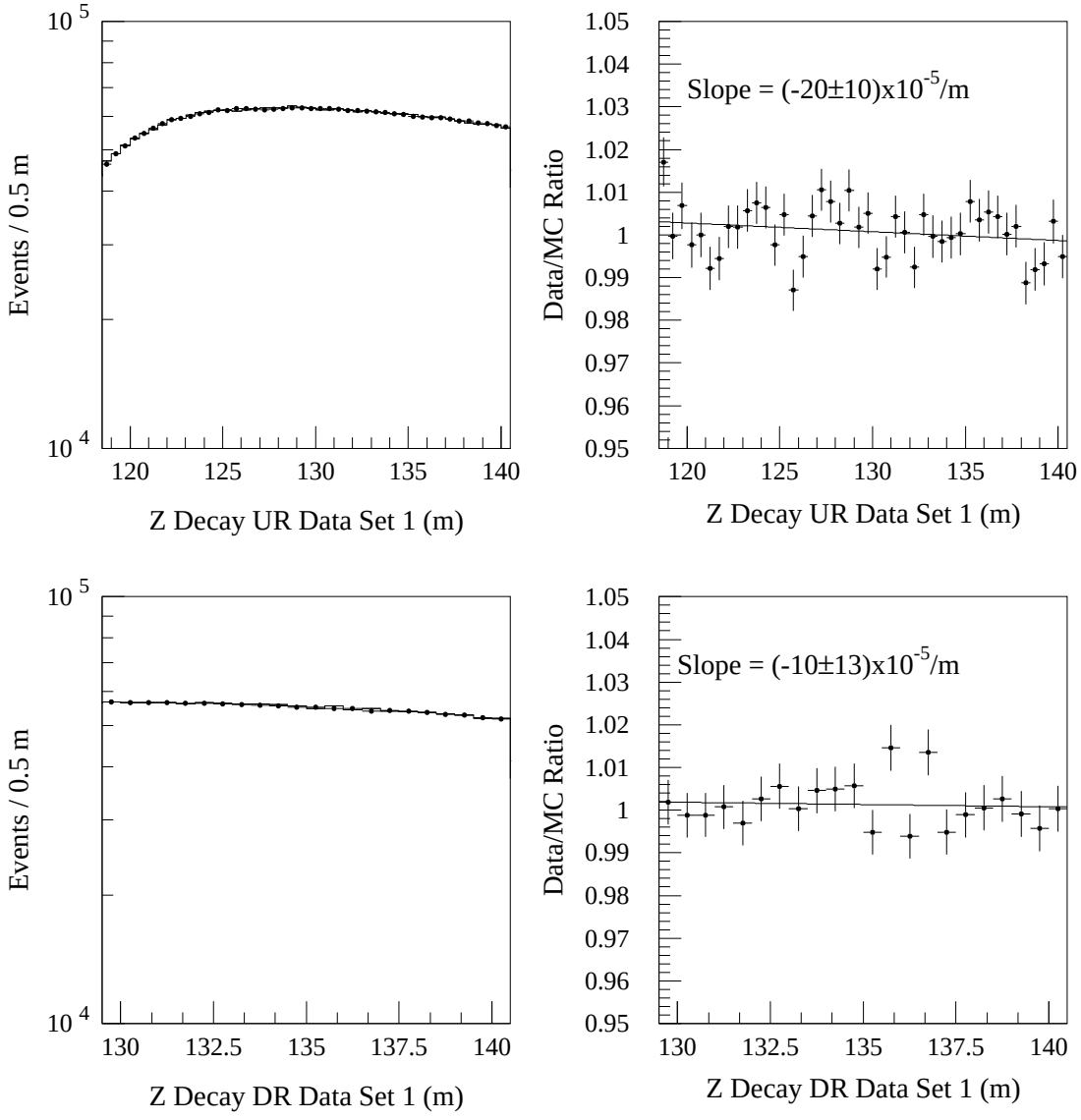

Figure 53. A comparison of the data and Monte-Carlo decay vertex distributions for $K \to \pi^{\pm} e^{\mp} \nu_e$ decays from Data Set 1. The histograms are data and the dots are Monte Carlo.

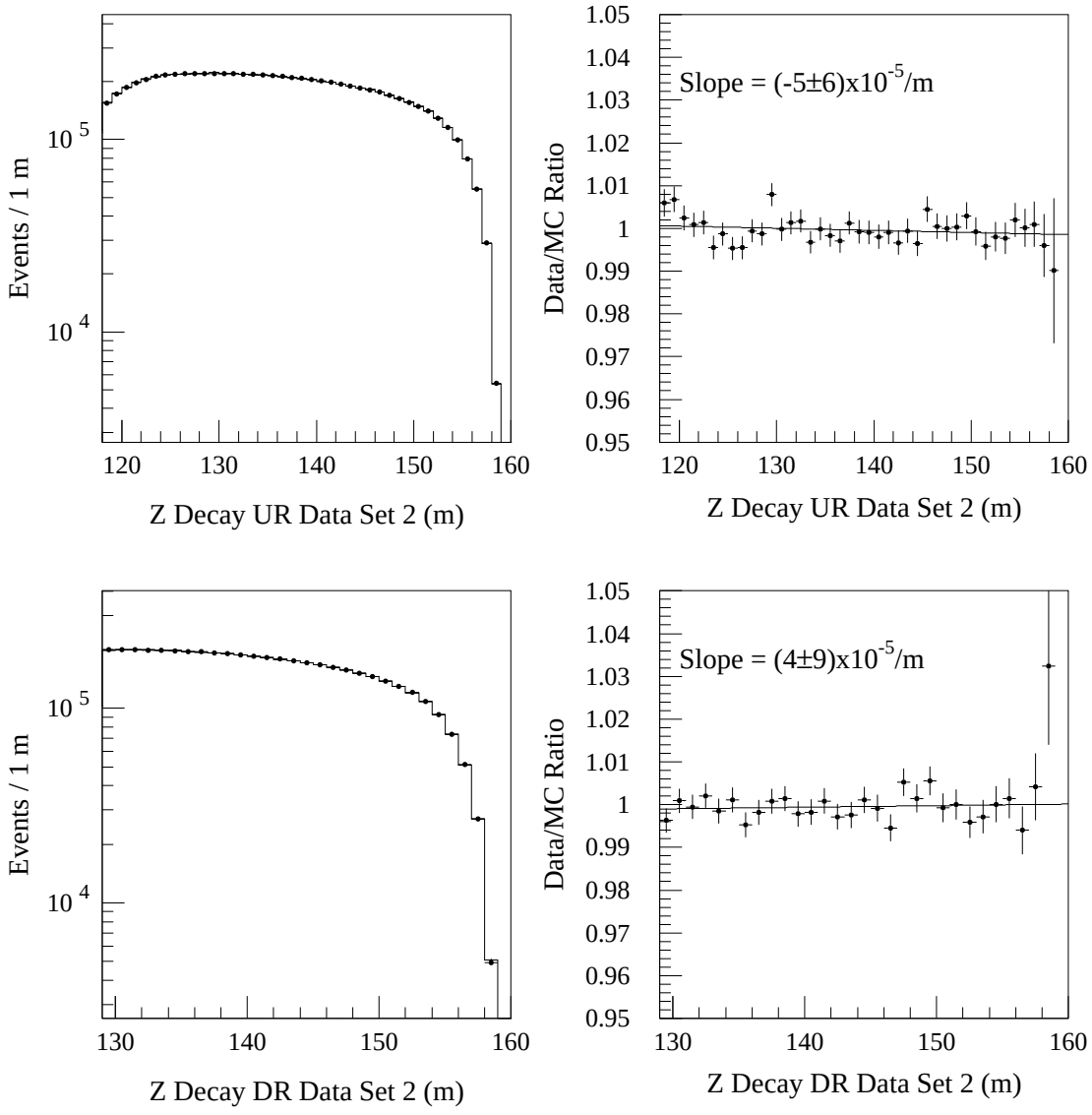

Figure 54. A comparison of the data and Monte-Carlo decay vertex distributions for $K \to \pi^{\pm} e^{\mp} \nu_e$ decays from Data Set 2. The histograms are data and the dots are Monte Carlo.

The results of studies with accidental are summarized in Chapter 9.

7.9 Summary

We have presented an outline of the Monte-Carlo simulation of our experiment. The simulated data agree well with the actual data collected, and gives us confidence in our understanding of the detector. The final acceptance determined for the UR beam in Data Set 2 is shown in Figure 55. We will now proceed to describe the details of fitting our data to extract results; this process relies on the Monte-Carlo simulation for a determination of the experimental acceptance.

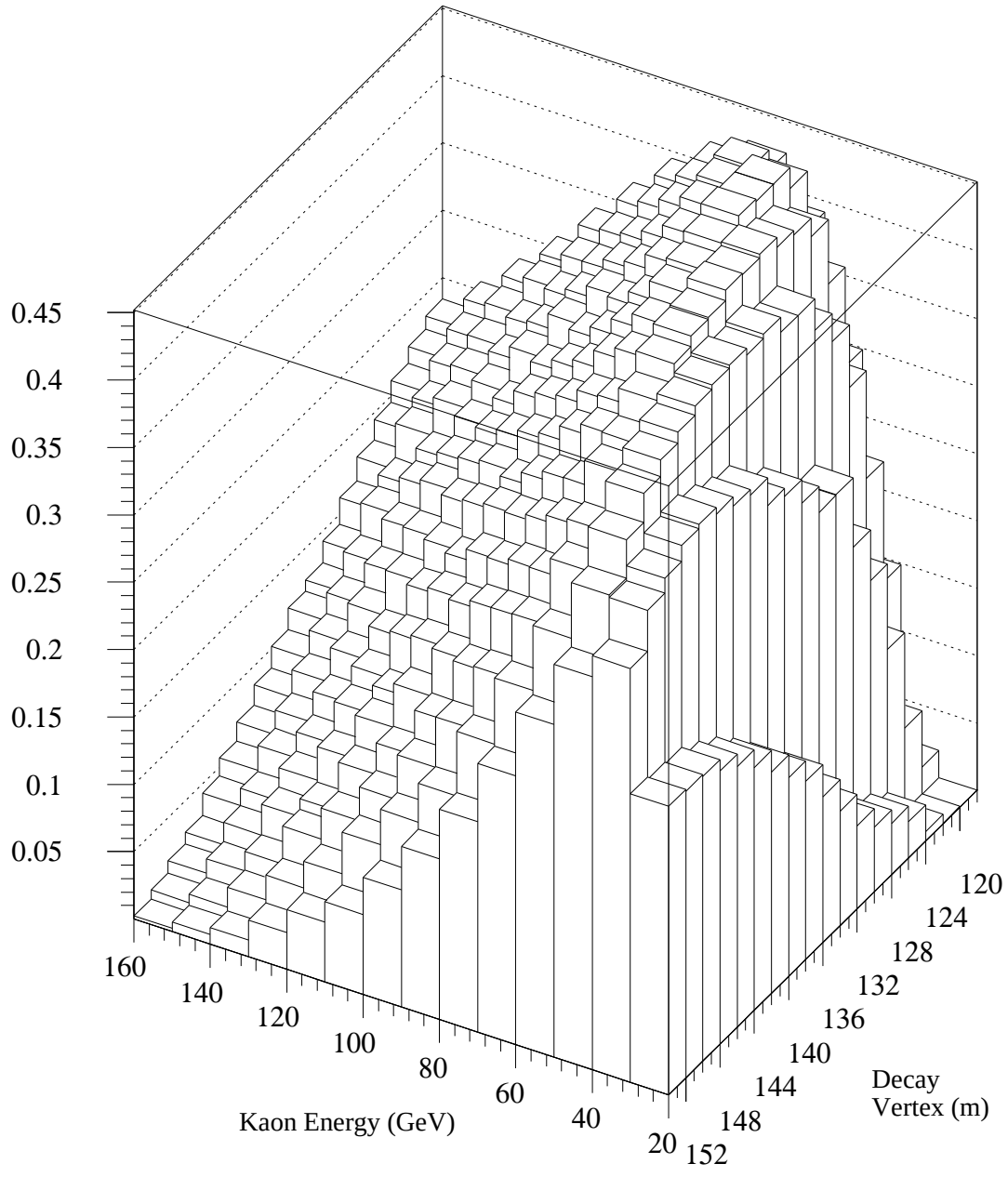

Figure 55. The acceptance for the UR beam in Data Set 2.

CHAPTER 8

FITTING

In Chapter 6, we described the reconstruction and analysis of the data. Chapter 7 then discussed the Monte-Carlo simulation of our experiment. With this simulation and the analysis, we are able to determine the acceptance of our apparatus and reconstruct the actual decay rate from the observed rate. We will now describe the details of the fits used to extract the physics parameters of interest. The basic procedure is straightforward: one simply corrects the observed decay rate for the detector acceptance and performs a fit to an analytic expression for this rate, minimizing the χ^2 with respect to the parameters of interest. In practice, however, some care must be taken to extract results properly. At the end of this chapter, we will present the results of our fits with statistical errors.

8.1 Introduction

It is useful to keep in mind the necessity of studies that will have to be performed in order to determine reasonable systematic errors for our results. Some of these studies will be done by varying the analysis or simulation, but others will take advantage of the versatility of our fitting procedures. Our philosophy is to construct a fitting program which is accurate, while also being fast and flexible. We therefore use analytic expressions whenever possible, and we start our rate calculations with kaon production at the target.

It is instructive to contrast what is necessary for accurate fitting with what was necessary for an accurate Monte-Carlo determination of the acceptance. We now have the

acceptance in hand, and need to be able to regenerate the decay rate rapidly as parameters are varied during the fit. Features such as the transverse beam profile which were relevant in the Monte Carlo are not important here. When determining the acceptance, the transverse position of the kaon is important since the acceptance is a non-trivial function of this position. However, when calculating the decay rate only, such detail is irrelevant; the amount of regeneration and subsequent decay probabilities are independent of the transverse position.

8.2 An Outline of the Basic Fitting Procedure

We first give an expression for the χ^2 which will be minimized; later sections will detail the task of determining each of the required parts.

The χ^2 calculation uses Gaussian counting errors on the data and binomial errors on the Monte-Carlo used to measure acceptance. The expression for the χ^2 is

$$\chi^2 = \sum_i \frac{(N^i_{prd}\, a_i - N^i_{obs})^2}{((N^i_{prd}\, \sigma^i_a)^2 + N^i_{prd}\, a_i)} \tag{8.1}$$

where the observed rate is given by the difference of the number of reconstructed data events and the estimated background: $N^i_{obs} = N^i_{dat} - N^i_{bkg}$. The fitter predicts the actual decay rate, N^i_{prd}. The acceptance, a^i, and its error, σ^i_a, are

$$a^i = N^i_{mc}/N^i_{gen} \tag{8.2}$$

$$\sigma^i_a = \sqrt{\frac{a^i(1-a^i)}{N^i_{gen}}}. \tag{8.3}$$

In all cases, the index i refers to a particular data bin in the fit; this index runs over the p and z bins as well as the UR and DR beams and the two Data Sets. Note that we have used $\sqrt{N^i_{prd}\, a_i}$ as the counting error on N^i_{obs}, since this is more reliable than $\sqrt{N^i_{obs}}$ when the statistics are low.

8.3 Data Input to the Fitter

8.3.1 The Basic Data Tables

For charged mode fits, we require four types of tables:

- The reconstructed data (N_{dat})
- The generated Monte-Carlo (N_{gen})
- The reconstructed Monte-Carlo (N_{mc})
- The estimated background (N_{bkg})

Each table gives the number of events in an array of p-z bins. For each type, say reconstructed data, there are 8 separate p-z tables corresponding to the 8 combinations of: Data Set 1 or 2, UR or DR, high beam or low beam. The data from the high and low beams is combined before the actual minimization; the resulting four sections of the data must be treated separately: the UR and DR have different regenerators, while the two Data Sets employ different triggers.

8.3.2 Averaging the High and Low Beam Data

The data from the high and low beams are combined using a geometric mean which is effective in canceling most potential biases depending on the beam. This is discussed in detail for the case of ε'/ε fits in E731 in [136, 140]. Since we have somewhat simpler requirements, since we are not concerned with losses independent of p and z for our fits, we present a shorter discussion of the relevant points here. For fits to ε'/ε, the case for the geometric mean is much stronger.

Consider the effect of an acceptance difference between the high and low beams for a particular bin. We compare the various formulae, arithmetic and geometric means, that could be used to calculate the true decay rate from the observed rate divided by the Monte-Carlo acceptance. We assume the acceptance is correctly known for each beam.

We denote by N the true total decay rate, from both beams, which we wish to recover and fit. a_h and a_l are the acceptance in the high and low beams, respectively, and f_h and f_l are the fractions of events in each beam: $f_h + f_l = 1$. The acceptance a_h and a_l are not equal due to small asymmetries in the detector. The event fractions, f_h and f_l are also not equal in general due to differences in beam intensity, live time with the regenerators in each of the two positions, and differences in accidental losses. Let us write $a_h = a(1+\alpha)$ and $a_l = a(1-\alpha)$ and $f_h = (1+\beta)/2$ and $f_l = (1-\beta)/2$, where α and β are small parameters. Furthermore, the event fractions $f_{h,l}$ in the numerator are the true values, while those in the numerator are the values given by the Monte Carlo. The arithmetic mean gives the measured decay rate as

$$\frac{a_h f_h N + a_l f_l N}{(a_h + a_l)/2} \tag{8.4}$$

or

$$\frac{a_h f_h N + a_l f_l N}{f_h a_h + f_l a_l}, \tag{8.5}$$

depending on the manner in which the averaging is done. The first formula takes the acceptance in each beam and then averages. The second averages the reconstructed and generated events from each beam first and then divides to get the acceptance; i.e., it uses a weighted average of the acceptances. The geometric mean gives

$$\frac{2\sqrt{(a_h f_h N)(a_l f_l N)}}{\sqrt{a_h a_l}}. \tag{8.6}$$

The geometric mean correctly recovers N up to terms of order β^2; no further errors are incurred if the Monte-Carlo event fractions are not exactly those in the data. This is a very desirable feature. The first version of the arithmetic mean contains an error of order $\alpha\beta$. The second version of the arithmetic mean contains no errors in terms of α and β, but it also depends on the Monte-Carlo event fractions being correct. We choose the geometric mean, but also try the (second) arithmetic mean as a systematic check.

8.3.3 Universal p-z Binning

The required data is input in a small, universal p-z binning to allow fitting in any bin size that can be formed by combining (re-binning) these. These 'micro bins' are chosen to be 1 GeV/$c$by 0.5 m. Typical fits are done in 'fit bins' that are 10 GeV/c by 2.0 m bins.

We are now able to calculate the observed decay rate, N_{obs}, and the acceptance, a, in each p-z bin for each of the four portions of the data: Data Set 1 UR, Data Set 2 UR, Data Set 1 DR, and Data Set 2 DR.

The only piece remaining is a calculation of N_{prd}, the predicted decay rate, as a function of the parameters which are to be fit.

8.4 Decay Rate Generator

A major task of the fitter is the calculation of the decay rate in a given p-z bin. This task is broken into three parts:

- Generation of the kaon beams incident on the regenerators.
- Propagation of the kaons through the regenerators.
- Calculation of the decay rate.

Each of these parts is presented in detail in the following sections. In all three parts, we will encounter some parameters which are to be determined by the minimization process.

8.4.1 Kaon Spectrum and Evolution

We first must generate the K^0 and $\bar{K}^0$ production spectra and evolve these through the beamline to the each regenerators. The beams incident on the two regenerators differ due to the presence of the movable absorber which shadows the DR. The K^0 and $\bar{K}^0$ initial states behave differently due to the different relative phases of the K_L and K_S component in each. This distinction is only relevant to the extent that a portion of the initial K_S component remains in the beam at the distance and energy of interest.

The kaon production spectrum used is the same modified Malensek spectrum [140, 152] used by the Monte Carlo. It gives the appropriate relative flux of K^0 and $\bar{K}^0$ as a function of kaon momentum. The K^0 and $\bar{K}^0$ are incoherent with each other, but each evolve as coherent superpositions of K_S and K_L.

The K^0 and $\bar{K}^0$ spectra are determined once at the beginning of each fit, in 1 GeV/c momentum bins spanning 20 – 160 GeV/c. These are then evolved through the absorbers and vacuum to give the K_L and K_S amplitudes at a fixed z of 100 m. This z location is in vacuum, after the full collimation system, but before the regenerators. The spectrum is evaluated separately for the UR and DR beams, and for each of the initial K^0 and $\bar{K}^0$ components of kaon production. Absorption and coherent regeneration of the beam in the common and movable absorbers is included in the kaon evolution; these are done with the full matrix propagation discussed in Appendix F.

There are two corrections to the spectrum which must be treated. As discussed in Chapter 7, forward elastic scattering in the absorbers has an appreciable effect on the spectrum. Also, the Malensek parameterization of kaon production is a function of the production angle, and hence should be integrated over the solid angle of the beams. Both of these effects are time-consuming to calculate.[1] We therefore calculate these effects with special runs of the Monte-Carlo, determining correction functions that can be applied analyticly in the fitter. We calculate the ratio of kaon spectrum in 1 GeV/c momentum bins for two runs of the simulation: the first a standard run, and the second one with no scattering in the absorbers and a very small solid angle 'pencil' beam. This ratio is then fit to a polynomial to parametrize the correction smoothly. The fitter then simply evaluates the spectra at a fixed production angle, corresponding to that used for the pencil beam, and ignores the scattering in the absorbers and the finite solid angle. The multiplicative flux corrections, relating these simple calculations to the full treatment of the Monte Carlo, are then applied. The flux corrections are shown in Figure 56. Note that they differ for the UR and DR because of the movable Be absorber shadowing the DR.

We thus end up with a set of coefficients, $a_S(p)$ and $a_L(p)$, where we have labeled the discrete 1 GeV/c momentum slices with p, for each of the four K^0 - $\bar{K}^0$, UR - DR combinations. The wavefunction of the kaon is $|K\rangle = a_S(p)\,|K_S\rangle + a_L(p)\,|K_L\rangle$ and the relative beam intensity is $|a_S(p)|^2 + |(a_L(p)|^2$.

One may wonder why the full spectrum from a position somewhere downstream of the absorbers is not simply read in after external determination. Although this would suffice in

[1] It is the *limits* of the integration that are difficult, because of the collimation system; the indefinite angular integrals of the Malensek parameterization are trivial.

general, the method outlined above is versatile enough to allow studies of the effects of the dilution factor and other simple spectrum modifications very rapidly since the corrections need not be re-determined.

We have thus taken care to preserve the correct quantum mechanical amplitudes of the kaons striking on the regenerators. The overall normalizations for the UR and DR beams as well as a common adjustment to the spectrum shape as a function of momentum may be adjusted easily during the remainder of the fit by simple scalings. For study purposes, we also allow the user to zero-out the small K_S component of the wavefunctions incident on the regenerators.

8.4.2 The Regenerators

The next step is to evolve the kaons through the regenerators. The length and other material characteristics of the DR are identical to those used in the Monte-Carlo (See Chapter

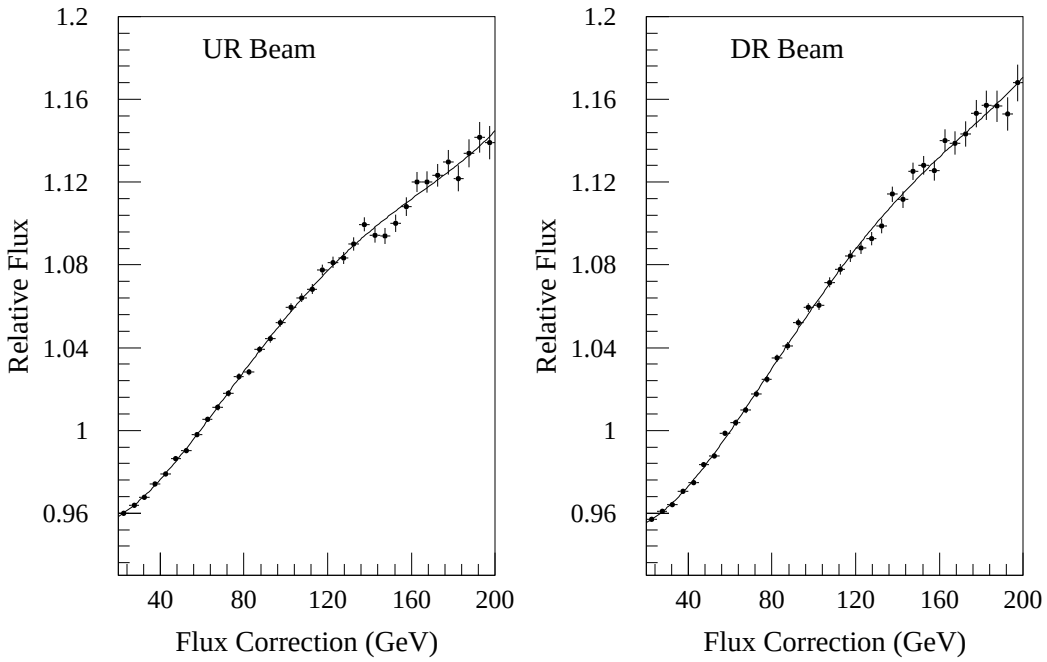

Figure 56. The flux corrections due to elastic scattering of kaons in the absorbers. The fits are fourth-order polynomials; these are used by the fitter.

7 and Appendix G.). The UR is modified very slightly, with respect to the treatment used in the Monte Carlo, to account for the tiny gaps between the scintillator blocks. These are virtually negligible, but were put in for completeness. Only absorption and coherent forward regeneration are treated; diffractive and inelastic processes are considered backgrounds and have been subtracted from the data, as described in Chapter 6.

The treatment of the regeneration amplitude from $CH_{1.1}$ is more sophisticated than that in the Monte-Carlo. This is necessary for two reasons. First, the extracted parameters are sensitive to the precise details of regeneration, which affect the decay rate. The acceptance is *not* significantly affected, and this sophistication is thus not necessary in the Monte Carlo. Second, due to this sensitivity, we will have to consider systematic effects due to regeneration and the fitter will be useful to perform the necessary studies. The physical size and composition of the regenerators is the same as in the Monte Carlo (with the exception for the UR noted above) and all of the sophistication lies in the parameterization of the scattering amplitude difference, $(f - \bar{f})/k$, for $CH_{1.1}$.

Several options for the parameterization of this amplitude are provided. Here, we will describe two: the most simple and then the more complex one actually employed in the final fits. It will turn out that the difference between these two treatments is virtually negligible; more details are provided during the discussion of systematic errors.

The simplest method of treating regeneration is to parametrize the amplitude for regeneration from $CH_{1.1}$ as

$$|(f - \bar{f})/k| = A\ e^{i\phi}\ (p/70)^{\alpha-1} \tag{8.7}$$

$$\phi = -(\pi/2)(1 + \alpha) \tag{8.8}$$

where A gives the amplitude at a kaon momentum of 70 GeV/c, and α describes the momentum-dependence of the amplitude as a function of p, given in GeV/c. The phase, ϕ, is related to the magnitude of the amplitude by dispersion relations based on analyticity of the scattering amplitude. This was the method used in E731 to describe the behavior of regeneration from the B_4C regenerator.

We now describe the more complex treatment. The first step is to separate the hydrogen and carbon contributions. We fix the hydrogen amplitude according to the form given in

Ref. [155]. The regeneration off carbon is parameterized as a 'bare' power law, which is floated in the fit, modified by an externally calculated correction.

$$|(f - \bar{f})/k| = A\ a(p)\ e^{i\phi}\ (p/70)^{\alpha-1} \tag{8.9}$$

$$\phi = -(\pi/2)(1+\alpha) + b(p). \tag{8.10}$$

The correction $a(p)$ modifies the magnitude of the amplitude; it is always with a few percent of unity. The correction $b(p)$ modifies the phase; it is always within a few degrees of zero. The terms $a(p)$ and $b(p)$ are used to take into account the effects of nuclear screening and electromagnetic regeneration, as well as other effects considered in studies of systematics. The bare power-law exponent, α, may be identified with the ω trajectory intercept, $\alpha_\omega(0)$, in the Regge-pole language (see Appendix D). Due to the momentum dependence of the screening corrections, which bring in other trajectories, the net behavior of the carbon amplitude is no longer a simple power law. Full details are given in Chapter 9 and Appendix H.

8.4.3 The Decay Rate

The decay rate is given by

$$\begin{aligned} r(p,z) \quad &\propto \quad |\rho(p)|^2 e^{-\Gamma_S t} + |\eta_{+-}|^2 e^{-\Gamma_L t} \\ &+ \quad 2|\rho(p)||\eta_{+-}| \cos(\Delta m t + \phi_\rho - \phi_{+-}) e^{-\bar{\Gamma} t}. \end{aligned} \tag{8.11}$$

The z dependence is contained in $t = (z - z_{reg})/\gamma\beta c$. The momentum-dependent regeneration amplitude is $|\rho(p)|e^{i\phi_\rho}$, and we have written $\bar{\Gamma} = (\Gamma_S + \Gamma_L)/2$. The decay rate is analyticly integrated over the z range of the fit bin. This is done separately in each 1 GeV/c momentum slice; these slices are then summed to give the total prediction for the momentum-span of a given fit bin. Momentum slices are used to maintain accuracy since the proper time interval of the fit-bin z range and the kaon flux are both momentum-dependent quantities.

8.5 Choice of Fits to Perform

We now describe the particular fits we choose to perform.

To extract τ_S, we float Δm, and assume CPT invariance for ϕ_{+-}; that is, we use $\phi_{+-} = \phi_{SW}$. Floating Δm is appropriate given the current controversy over its precise value [126]. The assumption of CPT invariance, allowing us to fix ϕ_{+-}, helps the statistical error significantly. The only drawback is that the result should be used with care, if at all, when tests of CPT are to be performed.

For our measurement of Δm, we fix τ_S to the world average and float ϕ_{+-}. We will see that the value of Δm is a subject of great interest currently because of a recent measurement which obtained a somewhat lower value than previous experiments and the effect this low value has on measurements of ϕ_{+-} [126]. Since we wish to include information from our Δm fits in choosing parameters for later fits for ϕ_{+-}, we float ϕ_{+-} to avoid any assumptions about CPT.

For the extraction of ϕ_{+-}, it is convenient to fix the values of Δm and τ_S and quote the sensitivities to these parameters. This allows a smaller error, since external information on the values of Δm and τ_S may be used. The result may also be adjusted later when new information becomes available.

We also will present the first simultaneous fit to all three parameters, $\phi_{+-} - \phi_{SW}$, Δm, and τ_S. An additional fit to the regeneration amplitude in momentum bins is performed in order to check that the amplitude behaves as expected.

8.5.1 Flux and Normalization Parameters

The fits for τ_S, Δm, and ϕ_{+-} allow all of the following quantities to float:

- The value of $|(f - \bar{f})/k|$ for carbon at 70 GeV/c.
- The power-law exponent, α, describing the momentum dependence of $|(f - \bar{f})/k|$.
- An overall flux normalization for the total number of kaons.
- The relative kaon flux between the two Data Sets.

- The relative absorption in the UR and DR beams.
- Two parameters to describe a momentum-dependent correction to the overall kaon flux.

The relative absorption between the UR and DR beams is known quite well a priori; it can be calculated from the properties of the two regenerators and the movable absorber. It is floated to avoid biasing the fits. The result is consistent with a calculation based on the material parameters and known cross sections; fixing this parameter has an insignificant effect on the statistical error of other parameters.

As noted, two parameters describing a possible quadratic correction to the modified Malensek spectrum are allowed to float. This correction is the same for the UR and DR beams. Specifically, the calculated flux is multiplied by:

$$1 + c_1 p + c_2 p^2 \tag{8.12}$$

where c_1 and c_2 are the two floating parameters. The momentum dependence of the flux is not known to sufficient accuracy to allow it to be fixed. This is unfortunate, since floating the flux degrades the statistical precision noticeably. These two parameters are highly correlated to the regeneration parameters. For each beam, regeneration and flux are degenerate in the approximation that only the K_S decay term is relevant. In practice, the K_L - K_S interference and K_L decay terms distinguish the the flux from the regeneration amplitude; this is most effective at low energy where many proper lifetimes are observable.

8.5.2 Range of Fits

Both Data Sets and both regenerators are fit simultaneously. The z region for the Upstream Regenerator beam extends from 118.5 m to 127 m and from 129 m to 154 m (140 m) for Data Set 2 (Set 1). The z region for the Downstream Regenerator beam extends from 130 m to 154 m (140 m) for Data Set 2 (Set 1). The regions near the regenerators are removed due to the increased background from beam interactions and the complications of calculating the decay rates in the presence of vacuum windows and air. Both of these can be treated quite accurately, but the loss of statistical power incurred by their exclusion is

quite small. Sensitivity to the exact locations of the regenerator faces and the veto power for decays occurring just before the ends of the regenerators is also reduced by not fitting to bins including the regenerator edges. Only fit bins with more that 10 reconstructed events are used.

8.6 Results

We are now ready to report the results of our fits. We remind the reader that all errors are statistical only; the systematic errors are evaluated in the Chapter 9. Interpretation of the results is given in Chapter 10, after the inclusion of systematic errors.

8.6.1 The Fit for τ_S, the K_S Lifetime

Our fit for K_S lifetime floats τ_S and Δm in addition to the standard parameters listed above. We set ϕ_{+-} equal to ϕ_{SW}, which is updated as Δm and τ_S change during the fit. The result of this fit is:

$$\tau_S = (0.8941 \pm 0.0014) \cdot 10^{-10} \text{ s} \tag{8.13}$$

with a χ^2 of 656 for 630 bins and 9 free parameters. The value of Δm obtained in this fit is $(0.5288 \pm 0.0030) \cdot 10^{10}\ \hbar\text{s}^{-1}$. There is very little correlation between Δm and τ_S.

8.6.2 The Fit for Δm, the K_L-K_S Mass Difference

To extract Δm, we fix $\tau_S = 0.8926 \cdot 10^{-10}$ s, the current PDG average [39]. The value of ϕ_{+-} is also floated in this fit. The result is:

$$\Delta m = (0.5297 \pm 0.0030) \cdot 10^{10}\ \hbar\text{s}^{-1} \tag{8.14}$$

with a χ^2 of 656 for 630 bins and 9 free parameters. The value of $\phi_{+-}$is $(43.79 \pm 0.78)^\circ$.

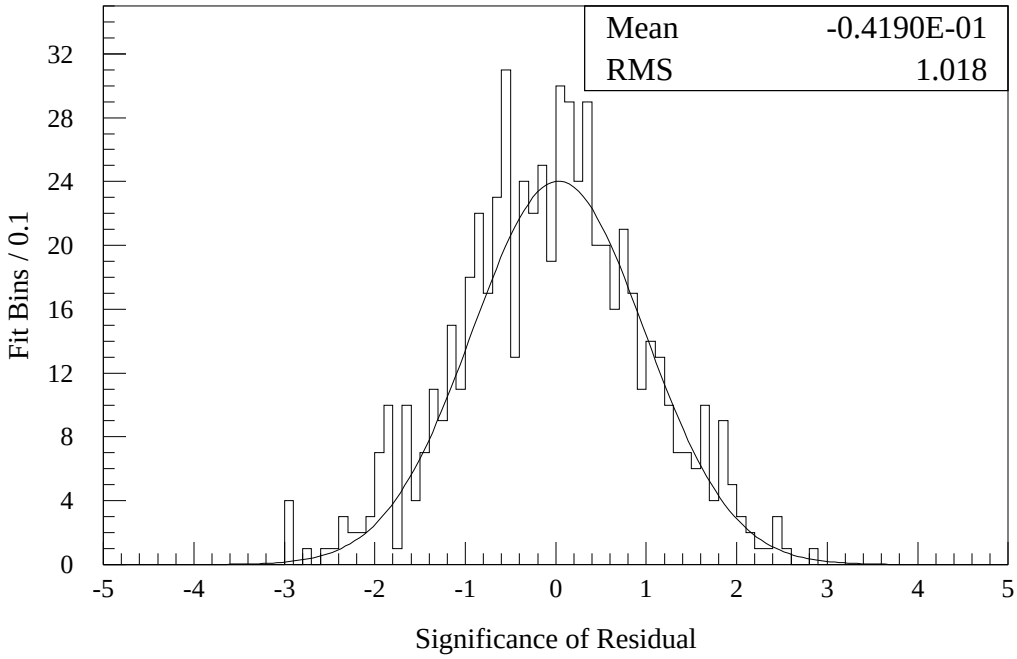

Figure 57. The signed residuals between the data and the fit decay rate, in standard deviations. The curve is a fit to a Gaussian; the mean and rms are for the actual histogram.

8.6.3 The Fit for ϕ_{+-}, the Phase of η_{+-}

The fit determining ϕ_{+-} is done with Δm and τ_S fixed; the dependences on these parameters are then determined in addition. The result for ϕ_{+-}, along with these dependences, is:

$$\phi_{+-} = 43.53^\circ \pm 0.58 + 0.52^\circ \times \left(\frac{\Delta m - 0.5282}{0.0030}\right) - 0.33^\circ \times \left(\frac{\tau_S - 0.8926}{0.0012}\right) \qquad (8.15)$$

with a χ^2 of 656 for 630 bins and 8 free parameters. The units of τ_S are 10^{-10} s and the units of Δm are $10^{10}\ \hbar\text{s}^{-1}$. We have used the PDG average for τ_S, and an average of E731 and E773 values for Δm; this Δm value is presented in Chapter 10, after systematic errors are available. For this fit, we exhibit a plot of the significance of the signed residual in each bin in Figure 57. The distribution is Gaussian, as expected. Figure 58 shows the distribution of residuals as a function of energy and decay position; there are no significant trends visible.

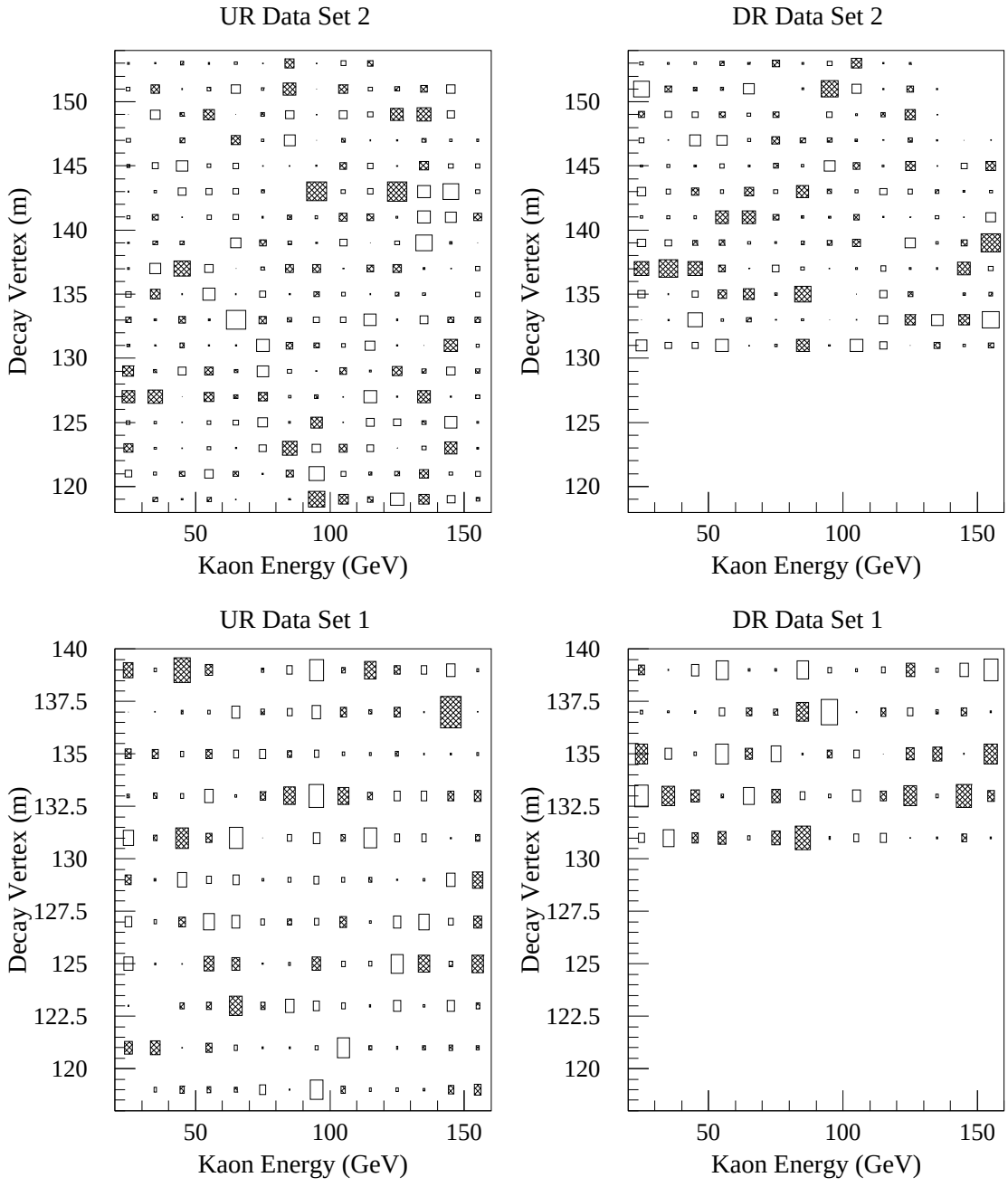

Figure 58. The signed residual in each fit bin, as a function of kaon energy and decay vertex, in standard deviations. The open (shaded) boxes denote positive (negative) residuals. The largest box corresponds to approximately three standard deviations.

8.6.4 *Simultaneous Fit for $\phi_{+-} - \phi_{sw}$, Δm, and τ_s*

We have also performed a simultaneous fit to all three of the above parameters. For the phase, we float $\phi_{+-} - \phi_{sw}$, since this is the physically interesting quantity and we wish to properly account for all correlations. The results are

$$\tau_s = (0.8958 \pm 0.0026) \cdot 10^{-10} \text{ s} \tag{8.16}$$

$$\Delta m = (0.5265 \pm 0.0040) \cdot 10^{10} \ \hbar\text{s}^{-1} \tag{8.17}$$

$$\phi_{+-} - \phi_{sw} = -0.99^\circ \pm 1.31 \tag{8.18}$$

with a χ^2 of 655 for 630 bins and 10 free parameters.

All results are in excellent agreement with expectations. A preliminary look at systematic errors indicates that this simultaneous fit has somewhat more sensitivity to systematic effects than our standard fits; we believe this would be somewhat lessened in an experiment which had a vacuum beam to assist with kaon flux normalization. We will not discuss the simultaneous fit further in this thesis. However, the statistical errors from this fit are promising; future experiments should be able to achieve precise results from such a fit.

8.6.5 *Fit for Regeneration Amplitude*

A special fit was performed to extract the momentum-dependence of the regeneration. For this fit, we fix τ_s to the PDG average of $0.8926 \cdot 10^{-10}$ s, fix Δm to the E731-E773 average of $0.5282 \cdot 10^{10}$ $\hbar\text{s}^{-1}$, and fix $\phi_{+-} = \phi_{sw}$. The value of $|(f - \bar{f})/k|$ and ϕ are allowed to float independently in each 10 GeV/c momentum bin. The usual flux and momentum spectrum parameters are floated in addition. The entire p-z region is fit simultaneously, such that the normalizations and spectrum shape parameters are shared. This introduces correlations between the momentum bins. Also, $|(f - \bar{f})/k|$ and ϕ are correlated within each bin.

The results of the fit are shown in Figure 59. The best-fit power law exponent is $\alpha = 0.4259 \pm 0.0051$, while the best-fit constant for the phase data is $(-128.83 \pm 0.34)^\circ$. Note that this power-law is for the net behavior of regeneration from carbon; the effects of the hydrogen in the scintillator are corrected for, but no other adjustments (i.e., for nuclear

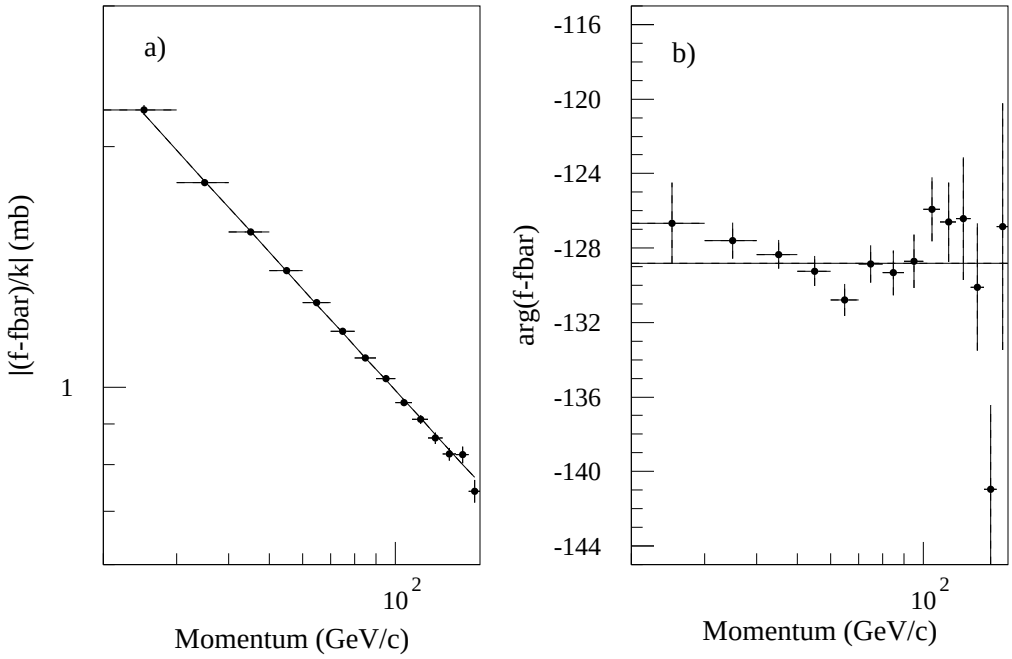

Figure 59. The magnitude and phase of regeneration from carbon, fit in 10 GeV/c momentum bins. In Plot a), the line shows the best-fit power law: $p^{-0.574}$. In Plot b), the fit is to a constant phase, with a result of $-128.8°$. See the text for further discussion.

screening effects relative to the bare ω-exchange) are made. The phase-power relation for the measured α predicts a phase of $(-128.33 \pm 0.46)°$. This is remarkably consistent with the phase obtained by directly fitting, assuming CPT. We thus see that it is quite consistent to posit both that CPT is a good symmetry and that the phase-power relation is accurate. Of course, in order to test CPT, we will have to discuss the systematics of the phase-power relation; we cannot simply assume it to be perfect. However, a conspiracy of canceling effects between CPT violation and discrepancies in the phase-power relation is very unlikely, and this result is a reassuring one for the validity of CPT symmetry.

8.6.6 Plots of Interference

In Figure 60, we display some acceptance-corrected data, including comparisons to the predicted decay rate with and without interference. The interference is clearly visible, both in the K_S region as well as in the 'dip' region further out in proper time.

8.7 Comments on Floating the Kaon Flux as a Function of Momentum

The flux can in principle be constrained via other decay modes, but this is somewhat difficult. A fully-reconstructible mode such as $K \to \pi^+\pi^-\pi^0$ could be used, but this brings in much more reliance on the lead glass calorimeter because of the π^0 reconstruction. Also, the $\pi^\pm$ showers can confound the π^0 reconstruction, and fiducial cuts are generally necessary to keep them separated. The $K \to \pi^\pm e^\mp \nu_e$ mode has higher statistics and has only charged tracks, like $K \to \pi^+\pi^-$, but it suffers from a two-fold ambiguity in the initial kaon energy due to the unseen neutrino. The ambiguity stems from a sign ambiguity in the longitudinal neutrino momentum in the kaon center-of-mass frame. This can be dealt with in principle, but in our case the effects of scattering in the regenerator further confuse the issue since the p_T^2 of the scatter is convolved with the p_T^2 of the unmeasured neutrino. Unfolding the spectrum precisely from such events would demand an excellent simulation of scattering; $K_L \to K_L$ scattering is difficult to study with $K \to \pi^+\pi^-$ due to low statistics.

A vacuum beam avoids the scattering problem in $K \to \pi^\pm e^\mp \nu_e$, and also would allow direct normalization to $K_L \to \pi^+\pi^-$. Although lower statistics than the $K \to \pi^\pm e^\mp \nu_e$ potential biases in the reconstruction, such as the pion losses due to an E/p cut, are avoided since the final state is the same as that being fit. Both normalizations to vacuum $K \to \pi^\pm e^\mp \nu_e$ [137] and vacuum $K \to \pi^+\pi^-$ [126] have been used with success in the past, but these options were not available in our two-regenerator configuration.

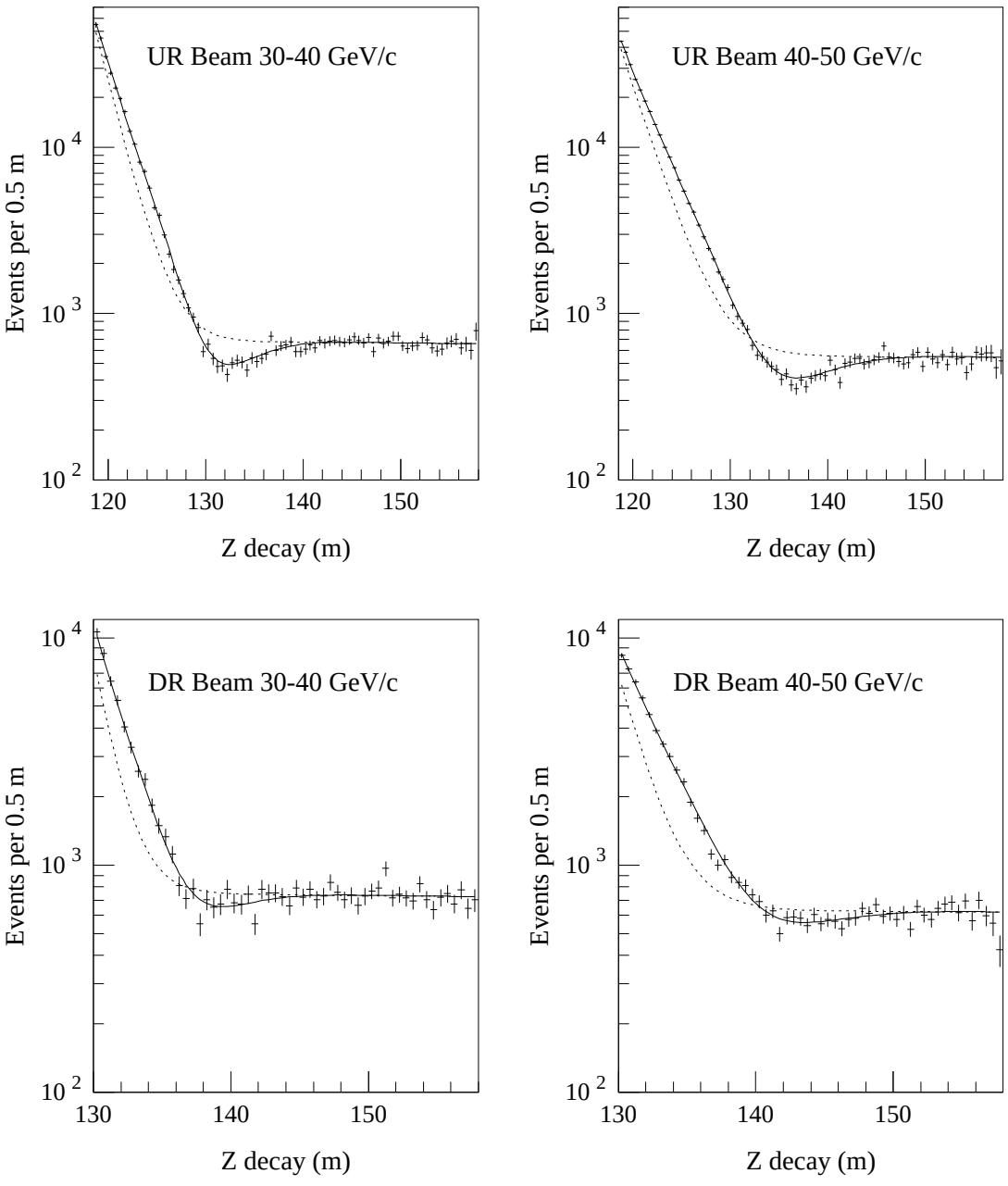

Figure 60. The acceptance corrected data compared to the fit decay rate for various 10 GeV/c momentum bins. The predicted decay rate is shown as the solid line; the same prediction with the interference term omitted is shown as the dotted line.

8.8 Summary

We have explained in detail the mechanics of our fitting procedure and presented the results of fits to the physically interesting quantities. The results for ϕ_{+-}, Δm and τ_S are each quite precise; we will defer a comparison of our results with previous measurements until we have evaluated the systematic errors in the following chapter. We have also performed a simultaneous fit to all three of these quantities.

The data has also been used to extract the regeneration amplitude off carbon as a function of momentum. The consistency of the directly-measured regeneration phase, using the the assumption of $\phi_{+-} = \phi_{SW}$, and the prediction form the power-law exponent, based on analyticity, is excellent. These results show that the phase of ϕ_{+-} predicted from CPT invariance and the regeneration phase determined from the phase power relation give a consistent representation of the data. It is true, however, that we have not yet addressed in detail the robustness of the of the phase-power relation. This must be done in order to perform a true CPT test. We address this issue, and perform studies of other systematics, in the following chapter. The fitting program we have described will be a valuable and versatile tool for investigating the stability of of our results.

CHAPTER 9

SYSTEMATICS

We now turn to a discussion and evaluation of the systematic errors for each of our measurements. First we describe some consistency checks performed, then we turn to a quantitative evaluation of systematic errors from specific sources. We consider effects due to acceptance, backgrounds, regenerator characteristics, and the regeneration phase.

9.1 Cross-Checks on the Fitting Procedure

Before fits to data were performed, the fitting procedure was checked with Monte-Carlo data samples. The Monte-Carlo statistics were about 10 times the actual data. The code for the modified Malensek spectrum and the code which calculates the kaon evolution, through vacuum or material, were essentially the same in the Monte Carlo and the fitting program; all the other portions of the software were quite different.

The simplest test, which also was very exacting, is a fit to the p-z tables of generated events produced by the Monte-Carlo. This involves no acceptance corrections or background subtraction, but is an excellent high-statistics test of the treatment of the kaon beams, regenerators, and decay rate. The fits successfully reproduce the Monte-Carlo kaon parameters, with errors much smaller (roughly an order of magnitude smaller) than those achieved in the real analysis.[1]

[1] In fact, an early lower-statistics version of this test was already sufficiently accurate to reveal a typographical error in the Monte Carlo which resulted in the regeneration phase differing by about 0.2° from the analytic value!

Fits could also be done with one Monte-Carlo sample serving a fake data, and another, larger sample used for acceptance. Using identical analysis and fitting procedures as were used with the actual data, the results were once again consistent with the input parameters.

Many variations in the fits were tried to check the robustness of the results. Some of the alternative fits performed included:

- Fitting the low ($20 - 70$ GeV/c) and high ($70 - 160$ GeV/c) momentum regions separately.
- Fitting the UR and DR data separately.
- Fitting Data Set 1 and Data Set 2 separately.
- Fitting to the arithmetic, instead of geometric, mean of the high and low beams.
- Fitting the high and low beams separately.

Each of these checks gave consistent results, within statistical fluctuations. We note that changing to the arithmetic mean shifts ϕ_{+-} by only $0.08°$.

9.2 Detector Acceptance

The acceptance of the detector is crucial to the fitting procedure. A large sample of $K \to \pi^{\pm} e^{\mp} \nu_e$ decays was used to check our understanding of the detector. This is useful because it consisted of a higher-statistics sample than the $K \to \pi^+\pi^-$ while also being independent of it. In addition, there is essentially no sensitivity to the regeneration parameters as there is for the $K \to \pi^+\pi^-$ decays. Such a dependence would complicate a study of the acceptance.

The $K \to \pi^{\pm} e^{\mp} \nu_e$ analysis has been described in detail in Chapter 6. Every attempt was made to keep the analysis as similar as possible to that for the $K \to \pi^+\pi^-$ signal. The slopes of the overall z distributions for each data subset, as displayed in Figures 53 and 54, are well within the value of 3×10^{-4}/m used in the systematic study. We also considered the possibility of slopes in the z acceptance as a function of p. Distortions as a function of p can be absorbed into the flux parameters floated in the fit. Distortions as a function of z

Table 16. Results of studies of systematic errors due to acceptance.

Change	ϕ_{+-}	Δm	τ_S
	degrees	$10^{10}\ \hbar s^{-1}$	10^{-10} s
z slope	-0.16	-0.0008	-0.0005
p-dependent z slope	-0.34	$+0.0003$	-0.0005
Total Systematic	± 0.30	± 0.0008	± 0.0006

are very restricted by the excellent data-Monte Carlo comparisons of $K \to \pi^{\pm} e^{\mp} \nu_e$ decays. That leaves the possibility of a second-order distortion coupling p and z. In particular, we considered a z slope varying smoothly from 3×10^{-4}/m to -3×10^{-4}/m as the momentum varies from $20 - 160$ GeV/c. We show the slopes of Data-Monte Carlo z comparisons in 10 GeV/c momentum slices for the Data Set 2 in Figure 61. The sensitivities to uncertainties in the acceptance are summarized in Table 16.

In addition, we performed fits where the detector apertures were changed in the real data analysis, but not in the Monte-Carlo samples used to calculate the acceptance. Movements of the edges of VA0, the HDRA, the CA, and the outer lead glass radius cut were tried. There was only minor sensitivity to any of these; to equal the size of the shift caused by the z slope discussed above required extremely large shifts.

9.3 Background Subtraction

The background subtraction technique was described in Chapter 6. Recall that there are two primary sources for background in the $\pi^+\pi^-$ sample. The first is the real $\pi^+\pi^-$ decays of non-coherent kaons, and the second is residual $K \to \pi^{\pm} e^{\mp} \nu_e$ contamination. We will estimate the systematic error by varying the subtraction technique.

The first thing to try is simply subtracting no background. The shifts in the extracted parameters are shown in Table 17. These shifts are clearly an overestimate of the systematic, but they help set the scale.

Next, we tried subtracting only the $K \to \pi^+\pi^-$ non-coherent background, based on our

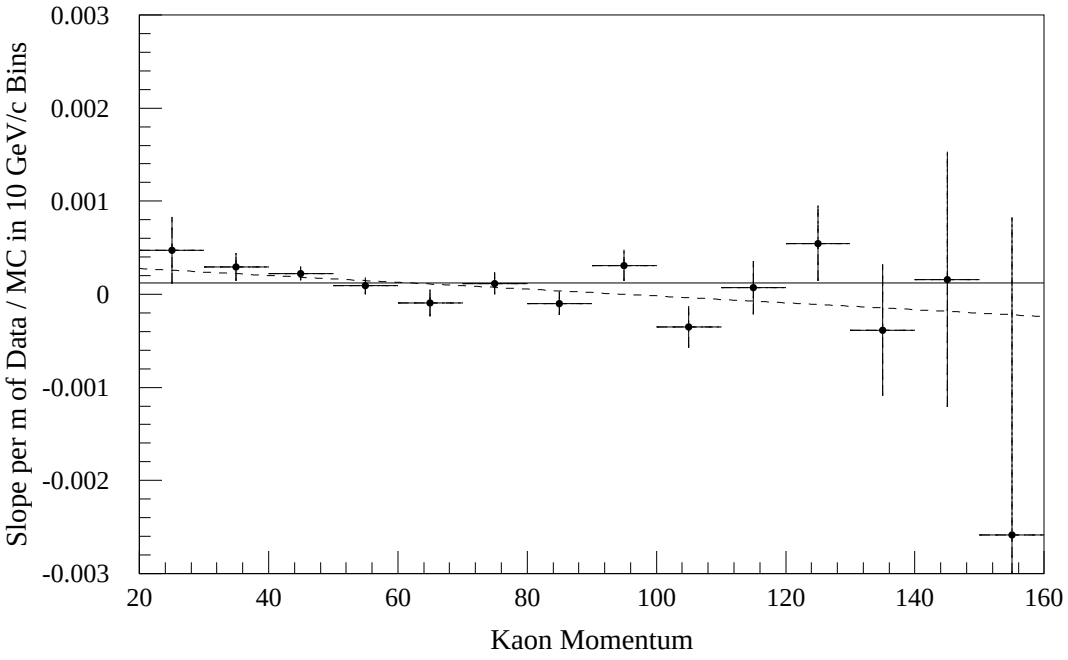

Figure 61. The slope of data/MC comparisons of $K \to \pi^{\pm} e^{\mp} \nu_e$ decays from Data Set 2, in 10 GeV/c kaon momentum bins. The solid line is the best-fit momentum-independent acceptance slope. The dotted line is the best fit momentum-dependent acceptance slope.

Monte Carlo, leaving any $K \to \pi^{\pm} e^{\mp} \nu_e$ component in the data. Comparing the observed shifts to the no-subtraction study, we see that the $K \to \pi^{+}\pi^{-}$ subtraction has a much larger effect on the fit quantities than the $K \to \pi^{\pm} e^{\mp} \nu_e$ subtraction.

Another interesting study involved widening the analysis cut to accept events from $0 - 500$ MeV$^2/c^2$ (the standard cut was $0 - 250$ MeV$^2/c^2$). This has only a marginal effect on the signal, but doubles the background, since they have little structure at the scale of the cut width. The background was recalculated for the new cut. The observed changes in fit results are quite small, as summarized in Table 17. These changes are presumably a combination of statistical fluctuations and of any systematic effects worsening due to the increased background level.

Finally, one may attempt to treat the background without recourse to the MC. The data in the region from 250 to 500 MeV$^2/c^2$ may be used to estimate the background in the 0 to 250 MeV$^2/c^2$ region. Since none of the background sources varies appreciably over

Table 17. Results of studies of systematic errors due to background subtraction.

Change	ϕ_{+-} degrees	Δm $10^{10}\ \hbar s^{-1}$	τ_S 10^{-10} s
no bkg. subtraction	-0.32	-0.0038	-0.0011
No Ke3 subtraction	-0.08	-0.0004	-0.0003
500 MeV/c^2 p_T^2 cut	-0.08	$+0.0005$	-0.0003
Data-based subtraction	-0.09	-0.0014	-0.0003
Total Systematic	± 0.15	± 0.0010	± 0.0003

this range, the estimate should be reasonable. In addition, one will also include some events that have smeared out from the peak due to resolution.

The final line of Table 17 shows the total error due to background subtraction that was chosen for each quantity. The errors for τ_S and Δm correspond to the background being known to about 25% of themselves, which is quite conservative based on the data-Monte Carlo comparisons. The ϕ_{+-} error is even more conservative, but it is not a large factor in our total error.

9.4 Regenerator Properties

For the present section, we assume that the nuclear scattering properties are known, and ask how the other properties of the regenerators may affect the results. The most crucial parameters concerning the physical nature of the regenerators are their position with respect to the decay volume, their total material content, and their overall length. The longitudinal distribution of material is taken as uniform for the UR, and a combination of uniform blocks and gaps for the DR. Deviations in the longitudinal distribution of the material from these assumptions are small and unimportant for our regenerators.

The first effect we consider is a shift in the z position of the downstream face of the regenerator. The machines controlling the motion of the regenerators were quite heavy, and hence very stable. At the end of the data run, the positions of the downstream face of

Table 18. Results of studies of systematic errors due to regenerator positions and sizes.

Change	ϕ_{+-} degrees	Δm $10^{10}\ \hbar s^{-1}$	τ_S 10^{-10} s
1 cm z shift of UR	-0.05	$+0.0001$	-0.0003
1 cm z shift of DR	-0.01	$+0.0000$	$+0.0000$
0.5% DR/UR length change	-0.04	$+0.0010$	-0.0002
Total Systematic	± 0.1	± 0.0010	± 0.0003

each regenerator were carefully surveyed in each of the two beam positions. The relative z values agreed to better than 0.5 mm in the two positions for both regenerators. The z positions in our detector coordinates are established to a few mm from surveys. All of our fits begin over 1 m downstream of the regenerators which greatly reduces our sensitivity to their precise locations. We choose to evaluate the systematics based on 1 cm shifts in z. These shifts are larger than our surveying accuracy, but are roughly the level that the survey results may be checked with data.

The other source of systematics is in the calculation of the regeneration amplitude itself. The relevant quantities are the quantity, identity, and spatial distribution of the materials in the regenerator. For a uniformly dense, mon-atomic regenerator, the total material and the length need to be known. Our regenerators are dominantly scintillator, and the small amounts of other material are treated as equivalent amounts of scintillator. The gaps between the DR blocks are also be accounted for. The composition of the two regenerators is discussed in detail in Appendix G.

The density of the scintillator was carefully measured to be (1.299 ± 0.002) g/cm^3, which agrees with the value of 1.302 g/cm^3 stated by the manufacturer. The hydrogen-to-carbon ratio is given by the manufacturer as 1.1. We will see later, when we discuss the regeneration phase, that there is little sensitivity to the precise amount of hydrogen.

We need the regenerator lengths, which determine the 'geometric' corrections (due to K_S decay). We are sensitive to the length at the 1 cm scale: if the UR was 1 cm longer and correspondingly less dense (keeping the total material fixed), the change in ϕ_ρ would

be 0.1°. Since the overall length is easily measured to better than 1 mm, this effect is negligible.

An error in the density of the scintillator will be absorbed into the extracted regeneration amplitude, but will not affect any other fit parameters. An error in the relative amount of material in the two regenerators can lead to a bias, however. We therefore have tried increasing the material of the DR by 0.5% relative to the UR. This is roughly the accuracy to which the relative amount of material is known. The uncertainty is dominated by properties of the wrapping material used for the DR blocks. The effects of a relative length change are shown in Table 18.

The exact spacing of the 12 subunits in the DR is not particularly crucial. Recall that the gaps are about 1.7 cm. If we imagine fixing the two end units, and allowed all 10 of the other units to shift in z coherently by 1 cm, then this would give a smaller effect than the 1 cm shift of the entire DR evaluated above. In practice, the spacings are uniform at the 1-2 mm level, and are not shifted coherently; any effects of this are thus negligible.

Table 18 also shows the total systematic assigned for all of the above effects.

9.5 Treatment of the Regeneration Phase

It is very important in our experiment to establish that we can correctly account for the regeneration phase, ϕ_ρ, when fitting our data. An error on the value of this phase directly affects the extracted value of ϕ_{+-} and would also affects our measurements of Δm and τ_S. As discussed in Chapter 2, the regeneration amplitude is well-represented by a power law as a function of kaon energy, and this energy dependence is related to the phase via analyticity. Thus, our starting point will be to take

$$|(f - \bar{f})/k| = E^\alpha/k \tag{9.1}$$

and

$$\phi = arg(f - \bar{f}) = -(\pi/2)(1 + \alpha) \tag{9.2}$$

as an excellent first approximation of the behavior of regeneration. We will then study in detail a number of potential sources of deviation from this form.

Table 19. Results of studies of systematic errors due to the regeneration phase. See the text for a description of how the results of the studies are used to generate the total systematic.

Change	ϕ_{+-} degrees	Δm $10^{10}\ \hbar s^{-1}$	τ_S 10^{-10} s
Ignore EM regeneration	-0.10	-0.0001	-0.0002
Low-Energy part of Disp. Relation	$+0.10$	-0.0001	$+0.0002$
Daughter Trajectories	< 0.10	< 0.0001	< 0.0002
C-even Inelastic Screening	-0.18	-0.0003	-0.0003
C-even and C-odd Inelastic Screening	$+0.22$	$+0.0006$	$+0.0004$
Total Systematic	± 0.35	± 0.0008	± 0.0006

In particular, we consider the effects of:

- Electromagnetic (EM) regeneration.
- Low-energy contributions to the dispersion relation.
- The presence of secondary power laws (Regge daughter trajectories).
- Screening in the carbon nucleus.

The results of studies of these effects are summarized in Table 19. The total error is arrived at as follows. The error from EM regeneration is 50% of the effect of EM regeneration listed in the table; this is due to the uncertainty in the kaon charge-radius. The determination of the low-energy contributions to the dispersion relations is difficult, we double the effect listed. The error from the screening calculation for carbon is taken to be the largest change seen in the the inelastic screening studies listed; which bracket the allowed variations. The effect of daughter trajectories is small. More details of all of these studies are given in Appendix H. We note that the value of ϕ_{+-} shifts by only 0.04° between a fit assuming a pure power-law and one including our best estimate of all of the effects listed above altering this behavior. Thus, the size of the correction from these effects is much less than our quoted systematic error.

9.6 Potential Bias from Accidental Activity

In the charged-mode analysis, accidental events were not overlayed in standard MC event generation. We need to be sure that the acceptance is not biased by the additional activity. We have evaluated the effect by comparing the z distributions of MC samples with and without accidental overlays and examining the results of fitting with the different MC samples used to determine the acceptance.

The Monte-Carlo simulation is capable of overlaying accidental events as described in Chapter 7. A sample of $K \to \pi^+\pi^-$ decays was generated with accidental overlays and compared to events generated with no overlays. A comparison of the energy spectrum with and without overlays is shown in Figure 62; a similar comparison of the decay vertex distribution is shown in Figure 63. There is no evidence of any significant changes in the acceptance. Also, a discrepancy caused by accidentals would have been evident in the data-MC comparisons (with no accidental overlays) shown in Chapter 7. Therefore, we add no additional systematic error based on this study. We have also performed fits using the MC sample with overlays to determine the acceptance, and the results were completely consistent with the standard fits.

9.7 Sensitivity to other Parameters

The decay rate is sensitive to many parameters other than those we wish to extract. We briefly describe some of these now.

The sensitivities of our results to the parameters τ_S and Δm are explicitly included whenever these parameters are fixed. In particular, the dependence of ϕ_{+-} on Δm and τ_S was given in Eqn. 8.15. For the Δm fit, we treat the uncertainty in τ_S as a systematic error.

The value of Γ_L is known to better that 1%; the effects of this uncertainty on the extracted parameters are negligible: ϕ_{+-} changes by 0.02° for a 1% change in Γ_L. The *shape* of the decay rate is only sensitive to ρ/η and we float the kaon flux in the fits; any error in the value of $|\eta|$ is absorbed into the extracted value of $|\rho|$. The separation of ϕ_ρ and ϕ_{+-} has already been discussed in Section 9.5. The geometric correction to the regeneration

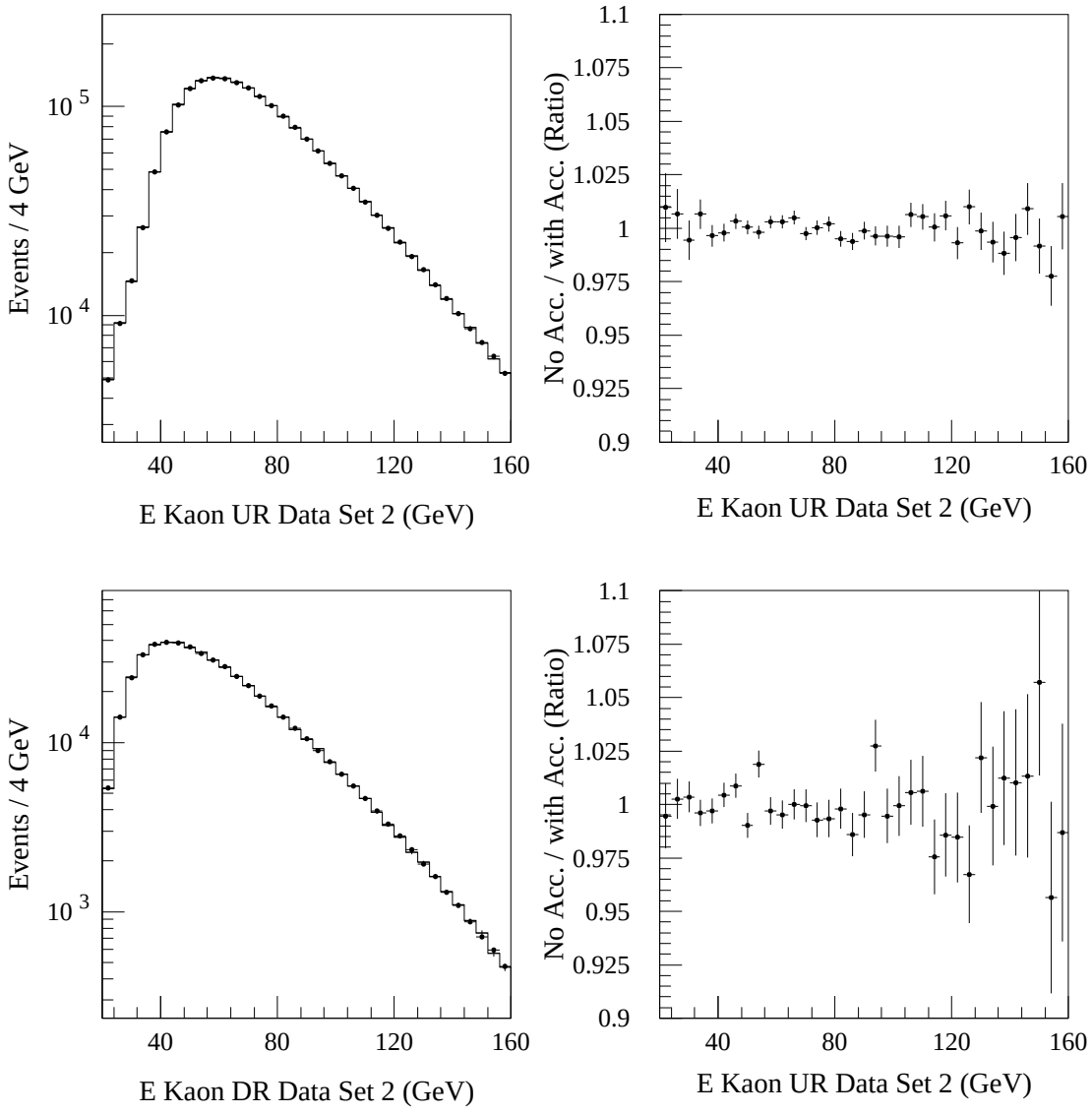

Figure 62. A comparison of the kaon energy spectrum from Monte Carlo, with and without accidental overlays. All plots ore from Data Set 2; both UR and DR beams are shown, as indicated in the axis labels. The histograms are Monte Carlo without accidental overlays, while the dots are Monte Carlo with accidental events overlayed.

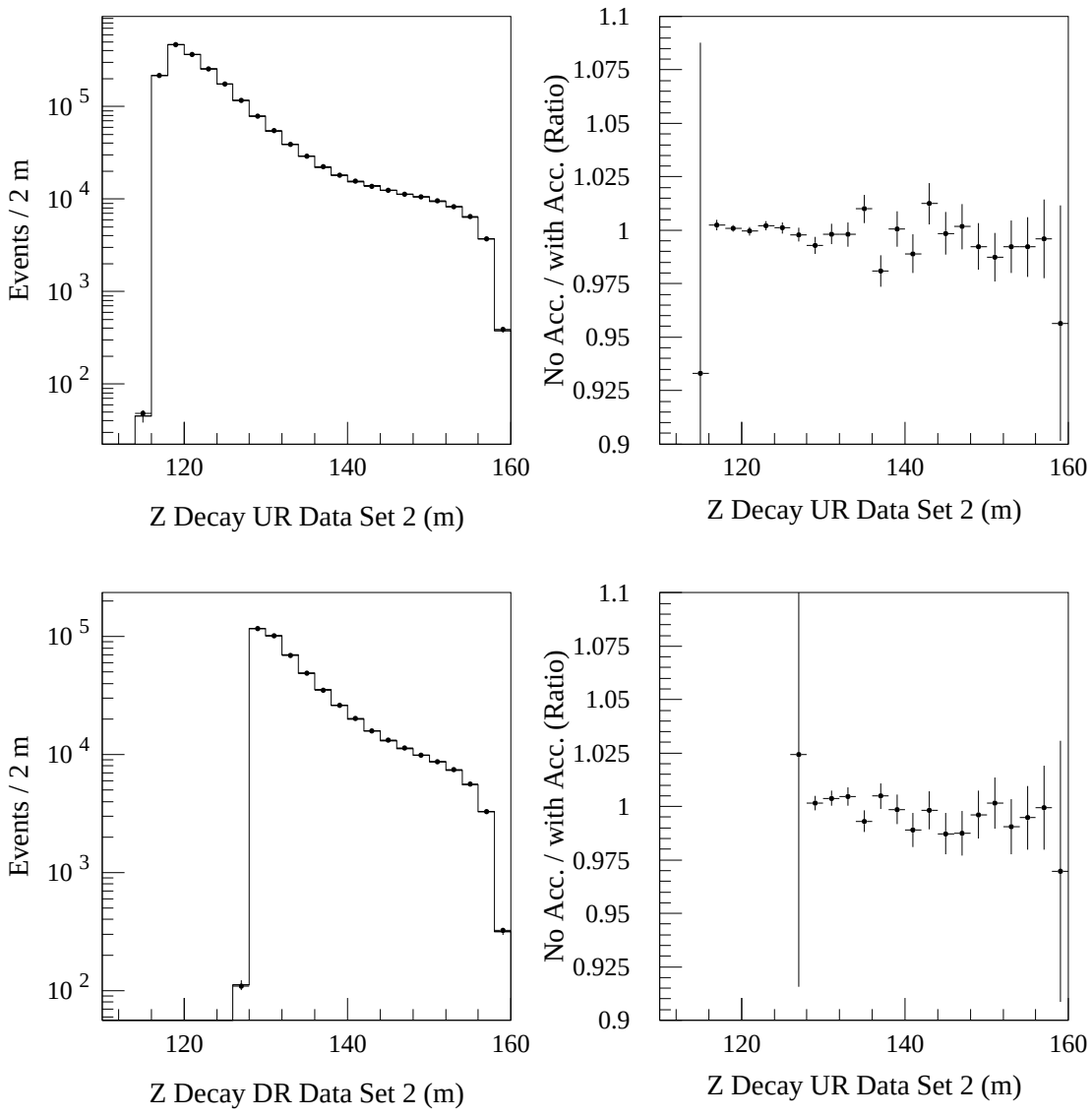

Figure 63. A comparison of the kaon decay vertex distribution from Monte Carlo, with and without accidental overlays. All plots ore from Data Set 2; both UR and DR beams are shown, as indicated in the axis labels. The histograms are Monte Carlo without accidental overlays, while the dots are Monte Carlo with accidental events overlayed.

Table 20. Summary of systematic errors for the charged-mode fits. The individual sources were added in quadrature to give the total error.

	Φ_{+-}	Δm	τ_S
	degrees	$10^{10}\ \hbar s^{-1}$	10^{-10} s
regenerator positions, sizes	0.10	0.0010	0.0003
acceptance	0.30	0.0008	0.0006
background subtr.	0.15	0.0010	0.0003
regeneration phase	0.35	0.0008	0.0006
τ_S dependence	-	0.0012	-
total	0.49	0.0022	0.0009

amplitude is a function of the regenerator length and the parameters Δm, Γ_S, and Γ_L. This correction is recalculated by the fitter as each of these parameters is changed to correctly include any effects.

9.8 Summary

We have presented a detailed examination of the possible sources of systematic errors on our measurements. We have evaluated the effects of each quantitatively so they may be included in our final errors. The systematic effects are summarized in Table 20.

CHAPTER 10

CONCLUSION

10.1 The Final Results

Combining the results of the previous two chapters, we find:

$$\phi_{+-} = (43.53 \pm 0.97)^\circ \tag{10.1}$$

$$\Delta m = (0.5297 \pm 0.0037) \cdot 10^{10}\ \hbar\mathrm{s}^{-1} \tag{10.2}$$

$$\tau_S = (0.8941 \pm 0.0017) \cdot 10^{-10}\ \mathrm{s} \tag{10.3}$$

The statistical and systematic errors have been added in quadrature. The latter two measurements imply:

$$\phi_{SW} = 43.50^\circ \pm 0.17^\circ \tag{10.4}$$

If we average our Δm measurement with that of E731, $(0.5257 \pm 0.0049) \cdot 10^{10}\ \hbar\mathrm{s}^{-1}$, we find

$$\Delta m = (0.5282 \pm 0.0030) \cdot 10^{10}\ \hbar\mathrm{s}^{-1}. \tag{10.5}$$

Note that the published Δm is from a fit with τ_S floating and Δm fixed [126]. The PDG uses a value from E731 obtained with ϕ_{+-} floating and τ_S fixed; we use that value [136] here also. The PDG average, without E731, is [156]:

$$\Delta m = (0.5351 \pm 0.0024) \cdot 10^{10}\ \hbar\mathrm{s}^{-1}. \tag{10.6}$$

The E731-E773 average is 1.8 standard deviations lower than the PDG average. The rather significant effect of a lower Δm value on CPT tests involving ϕ_{+-} has been discussed in Ref. [126] and will be reviewed below.

For completeness, we also present here the results of the $\Delta\phi$ analysis of E773 [141],

$$\Delta\phi = 0.62^\circ \pm 1.03^\circ \tag{10.7}$$

10.2 Comparison with Previous Results

Some care must be taken when examining the collection of measurements for each parameter we have extracted. This is necessitated by the frequent presence of strong correlations among parameters as well as the fact that experiments often measure more than one quantity. It is therefore useful to examine the list of significant measurements in some detail.

10.2.1 The K_S Lifetime, τ_S

The K_S lifetime is a classic example of a sudden and ill-understood shift in the accepted value of a parameter. The 1978 PDG compilation [157] discusses this case. Currently, the situation is quite stable and acceptable. The 1994 PDG compilation [39] lists six significant measurements of τ_S. All use the $K \to \pi^+\pi^-$ decay mode, with one exception noted below. These are listed, along with the current measurement, in Table 21. A plot of the measurements is shown in Figure 64.

The oldest is Skjeggestad, *et al.* [158], performed in a 2 m hydrogen bubble chamber at CERN. The K^0 were produced with a $1.2 - 1.7$ GeV/c K^+ beam via the reaction $K^+p \to K^0p\pi^+$. The typical K^0 momentum was 0.75 GeV/c; the range was $0.1 - 1.5$ GeV. Small corrections are made for CP-violation, regeneration, and kaon interactions. The total correction is only $-0.0006 \cdot 10^{-10}$ s. Each correction includes a corresponding systematic error. Systematic errors from momentum-scale uncertainties and flight-path length are also included. This experiment was responsible for beginning the revision of the accepted lifetime, and also published results for other two-track decay modes. Previous to this measurement, the PDG average of $(0.862 \pm 0.006)\cdot 10^{-10}$ s was dominated by three measurements done in the late 1960's.

Geweniger, *et al.* [159], were the first to confirm the longer lifetime. This was one of

Table 21. Summary of significant measurements of K_S lifetime, τ_S. All values have been adjusted to a consistent set of kaon parameters.

Experiment	τ_S 10^{-10} s	Error 10^{-10} s	Technique	Energy GeV	Decay region m
Skjeggestad [158]	0.8958	0.0045	bubble ch.	0.1 – 1.5	2
Geweniger [159]	0.8937	0.0048	target	5 – 12.5	9.4
Carithers [160]	0.8929[a]	0.0032	regenerator	4 – 10	5.6
Aronson [161]	0.879[b]	0.009	target	3 – 8	0.8
Grossman [162]	0.8920	0.0044	target	100 – 350	16
Gibbons [126]	0.8929	0.0016	regenerator	20 – 160	10,27
Schwingenheuer [163]	0.8941	0.0017	regenerator	20 – 160	35

[a] This number is adjusted to our preferred value of $\Delta m = 0.5282 \cdot 10^{10}\ \hbar s^{-1}$. For the 1994 PDG value of $\Delta m = 0.5333 \cdot 10^{10}\ \hbar s^{-1}$, the value is 0.8916; note that the PDG has *not* made this correction in spite of listing the sensitivity correctly in a footnote.

[b] We have adjusted this result for parameter dependences noted in the paper.

a set of important measurements in the kaon system by the CERN-Heidelberg-Dortmund group. The experiment was performed at the CERN Proton Synchrotron. The helium-filled decay region decay region extended from 2.2 – 11.6 m after the production target and momentum was 5 – 12.5 GeV/c. The experiment used Cerenkov counters for particle identification and a spark-chamber spectrometer for tracking. One analysis focused on the time dependence of $\pi^+\pi^-$ decays. There were about 6×10^6 events, and a similar number of Monte-Carlo events for acceptance determination. The background varied form 2 – 7%. The parameters Γ_S, $|\eta_{+-}|$, and ϕ_{+-} were extracted simultaneously. The K^0 and $\bar{K}^0$ fluxes were independently floating in each 0.5 GeV/c momentum bin. The values of Δm and Γ_L were fixed; the dependence of ϕ_{+-} (only) on Δm is given. Systematics included effects of absorbers, collimators, regeneration in the helium decay volume, and uncertainties in the magnetic field. Sensitivity of τ_S to the value of Δm used ($0.540 \cdot 10^{10}\ \hbar s^{-1}$) is not mentioned. It is interesting to note that this experiment was the first to revise the value of $|\eta_{+-}|$ upwards. This parameter suffered a shift much like that of τ_S [157], but we will not have time to discuss this further.

Carithers, *et al.* [160], also studied the time dependence of $\pi^+\pi^-$ decays. The experiment

was performed at the Brookhaven Alternating Gradient Synchrotron. The kaon momenta spanned $4 - 10$ GeV/c. The spectrometer was previously used in the first observation of $K_L \rightarrow \mu^+\mu^-$; it now included a two-interaction length carbon regenerator before its helium decay volume. The analysis extracted the kaon flux, $|\rho/\eta|$, $\phi_{+-} - \phi_\rho$ and Γ_S, while fixing $\Delta m = 0.540 \cdot 10^{10}\ \hbar\text{s}^{-1}$. The value of ϕ_ρ had been determined independently from semileptonic decays [125]. The dependence of τ_S on Δm is given.

Aronson, *et al.* [161], was performed at the Argonne Zero Gradient Synchrotron. The kaon momenta ranged from $3 - 8$ GeV/c. An evacuated decay region of 0.8 m began 1.25 m from the production target. Dependences on the assumed values of $|\eta_{+-}|$, ϕ_{+-}, Δm, and the dilution factor are quoted. Systematics are investigated by varying cuts, and are found to be small.

The Grossman, *et al.* [162], result comes from the FNAL E621 (η_{+-0}) experiment at the Fermilab Tevatron. This experiment was performed in a region $9 - 25$ m from the production target. The kaon momentum ranged from $100 - 350$ GeV/c. To avoid sensitivity to CP-violating decays and the dilution factor, only these high energy kaons were used. Systematics errors from background and acceptance were considered. We note that the abstract of the paper lists an error of $0.0044 \cdot 10^{-10}$ s, while the body of the text lists a *statistical* error of $0.0044 \cdot 10^{-10}$ s, and a *systematic* of $0.0022 \cdot 10^{-10}$ s.

The measurement of Gibbons, *et al.* [126], was made as part of the effort by FNAL E731 to detect direct CP-violation. The experiment was very similar to the one described in this thesis. Most of the detector was the same; the major difference was the use of a single, two-interaction length B_4C regenerator as opposed to the configuration with two regenerators described earlier in this thesis. Except for the precise values certain parameters were fixed to, and some details of flux normalization, the E731 fits for τ_S, Δm, and ϕ_{+-} are the same as those presented in this thesis. The vacuum (no regenerator) beam in E731 allowed a determination of the kaon flux from $K_L \rightarrow \pi^+\pi^-$ decays that could be used when fitting the regenerator data. Kaons from $20 - 160$ GeV/c (charged mode) and $40 - 160$ GeV/c (neutral mode) were used. This is first time the $K \rightarrow \pi^0\pi^0$ decay has been used to measure τ_S. The statistical power was comparable for each decay mode. The fit fixed ϕ_{+-} to the superweak phase, and floated Δm. The regeneration phase was determined via analyticity from the

power-law exponent of the regeneration. This measurement alone is more accurate than all previous ones combined.

10.2.2 The K_L - K_S Mass Difference, Δm

The measurement of Δm is confounded by its correlations with other parameters, such as τ_S and ϕ_{+-}. In addition to older, imprecise experiments, others which are uncorrectable to current parameter values have also been dropped from the averages. For many years, the value of Δm was based on only three surviving measurements. The experiments are summarized in Table 22 and a plot of their results is shown in Figure 64.

The experiment of Cullen, *et al.* [164], at the CERN Proton Synchrotron, used a variation on the famous 'gap method' [165] of measuring Δm with regenerators and $K \to \pi^+\pi^-$ decays. The setup used insensitive to the value of τ_S and the effects of CP-violation. In particular, a quantity was constructed which had a zero crossing as a function of proper time which was independent of τ_S but sensitive to Δm. However, fitting this zero crossing involved data in a larger proper time region, where some sensitivity to τ_S is present; unfortunately this was not quantified. This experiment was done in 1970, before the 5-σ shift in the value of τ_S from $(0.862 \pm 0.006) \cdot 10^{-10}$ s to a more modern value near $0.892 \cdot 10^{-10}$ s (see above). There is no discussion of systematics.

The next input comes from a pair of measurements: Geweniger, *et al.* [166], and Gjesdal, *et al.* [167], both performed by the one collaboration at CERN. The first utilizes a modified gap method similar to Ref. [164]. Data from 3.5 to 13 GeV/c are fit. They fix $\tau_S = 0.8937 \cdot 10^{-10}$ s, [1] $|\xi|$, and ϕ_ξ. Here, $\xi = \eta_{+-}/[i\,(f - \bar{f})/k]$, which is parameterized as $\xi = \sqrt{p} \times 0.54 \times 10^{-4} exp(i\ 1.58)$ mb^{-1} GeV$^{-1/2}$. Dependences on each of these are quoted, and are relatively small. In particular, the τ_S dependence is negligible given current errors. The ξ dependences are added as systematics; the sizes of the errors as well as the quoted parameterization, are derived from an auxiliary experiment (we do not know of a publication of these results, but the errors claimed are reasonable). However, the assumption of no momentum dependence of ϕ_ξ and the simple momentum dependence of $|\xi|$ are potentially

[1] The paper states $\Gamma_S = 1.1119 \cdot 10^{10}$ s^{-1}, but their previous result [159] was $\Gamma_S = 1.119 \cdot 10^{10}$ s^{-1}. Presumably, this is a typographical error.

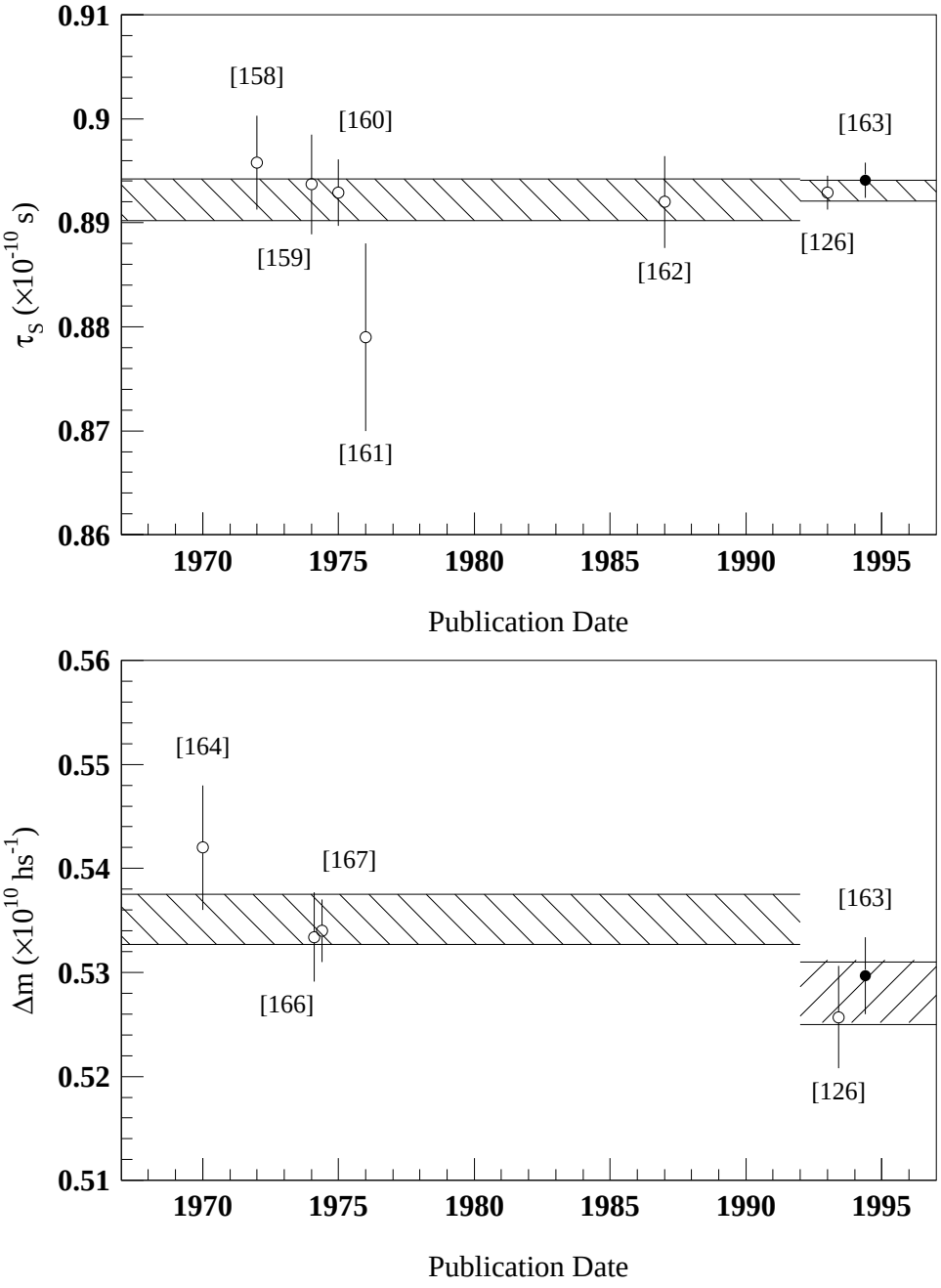

Figure 64. A plot of the history of measurements of Δm and τ_S. The upper plot shows measurements of τ_S; the bands show the world average in 1992, before E731, and the current average with all experiments. The lower plot shows measurements of Δm. The first band is the average of the three older experiments; the second band is the average of E731 and E773. The numbers give the reference(s) for each point.

Table 22. Summary of significant measurements of the K_L-K_S mass difference, Δm.

Experiment	Δm $10^{10}\ \hbar s^{-1}$	Error $10^{10}\ \hbar s^{-1}$	Technique	Energy GeV	Decay Region (m)
Cullen [164]	0.542	0.006	gap $\pi^+\pi^-$	low	~ 6
Geweniger [166]	0.5340	0.00255	gap $\pi^+\pi^-$	$3.5 - 13$	1
Gjesdal [167]	0.5334	0.0040	target $\pi^\pm\ell^\mp\nu$	$3 - 15$	9
Gibbons [126]	0.5257	0.0049	regen. $\pi\pi$	$20 - 160$	27
Schwingenheuer [163]	0.5288	0.0037	regen. $\pi^+\pi^-$	$20 - 160$	35

dangerous simplifications in light of nuclear screening effects at low energy, as well as the proximity to the resonance region which influences the phase through the dispersion relations (see Appendix C). The total parameter dependence corresponds to $\pm 0.0007 \cdot 10^{10}\ \hbar s^{-1}$. A systematic due to the momentum scale is also included. The second measurement uses the time-dependent charge asymmetry in $K \to \pi^\pm \ell^\mp \nu$ decays. Both electron and muon modes are analyzed and averaged. Corrections are applied,[2] with corresponding systematic uncertainties, for absorber and collimator effects, background to $K \to \pi^\pm \mu^\mp \nu_\mu$, and radiative $K \to \pi^\pm e^\mp \nu_e$ decays. There is also a momentum scale error, which is common with the first technique [168]. The error from τ_S dependence is again minimal.

The result of Gibbons, *et al.* [126, 136], is from the same data set as the τ_S measurement above. In the fit, ϕ_{SW} is floated and τ_S is fixed to $0.8922 \cdot 10^{-10}$ s. This was the first new determination of Δm in almost 20 years. It suggests the possibility that the value of Δm is lower than previously thought. As pointed out in [126], such a lowering of Δm will have a profound impact on the value of ϕ_{+-} and the CPT tests performed with it. Note that the PDG adopted a different Δm value than reported in the PRL, Ref. [126], preferring the fit described here.

10.2.3 The Phase of η_{+-}

[2] Apparently, another typographical error has crept in here, and the correction listed as $(0.0012 \pm 0.005) \cdot 10^{10}\ \hbar s^{-1}$ should read $(0.0012 \pm 0.0005) \cdot 10^{10}\ \hbar s^{-1}$.

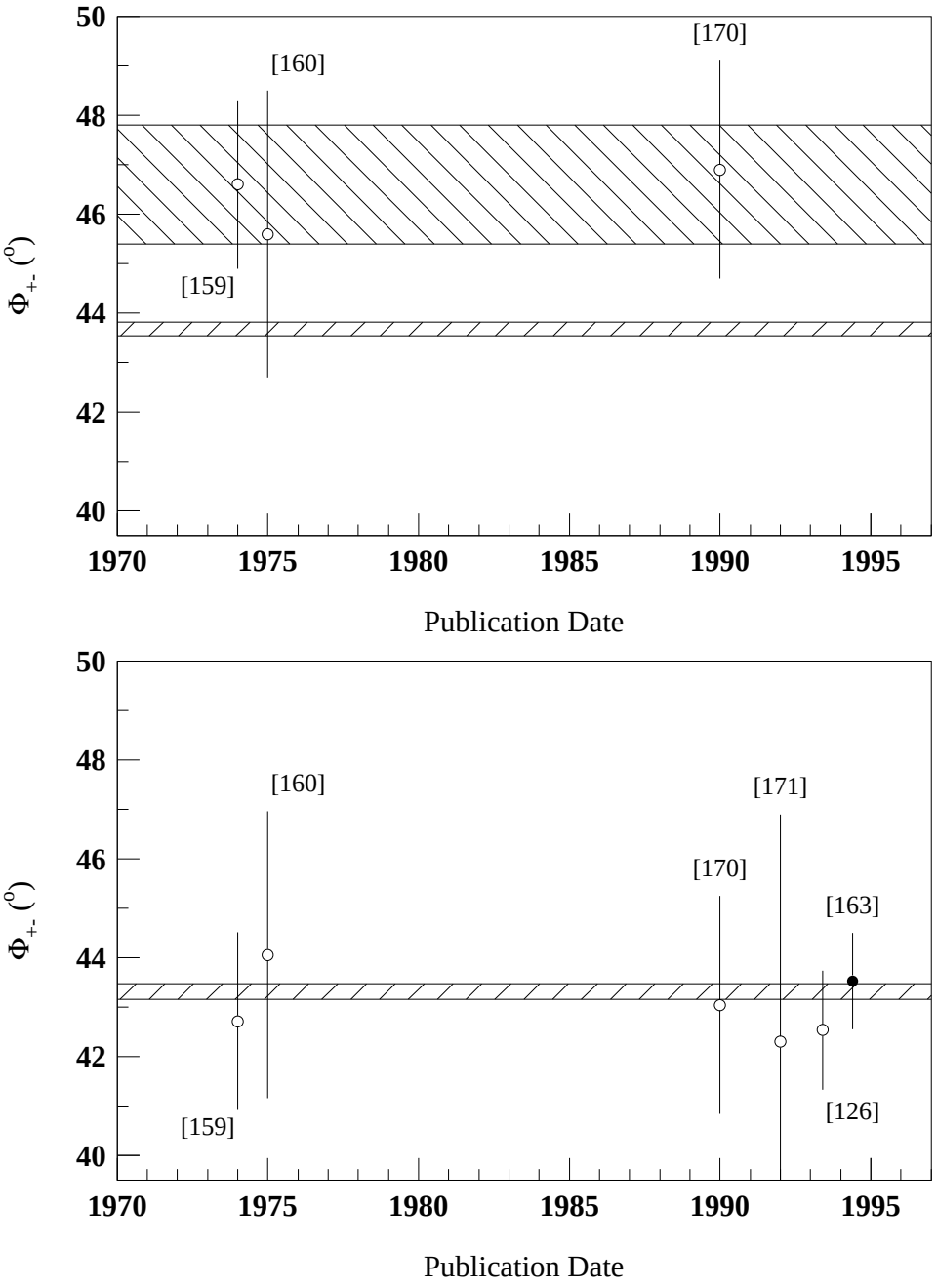

Figure 65. A plot of the history of measurements of ϕ_{+-}. The upper plot shows all measurements as of 1992; the wide band is the average and the narrow band is the value of ϕ_{SW}. The lower plot shows the current situation. The band is the value of ϕ_{SW}. The E731 and E773 results are included and the results adjusted to the E731-E773 value of Δm. The numbers give the reference for each point. The average is dominated by our measurement; there are large correlations due to the dependeces on Δm and τ_S.

Table 23. Summary of significant measurements of ϕ_{+-}, the phase of etapm. All values are quoted at $\Delta m = 0.5282 \cdot 10^{10}\ \hbar s^{-1}$ and $\tau_S = 0.8926 \cdot 10^{-10}$ s. The τ_S and Δm sensitivites are used as follows: the Carosi result is $\phi_{+-} = 43.03 \pm 1.6 + 579(\Delta m - 0.5282) + 303(\tau_S - 0.8926)$. Note that the central value of Adler is *not* adjusted, see text.

Experiment	ϕ_{+-} degrees	Error degrees	Δm sens.	τ_S sens.	Technique
Geweniger [159, 169]	42.73	1.0	565	(float)	target
Carithers [160]	44.02	2.8	224	(float)	regenerator
Carosi [170]	43.03	1.6	579	303	target
Adler [171, 172]	42.30	4.4			tagged K^0,$\bar{K}^0$
Gibbons [126]	42.49	0.9	189	-460	regenerator
Schwingenheuer [163]	43.53	0.76	167	-275	regenerator

The value of ϕ_{+-} is discussed last due to the dependence of its value on τ_S and Δm. Hopefully, the reader now has some feeling for experimental determinations that give us these parameters. A summary of the experimental results is given in Table 23; they are also plotted in Figure 65.

The experiment of Geweniger, *et al.* [159, 169], was described above when we discussed measurements of τ_S.

The experiment of Carithers, *et al.* [160], was also described above. The $K \to \pi^+\pi^-$ data was fit for $\phi_\rho - \phi_{+-}$. The regeneration phase, ϕ_ρ, is measured independently by the same collaboration from $K \to \pi^\pm \ell^\mp \nu$ decays [125].

The Carosi, *et al.* [170], result is from a special run by the NA31 collaboration at CERN. This is a target experiment, but the target is alternated each day between two different positions 14.4 m apart. The ratio of events from the two positions is analyzed to reduce sensitivity to acceptance. Kaons from $70-170$ GeV/c in a 48 m vacuum decay region are used. Dependences of the result on values of Δm and τ_S are quoted; a dependence on η_{+-} is not quoted.

The CPLEAR collaboration at CERN has also been producing new results. The PDG quotes Adler, *et al.* [171, 172], for a value of ϕ_{+-} based on the 1989/1990 data. Note that

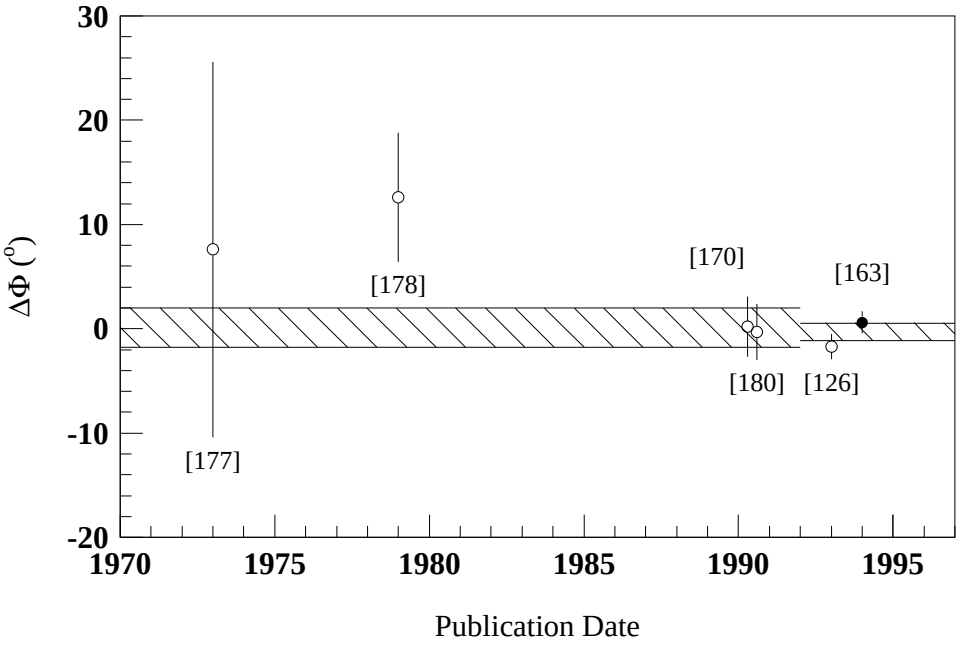

Figure 66. A plot of the history of measurements of $\Delta\phi$. The solid point is our measurement. The wide band is the world average in 1992; the narrow band is the new wolrd average with the results of E731 and E773 averaged in. The numbers give the reference for each point.

the result is quoted at $\Delta m = 0.5351 \cdot 10^{10}\ \hbar s^{-1}$, but that the *sign* of the dependence on Δm is not given; hence, we have not corrected the central value in the table. The magnitude of the correction is 2.9°. There have also been journal publications [173, 174, 175], albeit based on conference talks, with results from the 1990/1991 data. Many more recent results have since been shown at other conferences [101, 176]. This experiment uses the reactions $p\bar{p} \to K^0 K^- \pi^+, \bar{K}^0 K^+ \pi^-$ for production. Charged particle identification then allows tagging of the initial state as a K^0 or $\bar{K}^0$. This allows some novel tests and techniques not otherwise available.

Gibbons, *et al.* [126], also measured ϕ_{+-} in addition to τ_S and Δm.

We also display, for completeness, a plot of measurements of $\Delta\phi$in Figure66, including the older results of Refs. [177, 178, 179, 180]. This quantity should be equal to zero if CPT is a good symmetry. The most recent measurement is from our experiment; further details are given in Ref. [141].

10.3 Interpretation of Results

The basic test of CPT we set out to perform was a comparison of ϕ_{+-} and ϕ_{sw}. These quantities should be equal if CPT is a good symmetry. We have performed the first measurement of ϕ_{+-} with a sensitivity of better than 1°. The result is in good agreement with expectations based on CPT invariance. In addition, our new measurement of Δm is consistent with the low value obtained by E731. As discussed above, this value is itself very important to CPT tests with ϕ_{+-}.

The result of E773 for ϕ_{+-} and the combined E773 and E731 result for $\Delta\phi$ may be combined to obtain a limit on the K^0-$\bar{K}^0$ mass difference. Such an analysis yields [94, 181]

$$\frac{|m_{K^0} - m_{\bar{K}^0}|}{m_{K^0}} \simeq \frac{2\Delta m}{m_{K^0}} \frac{|\eta_{+-}|}{\sin\Phi_{sw}} |\Phi_{+-} - \Phi_{sw} + \Delta\Phi/3| \tag{10.8}$$

With the E773 ϕ_{+-} and $\Delta\phi$, the E731-E773 average Δm and the PDG τ_S, we find that

$$\frac{|m_{K^0} - m_{\bar{K}^0}|}{m_{K^0}} < 1.3 \cdot 10^{-18} \quad 90\% \text{ CL.} \tag{10.9}$$

We note that there are many, often related, ways that CPT-violation limits are extracted. We mention the method of Sachs [34] and the Bell-Steinberger relation [93, 101, 182].

10.4 The Future of CPT Tests with Kaons

Many new efforts are underway to explore the mysteries of discrete symmetries in the neutral kaon system. The KTeV experiment at Fermilab is a large, new effort by many of the collaborators from E731 and E773 and others. The general setup is the same as E731, i.e., a single, two-interaction length regenerator. New features include incorporation of the active regenerator technique, construction of a pure CsI calorimeter, addition of TRD modules, and construction of improved photon veto modules. The new calorimeter will give much better energy resolution and better position resolution; this will help reduce backgrounds in neutral mode. The improved E/p resolution, coupled with a better response to pions, will lead to excellent rejection of $K \to \pi^{\pm} e^{\mp} \nu_e$ decays in the $K \to \pi^+\pi^-$ analysis with almost no bias from losses of showering pions. More care to limit material in the spectrometer and a

higher magnetic field will also improve the charged-mode resolution. The higher statistics will naturally benefit all measurements; in particular, they will allow a direct measurement of the regeneration phase from $K \to \pi^{\pm} e^{\mp} \nu_e$ decays to about 0.5°. In addition, the energy dependence of ϕ_ρ can be studied by measuring $\phi_\rho - \phi_{+-}$ with $K \to \pi^+\pi^-$ decays; we note that much of the statistical error on ϕ_{+-} is due to the uncertainty in the power-law exponent, α, which does not affect studies of this energy dependence. These last two measurements will help check our treatment of the regeneration phase.

CPLEAR is expected to publish new results on both Δm and ϕ_{+-} shortly. We look forward to confirmation of our low value of Δm.[3] In addition, we expect this experiment to produce other kaon measurements of interest. Tests of the $\Delta S = \Delta Q$ rule and measurements of η_{+-0} will help to firm up the expected equality of ϕ_{+-} and ϕ_{SW} (see Appendix A). The first direct observation of T violation is also on the horizon; effects over 2 standard deviations are in hand.

The KLOE detector at DAΦNE will be able to study kaons produced at the ϕ resonance beginning in 1996. The ϕ decays part of the time into coherent superpositions of neutral kaons. At Novosibirsk, an e^+e^- collider is already operating on the ϕ resonance at sub-factory luminosity. Much experience is being gained, and more luminosity is planned. A discussion of the possibilities of these ϕ experiments is beyond the scope of this thesis. Suffice to say there are many new angles (sic) to be explored.

10.5 Summary

Our measurement of ϕ_{+-} is the first with better that 1° precision. This measurement is a strong constraint on the possibility of CPT violation in the kaon system. We have also studied the systematics involving the regeneration phase, ϕ_ρ, in great detail for the first time and have shown that high-energy measurements using regenerators have still not reached their ultimate level of precision. In addition, we have made excellent measurements of Δm and τ_S the two parameters crucial for determining ϕ_{SW}. Our value of Δm is particularly interesting since it is one of a small number of recent results, all of which yield lower values

[3] The value $(0.5290 \pm 0.0036) \cdot 10^{10}\ \hbar s^{-1}$ was presented at a German Physical Society meeting recently.

than the older experiments. This is important since the measurement of ϕ_{+-} is particularly sensitive to the value of Δm.

In conclusion, although we have advanced the state of the art, CPT is still found to be a valid symmetry of nature.

APPENDIX A

Notes on Kaon Phenomenology

A few points of kaon phenomenology are explained in more detail here. The notation was introduced in Chapter 1. We note also that a convenient solution of the mass-matrix eigenvalue problem is given in Ref. [95].

A.1 Discussion of the Phase of ε_T

We now discuss the value of ϕ_ε in the case that CPT is a good symmetry. We work in the Wu-Yang phase convention such that $\varepsilon = \varepsilon_K = \varepsilon_T$. The expression for ε_K in terms of the mass matrix is

$$\begin{aligned} \varepsilon_K &\simeq \frac{-ImM_{12} + (i/2)Im\Gamma_{12}}{i(\lambda_S - \lambda_L)} \\ &= \frac{e^{\,i\phi_{SW}}}{\sqrt{2}\kappa\Delta m}\left[-ImM_{12} + (i/2)Im\Gamma_{12}\right] \end{aligned} \tag{A.1}$$

where

$$\kappa \equiv \sqrt{\frac{1}{2}\left(1 + \left(\frac{\Gamma_S - \Gamma_L}{2\Delta m}\right)^2\right)} \simeq 1 \tag{A.2}$$

Thus, one sees that $\phi_\varepsilon \simeq \phi_{SW}$ as long as $Im\ \Gamma_{12}$ is small. We now discuss the contributions to Γ_{12}, which comes from a sum over decay channels (see Eqn. 1.23).

- Γ_{12} is dominated by the $I = 0\ \pi\pi$ channel. With the Wu-Yang phase convention, this is *real*.

- The $I = 2$ term in $Im\ \Gamma_{12}$ is negligible since ε' is small.
- The semileptonic terms are negligible unless there are large violations of the $\Delta S = \Delta Q$ rule.
- The 3π terms are also small, unless there are anomalously large deviations from the expectation that $\eta_{3\pi} \simeq \varepsilon$.

If we are willing to make the assumptions about semileptonic and 3π contributions, then $\phi_\varepsilon - \phi_{SW}$ is essentially zero. If we demand that only experimental information be used for the $\Delta S = \Delta Q$ rule and CP-violation in the 3π final states, then we find that $\phi_\varepsilon - \phi_{SW} < 1.6^\circ$ [101]. We note that experimental progress is being made on checking both of these assumptions more closely.

Another effect to consider is the difference between ε and η_{+-}, namely ε'. Since ε' is not parallel to ε, it contributes to $\phi_{+-} - \phi_{SW}$ also. But, we know that ε' and ε are parallel to about 10° and that ε'/ε is small. This contribution is then about 0.02°, and need not concern us at our current precision.

A.2 Discussion of the Phase of ε_{CPT}

We now examine the relative phases of ε_T and ε_{CPT}. The derivation is based on one in Ref. [98]. The expression for δ_K in terms of the mass matrix is

$$\begin{aligned} \delta_K &\simeq \frac{iM_{11} - M_{22} + (\Gamma_{11} - \Gamma_{22})/2}{2\ i(\lambda_S - \lambda_L)} \\ &= \frac{i\ e^{i\ \phi_{SW}}}{2\kappa\sqrt{2}\Delta m}\,[M_{11} - M_{22} - (i/2)(\Gamma_{11} - \Gamma_{22})] \end{aligned} \tag{A.3}$$

If we take Γ_{11} and Γ_{22} to be dominated by $I = 0$ amplitudes, then

$$(\Gamma_{11} - \Gamma_{22})/\Delta\Gamma \simeq 2\ ReB_0/ReA_0 \tag{A.4}$$

We are assuming $B_0 >> B_2$. The analogous A amplitudes are known to obey a similar relation; this is just the $\Delta I = 1/2$ rule. Assuming that the $I = 0$ amplitudes are dominant in the CPT-violating sector, as they are in the CPT-conserving sector, may be somewhat questionable.

Using

$$2\Delta m/\Delta\Gamma \simeq 1 \longrightarrow \phi_{sw} \simeq 45^{\circ} \tag{A.5}$$

and therefore

$$1 - exp(i\phi_{sw})/\sqrt{2} \simeq -i\ exp(i\phi_{sw})/\sqrt{2}, \tag{A.6}$$

we can now combine the last four equations to show

$$\frac{ReB_0}{ReA_0} - \delta_K \simeq \frac{-i}{\sqrt{2}}\left[\frac{M_{11} - M_{22}}{2\ \Delta m} + \frac{ReB_0}{ReA_0}\right] e^{i\phi_{sw}}, \tag{A.7}$$

which is manifestly perpendicular to $e^{i\phi_{sw}}$ and ε.

APPENDIX B

Kaon Production Spectrum

It is desirable to have a good parameterization of the kaon spectrum in our experiment. In principle, the spectrum can be determined from the data, but some effects are hard to extract precisely. Variations in the spectrum as a function of production angle, which varies across the beam, and the size of the K_S component (the 'dilution factor') are both small effects where some external guidance is helpful.

At high energies, enough K_S survive after 100 m to warrant a correction to the approximation of a pure K_L beam. For E773, it is a very small correction due to the regenerators: these create many more K_S than remain from the target and absorbers, and they also restrict the beginning of the decay volume to be after 117 m. In an experiment with a vacuum beam, such as E731, the correction from the presence of K_S far upstream at the highest energies is sufficient to double the decay rate.[1]

One would like to have a reasonable starting spectrum, preferably with a parameterization based on the typical behavior of hadroproduction data. More data is available for charged kaons and one relates this to neutral production using isospin. The spectrum will need some tuning due to the sparseness of available data and the extrapolations involved.

A good starting point is the Malensek fit [152] to the Atherton et al. data [153] on K^+ and K^- production by protons on Be. Naively, it might be assumed that one can simply replace K^+ by K^0 and K^- by $\bar{K}^0$.

[1] Note that Figure 115 in Ref. [136] shows the correction from primary K_S in each bin relative to the total of all events in the fit p-z region, not relative to the bin itself. This gives the appropriate impression for the effect on ε'/ε, which essentially counts events. One should be aware, however, that the effect on certain individual bins is quite large.

This is the same as assuming

$$K^0 \ + \ \bar{K}^0 = K^+ \ + \ K^- \tag{B.1}$$

and

$$\frac{K^0 \ - \ \bar{K}^0}{K^0 \ + \ \bar{K}^0} = \frac{K^+ \ - \ K^-}{K^+ \ + \ K^-} \tag{B.2}$$

The reason for rewriting the two equations in a symmetric manner will become clear shortly; these equations give the physically interesting quantities. In these equations, I refer to the number of particles per unit solid angle produced at some fixed polar angle and momentum; I suppress the p and θ dependences and avoid constructions like $N_{\bar{K}^0}$ for simplicity: an implicit 'number of' is understood.

At first glance, Eqns. B.1 and B.2 might seem to follow from isospin symmetry. However, one must isospin reflect the initial state as well as the final state particles. Isospin relates $pBe^9 \rightarrow K^+X$ to $nB^9 \rightarrow K^0X$, which is not useful to us. A more sophisticated argument that will take us from charged to neutral kaons is needed.

A better relation between charged and neutral kaon production is given by

$$K^0 \ + \ \bar{K}^0 = (K^+ \ + 3 \ K^-)/2 \tag{B.3}$$

and

$$\frac{K^0 \ - \ \bar{K}^0}{K^0 \ + \ \bar{K}^0} = \frac{K^+ \ - \ K^-}{K^+ \ + \ 3K^-} \tag{B.4}$$

Let us attempt to motivate this form.

First, recall the quark content of the particles involved:

$$p = (uud) \qquad K^+ \ = (u\overline{s}) \qquad \bar{K}^0 \ = (\overline{d}s) \tag{B.5}$$

$$n = (udd) \qquad K^0 \ = (d\overline{s}) \qquad K^- \ = (\overline{u}s) \tag{B.6}$$

The valence partons in the target and projectile are all quarks (i.e., no anti-quarks), so we will clearly have to consider the contributions of $q\overline{q}$ pairs to explain kaon production. We will take the usual isospin assumption of $u\overline{u} = d\overline{d} \neq s\overline{s}$ for the sea parton distributions.[2] If we consider only one $q\overline{q}$ pair it must be an $s\overline{s}$ pair in order to get any kaons at all.

[2]Recall that the $q\overline{q}$ pairs communicate with the valence quarks through gluons, which do not sense the valence flavors at all. We distinguish $s\overline{s}$ because of mass; it will turn out not to matter, since there is exactly one strange quark in each kaon and hence any effect drops out of all ratios.

We will now make one crucial deduction. Since we are at high energies and produce a secondary beam at small angles, the meson production we wish to model is very forward. Therefore, only the valence quarks from the projectile proton (and not those in the target) will be relevant to this forward regime; the target valence quarks will simply not backscatter hard enough to show up in our beams. So, we will either

- Take a valence quark from the projectile proton and a sea antiquark.
- Take both the quark and the antiquark from the sea.

The probability of acquiring a $u\overline{u}$ or $d\overline{d}$ from the sea is denoted as x and the 'probability' of acquiring a $s\overline{s}$ as y. We then find the following *relative* production rates by simple quark-counting[3]

$$K^+ \sim 2y + xy \tag{B.7}$$

$$K^0 \sim y + xy \tag{B.8}$$

$$\bar{K}^0 \sim xy \tag{B.9}$$

$$K^- \sim xy \tag{B.10}$$

This implies

$$K^0 \sim (K^+ + K^-)/2 \tag{B.11}$$

$$\bar{K}^0 \sim K^-. \tag{B.12}$$

Simple algebra reproduces the relations in Eqns. B.3 and B.4. Note that we could have a distinct y parameter for valence-sea and sea-sea terms without any change in the outcome.

A few comments of a more general nature concerning the spectrum in our Monte Carlo are in order. First, the Malensek spectrum is an rough parameterization: the data was limited, particularly as a function of production angle, and it is fit to an empirically-motivated functional form. We are also extrapolating up in energy from the original data, assuming some scaling to hold. In consequence, E731 tuned the spectrum to reproduce the observed

[3]The term with a valence quark alone would give a situation where we only get $q\overline{s}$ states. These are, in fact, more plentiful than $\overline{q}s$ states. One usually argues this based on associated production: it is energetically easy to 'excite' a nucleon to a hyperon by interchanging one of the nucleon quarks with an s, leaving the $\overline{s}$ to form a meson.

vacuum beam decay rate. This rate is not very sensitive to propagation through the target and absorbers because of the long vacuum evolution before the decay volume; the full forward propagation through matter as well as the elastic diffraction effects are put in according to the best available information. The tuning was accomplished with a quartic function of the momentum. The multiplicative correction varies from 1.0 at 0 GeV to about 1.5 at 150 GeV and then decreases. Note that this correction is applied *both* to the K^0 and $\bar{K}^0$ spectra. That is, we tune only

$$N(p) = K^0 + \bar{K}^0 \tag{B.13}$$

and not

$$D(p) = \frac{K^0 - \bar{K}^0}{K^0 + \bar{K}^0}. \tag{B.14}$$

The second expression $D(p)$ is known as the 'dilution factor'; we now demonstrate its relevance.

A given interaction in our target produces either a K^0 or a $\bar{K}^0$. These are each *coherent* mixtures of K_L and K_S but are *incoherent* with each other. Ignoring ε in the state-mixing, we have

$$K^0 \sim K_S + K_L \tag{B.15}$$

$$\bar{K}^0 \sim K_S - K_L. \tag{B.16}$$

Note the sign change between the K_S and K_L components. Denote the number of K^0 and $\bar{K}^0$ produced at a given momentum as n and $\overline{n}$, respectively. Then, the decay rate may be written as

$$R = \frac{n}{2}\left[|S|^2 + |L|^2 + 2Re(SL^*)\right] \tag{B.17}$$

$$\bar{R} = \frac{\overline{n}}{2}\left[|S|^2 + |L|^2 - 2Re(SL^*)\right]. \tag{B.18}$$

This is easily rewritten as

$$R_{tot} = R + \bar{R} = \frac{1}{2}N(p)\left[|S|^2 + |L|^2 + 2D(p)Re(SL^*)\right]. \tag{B.19}$$

R_{tot} is what we one sees experimentally (in a vacuum beam), since, in general, there is no tagging of K^0 and $\bar{K}^0$. One immediately sees that the interference term is *diluted* by $D(p)$

in magnitude compared to a pure tagged beam. This is not the interference we fit, of course; we use the coherent regeneration from our regenerator. We are only discussing the effect of an incoherent sum of K^0 and $\bar{K}^0$ from a target now.

Since the vacuum beam is dominated by K_L decays, it is easy to directly tune $N(p)$; the rate simply scales with it. Tuning $D(p)$ in our experiments is very difficult since the so-called 'Primary K_S' from the target die away for all but the highest p and most upstream z in our sample. Since ϵ'/ϵ is essentially a counting experiment, the double ratio technique makes the result very insensitive to $D(p)$. For interference curve fitting, one must be a bit more careful in principle since the $D(p)$ term oscillates, but the effect is negligible for the same reason that it is hard to determine from the data. Note that for NA31, which gets its K_S flux from a target, $D(p)$ is very important. In fact, they measure it in their data [170, 183], and it agrees reasonably well with Eqns. B.3 and B.4 but not Eqns. B.1 and B.2. Note that the dilution factor is less than unity, and hence the interference is partly washed out in target experiments. In a regenerator experiment, the K_S are fully coherent with the K_L: there is no dilution. This helps compensate for the small magnitude of the regeneration amplitude, ρ.

The pronounced asymmetry in the K^0 and $\bar{K}^0$ production spectra due to the interplay between associated production and baryon number conservation. Were K^0 and $\bar{K}^0$ produced with equal spectra, we would have $D(p) = 0$ and the interference would not be observable in a target experiment! Also, a more CP-symmetric target experiment with matter and antimatter beams simultaneously hitting matter and antimatter targets would also wash the effect out. In all cases, one still observes the $K_L \rightarrow 2\pi$ decays after the K_S are depleted. However, the observation of interference from a coherent K_S-K_L superposition after a regenerator [184] was an important confirmation of the original observation of CP-violation [32], ruling many possible alternate interpretations involving non-identical final states.

We note that flavor tagging to distinguish K^0 and $\bar{K}^0$ would be very difficult in practice after a target, but has been done by CPLEAR using the reactions $p\bar{p} \rightarrow K^+\bar{K}^0\pi^-, K^-K^0\pi^+$ at the CERN LEAR storage ring. One then observes interference with no dilution *and* a

K_S-K_L ratio of one, barring a significant rate of mistags. Other tricks are available with kaon pairs from ϕ decays.

Finally, we mention that the arguments presented for relating charged and neutral kaon production are a bit simplistic. In particular, we have ignored the feed-down from the decay of the low-lying resonance states (i.e., $K^*(890)$), which are copiously produced. Efforts at including this and other effects may be found in Refs. [185, 186, 187].

APPENDIX C

Dispersion Relations

C.1 Some Basic Integral Dispersion Relations

Dispersion relations have been used in particle physics since the 1950s [188], but their roots in physics go back to the Kramers-Kronig relation for the index of refraction of light in a medium [189, 190]

$$n(\omega) - 1 = \frac{c}{\pi} \int_{-\infty}^{\infty} dx \, \frac{\beta(x)}{x^2 - E^2} \tag{C.1}$$

where the total index, $n + i(c\beta/2\omega)$ is decomposed into a real part, n, describing the phase velocity, and a real extinction coefficient, β, describing the absorption. We will see that this is precisely the form of the relations used in particle physics; this is not surprising since it rests on the same physical principles.

The derivation of such relations relies on the use of causality and the analytic behavior of functions. Causality severely restricts the behavior of amplitudes, or rather their continuations into the complex plane, and simple applications of Cauchy's theorem are all that is needed to derive the basic relations. A general review may be found in Ref. [191], for example.

In our discussion here, we will often overlook some of the subtleties involved with respect to ranges of integration, poles, and threshold effects. We caution the reader, however, to bear this in mind before blindly applying any of the equations given here. We also note that one should be careful in principle to distinguish p from E from the Mandelstam $\sqrt{s}$;

at our energies, however, the differences are negligible and we often write p where it is only an approximation.

It is easiest to deal with the symmetric and antisymmetric combinations of the amplitudes. Instead of using the amplitude, f, for AB scattering and $\bar{f}$ for $\bar{A}B$ scattering, we use

$$f_{\pm}(E) = [f(E) \pm \bar{f}(E)]/2 \tag{C.2}$$

which satisfies

$$f_{\pm}(E) = \pm f_{\pm}(-E). \tag{C.3}$$

Note that our normalization is such that $\sigma_T = (4\pi/k)Imf$. We first display the standard dispersion relations for the scattering amplitudes [192]

$$Ref_{+}(E) = P\frac{2}{\pi}\int_0^{\infty} x\,dx\,\frac{Imf_{+}(x)}{x^2 - E^2} \tag{C.4}$$

$$Ref_{-}(E) = P\frac{2E}{\pi}\int_0^{\infty} dx\,\frac{Imf_{-}(x)}{x^2 - E^2} \tag{C.5}$$

where P denotes principal value.

The different forms for even and odd amplitudes arise from the different symmetry properties of the amplitudes under $E \to -E$. This enters when the contour integral is reduced: only the integral along the real axis is kept, but it runs from $-\infty$ to ∞. The symmetries of the amplitudes are then used to relate the integral from $-\infty$ to 0 to that from 0 to ∞.

One often needs to use 'subtracted' dispersion relations, because those given above do not always converge. For example

$$Ref_{+}(E) = ERef_{+}(0) + P\frac{2E^2}{\pi}\int_0^{\infty} dx\,\frac{Imf_{+}(x)}{x(x^2 - E^2)} \tag{C.6}$$

$$Ref_{-}(E) = ERef_{-}{}'(0) + P\frac{2E^3}{\pi}\int_0^{\infty} dx\,\frac{Imf_{-}(x)}{x^2(x^2 - E^2)} \tag{C.7}$$

where $f'(x) \equiv df/dx$. Note that the first relation above may be obtained by explicitly subtracting Eqn. C.4 for Ref_{+}, evaluated at E and 0. It may also be obtained by inserting the odd amplitude, f_{+}/E, into Eqn. C.5 in place of f_{-}. The second relation may be obtained by inserting the even amplitude, f_{-}/E, into Eqn. C.4 in place of f_{+}. With the

substitution method, one must be careful about the pole at $E = 0$, which gives rise to the first terms on the right-hand side of the equations.

We note that one may also write inverse dispersion relations, relating Imf to an integral over Ref. One performs a similar mathematical derivation starting with the function $g = if$. Furthermore, by considering the function $g = logf = log|f| + i\phi_f$, we may apply the dispersion relations to g and thus relate the magnitude and phase of a scattering amplitude. Once again, some care must be taken in a proper derivation [193, 194, 195].

There are also pole terms as well as threshold effects at low energy; these have been treated by many authors (see Ref. [196] for a review). Threshold effects refer to contributions arising from energies $M_\Sigma < E < M_K + M_N$ due to the cut in the complex plane extending below the energies of physical scattering.

We may also ask what is the qualitative effect of deviations from a power-law behavior when these deviations are outside the energy range of our experiment. It is easy to show from the dispersion integrals that a distortion at low energy causes a correction to the result of the integral of the form c/E^2, while one at high energy causes a correction of the form cE; c is some constant in both cases. If one applies these results to a phase-magnitude dispersion relation, then the *shape* of the change from a constant phase in the range of an experiment due to changes in the power law outside its energy range is known. This will be useful when we study the regeneration phase systematic in more detail in Appendix H. Note that we expect high energy behavior of the amplitudes to be quite smooth. In addition, the known distortions at low energy, from resonances and thresholds, give effects that die away as $1/E^2$ and become quite small at high energy. We thus expect that the dispersion relations largely tell us about local behavior; we follow up on this in the next section.

C.2 Derivative Dispersion Relations

We now turn to a discussion of derivative dispersion (analyticity) relations, which we abbreviate as DDR (or DAR).

Skipping the technicalities, a DAR for f_- may be written as [197, 198, 199]

$$Re\left(\frac{f_-}{p^\alpha}\right) = tan\left[\frac{\pi}{2}\left(\alpha + \frac{d}{d\,ln\,p}\right)\right] Im\left(\frac{f_-}{p^\alpha}\right) \tag{C.8}$$

for arbitrary f_- and α. Some of the more detailed derivations are found in Refs. [200, 201]. Recalling that $tan(\frac{\pi}{2}\alpha) = cot(-\frac{\pi}{2}(\alpha+1))$, a little algebra shows that for a power law $f_- \sim p^\alpha$ this gives the usual analyticity relation, $\phi = -(\pi/2)(1+\alpha)$. For a constant f_-/k (i.e., $\alpha = 1$), f_- is purely real.

For f_+, one has

$$Re\left(\frac{f_+}{p^\alpha}\right) = tan\left[\frac{\pi}{2}\left(\alpha - 1 + \frac{d}{d\,ln\,p}\right)\right] Im\left(\frac{f_+}{p^\alpha}\right) \tag{C.9}$$

which give the analyticity relation, $\phi = -(\pi/2)\ \alpha$. For a constant f_+/k, f_+ is purely imaginary. Thus, nearly flat high-energy total cross-sections correspond to amplitudes that are largely imaginary.

These DARs hold exactly for the Regge parameterizations introduced in Appendix D. This is easily checked for the power laws and the Pomeron parameterization. For example, Eqn. C.9 applied with $\alpha = 1$, demands that the Pomeron obey $ReF = (\pi/2)\,(d\,ImF/d\,ln\,p)$.

The DARs are linear in F, hence a sum of two solutions also satisfies them. They also hold for products of solutions, such as those that occur in the Glauber series, since these also define valid amplitudes.

APPENDIX D

Regge Theory and Scattering Amplitudes

We will now present a brief introduction to Regge Theory; more detailed discussions may be found in Refs. [202, 203, 204, 205]. The discussion will be phrased in terms of KN scattering, but the results are general.

D.1 Introduction to Regge Theory

Through manipulations in the complex plane (the Sommerfeld-Watson transformation [204]), a scattering amplitude may be written as a sum of several pole contributions, each arising from a t-channel exchange of a 'Regge pole'. The dominant Regge poles for our purposes are the ω, ρ, A_2, and f. Each pole has various quantum numbers such as isospin and parity affecting whether or not it may be exchanged in a given scattering process. The poles listed above each occur for all four elastic (non-charge-exchange) neutral kaon-nucleon scatterings: $K^0p, \bar{K}^0p, K^0n, \bar{K}^0n$. The charged kaon processes are related by isospin; for example, $f(K^0p) = f(\bar{K}^0n)$. The poles enter each process with varying signs depending on the particular choice of K and N isostates. In addition, there is also a special Reggeon, the Pomeron (P), that also contributes to all these processes. We will see that while the effects of the other poles decrease with energy, the Pomeron exchange causes a roughly constant contribution. The Pomeron was originally inserted into the theory to explain the experimental observations; now there is a small industry trying to coax its existence out

of QCD via color-singlet two-gluon exchange and gluon ladders. Note that the two-gluon color-singlet is necessarily symmetric and only contributes to f_+.

We define $F = (4\pi/k)f$, where f is the usual scattering amplitude, such that $\sigma_{tot} = Im\,F$. Then we can write the contribution of a given Regge pole i as

$$F_i = \beta_i(t)\,\frac{1+\epsilon_i\,e^{-i\pi\alpha_i}}{sin\,(\pi\,\alpha_i)}\,\frac{1}{2m_N p_L}\left(2m_N\sqrt{p_L^2+m_K^2}\right)^{\alpha_i} \tag{D.1}$$

where p_L is the lab momentum.

The strength of a pole is governed by the residue, $\beta_i(t)$. The next term, the 'signature factor', determines the phase; ϵ_i is the signature of the pole. In particular, $\epsilon_P = \epsilon_f = \epsilon_A = +1$ and $\epsilon_\omega = \epsilon_\rho = -1$. The rest gives a energy dependence of $E^\alpha/p \simeq p^{\alpha-1}$. The resulting relation between the phase and the energy dependence is precisely that required by analyticity through the dispersion relations. We mention that the signature factor is written in *many* superficially dissimilar but equivalent forms in the literature. For the negative-signature ω and ρ responsible for regeneration, it gives a phase of $-(\pi/2)(1+\alpha)$.

The KN amplitudes are written as follows:

$$F_{Kp} = F_P - F_f - F_\omega + F_\rho + F_{A_2} \tag{D.2}$$

$$F_{\bar{K}p} = F_P - F_f + F_\omega - F_\rho + F_{A_2} \tag{D.3}$$

$$F_{Kn} = F_P - F_f - F_\omega - F_\rho - F_{A_2} \tag{D.4}$$

$$F_{\bar{K}n} = F_P - F_f + F_\omega + F_\rho - F_{A_2}. \tag{D.5}$$

Note that the P, f, and A_2 cancel for regeneration, which is a K^0-$\bar{K}^0$ amplitude difference. Thus, only the ω and ρ cause regeneration. Furthermore, for an isoscalar target such as ^{12}C, only the ω term remains.

Note that α is a function of t; $\alpha(t)$ is known as a Regge trajectory. Here, t is the usual Mandelstam scattering variable, $t = -q^2$. The forward scattering, and hence total cross section, is controlled by $\alpha(0)$, the intercept. This name comes from the fact that for unphysical $t > 0$, the trajectory may be thought of as a curve in the $J - M^2$ (spin - mass−squared) plane. Real particles exist where the trajectory has integral values of J; i.e. $\alpha(M^2) = J$. Actually, they only occur for every other integer; whether they exist for even or odd J is related to the signature, ϵ. Empirically, if one plots the mesons (say,

the ω and ω_3, etc.) on such a 'Chew-Frautschi' plot, the trajectory is found to be rather straight. This can be further checked by extrapolating to zero, determining $\alpha(0)$ and hence the energy dependence for the corresponding Regge pole. These $\alpha(0)$ values can also be determined from scattering data [206], and the general agreement is quite reasonable. A useful parameterization is thus $\alpha(t) \simeq \alpha(0) + \alpha' t$. The Pomeron has $\alpha' \simeq 0.25$ $(\mathrm{GeV}/c)^{-2}$ while the other Regge pole typically have $\alpha' \simeq 0.9$ $(\mathrm{GeV}/c)^{-2}$.

The values of $\alpha(0)$ for the ω, ρ, A_2, and f poles all are of order 0.5. Thus, the contributions from these poles decrease as the energy increases. Naively, the Pomeron is just a Reggeon with $\alpha(0) = 1$; this makes its contribution independent of energy and purely imaginary. In order to fit actual data, this is not sufficient, and in practice one uses an effective physical Pomeron. The exact structure of the Pomeron, in terms of poles and cuts in the complex plane, is likely quite complicated. A popular general parameterization of the Pomeron is

$$F_P = i\,(A + B(logE - i\pi/2) + C(logE - i\pi/2)^2) \tag{D.6}$$

The combination $(logE - i\pi/2)$ gives the proper analytic behavior of log terms, in order to obey dispersion relations, see Appendix C.

The q^2 dependence is governed by $\beta(t)$ and α'. If we take $\beta(t) \sim e^{at}$ and the full dependence as e^{bt}, then $b = a + 2\alpha' ln(s)$. At high energies, the Pomeron dominates, and the forward slopes, b, for the processes KN and $\bar{K}N$ approach each other asymptotically; see Ref. [207] for plots of some relevant data.

D.2 Asymptotic Behavior of Amplitudes

We are now prepared to discuss the general structure of scattering amplitudes.

An intercept of $\alpha(0) = 1$ is the largest power allowed by the Froissart bound on the behavior of total cross sections. The Froissart bound limits the total cross section for any process to at most $log^2(E)$ growth. This is allowed for in the parameterization of the Pomeron given above. If C is non-zero, then the Pomeron saturates the Froissart bound (at least in terms of the energy dependence; one can also try to determine the maximal

coefficient, C.). It is not clear whether current high-energy data require a log^2 term; good fits may be done with $C = 0$ [208].

Another important asymptotic result is the Pomeranchuk Theorem; it states that the ratio of cross sections for KN and $\bar{K}N$ scattering must approach unity as $E \to \infty$. Note that the *difference* of the cross sections need *not* vanish; in fact it may even diverge as E grows! These relations are often written in terms of the Mandelstam scattering variable, $s \simeq 2mE$.

For the symmetric amplitude, $f_+ \equiv (f + \bar{f})/2$, only the Pomeron contribution remains at high energy. An term analogous to the Pomeron contributing to the antisymmetric amplitude, $f_- \equiv (f - \bar{f})/2$, may also be considered [209]; this 'Odderon' (O) may be parameterized as

$$F_O = A' + B'(logE - i\pi/2) + C'(logE - i\pi/2)^2 \qquad \text{(D.7)}$$

Note that the real part of F_O diverges as $log^2(E)$, but the imaginary part (which contributes to the total cross-section) only diverges as $log(E)$. It is easy to see that F_O may not have a higher log power that F_P or the Pomeranchuk theorem will be violated; an equal power is allowed, since the leading term in the Odderon is real, and does not contribute to the total cross section. Since it contributes to f_-, the Odderon causes regeneration; for the parameterization above, it leads to regeneration that is at least constant, if not growing, with energy. Recall that the Regge poles all gave regeneration which decreased with energy, since α cannot be greater than one. In QCD, one naively expects that F_O might be generated by three-gluon exchange, which contain both even and odd color-singlet pieces.

D.3 Summary

We have given a quick overview of some of the standard formulas encountered in the Regge picture of hadronic scattering. Details are left to the references; we intend this merely as a convenient summary of what is used in the other appendices.

APPENDIX E

Glauber Theory of Nuclear Screening

In this appendix, we present a quick introduction to the Glauber theory of screening in hadron-nucleus scattering. Further details may be found in Refs. [210, 211, 212, 213]. The basic task is to develop techniques to calculate the scattering amplitudes of hadrons and complex nuclei given the corresponding hadron-nucleon amplitudes. We also give the methods used to perform the detailed calculations used later in Appendix H to evaluate the regeneration phase systematic error.

E.1 Introduction to Screening

The classic problem of nuclear screening is the hadron-deuteron cross section deficit. The hadron-deuteron cross section is not simply a sum of the hadron-proton and hadron-neutron cross sections; there is a shadowing effect that decreases the result.

The standard Glauber formula[214], neglecting a minor complication [215] is

$$\sigma_{hd} = \sigma_{hp} + \sigma_{hn} - \frac{\langle r^{-2} \rangle}{4\pi} \sigma_{hp}\ \sigma_{hn} \tag{E.1}$$

where h, p, n, d are hadron, proton, neutron, deuteron; and r is the $p-n$ separation in the deuteron.

This problem is important for two reasons. First, it motivated much of the early work on screening. Second, this correction is required to get σ_{hn} from σ_{hd} since the latter is as close to a neutron target as we can easily achieve. These elementary cross sections are

a necessary input to the phenomenology which expresses the scattering from a complex nucleus as a function of the corresponding processes off elementary nucleons.

A nice symmetry to exploit is $\sigma_{\pi^{\pm}n} = \sigma_{\pi^{\mp}p}$ which follows from isospin. This allows one to extract the value of $\langle r^{-2} \rangle$ from the data. In practice, this same value has then been applied to KD scattering to extract σ_{Kn}, although assuming such an equality is somewhat questionable. In particular, there are inelastic screening effects which may differ for kaons and pions and hence complicate matters.

E.2 The Glauber Theory of Elastic Rescattering

We now give a complete discussion of the standard Glauber formalism.

E.2.1 The Basic Formulae

Near the forward direction, many partial waves contribute to f. One may let the angular momentum quantum number, l, in the standard quantum mechanical treatment of scattering become continuous in the manner $kb = l + \frac{1}{2}$ and then work with the impact parameter, b. The usual phase shift expression is modified as

$$1 - e^{2i\delta_l} \rightarrow 1 - e^{i\chi(b)} \equiv \Gamma(b) \tag{E.2}$$

and the sum over l becomes an integral over b. Then f is written as (we use boldface for vectors, and $q = |\mathbf{q}|$, etc.)

$$f(\mathbf{q}) = \frac{ik}{2\pi} \int d^2b \; e^{i\,\mathbf{q}\cdot\mathbf{b}} \; \Gamma(\mathbf{b}) \tag{E.3}$$

and the inverse transform is

$$\Gamma(\mathbf{b}) = \frac{1}{2\pi ik} \int d^2q \; e^{-i\,\mathbf{q}\cdot\mathbf{b}} \; f(\mathbf{q}) \tag{E.4}$$

For a single nucleon, one can think of the 'profile function', Γ, as simply a different way of representing the scattering amplitude. But for a treatment of multiple scattering in a complex nucleus, Γ is essential. It is easiest to compute the *nuclear* profile function from the *nucleon* profile functions, and then transform back to f, rather than working with f

directly. The crucial step is the assumption that the phase shifts χ simply add from each scatter; this is related to the fact that the wave does not spread very much between scatters. We can also keep the neutrons and protons separate, anticipating the potentially different distributions of each, especially in neutron-rich heavy nuclei. In particular, we find

$$\Gamma_{nucleus} = 1 - \prod_i (1 - \Gamma_i) = 1 - (1 - \Gamma_p)^Z (1 - \Gamma_n)^N \tag{E.5}$$

We have assumed an independent particle model of the nucleus to write the second equality above; hence we are explicitly ignoring any position correlations among the nucleons. To get Γ_p (Γ_n), the contribution from a single proton (neutron) in the nucleus, the form is analogous to the transform for the bare nucleon, except for an additional convolution with the nuclear structure function, $S(\mathbf{q})$

$$\Gamma_{p,n} = \frac{1}{2\,\pi\,i\,k} \int d^2q\; e^{-i\,\mathbf{q}\,\cdot\,\mathbf{b}}\; f(\mathbf{q})\, S(\mathbf{q}) \tag{E.6}$$

Where $S(\mathbf{q})$ is given by

$$S(\mathbf{q}) = e^{i\,\mathbf{q}\,\cdot\,\mathbf{r}}\; \rho(\mathbf{r})\, d\mathbf{r}. \tag{E.7}$$

The distinct Γ_p and Γ_n arise from potentially different densities, $\rho(r)$.

We now have all of the essential formulae. We will manipulate the equations further and obtain some useful approximations.

E.2.2 Reduction to Simple Integrals

If $\rho(\mathbf{r})$ has azimuthal symmetry, then $S(\mathbf{q})$ becomes, using spherical coordinates,

$$S(q) = \frac{4\,\pi}{q} \int_0^\infty r\, dr\, sin(qr)\, \rho(r) \tag{E.8}$$

or alternatively, in cylindrical coordinates,

$$S(q) = 2\,\pi \int_0^\infty b\, db\, J_0(qb)\, T(b). \tag{E.9}$$

We have introduced

$$T(b) = \int_{-\infty}^{\infty} dz\, \rho(b, z), \tag{E.10}$$

the nuclear thickness function; it is normalized such that

$$\int d^3r\; \rho\,(r) = \int d^2b\; T(b) = 1. \tag{E.11}$$

Henceforth, we work with $T(b)$ and we will thus no longer explicitly see $S(q)$.

If further, $f(\mathbf{q})$ has azimuthal symmetry, then we may use

$$\int d^2q\, e^{-i\,\mathbf{q}\cdot\mathbf{b}}\, h(q,b) = 2\,\pi\, \int_0^\infty q\, dq\, J_0(qb)\, h(q,b) \tag{E.12}$$

valid for an arbitrary function, h, with such symmetry. The profile functions then become, in spherical coordinates,

$$\Gamma_p = -i \int_0^\infty dq J_0(qb)\, F_p(q) \int_0^\infty r\, dr\, sin(qr)\, \rho(r) \tag{E.13}$$

or, in cylindrical coordinates,

$$\Gamma_p = -\frac{i}{2} \int_0^\infty q\, dq J_0(qb)\, F_p(q) \int_0^\infty b\, db\, J_0(qb)\, T(b) \tag{E.14}$$

We remind the reader that the density $\rho(r)$, and therefore $T(b)$, may also differ for p and n.

E.2.3 An Approximation for Large Nuclei

For large nuclei, the profile function may be approximated as (using Neumann's integral)

$$\Gamma_p \simeq -\frac{i}{2} F_p(0)\, T(b) \tag{E.15}$$

This is valid if $S(q)$ is more sharply falling than $F(q)$, which may then be factored out of the integral and replaced by $F(0)$. We will also use this approximation to gain some intuition for the physics. We may combine Eqns. E.3, E.5, E.14, and E.15 to arrive at

$$f_{hA} = \frac{i\ k}{2\pi} \int d^2b \left[1 - (1 + i/2\ F_p\ T(b))^Z\, (1 + i/2\ F_n\ T(b))^N\right] \tag{E.16}$$

F_p and F_n are proton and neutron amplitudes. One easily checks that for $Z = 1, N = 0$, we get $4\pi f/k = F_p$ which is just our normalization convention.

If we write

$$I_n = \binom{A}{n} \int d^2b\ [T(b)]^n \tag{E.17}$$

and replace p and n by an average nucleon N then we can rewrite Eqn. E.16 as [216]

$$\frac{i}{2} F_{hA} = \sum_{n=1}^{A} I_n \left[\frac{i}{2} F_{hN}\right]^n \tag{E.18}$$

Note that the distribution of factors of i is very general. This can be seen by writing that the S-matrix as $S = 1 + iT$ and recalling that the f are T-matrix elements. Then, multiplying several successive S will show that the total f is structured as written above.

E.2.4 Inclusion of Forward Slopes

Another, better approximation technique is to define

$$I_n(a) = 2\pi \int b\, db \left[\int q\, dq \int b'\, db'\, e^{-aq^2}\, J_0(b'q)\, J_0(bq)\, T(b) \right]^n \tag{E.19}$$

where a is the forward slope of $F(q)$. In the approximation of a Gaussian $S(q)$, which corresponds to a Gaussian nuclear density, one finds

$$I_n(a) \simeq \left(\frac{< r^2 >}{< r^2 > +6a} \right)^{n-1} I_n(0) \tag{E.20}$$

where $< r^2 >$ is the mean-squared radius of the nucleus. We have introduced

$$I_n(0) = 2\pi \int b\, db\, [T(b)]^n. \tag{E.21}$$

Note that we have dropped the $\binom{A}{n}$ factor relative to Eqn. E.17 for convenience. Eqns. E.21 and E.20 may be used to avoid re-integrating when a changes as a function of energy. Our improved approximation then becomes

$$\frac{i}{2} F_{hA} = \sum_{n=1}^{A} I_n(a) \left(\frac{i}{2} \right)^n \binom{Z}{n-k} \binom{N}{k} [F_{hp}]^{n-k} [F_{hn}]^k \tag{E.22}$$

where Z and N are the number of protons and neutrons in the nucleus.

An important point about a should be made; one which seems to have been overlooked previously. It is usually assumed for simplicity that a is the same for neutrons and protons. However, it is observed to differ for K and $\bar{K}$. As the energy increases, the K and $\bar{K}$ forward slopes, a and $\bar{a}$, approach one another. This can be viewed as the dominance of a common Pomeron contribution, with the differences due to the Reggeon terms which decrease with energy. We adopt the parameterization of Ref. [217]

$$a = (2.37 + 0.208\, log(s)\,)(\mathrm{GeV}/c)^{-2} \tag{E.23}$$

$$\bar{a} = (3.13 + 0.122\, log(s)\,)(\mathrm{GeV}/c)^{-2} \tag{E.24}$$

We believe that it is a *mistake* to naively calculate with different a for K and $\bar{K}$. This procedure would ascribe the differing slopes to the entire amplitude F, and hence equally to each of the F_i contributing to it. Such calculations would lead, for example, to diffractive

regeneration gaining a contribution from the Pomeron at first order! This is easily illustrated in a simplified model of Kp scattering with only P and ω terms. Then, the treatment we claim is invalid states

$$f(q^2) = (P - \omega)\, e^{-aq^2} \tag{E.25}$$

$$\bar{f}(q^2) = (P + \omega)\, e^{-\bar{a}q^2} \tag{E.26}$$

If we add (subtract) these at finite q^2 to obtain the even (odd) amplitude, we obtain

$$f_+ = P(e^{-aq^2} + e^{-\bar{a}q^2}) - \omega(e^{-aq^2} - e^{-\bar{a}q^2}) \tag{E.27}$$

and

$$f_+ = P(e^{-aq^2} - e^{-\bar{a}q^2}) - \omega(e^{-aq^2} + e^{-\bar{a}q^2}) \tag{E.28}$$

If $a \neq \bar{a}$, then the even f_+ amplitude contains an ω term and the odd f_- amplitude term, which causes regeneration, contains a Pomeron, for any finite q^2. If the amplitudes at $q^2 = 0$ satisfy dispersion relations as they must, then at finite q^2, they will not. For example, the odd amplitude, f_-, now includes an even Pomeron term; recall from Appendix C that the phases of f_+ and f_- differ by $\pi/2$! In reality, we expect that *each* Regge pole term has its own unique q^2 dependence. This will *not* violate the dispersion relations. Thus, although the treatment with a and $\bar{a}$ seems innocent enough, it builds a violation of analyticity into the calculation. This will directly disturb the phase-power relation of regeneration that we wish to study. Even though we are only concerned with the exact forward amplitude ($q^2 = 0$) off the nucleus, the screening calculation integrates over *all* q^2 of the nucleon scattering amplitudes and thus will be affected by any non-analyticity present.

We note that the entire effect of including the forward slopes, as opposed to setting them to zero, is not large. An approximate treatment will do, but *we must not violate analyticity* in our parameterization of amplitudes. It would seem preferable, therefore, to use the average of a and $\bar{a}$. This is the technique we adopt: it includes the bulk of the effect of the forward slopes without compromising our assumption of analyticity. These considerations are particularly important when considering phases, since the naive technique leads to regeneration from even-signature poles. These poles have a phase-power relation differing from odd-signature poles by $\pi/2$, hence we are very sensitive to small, incorrect, admixtures of these poles.

E.3 Nuclear densities

The Woods-Saxon form for heavier nuclei is given by

$$\rho(r) = C\left(1 + exp\left(\frac{r-R}{s}\right)\right)^{-1} \tag{E.29}$$

where R and s are the nuclear radius and skin thickness. Typical values are $R \simeq 1.1\ A^{1/3}$ F and $s \simeq 0.5$ F. The normalization is given by

$$C \simeq \frac{3}{4\pi R^2}\left[1 + \frac{s^2\pi^2}{R^2}\right]; \tag{E.30}$$

note that this is an approximation. occasionally, one sees $4.39\,s$, the change in radius over which the density changes from 10% to 90%, referred to as the skin thickness.

The expansion coefficients $I_n(a)$ need to be evaluated numerically for this density. We choose to evaluate $I_n(0)$ numerically, and use Eqn. E.20 to obtain $I_n(a)$.

For light nuclei, a harmonic oscillator form is more appropriate. The density is then

$$\rho = \frac{4}{A}\left(\frac{1}{R\sqrt{\pi}}\right)^3\left(1 + \frac{A-4}{6}\frac{r^2}{R^2}\right)e^{-r^2/R^2}. \tag{E.31}$$

For carbon, $A = 12$ and we take $R = 1.6$ F. The expansion coefficients $I_n(a)$ can be evaluated in closed form for this density. After some computation, we find

$$I_n(a) = \frac{4\pi\alpha}{n}\left(\frac{1}{4\pi\alpha}\right)^n \sum_{k=0} n\binom{n}{k}k!\frac{1}{n^k}\left[1 - \frac{cR^2}{\alpha}\right]^{n-k}\left[\frac{cR^2}{\alpha}\right]^k \tag{E.32}$$

where we have defined

$$c \equiv \frac{1}{6} - \frac{2}{3A} \tag{E.33}$$

and

$$\alpha \equiv a + R^2/4 \tag{E.34}$$

For $A = 12$, Ref. [218] gives

$$I_n(a) = \frac{(n-1)!}{6}\frac{\left[6 - \frac{8}{3}\frac{R^2}{4a+R^2}\right]^n}{[6\pi(4a+R^2)]^{n-1}}\sum_{j=0}^{n}\frac{1}{(n-j)!\left[n(\frac{5}{4} + \frac{9a}{R^2})\right]^j} \tag{E.35}$$

which agrees with our form when evaluated (on a computer!) for carbon.

E.4 Application to Carbon

We now use an approximate formula to investigate the general behavior of nuclear effects in carbon. We will describe the results of more complete calculations in Appendix H.

Applying Eqn. E.18 for carbon, we find

$$\frac{f \pm \bar{f}}{k} \simeq \frac{1}{4\pi}\left[I_1\left(F_{KN} \pm F_{\bar{K}N}\right) + \frac{i}{2}I_2\left(F_{KN}^2 \pm F_{\bar{K}N}^2\right) - \frac{1}{4}I_3\left(F_{KN}^3 \pm F_{\bar{K}N}^3\right)\right]. \qquad \text{(E.36)}$$

Note that we are using I_n, *not* $I_n(0)$. I_1 is just the total number of nucleons, $A = 12$; the other I_n depend on the particular nuclear density. For a typical Woods-Saxon (WS) density for carbon, $I_2 = 0.187$ mb^{-1}; $I_3 = 2.2 \cdot 10^{-3}$mb^{-2}. A harmonic oscillator (HO) form for carbon gives $I_2 = 0.269$ mb^{-1}; $I_3 = 4.6 \cdot 10^{-3}$ mb^{-2}. This latter form seems to be preferred by electron scattering data. The I_n scale as r^{2-2n}; one can use this to get a feel for the sensitivity of the calculations to the nuclear radii. For example, a 5% change in the scale of the carbon nucleus is a 10% change in I_2, which leads to a $\sim 5\%$ change in the level of regeneration.

Pulling out the naive sum-over-nucleons prediction, we get for $(f + \bar{f})/k$:

$$\frac{f+\bar{f}}{k} = \frac{12}{4\pi}\left(F_{KN} + F_{\bar{K}N}\right)\left[1 + i\,(I_2/24)\left(\frac{F_{KN}^2 + F_{\bar{K}N}^2}{F_{KN} + F_{\bar{K}N}}\right) - (I_3/48)\left(\frac{F_{KN}^3 + F_{\bar{K}N}^3}{F_{KN} + F_{\bar{K}N}}\right)\right] \qquad \text{(E.37)}$$

and for $(f - \bar{f})/k$:

$$\begin{aligned}\frac{f-\bar{f}}{k} \;=\; & \frac{12}{4\pi}\left(F_{KN} - F_{\bar{K}N}\right) \times \\ & \left[1 + i\,(I_2/24)(F_{KN} + F_{\bar{K}N}) - (I_3/48)(F_{KN}^2 + F_{\bar{K}N}F_{KN} + F_{\bar{K}N}^2)\right]\end{aligned} \qquad \text{(E.38)}$$

We can approximate $F_{KN} \simeq i\ ImF_{KN} = i\ \sigma_{tot}$ to investigate these expressions. Since $\sigma_{KN} \simeq \sigma_{\bar{K}N}$, we note that the dominant I_2 term is twice as large for regeneration as for total cross section.[1] Both expressions are of the form of the naive expectation multiplied by a correction.

We can check how well this model does for screening. The dominant corrections are $P - P$ and $P - \omega$ double exchanges. For carbon, the naive σ_{tot} is $6\ (\sigma_{KN} + \sigma_{\bar{K}N}) \simeq 230\ mb$. The observed value is $\simeq 190\ mb$ giving a screening correction of -0.17. The formula above

[1] This is due to the observation that, for $a \simeq b$, $(a^2+b^2)/(a+b) \simeq a$ while $(a^2-b^2)/(a-b) = (a+b) \simeq 2a$.

gives a screening correction of $-0.18(-0.13)$ for the HO (WS) density. Some difference may be attributed to inelastic screening. This occurs for multiple scatters which need not always be elastic, as long the total process appears elastic. For carbon on carbon, the naive expectation is about 1.68 mb at 70 GeV I observe 1.21 mb; for a screening of -0.28. The formula predicts about $-0.32(-0.25)$ for HO (WS) densities. One must remember the many approximations used as well as the presence of inelastic screening effects.

E.5 Miscellaneous Formulae

We give Neumann's Integral, valid for any function $T(b)$, which is useful in deriving Eqn. E.15

$$\int_0^\infty q\,dq\,J_0(qb)\int_0^\infty b'\,db'\,J_0(qb')\,T(b') = T(b) \tag{E.39}$$

In calculating $I_n(a)$ for the harmonic oscillator nuclear density, Eqn. E.32, one makes use of

$$\int_0^\infty x\,dx\,e^{-\alpha x^2}\,J_0(\beta x) = \frac{1}{2\alpha}\,e^{-\beta^2/4\alpha} \tag{E.40}$$

and

$$\int_0^\infty x^3\,dx\,e^{-\alpha x^2}\,J_0(\beta x) = \frac{1-\beta^2/4\alpha}{2\alpha^2}\,e^{-\beta^2/4\alpha}. \tag{E.41}$$

The connection to optical models can be made by noting

$$\Gamma_{nuc} = 1 - e^{i\,\chi(b)} = 1 - (1-\Gamma)^A \simeq 1 - e^{-A\,\Gamma} \tag{E.42}$$

and

$$\left(1 + i\,\frac{\chi}{A}\right)^A \simeq e^{i\,\chi} \tag{E.43}$$

APPENDIX F

Kaon Scattering and Regeneration

In the preceeding appendices, we have discussed dispersion relations, the basic structure of scattering amplitudes, the Regge picture of hadron-hadron scattering, and the Glauber treatment of nuclear screening effects. We are now ready to put all these pieces together to give a full picture of the interactions of kaons with matter relevant to our experiment.

We will now consider multiple scattering in bulk matter; i.e., interactions off different nuclei in a macroscopic piece of material. In some respects, this is similar to the multiple interactions with different nucleons in a single nucleus which we encountered in the discussion of Glauber theory.

I first discuss coherent forward regeneration, the process central to our experimental technique, in some detail. I will then discuss the basic physics of diffractive scattering of kaons. There is some interesting physics that occurs due to regeneration and interference between different processes. These effects are very important to the experimentalist and are also fascinating physics in their own right.

F.1 Scattering Review and Notation

First, I recall a few points of scattering theory. The differential cross-section may be written as

$$\frac{d\sigma}{d\Omega} = |f(k,\theta)|^2 \tag{F.1}$$

or, equivalently,

$$\frac{d\sigma}{dq^2} = \pi \left| \frac{f(k,q^2)}{k} \right|^2 \tag{F.2}$$

with $q^2 \simeq {p_t}^2 = p^2 sin^2\theta$. Hereafter, I will often suppress the momentum and angular dependence to keep the equations neat.

Empirically, one finds that the q^2 dependence of the scattering is well-represented by

$$\frac{d\sigma}{dq^2} \simeq e^{-bq^2} \tag{F.3}$$

For a black-disk target, this is just the small-q^2 approximation to the Bessel function that arises from the Fourier-Bessel transform of the target distribution. In general, b is a function of the projectile and target as well as the momentum. The scattering is dominated by the strong interaction, and has markedly different strengths, denoted by f and $\bar{f}$, for K^0 and $\bar{K}^0$. When projectile and target are both charged, there are large effects in the very forward direction due to Coulomb scattering. While this is not directly relevant to neutral kaons, it does affect the charged kaon experiments. Much of our knowledge of neutral-kaon scattering comes from applying isospin to charged-kaon scattering data, so it is important that Coulomb scattering is properly treated by the experiments.

F.2 Total Cross Sections and Regeneration

The symmetric and anti-symmetric combinations of f and $\bar{f}$ are more convenient to use, since the K_L and K_S are the symmetric and anti-symmetric combinations of K^0 and $\bar{K}^0$. It is easy to show that $f + \bar{f}$ results in $K_L \rightarrow K_L$ and $K_S \rightarrow K_S$ scattering, while $f - \bar{f}$ gives $K_L \rightarrow K_S$ and $K_S \rightarrow K_L$ scattering. In the forward direction, these combinations are easily measurable via total cross-sections and regeneration. It is often convenient to work with

$$f_{21} = \frac{f - \bar{f}}{2} \tag{F.4}$$

$$f_{22} = \frac{f + \bar{f}}{2} \tag{F.5}$$

where the subscripts refer to the transitions induced between the K_1 and K_2 states.

A few comments on the total cross-section are in order. Note that the optical theorem for neutral kaons is $\sigma_t = 4\pi Im(f_{22}(0)/k) \simeq -4\pi i f_{22}(0)/k$, the latter step assuming f_{22}/k

is almost purely imaginary. This is known to be a good approximation. One can get at the real part of f_{22}/k by various techniques. It can be measured with Coulomb-nuclear interference in diffractive scattering of charged kaons, related by isospin. Use can also be made of dispersion relations.

There are nice curves for $K^{\pm}N$ scattering in the PDG compilation [39]. The cross-sections vary at low energy as the contributions from various Regge poles shrink away. At higher energies, they become relatively flat due the continued constant contribution of the Pomeron, but have a slow, logarithmic rise.

Measurements have been made of σ_{tot} for K_L-Nucleus scattering [219]. These show roughly flat cross-sections above 30 GeV or so. Screening effects conspire to flatten the rise observed in the single-nucleon case. There is both elastic screening (shadowing) and inelastic screening involving complex intermediate states. These effects can be modeled fairly easily (see Appendix E) and agree well with the data. For our purposes, the important thing is that $f_{22}(0)/k$ is largely constant over our energy range. It is also found experimentally that the nuclear A-dependence is well-modeled by [219]

$$\sigma_{tot}(K_L A) \simeq 190 \left(\frac{A}{12}\right)^{0.84} mb \tag{F.6}$$

F.3 Transmission Regeneration

We will first discuss coherent, or transmission, regeneration; i.e. regeneration in the forward direction. For a pure K_L state incident on a regenerator, the state upon exit is $\sim \rho K_S + K_L$ where

$$\rho = i\pi N L \left(\frac{f - \bar{f}}{k}\right) = 2i\pi N L \frac{f_{21}}{k} \tag{F.7}$$

The above expression is known as the thin regenerator formula; it is valid only in this limit since it neglects the decays of the regenerated K_S as they traverse a finite regenerator. The scale for 'thin' is thus set by the (energy-dependent) K_S decay length. Note that $(f - \bar{f})/k$ is well-represented by [138]

$$\left|\frac{f - \bar{f}}{k}\right| = 2.23 A^{0.758} \left(p[\mathrm{GeV}/c]\right)^{-0.614} mb \tag{F.8}$$

$$arg\left(\frac{f-\bar{f}}{k}\right) = -\frac{\pi}{2}(1+\alpha) \simeq -125^\circ \tag{F.9}$$

where α is the exponent in the $p^{\alpha-1}$ dependence of $(f-\bar{f})/k$. It is this power-law dependence that leads to the relation given above for $arg((f-\bar{f})/k)$. It is easy to include the finite-length effect: one merely averages the differential evolution factor, $e^{-i(\lambda_S-\lambda_L)\tau}$, over the length of the regenerator, producing the thick-regenerator expression

$$\rho = i\pi N L\left(\frac{f-\bar{f}}{k}\right)\delta(L) \tag{F.10}$$

$$\delta(L) = \frac{1-e^{-i(\lambda_S-\lambda_L)l}}{i(\lambda_S-\lambda_L)\,l} \simeq 1 - i(\lambda_S-\lambda_L)\,l/2 \tag{F.11}$$

Here, $l = L/(\beta\gamma)$, and λ_S and λ_L were defined in Eqn. 1.29. This correction is significant in typical geometries. Note that the phase of ρ is given by the phase of $(f-\bar{f})/k$ plus a constant rotation from the i plus a contribution from the correction term (the 'geometric' phase). For completeness, we mention a further layer of complication. We have still not considered higher-order processes like $K_L \to K_S \to K_L$, etc. It is straightforward to time-evolve the system with the correct 2x2 effective Hamiltonian, and calculate ρ. The size of the correction relative to the thick formula is fairly small. Details are provided later. Eqn. F.10 can be (and is!) written in *many* different forms, we prefer the one given here. Also, many of the expressions we have seen contain typos.

There is one final amusement, an effect which may lead to eventual decoherence. It is due to the finite mass difference, which implies that the scatter is not truly elastic. This is never relevant in our regime but is discussed in an appendix.

Recall that the rate of $K \to 2\pi$ decays downstream of a regenerator is given by

$$R_{2\pi} = B\left|\rho e^{-i\lambda_S\tau} + \eta e^{-i\lambda_L\tau}\right|^2 \tag{F.12}$$

where

$$B = e^{-X} N_{K_L}\,\Gamma_S\,BR(K_S \to \pi^+\pi^-) \tag{F.13}$$

The normalization, B, depends on the number of interaction lengths, X, of the regenerator, the number of incident K_L, N_{K_L}, the K_S lifetime, and the branching ratio of K_S to $\pi^+\pi^-$. In general, $|\rho/\eta| > 1$, so the $|\rho|^2$ term dominates. In this limit, the decay rate scales as

$e^{-L/X}L^2$, where X is the kaon interaction length. This is maximized for a *two* interaction-length regenerator, in contrast to an optimal production target, where we would have L in place of L^2.

F.4 Diffraction Regeneration

For diffractive events, the expression for a single scatter is[1]

$$\frac{dR_{2\pi}}{dq^2} = B\pi NL \left| \left(\frac{f_{21}}{k} + \rho \frac{f_{22}}{k} \right) e^{-i\lambda_S t} + \eta \frac{f_{22}}{k} e^{-i\lambda_L t} \right|^2 \tag{F.14}$$

where B is the same normalization factor given previously. Although not explicitly shown, all p- and q^2- dependence is embodied in the f_{21}/k and f_{22}/k functions. Recall that f_{22}/k is largely p-independent in our momentum range, while the p-dependence of f_{21}/k is the power law given earlier. The rate generally falls as e^{-bq^2}, with $b \simeq 13A^{2/3}$ GeV^{-2}.

It is interesting to compute ρ/η for the diffraction in terms of ρ/η for the coherent process. We want to compare the K_S to K_L ratio in the above expressions and so need to simplify

$$\left(\frac{\rho'}{\eta}\right)_{dif} = \frac{f_{21}/k + \rho f_{22}/k}{\eta f_{22}/k} \tag{F.15}$$

Multiplying numerator and denominator by $-4i\pi NL$ one finds

$$\left(\frac{\rho'}{\eta}\right)_{dif} = -\left(\frac{2-x}{x}\right)\left(\frac{\rho}{\eta}\right)_{coh} \tag{F.16}$$

where $x = NL\sigma_{tot}$, the number of interaction lengths of the regenerator. We have also used the approximation that f_{22} is mostly imaginary such that $\sigma_{tot} \simeq -4\pi i NL f_{22}/k$. Eqn. F.16 is a fascinating formula! First, we see that for a two interaction length regenerator, the single scattering production of $K_S$vanishes. This is the same length that we recently showed maximized the coherent event rate. Also, one sees that for a shorter regenerator, $(\rho'/\eta)_{dif}$ is larger and has an opposite phase relative to the coherent ρ. We have assumed that f_{22}/k is totally imaginary, and have also neglected any differences in the q^2-dependence of f_{21}/k versus f_{22}/k. An illustration of the differences between the coherent and diffractive regeneration processes is shown in Figure 67.

[1] The two K_S terms are a regenerative scatter and a simple scatter accompanied by coherent regeneration. The K_L term is a simple scatter with a CP-violating decay.

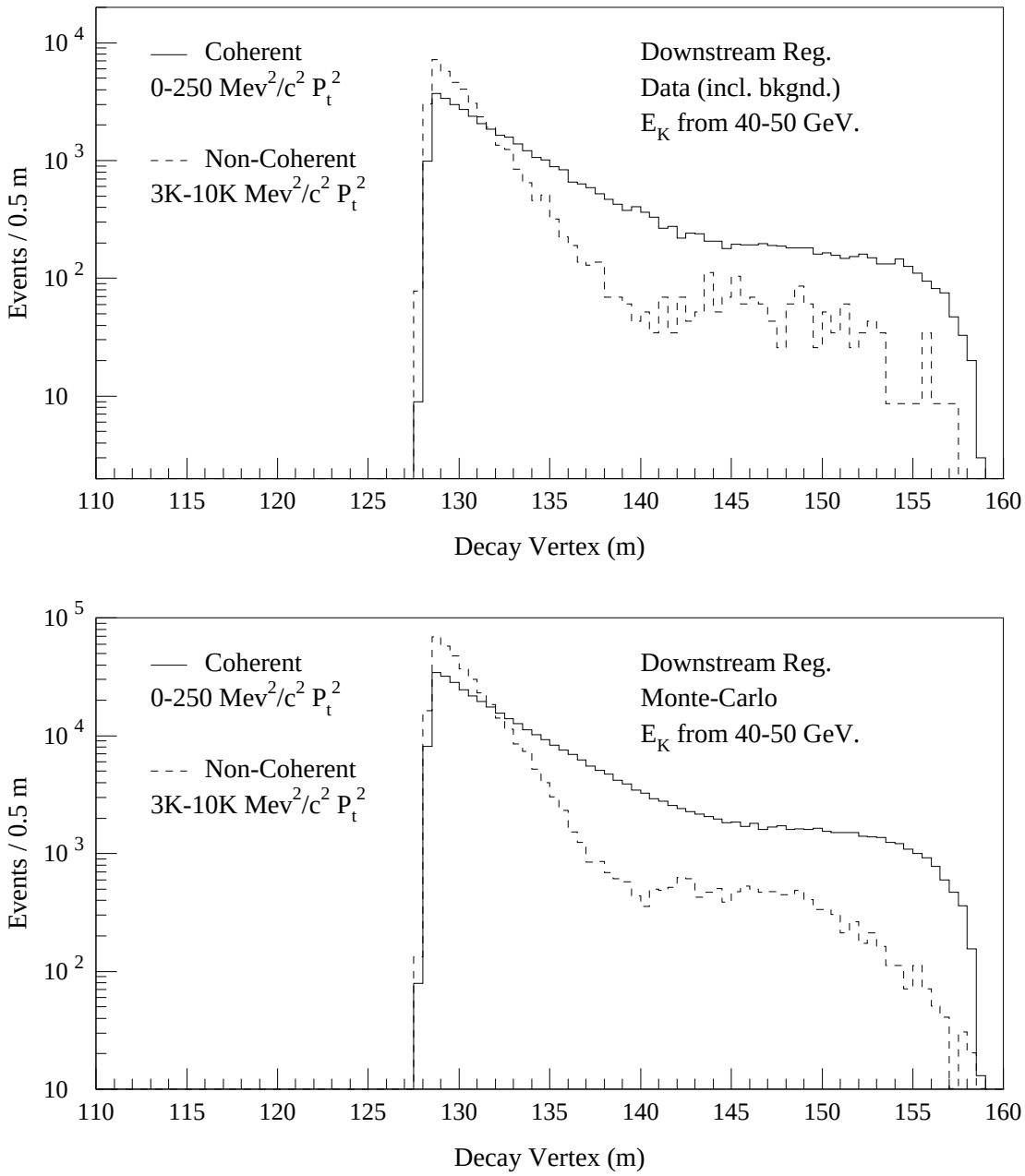

Figure 67. Decay vertex distribution for coherent and diffractive events. The diffractive events are normalized to the same total number of events as the coherent. The events are selected from Data Set 2 with the indicated p_T^2 cuts such that the coherent and diffractive processes dominate each sample. A difference in the sign and magnitude of ρ is evident and it is well-modeled by our Monte Carlo.

The result generalizes easily to n scatters, especially if we ignore powers of f_{21}/k higher than linear; this is a good approximation since $(f_{21}/k)/(f_{22}/k)$ is small. The diffractive K_S-to-K_L ratio becomes

$$\left(\frac{\rho'}{\eta}\right)_{diffr,n} = \frac{n(f_{21}/k)(f_{22}/k)^{n-1} + \rho(f_{22}/k)^n}{\eta(f_{22}/k)^n} = \frac{n(f_{21}/k)(f_{22}/k) + \rho f_{22}/k}{\eta f_{22}/k} \tag{F.17}$$

The extra n is simply a binomial coefficient for which of the n scatters is the f_{21}/k term. This gives

$$\left(\frac{\rho'}{\eta}\right)_{diffr,n} = -\left(\frac{2n-x}{x}\right)\left(\frac{\rho}{\eta}\right)_{coh} \tag{F.18}$$

The ratio of double- to single-scatters is given by

$$\frac{N_2}{N_1} = \frac{x}{2}\left(\frac{\sigma_{el}}{\sigma_{tot}}\right) \tag{F.19}$$

The observed value of σ_{el}/σ_{tot} is about 15%.

We are now able to calculate the 'Good ratio': the coherent to diffractive event ratio after a cut on p_t^2 allowing for resolution effects is made. We will assume that only the $|\rho|^2$ is appreciable, and carry through both single and double diffraction. After a bit of algebra, one finds

$$\frac{4.89}{\sigma_{tot}[mb]\Delta q^2[\mathrm{GeV}^2]}\left(\frac{x}{(1-x/2)^2 + (\alpha x/4)(2-x/2)^2}\right) \tag{F.20}$$

where $\alpha = \sigma_{el}/\sigma_{tot}$. The 4.89 is just $4\pi(\hbar c)^2$, with $(\hbar c)^2 = 0.389\ mb\ \mathrm{GeV}^2$.

F.5 Electromagnetic Regeneration

The effects of the electromagnetic interaction can be very interesting. Because the photon has a C-parity of -1, it always causes regeneration. This leads to at least two interesting phenomena, both of which have been exploited, and both of which are relevant for us here.

The first is that there is regeneration of kaons from any charged particle. Although neutral and having no spin, and hence no multipole moments, a neutral kaon may have a non-zero mean-squared charge-radius,[2] $\langle R^2 \rangle$. An electron has electromagnetic regeneration

[2] One may think of it as due to a heavy positive $\bar{s}$-quark and a lighter negative d-quark orbiting a common center closer to the heavy $\bar{s}$-quark.

of strength

$$\frac{f_{22}}{k} = -(\alpha_{EM}/3)\langle R^2 \rangle \tag{F.21}$$

where α_{EM} is the fine-structure constant. This effect can be used, coupled with a very clever experimental technique, to measure the charge radius [220]. Note that $\langle R^2 \rangle < 0$; this is expected since in the K^0 the lighter, negative d quark orbits at a larger radius than the heavier, positive $\bar{s}$ antiquark. The nucleus also can cause electromagnetic regeneration, but part of the nuclear charge is screened (see Appendix E). Hence, there is a net effect from the electrons, with $f_{22}/k > 0$.

The more easily seen effect is Primakoff production of the K_S^* resonance [148]. This often decays as $K_S^* \to K_S\pi^0$, giving K_S decays with a characteristic p_t^2 spectrum [221]. By using a lead target to maximize the photonuclear field, this has been used to measure the $K_S^* \to K_S\gamma$ width [149] via detailed balance. There is also strong production the K^*. However, the electromagnetic production is very sharply forward peaked. The strong production has a large ω component, which has the same C-parity behavior as the photon-mediated process. Thoughts of using this as a source of tagged K_S have been entertained [222]. Production of the tensor $K^*(1430)$ is highly suppressed compared to the $K^*(890)$. The different quark spins cause the magnetic moments to nearly cancel for the tensor meson; experiment has not yet reached the expected level [223]. Figure 68 shows some relevant plots from our data.

For us, the Primakoff K^* is simply an added contribution to our observed non-coherent $K \to \pi^+\pi^-$ rate. It gives a characteristic Jacobian peak near 60,000 MeV/c^2; the q^2 of the $K_S^* \to K_S\pi^0$ process is 85,000 MeV/c^2 with smearing from the polar angle projection and the q^2 of the absorbed γ^*.

F.6 Inelastic Scattering and Other Decay Modes

There are also 2π decays due to inelasticly produced kaons. The observed inelastic rate seems to be dominated completely by the K_S. For charged mode there is also the $\pi\pi\gamma$ decay. For neutral mode there is cross-over, since only the center-of-energy is known.

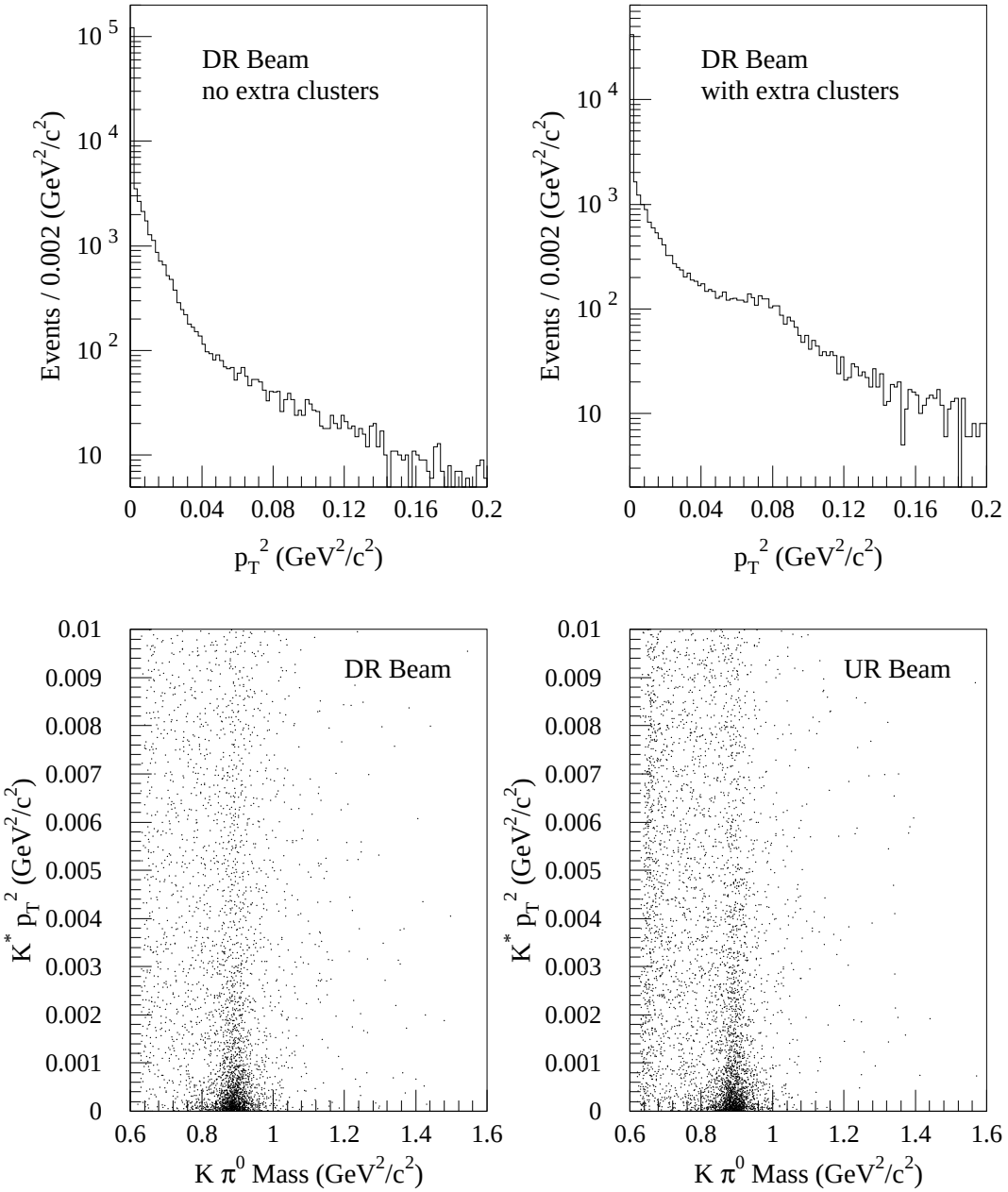

Figure 68. The kaon p_T^2 distribution for events with and without extra clusters, and reconstructed K^* kinematic quantities. The top plots show DR beam data, with all standard analysis cuts, broken into two subsets. The Jacobian peak in p_T^2 is evident in the sample with extra clusters (photons). The bottom plots show the $K\pi^0$ mass and p_T^2 for events where there is a good $\pi^+\pi^-$ mass and a good π^0 formed from two extra clusters. All events are from Data Set 1, where the trigger is less restrictive.

In both charged and neutral modes, there are non-2π decays such as πl_3 and $3\pi^0$, as well as misreconstruction. All of these things complicate life in the real world.

It is found empirically that the acceptance of our spectrometer is reasonably well-represented (for charged mode) by e^{-aq^2}, where $a \simeq 12$ $(\mathrm{GeV}/c)^{-2}$, and varies by $\pm$ 50% as a function of p and z. It is also observed that with our fully-active regenerator, the inelastics have a e^{-aq^2} behavior, with $a \simeq 5$ $(\mathrm{GeV}/c)^{-2}$.

In charged mode, the p_t^2-background has historically been handled by simple empirical fits. Due to poorer resolution, beam cross-over, and higher background, neutral mode has made use of a Monte-Carlo treatment to help untangle the various contributions to the background. Care must be taken when using the charged data to tune the Monte Carlo: the non-2π backgrounds are *very* different in the two cases. Also, one must be careful about using identical cuts on things such as photon vetoes and the number of clusters that may alter the inelastics. Since neutral mode allows no extra clusters at the trigger level, charged-mode should have a cut added demanding no extra clusters before using the p_T^2 distribution to tune Monte Carlo intended for neutral background subtraction.

F.7 Multiple Scattering Series

It is instructive to write the various things that may happen to an interacting kaon passing through a slab of material. The probability may be broken down as

$$1 = e^{-x}(1 + x + x^2/2 + ...) = \sum_{n=0}^{\infty} e^{-x} \left(\frac{x^n}{n!}\right) \tag{F.22}$$

where x is the number of interaction lengths of the slab. There are many ways to see this. For instance, by definition of an interaction length we have a Poisson process with a mean of x. If one demands that certain interactions are elastic, for example, factors of $\alpha = \sigma_{el}/\sigma_{tot}$ appear also. We find it instructive to derive the double scattering term, say, by integrating out over all pairs of possible scattering centers without using a statistical argument or forced normalization.

F.8 Full Matrix Propagation for Kaon Evolution

One can treat the effect of many independent, uncorrelated scatterers with an effective index of refraction $n = k'/k$ [224, 104]. It can be shown that $k'^2 = k^2 + 4\pi N f$. The effective Hamiltonian in matter due to forward scattering is given by

$$H_{scat} = -2\pi N \beta\gamma \begin{pmatrix} f/k & \\ & \bar{f}/k \end{pmatrix} \tag{F.23}$$

This is added to the normal vacuum Hamiltonian, or mass matrix, to get the full Hamiltonian in matter:

$$H_{medium} = H_{vac} + H_{scat} \tag{F.24}$$

After computing the eigenvalues and eigenvectors of the this full Hamiltonian, the incident K_L, or any admixture, is decomposed into the matter eigenstates, evolved with the simple time evolution given by the matter eigenvalues, and then changed back to the original K_S-K_L basis. A straightforward calculation gives

$$e^{-[\bar{\Gamma}/2 \, + \, Im(g_+)]\tau} \begin{pmatrix} cosh(i\delta\tau) - (h/\delta)sinh(i\delta\tau) & (g_-/\delta)sinh(i\delta\tau) \\ (g_-/\delta)sinh(i\delta\tau) & cosh(i\delta\tau) + (h/\delta)sinh(i\delta\tau) \end{pmatrix} \tag{F.25}$$

where

$$h = -(\lambda_S - \lambda_L)/2 = -\Delta m/2 - i\Delta\Gamma/4 \tag{F.26}$$

$$\bar{\Gamma} = (\Gamma_S + \Gamma_L)/2 \tag{F.27}$$

$$g_\pm = \pi N(f \pm \bar{f})/k \tag{F.28}$$

$$\delta = (h^2 + {g_-}^2)^{1/2} \tag{F.29}$$

The effect of using this matrix instead of the thick regenerator formula, Eqn. F.10, is the inclusion of multi-step processes such as $K_L \to K_S \to K_L$, etc. These are small corrections, but it is easy to use the matrix and we do so for our Monte-Carlo and fitting programs.

A comparison of the various formulae discussed for calculating regeneration is given in Figure 69. We also illustrate the effects caused by the Downstream Regenerator air gaps in Figure 70.

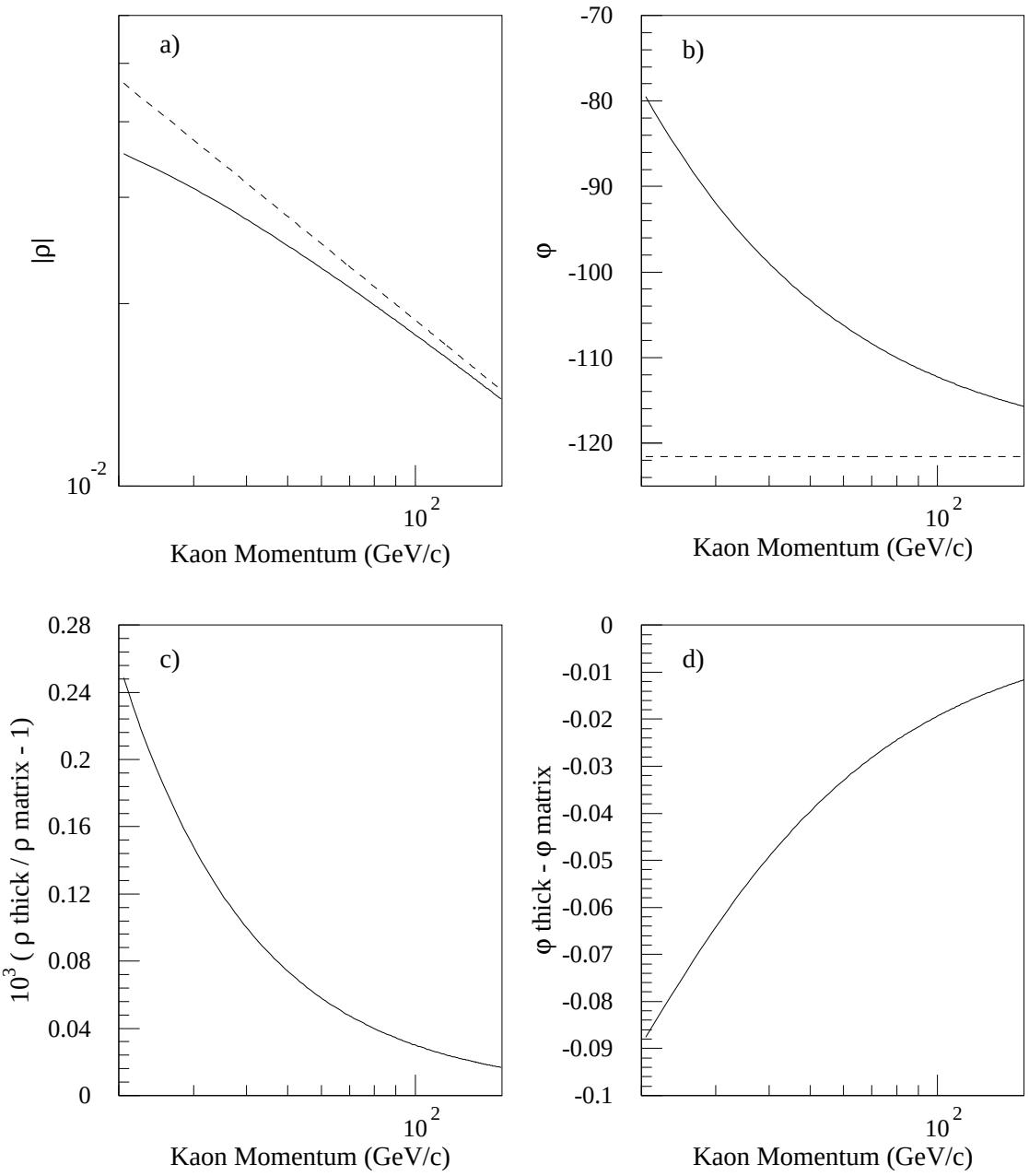

Figure 69. A comparison of various approximations for calculating the regeneration parameter, ρ. We have calculated ρ for the E773 upstream regenerator. Plots a) and b) show the $|\rho|$ and ϕ_ρ respectively, calculated with the full matrix method (solid curves) and the thin regenerator approximation (dashed curves). The effect of the 'geometric' correction, due to the relative K_S-K_L evolution, is evident in both plots. The very small differences between the full matrix calculation and the thick regenerator formula are depicted in Plots c) and d).

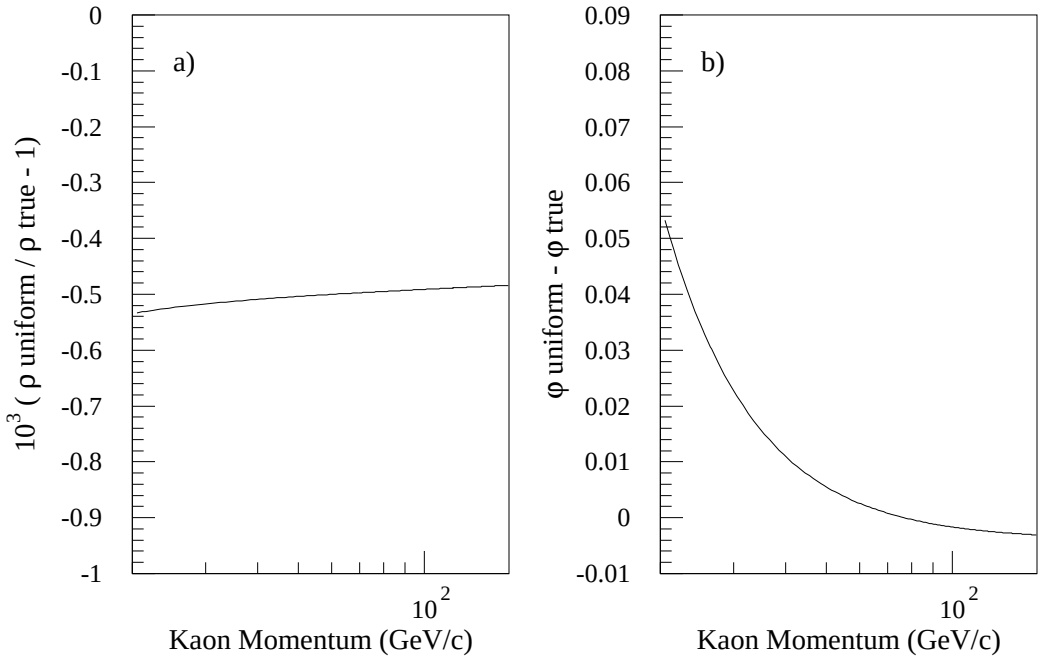

Figure 70. An illustration of the effects of the air gaps in the E773 Downstream Regenerator. We have compared a full calculation with a calculation assuming a uniform regenerator of lower density, such that the total material is fixed. Plots a) and b) show the effect on $|\rho|$ and ϕ_ρ respectively. The air gaps are about 1.7cm, while the K_S lifetime at 20 GeV/c (the lowest value plotted) is 1.1 m; this small ratio sets the scale of the effect.

F.9 Dephasing in Long Regenerators

The K_S and K_L portions of the wave-function evolve differently, and we have discussed how this is taken into account with the thick regenerator formula. But we have implicitly assumed that the energy and momentum of the K_S is the same as the K_L. However the masses are different, so this cannot strictly be true. The nucleus may absorb a small longitudinal momentum component with a negligible change in energy due to the large recoil mass, so it is the momentum that changes to first-order. Thus, when the K_S regenerates, we not only must evolve with a different *eigenvalue*, but also with a different *momentum*! This fact will eventually lead to decoherence for sufficiently long regenerators or sufficiently low energies. It is easy to show that the change in momentum is

$$\delta p \simeq \Delta m/\beta\gamma \tag{F.30}$$

Denote the phase factor between a scatter in the center of the regenerator and one end by ϕ. Then,

$$\phi \simeq (\delta p)\left(\frac{L}{2\beta\gamma}\right) \tag{F.31}$$

or

$$\phi \simeq \left(\frac{1}{\beta\gamma}\right)^2 \left(\frac{\Delta m}{\Gamma_S}\right)\left(\frac{L}{2c\tau_S}\right) \tag{F.32}$$

It is easy to consider now the sum of very many scatterers along the length of the regenerator adding with phases varying from $e^{-i\phi}$ to $e^{i\phi}$, instead of the usual full coherence. The resulting geometric series is easily summed to $1 - \phi^2/3$. This correction is completely negligible for any reasonable setup. The deficit in regeneration , $\phi^2/3$, varies as $(L^2)/(\gamma^4)$. Dimensional analysis might have proven dangerous here.

APPENDIX G

E773 Regenerator Composition

The two regenerators from E773 were carefully measured after the data run ended. In this appendix, we describe the details of their composition and discuss how the mixture of materials was treated.

The basic construction consisted of a set of nominally identical blocks of scintillator and the materials that were wrapped around them. The wrappings increased light collection efficiency and also made each unit light tight and optically independent.

For each material, we require knowledge of the thickness and chemical composition. In addition, some of the wrapping materials consist of narrow tapes that were wound around the blocks creating overlap regions were there are thus two layers. These overlaps were carefully measured. We quote an overlap fraction which is equal to the portion of the area that was covered by a second layer of material.

The chemical compositions and densities are from standard references or the manufacturer. We have approximated black electrical tape and clear plastic packing tape as pure PVC, which is the base material of the backing. Since we can easily measure the bulk properties of the materials, the nucleon density of the regenerators is well known. The particular elemental composition is relevant because of two factors. First there is roughly a factor of two difference in regeneration amplitude for protons and neutrons, neutrons being larger. Second, nuclear screening makes a nucleus regenerate less than the sum of its nucleons: for a fixed density of nucleons, the presence of heavy elements in the regenerators *decreases* $(f - \bar{f})/k$.

The thicknesses of the scintillator blocks were measured in the beam direction at several transverse points and an average of the measurements was used. Both the black tape and the Teflon on the DR seem somewhat thinned by stretching; typical measured values from the actual material are used. We have ignored the aluminizing on the DR mylar. The air content of the regenerators is constrained to give the measured bulk length when added to the other materials. For the DR the air gaps are taken to be uniform; actual measurements showed some variations, but the effect of these is negligible.

For hydrogen, we use measured values for σ_{tot} and $(f-\bar{f})/k$ [39, 155]. For carbon, we use a measured σ_{tot} [219]. The value of $(f-\bar{f})/k$ for carbon is floated in our fits, but we employ a value here to covert the non-carbon contributions to an equivalent amount of carbon. We use a value suggested by our fits; it is somewhat higher than previously measured [137]. For σ_{tot} on other nuclei, we scale as $A^{0.84}$ [138] relative to carbon. Similarly, other values of regeneration are obtained using $(f-\bar{f})/k = 2.23p^{-0.614}A^{0.756}$ [138]. The composition of materials in listed in Table 24 and the nuclear scattering amplitudes used are summarized in Table 25. The amount of each of the materials in each regenerator is listed in Tables 26 and 27.

With all the information in the tables, it is straightforward to calculate the total interaction length of each regenerator. One finds $X_{UR} = 1.2042$ and $X_{DR} = 0.4135$.

A quick note on the movable absorber is in order. It consists of 45.72 cm of Beryllium. Using the σ_{tot} scaling the average value of the carbon data from Ref. [219] with $A^{0.84}$ one finds $X_{MABS} = 0.841(11)($ for $\sigma_{tot} = 149(2)$ mb. A study of $K \to \pi^{\pm}e^{\mp}\nu_e$ decays in a special no-regenerator run gives $X^{raw}_{data} = 0.828(3)$. The average flux correction from elastic scattering, in the movable absorber only, is about 1.5%. Recall that this is due to particles forward elastic scattering at small angles and staying in the beam. The p_T^2-dependence of the scattering is approximately energy-independent; this induces an energy dependence since angle, not p_T^2, determines what stays contained in the beam. The corrected value is $X^{corr}_{data} = 0.840(3)$, in excellent agreement.

For simplicity, we wish to treat everything as an equivalent amount of scintillator. Note that the 'Total/Scint.' ratios in Tables 26 and 27 are approximately equal for σ_{tot} and $(f-\bar{f})/k$. Since we do not need the relative absorption in the MC to the sub-percent level, we

will base our numbers on the regeneration properties and this will suffice to simultaneously explain absorption.

For the DR, we take the 39.56 cm scintillator thickness scaled by the 1.0335 effective enhancement due to wrapping and distribute the resultant length among the 12 blocks. This gives an effective thickness of 3.407 cm. We then constrain the total length for be the measured 59.20 cm, and find the mean air gap to be 1.665 cm. The net effect thus includes the wrapping thickness as part of the scintillator block with a slight additional enhancement due to the higher density of the wrappings. The error incurred should be quite tolerable.

For the UR, we similarly scale the 118.78 cm of scintillator by the 1.0038 effective enhancement due to wrapping to get 119.23 cm. This is shorter than the bulk length of 120.25 cm. This small difference is ignored in the Monte-Carlo, however, a full treatment with small air gaps is used in the fitting program used to extract results. The error incurred is in the geometrical correction term of the thick regenerator formula the regenerator. The scale of this effect is easily shown to be $\sim \Delta l/2\gamma c\tau_S$, which is $\sim 0.4\%$ at 25 GeV and decreases with energy.

Table 24. Properties of materials in the regenerators. The value of $(f-\bar{f})/k$ is given at 70 GeV/c.

Material	Composition	A	Density	σ_{tot}	$(f-\bar{f})/k$	n
			g/cm^3	mb	mb	mb^{-1}cm^{-1}
Air	$(N_{0.78}O_{0.21}Ar_{0.01})_n$	14.685	$1.205\ 10^{-3}$	227	1.25	$4.94\ 10^{-8}$
Aluminum	Al	26.982	2.699	379	1.99	$6.02\ 10^{-5}$
Mylar	$C_{10}H_8O_4$	192.07	1.38	3048	17.8	$4.33\ 10^{-6}$
Scintillator	$CH_{1.1}$	13.110	1.032	213	1.27	$4.74\ 10^{-5}$
Tape(PVC)	$(CH_2CHCl)_n$	62.479	1.3	918	5.06	$1.25\ 10^{-5}$
Teflon	$(C_2F_2)_n$	62.018	2.2	948	5.4	$2.14\ 10^{-5}$

Table 25. Kaon-Nucleus scattering data.

Element	Z	A	σ_{tot}	$(f-\bar{f})/k$@70GeV
			mb	mb
H	1	1.008	19	0.089
Be	4	9.012	150	0.868
C	6	12.011	192	1.17
N	7	14.007	219	1.21
O	8	15.999	244	1.34
F	9	18.998	282	1.53
Al	13	26.982	379	1.99
Cl	17	35.453	477	2.45
Ar	18	39.948	527	2.67
Pb	82	207.2	2101	9.35

Table 26. Summary of materials in the upstream regenerator.

Material	Thickness (*as noted*)	layers	overlap %	Thickness cm (net)	X_{int}	$nl(f-\bar{f})/k$
Scintillator	3.299 cm	36	0.	118.78	1.1992	$7.15\ 10^{-3}$
Black Tape	7.0 mils	18	23.	0.39	0.0045	$2.47\ 10^{-5}$
Aluminum	0.5 mils	18	0.	0.02	0.0005	$2.4\ 10^{-6}$
Air		35		1.06	0.0000	$0.1\ 10^{-6}$
Totals				120.25	1.2042	$7.18\ 10^{-3}$
Total/Scint.				1.0124	1.0042	1.0038

Table 27. Summary of materials in the downstream regenerator.

Material	Thickness (*as noted*)	layers	overlap %	Thickness cm (net)	X_{int}	$nl(f-\bar{f})/k$
Scintillator	3.297 cm	12	0.	39.56	0.3994	$2.38\ 10^{-3}$
Black Tape	6.25 mils	24	41.	0.54	0.0061	$3.42\ 10^{-5}$
Teflon	3.0 mils	26	29.	0.26	0.0053	$3.00\ 10^{-5}$
Clear Tape	2.5 mils	22	0.	0.14	0.0016	$8.9\ 10^{-6}$
Mylar	0.5 mils	24	0.	0.03	0.0004	$2.3\ 10^{-6}$
Al Windows	0.5 mils	2	0.	0.00	0.0000	$0.3\ 10^{-6}$
Air	1.697 cm	11	0.	18.67	0.0002	$1.2\ 10^{-6}$
Totals				59.20	0.4130	$2.46\ 10^{-3}$
Total/Scint.				1.0245	1.0341	1.0335

APPENDIX H

The Regeneration Phase Systematic Error

This appendix discusses in more detail the estimation of the systematic error from the regeneration phase. A condensed version of the arguments presented here was given in Ref. [225]. Several of the other appendices, in particular Appendix E, provide some useful background material.

H.1 Introduction

As discussed in Chapter 9, a power-law amplitude with a constant phase is an excellent first approximation to the behavior of $(f - \bar{f})/k$. We will present a detailed discussion of modifications to this naive view and determine their effects on the parameters we wish to extract from our data, in particular ϕ_{+-}.

Although our analysis will not rely on the accuracy of Regge Theory, it will be useful to develop the Regge picture of high-energy scattering somewhat to give a framework for discussing the amplitudes. More details are provided in Appendix D; we will just present the essential points now.

In the Regge picture, scattering amplitudes are thought of as arising from the t-channel exchange of one or more Regge poles. These poles will in general have a correspondence to various particles, such as the ω, ρ, A_2 and f. Each pole contributes an amplitude which behaves like E^{α}, where α is a property of the particular pole. Regeneration is dominated

by the exchange of the ω and ρ poles. Other poles contribution to KN scattering cancel in the amplitude difference, $f - \bar{f}$. Furthermore, for an isoscalar target, only the ω will contribute to lowest order. Therefore, the picture for our regenerator is the following: regeneration off carbon nuclei is due to ω exchange, while regeneration off the protons in hydrogen is due to a sum of ω and ρ exchanges.

We now present a list of the various corrections we will consider to the single power-law picture.

- The presence of hydrogen. Since its regeneration is the sum of two power laws with different values of α, the resulting amplitude is neither a simple power nor does it have a constant phase.

- Carbon is only a pure ω-exchange to lowest order. The kaon may multiple scatter in a carbon nucleus, bringing in other terms.

- The strong interaction between the kaon and the nucleons is also not the only source of regeneration; we will also need to consider electromagnetic regeneration.

- Even in the absence of any of the foregoing corrections, the phase-energy relation is only valid if the power law extends over all energies. We must therefore include any effects due to the known deviations from this form in the low-energy resonance region.

- We also must consider deviations from the power law at high energies; we consider the possibility of additional odd amplitudes.

- Finally, motivated by Regge Theory, we consider the presence of additional, weaker amplitudes present to first order in addition to the dominant ω.

We now discuss each of these in detail. For each correction above, we can parametrize the change of the magnitude and phase of regeneration relative to a pure power in the form of Eqns. 8.9 and 8.10. Note that $a(p)$ and $b(p)$ in those equations are largely independent of small changes in the exponent of the bare power they modify. The change in ϕ_{+-} resulting

from fits with and without these corrections can then be obtained. This appendix only directly discusses the studies done to determine the error on ϕ_{+-}. Identical systematic studies were performed for the τ_S and Δm fits; the results of all of these are summarized in Table 19.

H.2 Correcting for the Presence of Hydrogen

Let us first consider hydrogen, where regeneration is due to ω and ρ exchange. The full expression for the amplitude is

$$(f - \bar{f})/k = \beta_\omega e^{i\phi_\omega} p^{\alpha_\omega - 1} - \beta_\rho e^{i\phi_\rho} p^{\alpha_\rho - 1}. \tag{H.1}$$

We take [155] $\alpha_\omega\,(\alpha_\rho) = 0.44\,(0.575)$ and $\beta_\omega\,(\beta_\rho) = 11.5\,(1.67)$. The phases, $\phi_\rho = -141.8°$ and $\phi_\omega = -129.6°$ are given by using the phase-power relation for each term. Over the range $20 - 160$ GeV/c, the full expression above follows a single power to within 1%; the phase varies from $-123.7°$ to $-120.3°$. Ignoring the mixture, the single-power fit gives a phase of $-122.3°$, using the phase-power relation. Figure 71 shows the behavior of the hydrogen amplitude.

Note that the single-power fit yields a determination of the average phase to better that 1° even though it differs from that of either the ω or ρ alone, by more than 7°. This type of behavior is well known in electrical network theory [226], and it illustrates quantitatively a derivative analyticity relation relating the phase to the *local* power law [197, 198]

$$\phi = -\pi - \tan(\frac{\pi}{2}\frac{d}{d\,ln\,p})\ln|(f - \bar{f})/k| \sim -\pi - \frac{\pi}{2}\frac{d}{d\,ln\,p}\ln|(f - \bar{f})/k| \tag{H.2}$$

This relation follows from the dispersion integral for sufficiently well-behaved functions. For a power law, only the first term in the series expansion of the tangent is non-zero. The above relation with only this first term holds asymptotically [199]. Measurements [138] of high-energy regeneration show essentially perfect power laws; we then expect corrections to the deduced phase to be small.

Now consider $CH_{1.1}$, assuming for now that the regeneration off C is due only to ω exchange. Such a mixture behaves like the ω and ρ sum above, with the ω term an order of magnitude larger. Hence, the deviations from the naive power-phase relation induced by

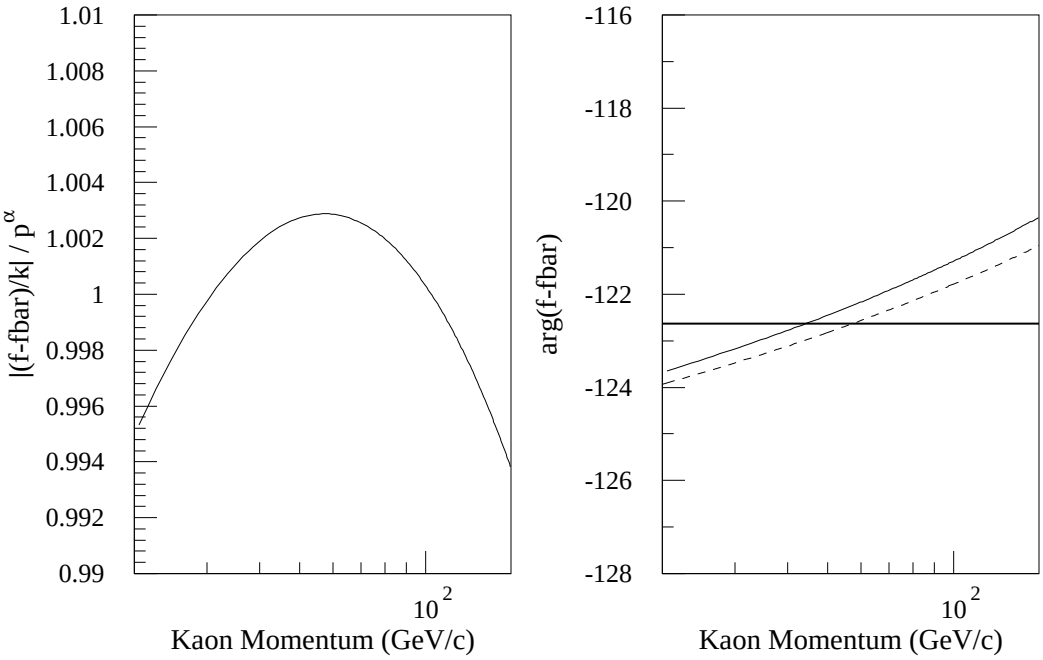

Figure 71. The regeneration amplitude for hydrogen. Plot a) shows the residual difference between the parameterization of the amplitude and the best-fit power law. In Plot b), the constant line is the phase that corresponds to the best-fit power; the other solid line is the true phase from the parameterization. The dashed line is the result of keeping only the first term in the *tan* expansion of the DAR.

the ρ admixture from will be much smaller. With such a mixture of ω and ρ, an extraction of ϕ_{+-} by fitting a single power-law would give a systematic bias $< 0.1°$. Uncertainties in the hydrogen parameterization itself have a negligible effect.

H.3 Rescattering in Carbon

Nuclear screening in carbon modifies the above assumption; single ω exchange is not a complete description of carbon regeneration. Screening is the largest of the effects we consider in this appendix. We note that studies of K_L scattering with C and Pb have been performed both in our momentum range and at significantly lower momenta [138, 227, 228, 219]. Data with heavier nuclei (e.g., Pb), where screening effects are very large, will help check our calculations. Our calculational technique is described in Appendix E; see

especially Sections E.2.4 and E.3. In that Appendix, we described only elastic screening; now, we will have to also consider inelastic screening.

The input to the calculation consists of KN cross sections and the nuclear densities of the target nuclei. The cross section data are fit to theoretically motivated forms; this smooths the data and uses analyticity to obtain the proper real parts which agree well with measurements. We use the Regge-inspired fits performed in Ref. [217]; these provide excellent representations of the best available data. The exact functional forms are *not* important.

The four KN amplitudes are written as a sum of Regge terms as discussed in Appendix D. The Pomeron is parameterized as $F_P = a/p + b\,\pi\,log\,p + i\,\left(c + b\,log^2\,p\right)$. The a/p term is used to tune the low-energy real parts and its magnitude is not important to our conclusions. We have also performed an equally good fit to the KN data using $F_P = a/p + b\,\pi/2 + i\,\left(c + b\,log\,p\right)$. Our conclusions are not sensitive to the choice of F_P parameterizations. Either parameterization of the Pomeron also provides excellent fits to both the magnitude and phase of pp and $p\bar{p}$ scattering at very much higher energies [208].

In Table 28, we compare the data for carbon and lead to our calculations, with and without elastic screening. Note that the bulk of the observed screening is due to this easily calculated elastic effect and that the effects are also much larger in lead than carbon.

Figure 72 shows a comparison of our calculations for various nuclei with the available data. In Figure 73, as a reminder of the importance of screening effects, we show some calculations with no screening; the nucleon amplitudes are simply summed to obtain the nuclear amplitude.

To better treat the nuclear effects, we must consider inelastic screening [232, 233]. Here the incoming K is scattered into inelastic intermediate states K' which then reform into a K upon a subsequent scatter. Data on total cross sections [219, 234] provide clear evidence for the presence of this effect. Treatments of this necessarily involve approximations, but reasonable procedures at high energy are available. The effects are qualitatively similar to elastic screening. The screening depends on the amplitudes f^* and $\bar{f}^*$ for scattering into inelastic states; at high energies these may be related to the behavior of $d^2\sigma/dq^2dM^2$, where M is the invariant mass of, and q the momentum transfer to, the inelastic state. Thresholds

Table 28. A comparison of calculations and data for total cross sections and regeneration from carbon and lead. The data are interpolations from this thesis and Refs. [219, 227, 228, 138]. Our models are based on Ref. [217] (see text) and do not make use of any regeneration data to fix parameters. $\Delta\sigma_{tot}$ and $\Delta\phi$ are the changes in the total cross section and regeneration phase for the noted energy ranges. The inelastic calculations give the range as the C-odd inelastic term is varied from the maximum considered (from factorization) to zero; only regeneration is sensitive to these terms.

Element	Model	σ_{tot} [mb]	$\Delta\sigma_{tot}$ [mb]	$(f-\bar{f})/k$ [mb]	$\Delta\phi$ [deg]
		70 GeV/c	30-150 GeV/c	70 GeV/c	5-70 GeV/c
C	no screening	232	12	1.70	-0.3
C	elastic screening	194	9	1.17	2.5
C	inel. screening	182	3	1.08 $\rightarrow$ 1.21	5.7 $\rightarrow$ 1.4
C	Data	190(2)	3(10)	1.21(1)	1.5(0.8)
Pb	no screening	4024	203	32.3	-0.3
Pb	elastic screening	2249	64	9.3	8.3
Pb	inel. screening	2042	-45	9.3 $\rightarrow$ 11.2	10.8 $\rightarrow$ 2.6
Pb	Data	2047(8)	-106(44)	9.5(1)	8.5(3.8)

to reach high-mass intermediate states make inelastic screening unimportant at low energies. At high energies, the effect can be significant. Analyses of inelastic effects relevant to high-energy regeneration were performed in Refs. [216, 235, 231, 217]. Ref. [231] pointed out the importance of C-odd terms in inelastic screening which were previously neglected. We use the treatment of Ref. [217], where the relevant inelastic coupling constants are determined by fitting to the high-energy data of Refs. [137, 138] with generally excellent quantitative agreement. We use the C-even inelastic parameters as extracted in Ref. [217] by fitting the total cross-section data [219]. These parameters also impact regeneration, whereas the C-odd inelastic terms essentially affect only regeneration. We vary these C-odd parameters, using as guides our new measurements of carbon regeneration, and the same lead data [138] as Ref. [217], rescaled for the modern value of η_{+-}. The approximations used are more accurate for carbon, where the multiple scattering series converges faster than for lead.

Since ϕ_{+-} is independent of momentum, any dependence of the measured difference $\phi - \phi_{+-}$ can be ascribed to the regeneration phase, ϕ, itself. Our calculations are compared

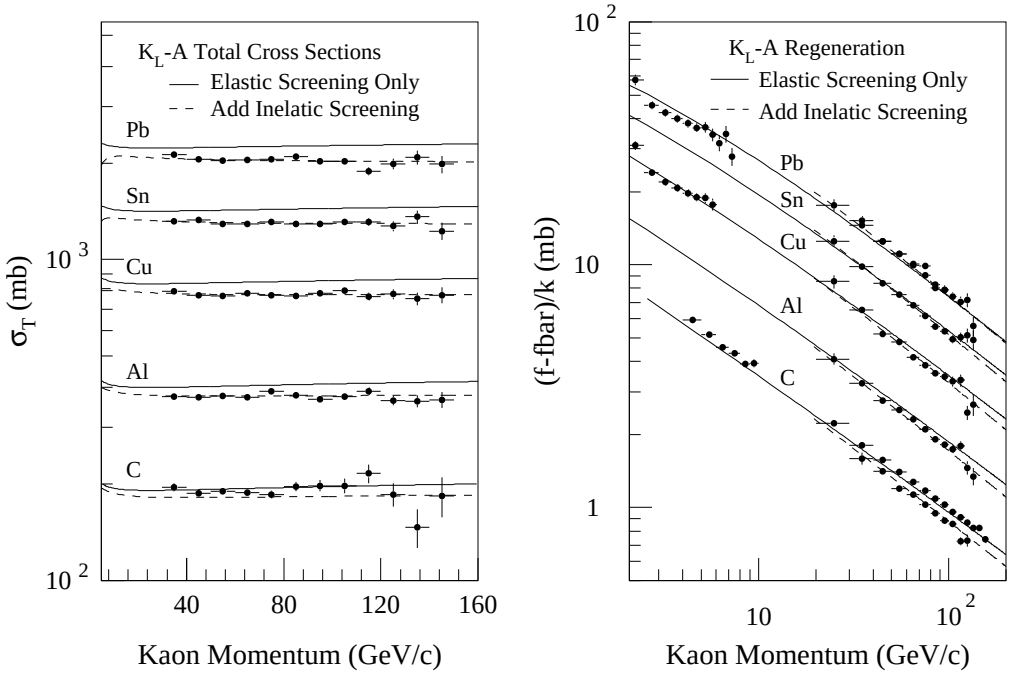

Figure 72. The total cross-sections and regeneration amplitudes for various nuclei compared to our screening calculations. The data are from [227, 229, 230, 137, 228, 138] and this thesis. The results of this thesis are the higher of the two high-energy carbon regeneration results plotted. The inelastic screening includes the C-even terms determined from the total cross-section data as well as the C-odd inelastic screening with a size fixed by factorization [231].

to the data in Table 28. We seen hat the C-even inelastic screening term alone reproduces the carbon phase change from $5 - 70$ GeV/c and that the C-odd term (using factorization – see Ref. [231]) disagrees by several σ. Examining the magnitude of the carbon regeneration leads to the same conclusion: only a small amount of the C-odd term is required to reproduce the data. However, the lead data is better described with more C-odd contributions.

Using elastic screening, and then adding on C-even and C-odd inelastic screening in turn, gives three functional forms for the full amplitude. With these terms, there is a 1° to 3° change in phase across our energy range while $|(f - \bar{f})/k|$ deviates by $\pm 0.3\%$ from a single power. We then do three fits to our data using these functional forms, with the amplitude and power of the ω exchange allowed to vary. (The hydrogen is easily corrected for.) To gauge the systematic error, we examine how each fit extrapolates through the low-

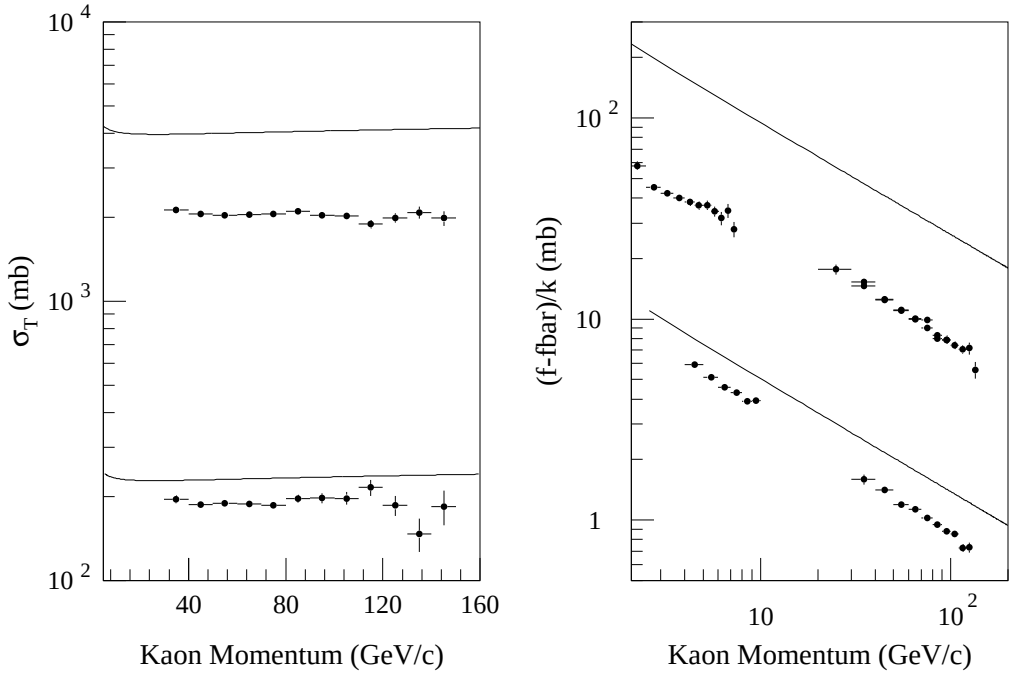

Figure 73. Regeneration and total cross sections for carbon and lead, calculated with no screening.

energy data, and also compare the amplitude and power to other extractions not reliant on understanding nuclear screening.

Figure 74 shows the results of the three fits; for our nominal fit we use elastic screening only, which adequately reproduces the data over the full energy range. Here the extracted ω intercept is 0.437(7) in excellent agreement with other determinations from scattering (0.43(1) [206]) and with a linear Chew-Frautschi plot through the ω and ω_3: 0.436. Additionally, the amplitude from this fit agrees well with the expectations as noted in Table 28. The fit with the C-odd term clearly disagrees with the low-energy data; in addition, the ω-intercept of 0.468(7) contradicts the other determinations. As the phase of the screening correction varies, so does its energy dependence; on average, these cancel via the phase-power relation. The residual movement of ϕ with respect to our nominal fit is $-0.17°$ ($+0.24°$) for the C-even (C-odd) fit. We take $\pm 0.25°$ as our systematic error from nuclear screening.

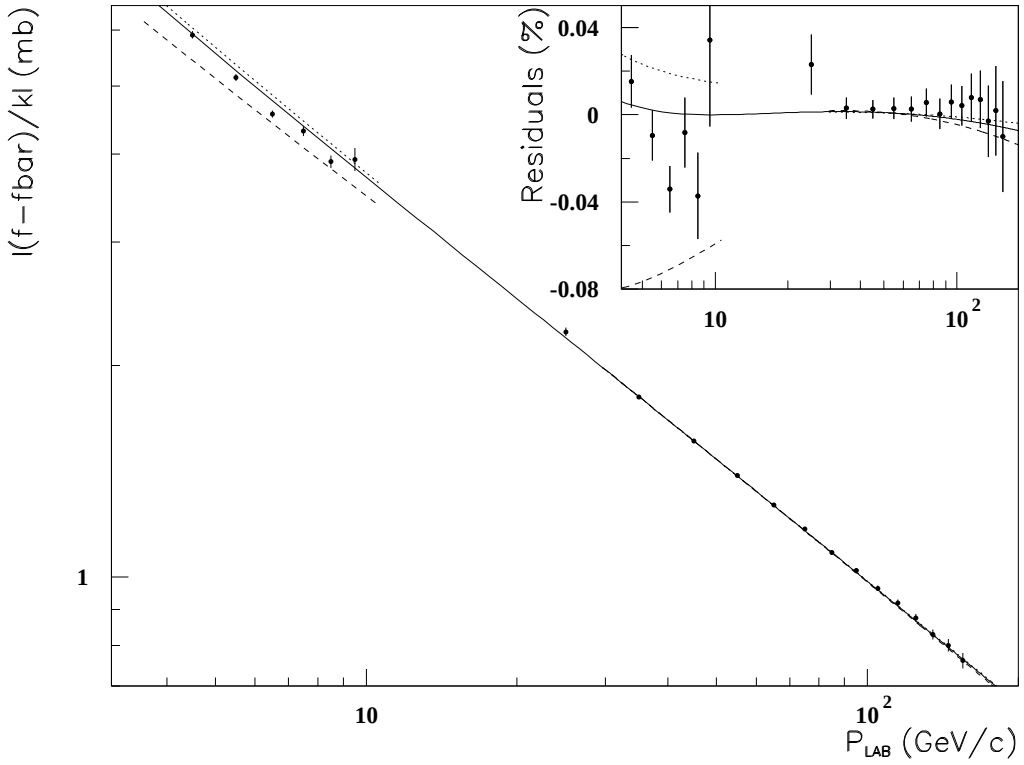

Figure 74. The calculated magnitude of $(f-\bar{f})/k$ for carbon. The inset shows the fractional deviations relative to a single power: $p^{-0.572}$. The solid curves are elastic screening only; the dotted curves include the C-even inelastics, fixed by the total cross-section data. The dashed curves show the effect of the maximum value of the C-odd inelastics considered. The data are from Ref. [15] and from a fit to the data of Ref [5] (the errors are correlated due to common fit parameters).

H.4 Electromagnetic Regeneration

For completeness, our calculations also include the effects of electromagnetic regeneration, which adds a constant real term. The interaction is a pointlike one between the charge-radius of the kaon and the electrons and protons in the regenerator material. Naively, the electron charge is canceled by the nuclear charge, but due to nuclear screening the cancelation is incomplete for carbon. About 1/3 of the nuclear charge is screened; the regeneration

is thus due to a residual charge of about $-2e$. Accounting for this effect amounts to a $(0.10 \pm 0.05)^\circ$ phase change. The error is dominated by the uncertainty in the kaon mean-square charge radius [220].

H.5 Low Energy Contributions to the Dispersion Integral

Using dispersion relations, one can also estimate the effects due to the detailed structure (not present in our parameterization of the amplitudes) of the low-energy amplitude on the phase at our energies. Such changes are constrained by the low-energy phase data [125]. Recall form Appendix C that we know the shape, as a function of energy, of the distortion of the phase-power relation caused by any low-energy structure. We use the maximal energy dependence allowed by the combination of the low-energy data and ours in a fit to obtain the effect on our results. After doubling the observed shift to account for some uncertainties, we obtain an uncertainty of 0.2°.

H.6 Additional (Daughter) Trajectories

In the Regge picture of scattering, sub-leading (daughter) trajectories may occur. We have considered the effects of a sub-leading trajectory with $\alpha = \alpha_\omega - 2$ as well as $\alpha = \alpha_\omega - 1$. Note that in this latter case, the phases of the two terms differ by 90°. We fit the data of Ref. [125] and this thesis simultaneously. The residual shifts in the predicted phase are $< 0.1^\circ$ with the second trajectory's amplitude statistically insignificant. Other fits give no significant evidence for a second trajectory of any α value.

H.7 High Energy Behavior of Scattering (Odderons)

There is the logical possibility of an Odderon contribution [209, 236] to regeneration. This amplitude, $F_O = d + e(lnp - i\pi/2) + f(lnp - i\pi/2)^2$, is C-odd and contributes to $F - \bar{F}$ at first order. The size of the Odderon can be severely limited by fitting existing pp and $p\bar{p}$ data. Such analyses see *no evidence* for these terms, and typically limit an Odderon to

$|F_O/F_P| \sim 10^{-3}$ at our energies [208]. Taking the hypothetical Odderon parameters from the best fit of these authors, we find the existence of such a term would cause a shift of $0.2 \pm 0.6°$ in the measured phase. Such a term is highly speculative; we present the issue for completeness but choose not to include it as a serious source of bias.

H.8 A Response to a Specific Critique

While this analysis was underway, we learned of a claim by Kleinknecht and Luitz, now published [237], that the techniques for extracting the regeneration phase at high energy in Ref. [126] have inherent uncertainties, on the order of 3°. We now comment on their calculation, which is easily reproducible. The authors of Ref. [237] utilize a phase-magnitude dispersion relation. The input to their calculation is the amplitude $|(f-\bar{f})/k|$ parameterized as $p^{\alpha-1}$ for three momentum ranges. For the high energy range, and low momenta when available, α is taken from published data. At higher momenta, the authors of Ref. [237] allow a large, unphysical change (kink) of ± 0.05 in the power law; this constitutes the dominant contribution to the phase uncertainty. Apparently, since changes in the power occurred from low to high energy, one has naively allowed for such changes at high energy. The changes in power introduced are abrupt and located just above the momentum range of the experiment where they have the greatest impact on the local phase. As we have seen, the dispersion relation is equivalent to a power series in derivatives; by placing sudden kinks in the amplitude, the phase is affected nearby with no affect the magnitude on the far side of the kink. This rather unphysical form of behavior 'forbids' the exchange of local information that keeps the phase-power relation valid with more physical shapes, as we saw in our example with hydrogen. In addition, the errors for the three regions are treated as fully correlated, producing the maximal error range. Furthermore, the error on the power-law exponent in the momentum range covered by the experiment is taken as *systematic* and included in their total error when in fact it is a dominant part of the *statistical* error in our fits, and is thus double-counted.

In addition, we point out the following. Regeneration was extensively studied in the $1 - 10$ GeV/c range [227, 228, 229, 230] with a variety of nuclei. When the Fermilab

data, in the range 30 – 150 GeV/c, were reported 15 years ago [137, 219], regeneration for copper and lead was indeed steeper. But this effect, along with its A-dependence, was well-understood and theoretical work further clarified the issue [216, 217, 231]: the power-law at *low* energies for heavy nuclei is in fact distorted. The distortion comes from changes in elastic screening from the very rapid drop in the $\bar{K}N$ cross sections over the 1 – 10 GeV/c range. For $\bar{p}p$, we now know that this decade shows *an order of magnitude* greater change than for any of the next *five* higher decades. Even without comparable measurements with kaons, this gives confidence that the screening mechanism leads to no further breaks in the power – even with heavy nuclei – at any momentum below $\sim 10^6$ GeV/c, let alone at 150 GeV/c as hypothesized in [237].

H.9 The Total Error from the Regeneration Phase

Adding the contributions to the systematic from EM regeneration, low-energy effects, daughter trajectories and screening, we obtain a final systematic of 0.35°. We note that this is much smaller than the error claimed in in Ref. [237], the paper discussed in the previous section. The result those authors were commenting on, that in Ref. [126], quoted a 0.5° error based on general arguments about the size of screening. In fact, we expect that their error would be even lower than the one obtained for this thesis, were the same methods used, due to the vacuum beam flux constraint.

In summary, we have shown that regenerator-based experiments are *not* substantially limited by systematic effects due to the need to separate ϕ_ρ and ϕ_{+-}.

APPENDIX I

Useful Kinematic Formulae and Chamber Properties

I.1 $K \rightarrow \pi^+\pi^-$ Kinematics

It is easy to show that the $\pi^+\pi^-$ mass is given by:

$$\begin{aligned} M^2_{\pi\pi} &= 2m^2_\pi + 2\left(E_1E_2 - p_1p_2cos\theta\right) \\ &\sim 2m^2_\pi + p_1p_2\theta^2 + m^2_\pi(R + 1/R) \end{aligned} \tag{I.1}$$

where $R \equiv p_1/p_2$, and the other notation is obvious. We have expanded the cosine of the track opening angle, θ, and the energy of the pions to lowest non-trivial order. This formula is accurate, with typical E773 events, to about 3 parts in 10^{-5} on average.

With this formula, it is easy to derive that a fractional shift in the momentum scale by δ will cause the mass to shift by $a\delta$, where a is given by:

$$a = 1 - (m_\pi/M_K)^2(2 + R + 1/R) \tag{I.2}$$

As an estimate, for $R = 1$, we find $a = 0.69$. For our mix of accepted events, we find that $\langle R + 1/R\rangle = 2.7$, such that $a = 0.63$. Note that a is less than one, since part of the mass is independent of the momentum scale.[1]

[1] The factor a is *incorrect* in Ref. [143], p. 135.

I.2 $K \rightarrow \pi^+\pi^-\gamma$ Kinematics

We wish to obtain a relation between $m_{\pi\pi}$ and the photon energy in the kaon center-of-mass, E^*_γ. Consider the 4-vector of the $\pi^+\pi^-$ system in the $\pi^+\pi^-$ center-of-mass, ($m_{\pi\pi}$, 0). In the kaon center-of-mass frame, this will be boosted to ($\gamma m_{\pi\pi}$, $\beta\gamma m_{\pi\pi}$). The photon 4-vector in the kaon center-of-mass is (E^*_γ, E^*_γ). We know that the two 4-vectors must sum to give (M_K, 0), thus

$$M_K = \gamma m_{\pi\pi} + E^*_\gamma \tag{I.3}$$

and

$$E^*_\gamma = \beta\gamma m_{\pi\pi} + \tag{I.4}$$

The latter equation may be used to obtain γ (from $\gamma^2 = 1 + \beta^2\gamma^2$), yielding

$$\gamma = \sqrt{1 + (E^*_\gamma / m_{\pi\pi})^2} \tag{I.5}$$

After a small amount of algebra, we find

$$\begin{aligned} M_{\pi\pi} &= \sqrt{M_K^2 - 2M_K E^*_\gamma} \\ &\simeq M_K - E^*_\gamma. \end{aligned} \tag{I.6}$$

for small E^*_γ.

This result is also easily obtained by considering the $\pi^+\pi^-$ and γ as a quasi-two-body system and applying the textbook formula [39] for the momentum of the decay products in the center of mass.

I.3 Λ Kinematics

It is commonly known that the p from a $\Lambda \rightarrow p\pi$ decay is generally stiffer than the π. It is useful to quantify this statement. One generally works with the ratio of the lab momenta of the decay products.

There are two steps to this calculation. In the first we prove the following statement: the extreme values of the momentum ratio are obtained when the boost is along the direction of the decay products.

An asterisk, *, denotes a quantity evaluated in the Λ center-of-mass. Let us calculate the momentum of one of the decay products in the lab frame

$$(p_{lab})^2 = p^{*2} sin^2\theta + (\gamma p^* cos\theta + \beta\gamma E^*)^2 \tag{I.7}$$

We differentiate with respect to $cos\theta$, yielding

$$d(p_{lab})^2/dcos\theta = 2p^{*2}\left[(cos\theta(\gamma^2-1) + \gamma^2\beta E^*/p^*\right] \tag{I.8}$$

A little algebra shows that this is always positive (the extreme case being $cos\theta = -1$) as long as $\beta < E^*/p^*$, which is trivially satisfied (compare each side to 1).

We now can examine the momentum ratio only in the extreme configuration of the proton going backwards, with respect to the boost direction, in the Λ center-of-mass. In this case, we have

$$\frac{p_p}{p_\pi} = \frac{-p^* + \beta E_p^*}{+p^* + \beta E_\pi^*} \tag{I.9}$$

This quantity varies from -1 in the COM (no boost) to an asymptotic limit where $\beta = 1$. This limit is 3.1 for $\lambda \to p\pi$ decay; even a moderate boost will give a ratio greater than 3. It is also to note where this ratio crosses $+1$; i.e., when the proton momentum is necessarily higher that the pion momentum. This occurs for $\beta \simeq 0.25$, which corresponds to a λ momentum of order 300 MeV/c.

I.4 Kinematics Related to Particle Mis-identification

We next discuss some simple kinematics relating to backgrounds involving particle identification. Our discussion will be phrased in terms of $\Lambda \to p\pi$ as a background to $K \to \pi^+\pi^-$, but may be easily adapted to other cases. We have two charged particles which are naively the two pion from $K \to \pi^+\pi^-$ decay; let us see under what circumstances a $\Lambda \to p\pi$ decay will reconstruct with the correct mass if the proton is misidentified.

$$M_\Lambda^2 = (E_p + E_2)^2 - (p_{tot}^2) \tag{I.10}$$

$$M_K^2 = (E_1 + E_2)^2 - (p_{tot}^2) \tag{I.11}$$

where $E_{1,2}^2 = p_{1,2}^2 + M_\pi^2$, and $E_p^2 = p_1^2 + M_p^2$. Subtracting and factoring yields

$$M_\Lambda^2 - M_K^2 = (E_p - E_1)(E_p + E_1 + 2E_2) \tag{I.12}$$

We may approximate $E_p + E_1 + 2E_2 \simeq 2(p_1 + p_2)$ in the large term, and expand the energies in $(E_p - E_1)$ in terms of the momenta and masses. We finally arrive at

$$M_\Lambda^2 - M_K^2 = \left(1 + \frac{p_2}{p_1}\right)\left(M_p^2 - M_\pi^2\right) \tag{I.13}$$

We note, as is shown in Section I.3 that one can always assume that the proton is the stiffer track, such that $p_2 < p_1$. We have shown that the reconstructed $\pi\pi$ invariant mass is, to the validity of our approximation, strictly a function of p_1/p_2. Equality occurs for $p_1/p_2 \sim 6.3$. This tells us that a mass cut is essentially identical to a momentum ratio cut. In particular, making a $p\pi$ mass cut only for some momentum ratios is not more efficient than making only a mass cut; events consistent with the $K \to \pi^+\pi^-$ hypothesis that have a low momentum ratio are kinematically unable to reconstruct to the Λ mass.

One can easily adapt the formula above to other pairs of decay modes. If we wish to discuss decays where only some of the particles are observed, such as $K \to \pi^\pm e^\mp \nu_e$ decays, we merely replace the appropriate mass-squared by the *range* of allowed values for the πe system, which results in somewhat less stringent restrictions.

I.5 Kinematics with Missing Particles

We now discuss the kinematics of decays with missing final state particles, as appropriate to our experiment. We assume that we know the parent particle identity, a kaon, and its initial direction, along the line from the target to the decay vertex. The $\pm$ subscript denotes the observed decay products, the $\pi^\pm e^\mp$, and the ν subscript denotes the unobserved neutrino. We employ notation specific to the $K \to \pi^\pm e^\mp \nu_e$ decay, but we note that it is completely general; we refer only to quantities describing the total observed and unobserved systems. We therefore refrain from setting the neutrino mass to zero. We use an asterisk, *, to denote quantities measured in the center-of-mass frame; all other quantities are measured in the lab frame.

Our starting point in the trivial relation among four-vectors

$$P_K = P_\pm + P_\nu. \tag{I.14}$$

Dotting this equation with P_ν and evaluating the left-hand side in the center-of-mass frame, we find

$$E^*_\nu M_K = P_\pm \cdot P_\nu + M^2_\nu \tag{I.15}$$

We then evaluate $P_\pm \cdot P_\nu$ using $M^2_K = (P_\pm + P_\nu)^2$ and $P^2_\nu = M^2_\nu$, etc., yielding,

$$E^*_\nu M_K = \frac{1}{2m_K}\left[M^2_K - M^2_\pm + M^2_\nu\right] \tag{I.16}$$

We also know that

$$(P^*_{L\nu})^2 = (E^*_\nu)^2 - M^2_\nu - P^2_T \tag{I.17}$$

where the L and T superscripts refer to components longitudinal and transverse with respect to the kaon flight direction. Note that we may write similar equations for the observed $\pm$ system by exchanging the ν and $\pm$ subscripts, since they are equivalent from the point of view of this derivation.

Now, we solve for $(P^*_{L\nu})^2 = (P^*_{L\pm})^2$ as follows

$$\begin{aligned}(P^*_{L\nu})^2 &= (E^*_\pm)^2 - M^2_\pm - P^2_T \\ &= \frac{1}{4M^2_K}\left[\left(M^2_K - M^2_\pm - M^2_\nu\right)^2 - 4M^2_\pm M^2_\nu\right] - P^2_T\end{aligned} \tag{I.18}$$

where we have simply substituted for $E^*_\pm$ and done some algebra. The right-hand side is now all measurable quantities. Note that there is a two-fold ambiguity in the solution of the kinematics, since we do not know which sign of the square-root to take for $P^*_{L\nu}$. On the other hand, we now have a kinematic quantity which is positive definite for real decays, and thus a useful quantity to cut on in an analysis. The right-hand side of Eqn. I.18 is sometimes called the 'argument', since it is the argument of a square-root that occurs often in the kinematics. Since there is more angular phase-space for large values of P^2_T, the distribution of values for the argument peaks strongly at zero. We note that in the case of E773, we do not actually know the direction of the kaon before decay, due to the possibility of scattering in the regenerators. Thus, our argument values are smeared somewhat; we measure an event P^2_T that is not solely from the decay. One sees from Eqn. I.18 that too

large a P_T^2 will make the value of the argument negative and unphysical. Fortunately, the scattering contribution is not so large on average, and may point in any direction relative to the intrinsic P_T^2 of the decay; hence, the argument is still a useful kinematic variable even in the presence of scattering.

The Lorentz factors for the two possible boosts from the center-of-mass to the lab frame are easily found. The boost equations are

$$E^* = \gamma(E - \beta\gamma P) \tag{I.19}$$

$$P^* = \gamma(P - \beta\gamma E) \tag{I.20}$$

for either the $\pm$ or ν systems. If we multiply the first equation by P and the second by E and take the sum and difference, we find

$$\beta\gamma = \frac{E_\pm^* P_{L\pm} \pm P_{L\pm}^* E_\pm}{E_\pm^2 - P_{L\pm}^2} \tag{I.21}$$

$$\gamma = \frac{E_\pm^* E_\pm \pm P_{L\pm}^* P_{L\pm}}{E_\pm^2 - P_{L\pm}^2} \tag{I.22}$$

These have a pleasing symmetry. Note that the denominators may be rewritten using

$$E_\pm^2 - P_{L\pm}^2 = M_\pm^2 + P_T^2 \tag{I.23}$$

We have already shown how to evaluate the necessary variables in the numerators in terms of quantities measurable in the lab.

In Chapter 6, a quantity k_{+-0} was introduced. The π^0 plays the role of the unobserved ν, and we have analogous results to those above. The quantity is defined as

$$k_{+-0} = \frac{(P_L^*)^2}{M_\pm^2 + P_T^2} \tag{I.24}$$

This is almost the same as the quantity 'pp0kin' used in many $K \to \pi^+\pi^-\pi^0$ analyses; in fact, 'pp0kin' $= 4M_K^2 k_{+-0}$.

I.6 Spectrometer Momentum Resolution

We first consider the multiple scattering contribution to the resolution. We write the rms scattering angle (in a plane) as

$$\theta_{rms} = \frac{13.6}{p}\sqrt{x}\ (1. + 0.038\ ln\, x)\ \text{mrad GeV}/c \tag{I.25}$$

where x is the radiation length of the scattering material. It is often convenient to write this as $\theta_{rms} = t(x)/p$.

We treat the scattering in the spectrometer as occurring entirely at the plane of the chamber. This is an excellent approximation for the bulk of the material, and an adequate approximation for the helium between the chambers. The helium between two chambers is split, with half assigned to each chamber. We find that the radiation length of Chamber 2 (Chamber 3) is $x_2 = 4.5 \times 10^{-3}$ ($x_3 = 4.2 \times 10^{-3}$).

The real bend angle is given by

$$\theta = k/p \tag{I.26}$$

where k is the p_T kick of the analysis magnet, $p_T = 0.2\text{GeV}/c = 200$ mrad GeV/c. With $t(x_2) = 0.72$ mrad GeV/c and $t(x_3) = 0.70$ mrad GeV/c, we find the fractional momentum resolution from multiple scattering to be

$$\left(\frac{\sigma_p}{p}\right)_{MS} = 5.0 \times 10^{-3}. \tag{I.27}$$

We next treat the effects of chamber resolution. Let the single-plane hit resolution be σ_0. We denote the distance between chambers 1 and 2 (chambers 3 and 4) as d_{12} (d_{34}). Each space point is known to $\sigma_0/\sqrt{2}$, due to the two hits, and the error on the segment slope is σ_0/d; the $\sqrt{2}$ is canceled by the use of 2 space points per segment. The fractional momentum resolution from chamber resolution is thus $\sqrt{(\sigma_0/d_{12})^2 + (\sigma_0/d_{34})^2}/(k/p)$, giving

$$\left(\frac{\sigma_p}{p}\right)_{res} = 1.3 \times 10^{-4}\ p\ (\text{GeV}/c). \tag{I.28}$$

I.7 Comments on Corkscrew Rotations

We now demonstrate explicitly the equivalence of two methods of determining the corkscrew rotations of the chamber system. The original method, explained in Ref. [136]., is somewhat less intuitive. The roots of the method lay in systematic studies of the behavior of the distance of closest approach for the two tracks in a kaon decay. The other method, explained in Chapter 5, is easier to see mathematically.

Let $\mathbf{r}_1$ ($\mathbf{r}_2$) be the vector connecting the points connecting the two tracks in chamber 1 (chamber 2). These vectors lie in the $x-y$ plane. Let $\mathbf{t}_1$ ($\mathbf{t}_2$) be the vector connecting of track 1 (track 2) between chambers 1 and 2. Note that the indices have different meanings for $\mathbf{r}$ and $\mathbf{t}$. Then we may relate the expression used in Ref. [136] to ours as follows

$$\begin{aligned} \mathbf{r}_2 \cdot (\mathbf{t}_1 \times \mathbf{t}_2) &= \mathbf{r}_2 \cdot (\mathbf{t}_1 \times (\mathbf{t}_1 - \mathbf{r}_2 + \mathbf{r}_1)) \\ &= \mathbf{r}_2 \cdot (\mathbf{t}_1 \times \mathbf{t}_1) - \mathbf{r}_2 \cdot (\mathbf{t}_1 \times \mathbf{r}_2) + \mathbf{r}_2 \cdot (\mathbf{t}_1 \times \mathbf{r}_1) \\ &= \mathbf{t}_1 \cdot (\mathbf{r}_1 \times \mathbf{r}_2) \\ &= d_{12} |\mathbf{r}_1 \times \mathbf{r}_2|. \end{aligned} \tag{I.29}$$

I.8 Track Segment χ^2 and SODs

A few points about our historical cut on segment χ^2 may be helpful. We have never properly normalized our χ^2. As calculated, it is the sum of the squared residuals (in m), relative to the fit line, divided by the number of degrees of freedom (2 or 1 for 4 or 3 hit segments). If the chamber resolution was 100 μm, then this quantity would be the true χ^2 scaled by 10^{-8} (the square of the resolution, in m). We tend to interpret the χ^2 as if this were the true resolution, when in fact it is somewhat better and slightly chamber-dependent. Our 'χ^2 cut at 30' is actually a cut on our un-normalized χ^2 at 30×10^{-8} m^2; if we take 90 μm resolution, then our cut is at a real χ^2 of $30/(0.9)^2 \simeq 37$.

We next consider the relationship between our χ^2 and SODs. Let us assume an idealized world where the single-hit resolution is a perfect Gaussian with a width σ. The hits in a hit-pair are uncorrelated, so they are $\sqrt{2}\sigma$ apart on average. The fitted line will split this evenly, giving a residual of $\sigma/\sqrt{2}$. Then, the segment χ^2 is, on average, $4 \cdot (\sigma/\sqrt{2})^2/2 = \sigma^2$ for a complete four-hit segment. Each of the four hits gives an equal contribution, and we divide by the number of degrees of freedom (2) at the end. For a three-hit segment, we get: $2 \cdot (\sigma/\sqrt{2})^2/1 = \sigma^2$. Note that by dividing out the degrees of freedom, we obtain a consistent χ^2 normalization between three- and four-hit segments.

We now argue that in a real fit to a segment, the contributions from each chamber are essentially independent. The only influence that one chamber can have on another is due

to changes in the segment slope. But, even *without* any timing information, the slope is known to about 1 mrad: the cell size divided by the chamber spacing. Thus, the error in the angular correction to the SOD, which arises due to the 1.1 cm spacing of the sense planes, is about 11 μm. This is much smaller than the intrinsic position resolution. Thus the segment is largely just a line through two points, each of which is simply at the midpoint of a hit-pair.

Now, a little though tells us that we can therefore use the average of the SODs from the hit pairs as a measure of track quality equivalent to the segment χ^2. In fact, in the Gaussian approximation above, we find that each SOD has width $\sqrt{2}\sigma$ and $\chi^2 \simeq (SOD_1^2 + SOD_2^2)/4$. For a three-hit segment, we find $\chi^2 \simeq (SOD^2)/2$.

We now note that we lose information by combining the SODs into a χ^2. There is a case were this matters. Consider the occurrence of a δ-ray on the segment. The probability of a δ-ray occurring is not that high, such that there is generally only one hit so affected. The presence of the δ-ray will make one of the SODs bad. Note that the effect on the χ^2 is *different* depending whether we have a three- or four-hit segment. Therefore, a loose cut on the χ^2 cuts events with δ-rays, but the cut is somewhat *tighter* for events with missing hits.

While this is not a big concern, it seems clear that cutting on the SODs directly is better course of action in the future.

REFERENCES

[1] E. Noether, *Nachrichten Gesell. Wissenschaft. Gottingen* **2**, 235 (1918).

[2] E.P. Wigner, *Events, Laws of Nature, and Invariance Principles*, Nobel Lecture, reprinted in *Symmetries and Reflections: Scientific Essays of Eugene P. Wigner*, (Indiana Univ. Press, Bloomington, 1967), p. 38.

[3] C.N. Yang, *The Discrete Symmetries P, T and C*, in *J. Phys.* **43**, Coll. C-8, Suppl. to No. 12, 1982, p. 439.

[4] E.P. Wigner, *Z. Phys.* **43**, 624 (1928).

[5] J.V. Neumann and E.P. Wigner, *Z. Phys.* **49**, 73 (1928).

[6] O. Laporte, *Z. Phys.* **23**, 135 (1924).

[7] H.N. Russell, *Science* **59**, 512 (1924).

[8] E.M. Purcell and N.F. Ramsey, *Phys. Rev.* **78**, 807 (1950).

[9] T.D. Lee and C.N. Yang, *Phys. Rev.* **104**, 254 (1956).

[10] C.S. Wu et al., *Phys. Rev.* **105**, 1413 (1957).

[11] R.L. Garwin, L.M. Lederman, and M. Weinrich, *Phys. Rev.* **105**, 1415 (1957).

[12] J.I. Friedman and V.L. Telegdi, *Phys. Rev.* **105**, 1681 (1957).

[13] P.A.M. Dirac, *Proc. Roy. Soc.* **A117**, 610 (1928).

[14] W.H. Furry, *Phys. Rev.* **51**, 125 (1937).

[15] E. Majorana, *Nuovo Cim.* **14**, 171 (1937).

[16] H.A. Kramers, *Proc. Ak. Wet. Amsterdam* **40**, 814 (1937).

[17] L. Landau, *Sov. Phys. JETP* **5**, 336 (1957).

[18] L. Landau, *Nucl. Phys.* **3**, 127 (1957).

[19] W. Pauli, in *Niels Bohr and the Development of Physics*, edited by W. Pauli, (Pergamon Press, Elmsford, NY, 1955), page 30.

[20] J. Schwinger, *Phys. Rev.* **82**, 914 (1951).

[21] J. Schwinger, *Phys. Rev.* **91**, 713 (1953).

[22] J. Schwinger, *Phys. Rev.* **94**, 1362 (1954).

[23] G. Lüders, *Dan. Mat. Fys. Medd.* **28**, 1 (1954).

[24] J.S. Bell, *Proc. Royal Soc.* **231**, 479 (1955).

[25] Res Jost, *Helv. Phys. Acta.* **30**, 409 (1957).

[26] Gerhart Lüders, *Annals of Physics* **2**, 1 (1957).

[27] M. Gell-Mann and A. Pais, *Phys. Rev.* **97**, 1387 (1955).

[28] S.B. Treiman and R.G. Sachs, *Phys. Rev.* **103**, 1545 (1956).

[29] V.F. Weisskopf and E.P. Wigner, *Z. Phys.* **63**, 54 (1930).

[30] V.F. Weisskopf and E.P. Wigner, *Z. Phys.* **65**, 18 (1930).

[31] T.D. Lee, R. Oehme, and C.N. Yang, *Phys. Rev.* **106**, 340 (1957).

[32] J.H. Christenson, J.W. Cronin, V.L. Fitch, and R. Turlay, *Phys. Rev. Lett.* **13**, 138 (1964).

[33] E.P. Wigner, *Gott. Nach. Math. Naturw. Kl.* **32**, 546 (1932).

[34] R.G. Sachs, *The Physics of Time Reversal*, The University of Chicago Press, Chicago, 1987.

[35] J.M. Emmerson, *Symmetry Principles in Particle Physics*, Clarendon Press, Oxford, 1972.

[36] H.A. Kramers, *Proc. Ak. Wet. Amsterdam* **33**, 959 (1930).

[37] R.F. Streater and A.S. Wightman, *PCT, Spin, Statistics and All That*, Benjamin, New York, 1964.

[38] Robert M. Wald, *Phys. Rev.* **D21**, 2742 (1980).

[39] Particle Data Group, L. Montenet, et al., *Phys. Rev.* **D50**, 1173 (1994).

[40] *J. Phys.* **43**, Coll. C-8, Suppl. to No. 12, 1982.

[41] *The Birth of Particle Physics*, edited by L.M. Brown and L. Hoddeson, (Cambridge Univ. Press, New York, 1983).

[42] Abraham Pais, *Inward Bound: Of Matter and Forces in the Physical World*, Oxford Univ. Press, New York, 1986.

[43] *Pions to Quarks: Particle Physics in the 1950s*, edited by L.M. Brown, M. Dresden, and L. Hoddeson, (Cambridge Univ. Press, New York, 1989).

[44] L. Leprince-Ringuet and M. L'Héritier, *Comptes Rendus* **219**, 618 (1944).

[45] G.D. Rochester and C.C. Butler, *Nature* **160**, 855 (1947).

[46] R. Brown et al., *Nature* **163**, 82 (1949).

[47] R. Armenteros et al., *Nature* **167**, 501 (1951).

[48] R. Armenteros et al., *Phil. Mag.* **42**, 1113 (1951).

[49] R.W. Thompson, Hans O. Cohn, and R.S. Flum, *Phys. Rev.* **83**, 175 (1951).

[50] W.B. Fowler et al., *Phys. Rev.* **90**, 1126 (1953).

[51] W.B. Fowler et al., *Phys. Rev.* **91**, 1287 (1953).

[52] Y. Nambu, K. Nishijima, and Y. Yamaguchi, *Prog. Theor. Phys.* **6**, 615 (1951).

[53] Y. Nambu, K. Nishijima, and Y. Yamaguchi, *Prog. Theor. Phys.* **6**, 619 (1951).

[54] K. Aizu and T. Kinoshita, *Prog. Theor. Phys.* **6**, 630 (1952).

[55] H. Miyazawa, *Prog. Theor. Phys.* **6**, 631 (1952).

[56] S. Oneda, *Prog. Theor. Phys.* **6**, 633 (1952).

[57] A. Pais, *Phys. Rev.* **86**, 663 (1952).

[58] R.W. Thompson et al., *Phys. Rev.* **95**, 1576 (1954).

[59] R. Armenteros et al., *Phil. Mag.* **43**, 597 (1952).

[60] Tadao Nakano and Kazuhiko Nishijinma, *Prog. Theor. Phys.* **10**, 581 (1953).

[61] Kazuhiko Nishijima, *Prog. Theor. Phys.* **12**, 107 (1954).

[62] Kazuhiko Nishijima, *Prog. Theor. Phys.* **13**, 285 (1955).

[63] R.G. Sachs, *Phys. Rev.* **99**, 1573 (1955).

[64] M. Gell-Mann, *Nuovo Cim.,* Suppl. to Vol. **6**, 848 (1956).

[65] M.W. Friedlander et al., *Nuovo Cim.* **2**, 666 (1955).

[66] M. Ceccerelli et al., *Nuovo Cim.* **2**, 828 (1955).

[67] W.B. Fowler et al., *Phys. Rev.* **103**, 208 (1956).

[68] W.A. Cooper et al., *Nuovo Cim.* **5**, 1388 (1957).

[69] Anatole M. Shapiro, *Rev. Mod. Phys.* **28**, 164 (1956).

[70] R.H. Dalitz, *Phil. Mag.* **44**, 1068 (1953).

[71] R.H. Dalitz, *Phys. Rev.* **94**, 1046 (1954).

[72] N. Cabibbo, *Phys. Rev. Lett.* **10**, 531 (1963).

[73] M. Kobayashi and T. Maskawa, *Prog. Theor. Phys.* **49**, 652 (1973).

[74] S. Weinberg, *Phys. Rev. Lett.* **19**, 1264 (1967).

[75] S.L. Glashow, J. Iliopoulos, and L. Maiani, *Phys. Rev.* **D2**, 1285 (1970).

[76] M. Gell-Mann, *Phys. Rev.* **92**, 833 (1953).

[77] George A. Snow, *Phys. Rev.* **103**, 1111 (1956).

[78] K. Lande et al., *Phys. Rev.* **103**, 1901 (1956).

[79] W.F. Fry, J. Schneps, and M.S. Swami, *Phys. Rev.* **103**, 1904 (1956).

[80] K. Lande, L.M. Lederman, and W. Chinowsky, *Phys. Rev.* **105**, 1925 (1957).

[81] M. Baldo-Ceolin et al., *Nuovo Cim.* **5**, 130 (1957).

[82] R. Ammar et al., *Nuovo Cim.* **5**, 1801 (1957).

[83] F. Eisler et al., *Nuovo Cim.* **5**, 1701 (1957).

[84] Elihu Boldt, David O. Caldwell, and Yash Pal, *Phys. Rev. Lett.* **1**, 150 (1958).

[85] A. Pais and O. Piccioni, *Phys. Rev.* **100**, 1487 (1955).

[86] K.M. Case, *Phys. Rev.* **103**, 1449 (1956).

[87] Myron L. Good, *Phys. Rev.* **106**, 591 (1957).

[88] Francis Muller et al., *Phys. Rev. Lett.* **4**, 418 (1960).

[89] Myron L. Good, *Phys. Rev.* **121**, 311 (1961).

[90] R.G. Sachs, *Phys. Rev.* **129**, 2280 (1963).

[91] R.G. Sachs, *Ann. Phys.* **22**, 239 (1963).

[92] T.D. Lee and C.S. Wu, *Ann. Rev. Nuc. Sci.* **15**, 381 (1965).

[93] J.S. Bell and J. Steinberger, in *Proceedings of the Oxford International Conference on Elementary Particles, 1965*, edited by A.E. Taylor T.R. Walsh and B. Southworth, (Rutherford Laboratory, Chilton, England, 1966), page 195.

[94] V.V. Barmin et al., *Nucl. Phys.* **B247**, 293, E:**B254**, 747 (1984).

[95] N.W. Tanner and R.H. Dalitz, *Annals of Physics* **171**, 463 (1986).

[96] L. Lavoura, *Phys. Rev.* **D42**, 273 (1990).

[97] L. Lavoura, *Phys. Rev.* **D42**, 3142 (1990).

[98] C.D. Buchanan et al., *Phys. Rev.* **D45**, 4088 (1992).

[99] C.O. DIb and R.D. Peccei, *Phys. Rev.* **D46**, 2265 (1992).

[100] M. Hayakawa and A.I. Sanda, *Phys. Rev.* **D48**, 1150 (1993).

[101] T. Nakada, in *Lepton and Photon Interactions (AIP Conference Proceedings No. 302)*, edited by Persis Drell and David Rubin, (AIP Press, New York, 1993), page 425.

[102] L. Wolfenstein, *Phys. Rev. Lett.* **13**, 562 (1964).

[103] B. Winstein and L. Wolfenstein, *Rev. Mod. Phys.* **65**, 1131 (1993).

[104] P.K. Kabir, *The CP Puzzle*, Academic Press, New York, 1968.

[105] H.W. Wyld and S.B.Treiman, *Phys. Rev.* **106**, 169 (1957).

[106] D. Dorfan et al., *Phys. Rev. Lett.* **19**, 987 (1967).

[107] Sheldon Bennett et al., *Phys. Rev. Lett.* **19**, 993 (1967).

[108] Sheldon Bennett et al., *Phys. Rev. Lett.* **19**, 997 (1967).

[109] L.K. Gibbons et al., *Phys. Rev. Lett.* **70**, 1203 (1993).

[110] G.D. Barr et al., *Phys. Lett.* **B317**, 233 (1993).

[111] R. Gatto, *Phys. Rev.* **106**, 168 (1957).

[112] J.D. Jackson, S.B. Treiman, and H. Wyld Jr., *Phys. Rev.* **106**, 517 (1957).

[113] J.D. Jackson, S.B. Treiman, and H. Wyld Jr., *Nucl. Phys.* **4**, 206 (1957).

[114] M.E. Ebel and G. Feldman, *Nucl. Phys.* **4**, 213 (1957).

[115] N.F. Ramsey, *Phys. Rev.* **109**, 225 (1958).

[116] E.P. Shabalin, *Sov. J. Nucl. Phys.* **28**, 75 (1978).

[117] M.J. Booth, R.A. Briere, and R.G. Sachs, *Phys. Rev.* **D41**, 177 (1990).

[118] R.D. Peccei, in *CP Violation*, edited by C. Jarlskog, (World Scientific, Singapore, 1989), page 503.

[119] J. Bernstein, N. Cabibbo, and T.D. Lee, *Phys. Rev. Lett.* **132**, 146 (1964).

[120] J.S. Bell and J.K. Perring, *Phys. Rev. Lett.* **13**, 348 (1964).

[121] Andrei D. Sakharov, *JETP Lett.* **5**, 24 (1967).

[122] T.T. Wu and C.N. Yang, *Phys. Rev. Lett.* **13**, 380 (1964).

[123] Erik Chell and M.G. Olsson, *Phys. Rev.* **D48**, 4076 (1993).

[124] R.A. Briere and L.H. Orr, *Phys. Rev.* **D40**, 2269 (1989).

[125] W.C. Carithers et al., *Phys. Rev. Lett.* **34**, 1240 (1975).

[126] L.K. Gibbons et al., *Phys. Rev. Lett.* **70**, 1199 (1993).

[127] L.K. Gibbons et al., *Phys. Rev. Lett.* **61**, 2661 (1988).

[128] A.R. Barker et al., *Phys. Rev.* **D41**, 3546 (1990).

[129] V. Papadimitriou et al., *Phys. Rev.* **D44**, R573 (1991).

[130] G.E. Graham et al., *Phys. Lett.* **B295**, 169 (1992).

[131] G. Makoff et al., *Phys. Rev. Lett.* **70**, 1591 (1993).

[132] E.J. Ramberg et al., *Phys. Rev. Lett.* **70**, 2525 (1993).

[133] E.J. Ramberg et al., *Phys. Rev. Lett.* **70**, 2529 (1993).

[134] A.R. Barker et al., Proposal for FNAL Experiment 799, December, 1989.

[135] Y.W. Wah et al., Proposal for FNAL Experiment 773, March, 1986.

[136] L.K. Gibbons, Ph.D. thesis (The University of Chicago, August, 1993).

[137] J. Roehrig et al., *Phys. Rev. Lett.* **38**, 1116, E:**39**,674 (1977).

[138] A. Gsponer et al., *Phys. Rev. Lett.* **42**, 13 (1979).

[139] M.B.Woods, Ph.D. thesis (The University of Chicago, June, 1988).

[140] J.R. Patterson, Ph.D. thesis (The University of Chicago, December, 1990).

[141] B. Schwingenheuer, Ph.D. thesis (The University of Chicago, March, 1995).

[142] D.A. Harris, Ph.D. thesis (The University of Chicago, June, 1994).

[143] K.S. McFarland, Ph.D. thesis (The University of Chicago, March, 1994).

[144] M. Asner et al., *Nucl. Instr. and Meth.* **A291**, 577 (1990).

[145] W.R. Nelson and H. Hirayama and W.O. Rogers, The EGS4 Code System, SLAC-Report-265, Stanford Linear Accelerator Center, 1985.

[146] M. Karlsson, Ph.D. thesis (Princeton University, August, 1990).

[147] Nick Solomey, private communication.

[148] H. Primakoff, *Phys. Rev.* **81**, 899 (1951).

[149] D. Carlsmith et al., *Phys. Rev. Lett.* **56**, 18 (1986).

[150] J.N. Matthews, *et al.*, submitted to Phys. Rev. Lett., 1995.

[151] J.N. Matthews, Ph.D. thesis (Rutgers University, June, 1995).

[152] A.J. Malensek, Preprint FN-341, FN-341A (errata), FNAL, October 1981.

[153] H. W. Atherton et al., Preprint CERN 80:07, CERN, 1980.

[154] A. Schiz et al., *Phys. Rev.* **D21**, 3010 (1980).

[155] G.J. Bock et al., *Phys. Rev. Lett.* **42**, 350 (1979).

[156] Particle Data Group, K. Hikasa, et al., *Phys. Rev.* **D45**, 1 (1992).

[157] Particle Data Group, C. Bricman, et al., *Phys. Lett.* **75B**, 1 (1978).

[158] J. Skjeggestad et al., *Nucl. Phys.* **B48**, 343 (1972).

[159] C. Geweniger et al., *Phys. Lett.* **48B**, 487 (1974).

[160] W.C. Carithers et al., *Phys. Rev. Lett.* **34**, 1244 (1975).

[161] S.H. Aronson et al., *Nuovo Cim.* **32A**, 236 (1976).

[162] N. Grossman et al., *Phys. Rev. Lett.* **59**, 18 (1987).

[163] B. Schwingenheuer *et al.*, submitted to Phys. Rev. Lett., 1994.

[164] M. Cullen et al., *Phys. Lett.* **32B**, 523 (1970).

[165] J.H. Christenson, J.W. Cronin, V.L. Fitch, and R. Turlay, *Phys. Rev.* **B140**, 74 (1965).

[166] C. Geweniger et al., *Phys. Lett.* **52B**, 108 (1974).

[167] S. Gjesdal et al., *Phys. Lett.* **52B**, 113 (1974).

[168] H. Wahl, in *Rare Decay Symposium: Proceedings*, edited by J. Ng and J.-M. Poutissou, (World Scientific, Teaneck, NJ, 1989), page 281.

[169] C. Geweniger et al., *Phys. Lett.* **52B**, 119 (1974).

[170] R. Carosi et al., *Phys. Lett.* **B237**, 303 (1990).

[171] R. Adler et al., *Phys. Lett.* **B286**, 180 (1992).

[172] R. Adler et al., *Sov. J. Nucl. Phys.* **55**, 840 (1992).

[173] Claudio Santoni, *Nucl. Instr. and Meth.* **A333**, 93 (1993).

[174] R. Adler et al., *Nucl. Phys.* **A558**, 437c (1993).

[175] R. Adler et al., *Nucl. Phys.* **A558**, 449c (1993).

[176] Results presented at the 27th International Conference on High Energy Physics (Glasgow, 1994).

[177] Barbiellini et al., *Phys. Lett.* **B43**, 529 (1973).

[178] J.H. Christenson et al., *Phys. Rev.* **43**, 1209 (1979).

[179] J.H. Christenson et al., *Phys. Rev.* **43**, 1212 (1979).

[180] M. Karlsson et al., *Phys. Rev. Lett.* **64**, 2976 (1990).

[181] K.R. Schubert et al., *Phys. Lett.* **31B**, 662 (1970).

[182] G.B. Thomson and Y. Zou, *Phys. Rev.* **D51**, 1412 (1995).

[183] V. Gibson, in *CP Violation in Particle Physics and Astrophysics*, edited by J. Tranh Van Tran, (Editions Frontieres, Gif-sur-Yvette, France, 1990), page 213.

[184] V.L. Fitch, R.F. Roth, J.S. Russ, and W. Vernon, *Phys. Rev. Lett.* **15**, 73 (1965).

[185] V.V. Anisovich and V.M. Shekhter, *Nucl. Phys.* **B55**, 455 (1973).

[186] V.M. Shekhter and L.M. Shcheglova, *Sov. J. Nucl. Phys.* **27**, 567 (1978).

[187] K. Fialkowski and W. Kittel, *Rep. Prog. Phys.* **46**, 1283 (1983).

[188] M. Gell-Mann, M.L. Goldberger, and W.E. Thirring, *Phys. Rev.* **95**, 1612 (1954).

[189] R. de L. Kronig, *J. Opt. Soc. Amer.* **12**, 547 (1926).

[190] H.A. Kramers, *Atti. Congr. Intern. Fisici, Como* **2**, 545 (1927).

[191] H.M Nussenzveig, *Causality and Dispersion Relations*, Academic Press, New York, 1972.

[192] Martin Block and Robert Cahn, *Rev. Mod. Phys.* **57**, 563 (1985).

[193] R. Odorico, *Nuovo Cim.* **54**, 96 (1968).

[194] J.A. McClure and S. Jorna, *Nuovo Cim.* **67**, 667 (1970).

[195] R.F. Alvarez-Estrada, *Annals of Physics* **68**, 196 (1971).

[196] Carl B. Dover and George E. Walker, *Phys. Rept.* **89**, 1 (1982).

[197] J. Bronzan, G.L. Kane, and U.P. Sukhatme, *Phys. Lett.* **B49**, 272 (1974).

[198] U. Sukhatme et al., *Phys. Rev.* **D11**, 3431 (1975).

[199] J. Fischer and P. Kolar, *Phys. Rev.* **D17**, 2168 (1978).

[200] G.K. Eichmann and J. Dronkers, *Phys. Lett.* **B52**, 428 (1974).

[201] J. Heidrich and E. Kazes, *Lett. Nuovo Cim.* **12**, 365 (1975).

[202] R.J. Eden, *High Energy Collisions of Elementary Particles*, Cambridge Univ. Press, Cambridge, 1967.

[203] P.D.B. Collins, *Phys. Rept.* **1C**, 103 (1971).

[204] N.M. Queen and G. Violini, *Dispersion Theory in High-Energy Physics*, Halstead Press, New York, 1974.

[205] P.D.B. Collins, *An Introduction to Regge Theory and High Energy Physics*, Cambridge Univ. Press, Cambridge, 1977.

[206] R.E. Hendrick et al., *Phys. Rev.* **D11**, 536 (1975).

[207] Mujahid Kamran, *Phys. Rept.* **108C**, 275 (1984).

[208] M.M. Block et al., in *Proceedings of the XXIII International Symposium on Multiparticle Dynamics* (Aspen, 1993), edited by M.M. Block and A.R. White, (World Scientific, Singapore, 1994), page 373.

[209] L. Lukaszuk and B. Nicolescu, *Lett. Nuovo Cim.* **8**, 405 (1973).

[210] R.J. Glauber, in *Lectures in Theoretical Physics* (Colorado, 1958), edited by W.E. Britten et al., (Interscience, New York, 1959), pages Vol. 1, p. 315.

[211] R.J. Glauber and V. Franco, *Phys. Rev. Lett.* **156**, 1685 (1967).

[212] R.J. Glauber, in *High Energy Physics and Nuclear Structure* (Rehovoth, 1967), edited by G. Alexander, (North-Holland, Amsterdam, 1967), page 311.

[213] R.J. Glauber, in *High Energy Physics and Nuclear Structure* (Columbia, 1969), edited by S. Devons, (Plenum, New York, 1970), page 207.

[214] R.J. Glauber, *Phys. Rev.* **100**, 242 (1955).

[215] Colin Wilkin, *Phys. Rev. Lett.* **17**, 561 (1966).

[216] B. Diu and A. Ferraz de Camargo, *Nuovo Cim.* **47A**, 495 (1978).

[217] B. Diu and A. Ferraz de Camargo, *Z. Phys.* **C3**, 345 (1980).

[218] B. Diu and A. Ferraz de Camargo, PAR-LPTHE 79/10 (1979).

[219] A. Gsponer et al., *Phys. Rev. Lett.* **42**, 9 (1979).

[220] W.R. Mozlon et al., *Phys. Rev. Lett.* **41**, 1213, E:**41**,1523,1835 (1978).

[221] K. Gottfried and J.D. Jackson, *Nuovo Cim.* **33**, 309 (1964).

[222] L.S. Littenberg, *Phys. Rev.* **D21**, 2027 (1980).

[223] D. Carlsmith et al., *Phys. Rev.* **D36**, 3502 (1987).

[224] L.L. Foldy, *Phys. Rev.* **67**, 107 (1945).

[225] Roy A. Briere and Bruce Winstein, submitted to Phys. Rev. Lett., 1994.

[226] H.K. Bode, *Network Analysis and Feedback Amplifier Design*, D. Van Nostrand, New York, 1945.

[227] H. Foeth et al., *Phys. Lett.* **31B**, 544 (1970).

[228] W.C. Carithers et al., *Nucl. Phys.* **B118**, 333 (1977).

[229] H. Faissner et al., *Phys. Lett.* **30B**, 544 (1969).

[230] F. Dydak et al., *Nucl. Phys.* **B102**, 253 (1976).

[231] L. Bertocchi and D. Treleani, *Nuovo Cim.* **50A**, 338 (1979).

[232] V.N. Gribov, *Sov. Phys. JETP* **29**, 483 (1960).

[233] V.A. Karmanov and L.A. Kondratyuk, *JETP Lett.* **18**, 266 (1973).

[234] P.V.R. Murthy et al., *Nucl. Phys.* **B92**, 269 (1975).

[235] A. Gsponer, Ph.D. thesis (ETH Zurich, 1978).

[236] D.W. Joynson and B.R. Martin, *Nucl. Phys.* **B134**, 83 (1978).

[237] K. Kleinknecht and S. Luitz, *Phys. Lett.* **B336**, 581 (1994).